The Role of Human Two-Pore Channel 1 in Membrane Protein Trafficking

William John Burton

Department of Pharmacology & The Queen's College

University of Oxford

A thesis submitted for the degree of

DPhil in Pharmacology

Trinity term 2026

Approximate word count: ~48,000

Publications

Burton WJ, Lin A, Morgan A, Davis LC, Chen CC, Galione A. Endosomal TPC1-mediated Ca^{2+} nanodomains regulate transferrin receptor trafficking and iron homeostasis. *Proceedings of the National Academy of Sciences of the United States of America*. 2026 Jul;123(29):e2530835123. doi: 10.1073/pnas.2530835123

Lin A, Lin NY, Keller M, Schütz R, Wu YZ, **Burton WJ**, Kinanti NP, Liu YW, Bracher F, Galione A, Hsu HJ, Kuo CY, Yao CY, Urban N, Chen CC. *O*-linked glycan-dependent gating of TPC2 controls lysosomal excitability and organelle remodeling. *Nature Communications*. 2026 Jun;17(1):7396. doi: 10.1038/s41467-026-74268-6

Gu ZQ, Wang HT, Li Y, Krogsaeter E, Lin AC, Lin J, Liu YS, Lin WS, **Burton WJ**, Liu ML, Feldmann C, Tang R, Po CW, Hou PS, Lin NY, Lin JY, Chao TL, Chang SY, Yang Z, Keller M, Leser C, Fenske S, Bracher F, Wahl-Schott C, Galione A, Tsai YH, Grimm C, Biel M, Chen CC. TRPML2 channel modulation by $PI(3,5)P_2$ and small-molecule agonists controls endosomal vesicle dynamics. *Biomedicine and Pharmacotherapy.* 2025 Aug;189(1):118350. doi: 10.1016/j.biopha.2025.118350

Abstracts, Presentations & Awards

Burton WJ, Lin A, Chen CC, Galione A. *Endosomal TPC1-mediated Ca^{2+} nanodomains regulate TfR trafficking and iron homeostasis.* British Pharmacology Society: Organelle Pharmacology Conference (2026). Abstract and poster 1st prize.

Burton WJ. *Characterisation of two-pore channel 1 (TPC1) in cell-surface protein trafficking.* University of Oxford Department of Pharmacology Paton Prize Presentation (2025). Presentation 1st prize.

Burton WJ & Galione A. *TPC1 regulates cell-surface protein trafficking via local Ca^{2+} nanodomains.* University of Oxford Department of Pharmacology Research Symposium (2025). Abstract and poster 1st prize.

Burton WJ. *Intracellular components and protein trafficking*. National Taiwan University Guest Lecture (2024 – 2026). Presentation.

Burton WJ & Galione A. *TPC1 requirement for cell membrane protein trafficking*. Endo-lysosomal Ion Channels and Diseases Symposium (2024). Abstract and poster.

Awards

The Waverley Scholarship	2022 – 2026	The Queen's College
Clarendon Scholarship	2022 – 2026	University of Oxford and EPSRC

Acknowledgment

First, I would like to thank my supervisor Professor Antony Galione for his guidance and support throughout my DPhil and his valuable feedback on my thesis. I would also like to express my thanks to the members of the Galione group, specifically Dr Anthony Morgan and Dr Lianne Davis who have generously dedicated their time to teaching me techniques, discussing physiological concepts, proofreading my work, and patiently answering my extensive questions. Thanks to Dr Julie Xiao from the Townsend lab for providing the *TPCN1* and *TPCN2* knockout HeLa cell lines.

I have built up an excellent collaboration with Professor Cheng-Chang 'Maxo' Chen at the National Taiwan University in Taipei. I would like to thank Maxo for his expertise in endo-lysosomal patch-clamping and for hosting me in Taiwan to teach me this challenging technique. I am very grateful to Maxo and his DPhil student Alice Lin who contributed towards this thesis, helping perform the TPC1 electrophysiology experiments. I would also like to thank Jackson Lin and Cindy Wang from the Chen group, for their kindness and hospitality during my stay in Taiwan.

Finally, a special thank you to my friends and family, who have supported me throughout my education, especially during my time at Oxford University.

The Role of Human Two-Pore Channel 1 in Membrane Protein Trafficking

William John Burton
The Queen's College

DPhil in Pharmacology
Trinity Term 2026

Abstract

Two-pore channels (TPCs) are recognised as Ca^{2+}/Na^{+}-permeable ion channels localised to endo-lysosomal organelles. Although the lysosomal isoform TPC2 has been extensively studied, the physiological processes that require TPC1 and how the channel properties of TPC1 are involved in these processes, remains less clearly defined.

Chapter 1 introduces the TPC family in the context of Ca^{2+} signalling and endo-lysosomal membrane protein trafficking. **Chapter 2** details the methodologies and techniques used throughout this thesis.

Chapter 3 investigates the regulatory role of TPC1 in the intracellular trafficking of iron-loaded transferrin for cellular iron homeostasis. Trafficking and recycling experiments in CRISPR-edited TPC-deficient HeLa cells revealed that TPC1 specifically regulates transferrin uptake by influencing cell surface levels of the transferrin receptor (TfR), through regulation of endosomal trafficking and recycling. Impaired iron-loaded transferrin uptake reduces intracellular labile iron and increases the prevalence of disease-like iron-deficiency phenotypes in mammalian cells and mice, thereby concluding that TPC1 expression is critical for iron homeostasis.

Chapter 4 characterises the TPC1 ionic fluxes integral for cell-membrane protein trafficking. Through organelle-targeted Ca^{2+} buffering and depletion, endosomal Ca^{2+} stores (10-12 μM) were identified as the source of Ca^{2+} required for efficient TfR trafficking, whose localised endosomal TPC1-mediated Ca^{2+} nanodomains are segregated from global ER-derived Ca^{2+} transients. Generation and expression of a Na^{+}-deficient Ca^{2+}-permeable TPC1 mutant revealed that it is the Ca^{2+} modality, not Na^{+} fluxes, or endosomal pH changes, that regulate TfR membrane trafficking.

Chapter 5 expands upon the previous chapters and evaluates the selective or generic role of TPC1 in cell membrane trafficking and how TPC1 activity is gated. Three discrete membrane protein trafficking pathways, the transferrin cycle, LDL cycle, and pinocytosis, were examined using fluorescently-labelled ligands. TPC1 was shown to selectively regulate transferrin trafficking and pinocytosis through distinct channel ion modalities, indicating that there is specificity for the membrane trafficking pathways TPC1 mediates. TPC1 activity depended on the lipid $PI(3,5)P_2$, since trafficking was impaired by a lipid-insensitive TPC1 and inhibitors of lipid synthesis.

Chapter 6 discusses the impact of the results obtained and future prospects for TPC1 research.

Declaration

A substantial part of my DPhil work has been published in the *Proceedings of the National Academy of Sciences* journal (Burton *et al*. 2026), work for which I performed and contributed to all experiments and wrote the original manuscript. Text and figures from this manuscript have been used in this thesis without modification. To avoid continuous citation, this manuscript is cited at the beginning of each results chapter.

The use of generative AI tools in this submission were critically assessed and confirmed as compliant with University, divisional, and departmental guidelines. ChatGPT5.3 (OpenAI) was used in moderation for small, local changes including checking spelling and sentence grammar, as well as to summarise background literature.

Contents

List of Abbreviations

AM	Acetoxymethyl ester
At	*Arabidopsis thaliana* (Thale cress)
ATP	Adenosine triphosphate
AMPA	Alpha-amino-3-hydroxy-5-methyl-4-isoxazolepropionic acid
BAPTA	1,2-bis(2-aminophenoxy)ethane-N,N,N',N'-tetraacetic acid
BCA	Bicinchoninic acid
BSA	Bovine serum albumin
cADPR	Cyclic ADP-ribose
cAMP	Cyclic adenosine monophosphate
CB	Calbindin-2
CAX	Ca^{2+}/H^{+} exchange
CaMKK2	Ca^{2+}/calmodulin-dependent protein kinase kinase 2
[Ca^{2+}]	Calcium concentration
CF	Cyanine-based fluorescence
CICR	Calcium-induced calcium release
CLIC	Clathrin-independent carriers
CPA	Cyclopiazonic acid
CREB	cAMP response element-binding protein
CTCF	Corrected total cell fluorescence
Dr	*Danio rerio* (Zebrafish)
DMEM	Dulbecco's Modified Eagle's Medium
DMSO	Dimethyl sulfoxide
DMT	Divalent metal transporter
DNA	Deoxyribonucleic acid
DUOX	Dual NADPH oxidase
ECM	Extracellular medium
EC_{50}	Half maximal effective concentration
EDTA	Ethylenediaminetetraacetic acid
EEA1	Early endosome antigen 1
EGF	Epidermal growth factor

EGFR	Epidermal growth factor receptor
EGTA	Ethylene glycol-bis (2-aminoethylether)-N,N,N',N'-tetraacetic acid
E_{rev}	Reversal potential
ER	Endoplasmic reticulum
ERES	Endoplasmic reticulum export sequence
EtOH	Ethanol
FBS	Foetal bovine serum
FKBP	FK506-binding accessory protein
Fou2	Fatty acid oxygenation upregulated 2
FRB*	FKBP-rapamycin-binding
fS	Femtosiemens
FTH1	Ferritin heavy chain 1
GECI	Genetically encoded calcium indicator
GEEC	GPI-anchored protein-enriched endosomal compartments
GOF	Gain of function
GPCR	G protein-coupled receptor
GPI	Glycosylphosphatidylinositol
GPN	Glycyl-L-phenylalanine-naphthylamide
gRNA	Guide RNA
GTP	Guanosine triphosphate
GTPase	GTP hydrolase
G6PDH	Glucose-6-phosphate dehydrogenase
HEDTA	N-(2-Hydroxyethyl)ethylenediamine-N,N′,N′-triacetic acid
HEPES	4-(2-hydroxyethyl)-1-piperazineethanesulphonic acid
HFE	High-Fe^{2+}
Hs	*Homo sapiens* (Human)
ICM	Intracellular-like medium
IC_{50}	Half maximal inhibitory concentration
IMDM	Iscove's modified Dulbecco's medium
IMPC	International Mouse Phenotyping Consortium
IP_3	Inositol-1,4,5-trisphosphate
IP_3R	Inositol-1,4,5-trisphosphate receptor
JNK	c-Jun N-terminal kinase
JPT	Jupiter microtubule-associated homolog 2

K_d	Binding affinity
KO	Knockout
LAMP	Lysosome-associated membrane protein
LB	Luria broth
LDL	Low-density lipoprotein
LDLR	Low-density lipoprotein receptor
LGCC	Ligand-gated calcium channel
LIMP-2	Lysosomal integral membrane protein-2
LRRK2	Leucine-rich repeat kinase 2
Lsm12	Like-Sm protein 12
MCU	Mitochondrial calcium uniporters
MCS	Membrane contact site
MEF	Mouse embryonic fibroblast
MES	2-(N-morpholino)ethanesulfonic acid
MSA	Methanesuphonic acid
MLIV	Mucolipidosis type IV
MOPS	3-(N-morpholino)propanesulphonic acid
Ms	*Mus musculus* (Mouse)
Mtb	*Mycobacterium tuberculosis*
mTOR	Mechanistic target of rapamycin
NAADP	Nicotinic acid adenosine dinucleotide phosphate
NADP	Nicotinamide adenine dinucleotide phosphate
NAD^+	Nicotinamide adenine dinucleotide
NCOA4	Nuclear receptor coactivator 4
NCX	Na^+/Ca^{2+} exchanger
NHE	Na^+/H^+ exchanger
NMDA	N-methyl-D-aspartate
NMDG	N-methyl-D-glucamine
PBS	Phosphate buffered saline
PCR	Polymerase chain reaction
PDGFRβ	Platelet-derived growth factor receptor β
PFA	Paraformaldehyde
PIP_2	Phophatidylinositol-4,5-bisphosphate
PI(3)P	Phosphatidylinositol-3-phosphate

PI(3,4,5)P_3	Phosphatidylinositol-3,4,5-trisphosphate
PI(3,5)P_2	Phosphatidylinositol-3,5-bisphosphate
PI(4)P	Phosphatidylinositol-4-phosphate
PI(4,5)P_2	Phosphatidylinositol-4,5-bisphosphate
PLC	Phospholipase C
PMCA	Plasma membrane Ca^{2+}-ATPase
PPIX	Protoporphyrin-IX
Rr	*Rattus rattus* (Rat)
RNA	Ribonucleic acid
ROI	Region of interest
ROS	Reactive oxygen species
RT-PCR	Reverse transcription PCR
RyR	Ryanodine receptor
SARM	Sterile alpha and TIR motif-containing 1
SDS	Sodium dodecyl sulphate
SERCA	Sarco/endoplasmic reticulum ATPase
sgRNA	Single guide RNA
SNARE	Soluble N-ethylmaleimide-sensitive factor attachment protein receptor
SOC	Store-operated channel
SPCA	Secretory pathway Ca^{2+}-ATPase
SR	Sarcoplasmic reticulum
STEAP3	Six-transmembrane epithelial antigen of the prostate 3
$t_{1/2}$	Half-time
TAE	Tris-acetate-EDTA
TFEB	Transcription factor EB
TF	Tetrafluoro
TfR	Transferrin receptor
TM	Transmembrane
T_m	Target annealing temperature
TMEM	Transmembrane protein
TPC	Two-pore channel
TRP	Transient receptor potential
TRPML	Transient receptor potential mucolipins
UV	Ultraviolet

V-ATPase	Vacuolar H^+-ATPase
VDAC	Voltage-dependent anion channel
VGCC	Voltage-gated calcium channel
VSD	Voltage-sensing domain
WT	Wildtype

Chapter 1 – Introduction

1.1 Calcium

Calcium (Ca^{2+}) is an ion involved in numerous biological and pathological processes and as such, is the most abundant metal in the human body. Accounting for approximately 1 kg in adults, Ca^{2+} is most commonly known for its presence in bones and teeth, where 99% of Ca^{2+} accumulates in the form of calcium phosphate (1). The remaining ~1% is distributed across various cellular compartments, where Ca^{2+} is crucially involved in diverse physiological processes. Intracellular Ca^{2+} can be divided into two discrete pools, free and bound, that serve distinct complementary roles for cellular processes. Whilst free Ca^{2+} is soluble and dissolved in the cytosol, bound Ca^{2+} is temporarily buffered by proteins, or sequestered inside organelles, acting as a source for Ca^{2+} signalling.

1.1.1 Ca^{2+} signalling

Ca^{2+} was first demonstrated as a potential signalling ion in 1883 by Ringer (2). Through the use of isolated rat hearts, Ringer identified that Ca^{2+} was required to initiate and maintain cardiac contractions. Since this landmark observation, Ca^{2+} is now acknowledged as a crucial communication ion, which acts as a rapid second messenger to convert extracellular stimuli into physiological responses. Through Ca^{2+} signalling, many cellular processes such as muscle contraction, neuronal excitability, and exocytosis are regulated (3). The resting intracellular Ca^{2+} concentration ($[Ca^{2+}]$) is maintained at approximately 100 nM, compared to the almost 10,000-fold increase in free extracellular Ca^{2+} (~1 mM). The low intracellular $[Ca^{2+}]$ is governed by Na^{+}/Ca^{2+} exchangers (NCX) and plasma

membrane Ca^{2+}-ATPase (PMCA) pumps, which actively transport Ca^{2+} across the plasma membrane. Additionally, cytosolic calcium-binding proteins bind and buffer Ca^{2+} to manage intracellular levels of Ca^{2+} (4,5).

In order for Ca^{2+} to modulate intracellular activities, a change in the intracellular [Ca^{2+}] is required. Almost every cell contains specialised cytoplasmic Ca^{2+}-sensing proteins, which upon Ca^{2+} binding to motif sequences, trigger a confirmational change and subsequent downstream signalling to amplify the original Ca^{2+} signal (4,5). In addition to Ca^{2+}-binding proteins, such as calmodulin, calcineurin and calretinin (3,4), Ca^{2+} can bind directly to specific Ca^{2+}-permeable channels on the surface of intracellular compartments, such as the endoplasmic or sarcoplasmic reticulum (ER/SR), to mobilise Ca^{2+} from these organelles and amplify Ca^{2+} signals.

1.1.2 Plasma membrane Ca^{2+} translocation

Although Ca^{2+} is essential for correct cellular functioning, a low intracellular [Ca^{2+}] must be maintained, since excess Ca^{2+} can precipitate with phosphate to form insoluble calcium phosphate crystals, that can disrupt cellular functions and lead to toxicity. Cell stress caused by the alteration of the physicochemical environment and dysfunction of Ca^{2+} translocation mechanisms act as key factors which contribute to an elevated intracellular [Ca^{2+}]. Cellular Ca^{2+}-overload activates Ca^{2+}-sensitive enzymes, such as the calpains and lipoxygenases, which degrade nucleic acids, lipids, and proteins, leading to cell death (4,6). In order for cells to maintain a low intracellular [Ca^{2+}], Ca^{2+} must be transported against its electrochemical gradient across the plasma membrane. This active process requires energy, provided from the hydrolysis of adenosine trisphosphate (ATP). Alternatively, gated Ca^{2+}-selective channels present on the plasma membrane provide a

means for Ca^{2+} to enter cells down its electrochemical gradient. Therefore, Ca^{2+} translocation is tightly regulated by channels, pumps and exchangers, in order to sustain equilibrium whilst allowing Ca^{2+} to act as an intracellular signalling ion.

1.1.2.1 Efflux

Two main mechanisms exist within cells to assist in Ca^{2+} extrusion across the plasma membrane and sustain a low intracellular [Ca^{2+}], PCMA pumps and NCXs (3–5,7). Four isoforms of PMCA exist, two of which are ubiquitously expressed (PMCA1 and PMCA4), while the remaining two isoforms (PMCA2 and PMCA3) are restricted to specialised cells predominantly in the nervous system and mammary glands (7,8). PMCA transports one Ca^{2+} ion for every one ATP molecule hydrolysed, and as a result, acts as a low transport capacity, high affinity pump (7). The extrusion of Ca^{2+} by PMCA is coupled to the counter-import of one or more protons, thereby influencing cytosolic pH (9). When autoregulated by calmodulin, the binding affinity (K_d) of PMCA for Ca^{2+} is increased, from 10-30 μM at rest to 0.2-0.5 μM, along with the rate of Ca^{2+} extrusion (8). Conversely, NCXs function as a high capacity, low affinity (K_d ~1 μM) exchange protein, coupling Ca^{2+} extrusion to the electrochemical gradient of Na^+, resulting in three Na^+ ions entering the cell for every Ca^{2+} ion exchanged (7,10). This means that as Na^+ enters into cells and subsequently reduces its electrochemical gradient, a reduction in Ca^{2+} extrusion by the NCX also occurs, leading to a rise in the intracellular [Ca^{2+}] – a mechanism utilised by excitable cells of the brain and the heart (7,10).

1.1.2.2 Influx

Due to the considerable increase in the extracellular [Ca^{2+}] compared to the intracellular [Ca^{2+}], Ca^{2+} is capable of passively entering cells down its electrochemical gradient. Three main routes of Ca^{2+} entry exist within cells, each involving channel proteins which are triggered by different physiological stimuli. Firstly, Ca^{2+} can enter cells through a series of highly selective voltage-gated calcium channels (VGCC), which are activated and open in response to plasma membrane depolarisation. VGCCs are composed of a five-subunit complex, containing a central α1 pore-forming subunit, a transmembrane glycoprotein γ subunit, an intracellular β subunit, and two subunits (α2 and δ) linked by a disulfide-bridge (11). Five distinct subtypes of VGCCs exist (L, T, N, P/Q and R), all of which are voltage-activated but vary in their activation threshold, inactivation rate, conductance, and localisation. For instance, although both are vital for cardiac muscle contraction, T-type channels open at a lower depolarising potential (-70 mV) compared to L-type channels (-20 mV) (12). This is a requirement of T-type channels, which provide strong rhythmic depolarisation bursts to the sinoatrial node of the heart (12,13).

The second route of Ca^{2+} entry is through ligand-gated calcium channels (LGCCs), which upon binding and activation by specific molecules, predominantly neurotransmitters, increases the channels permeability to Ca^{2+}. Examples of LGCCs include N-methyl-D-aspartate (NMDA) and α-amino-3-hydroxy-5-methyl-4-isoxazolepropionic acid (AMPA) receptors, two glutamate receptors crucial for fast neurotransmission within the central nervous system (7,13). Additionally, ATP-dependent P2X receptors function as an important LGCC in smooth muscle, in which P2X Ca^{2+} entry produces excitatory junction potentials, depolarising the cell membrane and activating L-type VGCCs, leading to smooth muscle contraction (13,14). LGCCs can also function as environmental sensors,

such are transient receptor potential (TRP) channels, which increase intracellular Ca^{2+} and Na^{+} upon sensing changes in either temperature, pH, or volatile chemicals (3). TRP channels are also modulated by G protein-coupled receptor (GPCR) agonists which regulate TRP channels through Ca^{2+} positive feedback activation (3,7). For this reason, TRP channels are commonly misinterpreted as their homologous relative, store-operated channels (SOCs) (3,7).

In the event of intracellular ER Ca^{2+} stores becoming depleted, a small Ca^{2+}-release activated current (I_{CRAC}) can be detected in cells as a result of store-operated Ca^{2+} entry by SOCs (15,16). With a small single-channel capacitance of approximately 20 femtosiemens (fS), almost 1000-fold smaller than that of other cation channels, SOCs can assist in increasing the intracellular [Ca^{2+}] by formerly re-plenishing ER Ca^{2+} stores (16). Stromal interaction molecule 1 (STIM1) and Orai1, have been identified as crucial complex proteins in providing the connection between the plasma membrane and ER for Ca^{2+} refilling, acting as an ER Ca^{2+}-sensing protein and CRAC plasma membrane channel respectively (17).

1.1.3 Intracellular membrane Ca^{2+} translocation

1.1.3.1 Ca^{2+}-mobilising messengers

The release of Ca^{2+} from within intracellular organelles is a tightly regulated process, in order for Ca^{2+} to perform as an essential cytosolic signal. Complex secondary messenger pathways, triggered by the activation of cell surface GPCRs, provide a link for extracellular ligands to stimulate organellular Ca^{2+} release. Additionally, receptor tyrosine kinases, such as the epidermal growth factor receptor (EGFR) and platelet-derived growth factor receptor β (PDGFRβ), act as cell surface receptors coupled to intracellular Ca^{2+}

release (18). The binding of growth factors to these receptors causes receptor dimerization and tyrosine-dependent autophosphorylation, resulting in the recruitment, phosphorylation, and activation of downstream proteins such as phospholipase C (PLC)-γ (13,18). Upon activation, PLC-γ acts as an essential intracellular signalling enzyme for second messenger production, Ca^{2+} release, and cell growth.

Two established endogenous second messenger molecules have been identified to transduce a Ca^{2+} signal via ER Ca^{2+} release. The first Ca^{2+}-mobilising messenger is inositol-1,4,5-trisphosphate (IP_3), which is synthesised by PLC-β-, or PLC-γ-catalysed hydrolysis of phophatidylinositol-4,5-bisphosphate (PIP_2) following $G_{q/11}$-coupled GPCR, or receptor tyrosine kinase activation respectively (18–20). IP_3 binds with nanomolar affinity and efficacy to its target receptor (IP_3R1-3) on the ER to promote Ca^{2+} release (21). Additionally, IP_3-sesnitive channels have also been identified on the Golgi and outer membrane of the nuclear envelope (22,23). The other established second messenger involved in ER Ca^{2+} release is the nicotinamide adenine dinucleotide (NAD^+) metabolite, cyclic ADP-ribose (cADPR) (24). This molecule induces ER Ca^{2+} release independently from IP_3 by indirectly interacting with ryanodine receptors (RyR1-3) through FK506-binding accessory proteins (FKBP) (25,26). Following either IP_3R- or RyR-induced Ca^{2+} release, increases in the intracellular [Ca^{2+}] can result in positive feedback, whereby Ca^{2+} is capable of further increasing cytoplasmic Ca^{2+} through IP_3R and RyR channel modulation, an occurrence known as calcium-induced calcium release (CICR) (4,5).

1.1.3.2 Uptake

Following the influx of Ca^{2+} across the plasma membrane, Ca^{2+} is readily transported into various intracellular Ca^{2+}-storage organelles in order to buffer cytoplasmic Ca^{2+} and refill

depleted stores for subsequential local intracellular Ca^{2+} release. The ER (SR in striated muscle) exists as the major Ca^{2+} store within cells. Despite a luminal free Ca^{2+} concentration of 100-800 μM (27), the majority of ER calcium is chaperoned by Ca^{2+}-binding proteins, such as calsequestrin and calreticulin (5). Not only does this luminal buffering enhance the ERs storage capacity, but also reduces the electrochemical gradient of which Ca^{2+} is translocated into the ER against. Sarco/endoplasmic reticulum ATPases (SERCA1-3) exist as the Ca^{2+} pumps responsible for actively filling ER/SR luminal Ca^{2+} stores (two Ca^{2+} ions per ATP hydrolysed) (3,5). Despite sharing fundamental mechanisms and irreversible inhibition by the SERCA inhibitor thapsigargin (K_d ~20 nM) (27), differences exist between isoforms, such as reduced activity and Ca^{2+} affinities. This is a reflection of lower catalytic turnover and different Ca^{2+}-complex residue interactions for SERCA2b and SERCA3 respectively (8,28).

The powerhouse of the cell, mitochondria, act as spatial cytoplasmic Ca^{2+} buffers in cells. Voltage-dependent anion channels (VDAC1-3) grant Ca^{2+} access through the outer mitochondrion membrane, whilst selective low affinity (K_d ~10-20 μM) mitochondrion Ca^{2+} uniporters (MCUs) transport Ca^{2+} into the mitochondrial matrix (3,29). Translocated Ca^{2+} contributes to Kreb cycle dehydrogenase enzyme regulation, such as isocitrate dehydrogenase, and assists in maintaining a large resting mitochondrial gradient from the cytoplasm relative to the interior of mitochondria (-150 mV to -200 mV) (3,30).

Spatially linked to the ER, the Golgi apparatus also acts as an intracellular Ca^{2+}-storage organelle. Equipped with its own unique luminal Ca^{2+} chaperones, the electrochemical gradient of Ca^{2+} across the Golgi membrane is tightly regulated by a family of ATPases homologous to SERCA pumps, known as the secretory pathway Ca^{2+}-ATPases (SPCA1,2) (8,31). Unlike SERCA pumps, SPCAs are capable of efficiently transporting manganese

(Mn^{2+}), as well as Ca^{2+} from the same mutually exclusive ion-binding site (31). This phenomenon is likely related to the high quantity of Gogi luminal Mn^{2+}-requiring enzymes, including glycosyltransferases (8). Ubiquitously expressed, SPCA1 is often referred to as the 'Golgi housekeeping Ca^{2+} and Mn^{2+} pump', despite the additional expression of SPCAs on the Golgi membrane. This can be explained by the high affinity of SPCA1 for Ca^{2+} (K_d ~10 nM) (32), which ensures a constant translocation of Ca^{2+} ions into the Golgi lumen to replenish Ca^{2+} stores. This continuous refilling of Golgi Ca^{2+} stores is essential for the optimal functioning of protein and lipid packaging enzymes, as well as vesicle secretion and trafficking (8,31).

Within the last two decades, an increasing body of research has established acidic compartments as intracellular Ca^{2+}-storage organelles. Various acidic organelles have been identified as Ca^{2+}-containing, including endosomes, lysosome-related organelles, secretory vesicles, and plant vacuoles. Although 10-fold smaller in volume (33), fluorescent probes suggest a free Ca^{2+} concentration of approximately 300-600 μM within acidic organelles (34–37), comparable to that of the ER. Unlike the Ca^{2+} chaperone proteins of the ER and Golgi, emerging data suggests that the morphological structure of endo-lysosomes, particularly the presence of negatively charged lipids and proteins, serve as Ca^{2+} storage sites; however, further experimental evidence is required to confirm these theoretical findings (38).

Although the mechanism of acidic organelle Ca^{2+}-filling is still ill-defined, several candidate proteins have been identified. Proposed transport proteins include a Ca^{2+}-ATPase (39,40), a lysosomal-targeted PMCA2 splice variant (41), and a Ca^{2+}/H^{+} exchange (CAX) protein that translocates Ca^{2+} against the strong cytoplasmic-acidic store gradient (42,43). Evidence of such an exchanger arises from the endosomal acidifier pump vacuolar

H^+-ATPase (V-ATPase), whose inhibition by bafilomycin-A1 prevents Ca^{2+} uptake in endo-lysosomes (44,45). Recently, the Golgi-resident transmembrane (TMEM) protein TMEM165 has been proposed to function as the unknown lysosomal CAX. Unlike conventional CAXs, the Ca^{2+} transport activity of TMEM165 appears to be dependent on lysosomal lumen pH, rather than proton transport, with luminal acidification increasing channel activity (46,47). Additional proteins that facilitate Ca^{2+} filling include the P-type ATPase ATP13A2 and a voltage-activated K^+ channel, the latter indirectly facilitating lysosomal Ca^{2+} refilling via membrane depolarisation (48).

1.2 Nicotinic acid adenosine dinucleotide phosphate as a Ca^{2+}-mobilising messenger

1.2.1 NAADP synthesis and degradation

Originally discovered alongside cADPR, nicotinic acid adenosine dinucleotide phosphate (NAADP) represents the most potent Ca^{2+}-mobilising messenger and is rapidly synthesised following cell membrane stimulation (24,49). To date, two mechanisms of NAADP biosynthesis have been proposed. The first major route of synthesis may involve a base-exchange reaction in which the nicotinamide group of NADP (nicotinamide adenine dinucleotide phosphate) is replaced by nicotinic acid, generating NAADP. Within mammals, this reaction is catalysed under acidic conditions by the lysosomal ADP-ribosyl cyclase CD38 (50,51), as shown in membrane preparations from wildtype and CD38-deficient mouse hearts, where CD38 enzymatic activity was identified as essential for supporting NAADP synthesis (52). More recently, the neuronal sterile alpha and TIR motif-containing 1 (SARM1) cleaving enzyme has been associated with NAADP production, possessing NADP base-exchange activity similar to CD38 (53,54). Finally,

evidence suggests that the reduced inactive form NAADPH, can also be rapidly oxidised by cytosolic dual NADPH oxidases (DUOXs) to yield NAADP in T-cells (55,56). Conversely, the reverse reaction catalysed by glucose-6-phosphate dehydrogenases (G6PDH), reduces NAADP into NAADPH (55). In relation to NAADP metabolism, CD38 (57) and phosphatases (58) have been shown to degrade NAADP into ADP-ribose 2'-phosphate or NAAD respectively, thereby terminating NAADP signalling.

1.2.2 NAADP and acidic organelles

Early research within sea urchin egg homogenates pioneered NAADP Ca^{2+} signalling, with many findings now having been extrapolated to mammalian cells. Initial investigations postulated the likelihood that NAADP stimulates Ca^{2+} release from an organelle unaffected by thapsigargin and distinct from ER Ca^{2+} stores (59,60). These ER-independent Ca^{2+} stores were visualised through the use of caged analogues of IP_3, cADPR, and NAADP, which enabled region-specific and visual segregation of cADPR-/IP_3- and NAADP-sensitive Ca^{2+} stores (61). A significant advance came with the discovery that the compartmental target of NAADP were acidic organelles (44). This work showed that within sea urchin eggs and isolated yolk platelets, pharmacological compounds that disrupt lysosomal function and the lysosomal proton gradient likewise abolish NAADP-evoked Ca^{2+} signals. Specifically, experiments involving glycyl-L-phenylalanine-naphthylamide (GPN), a substrate originally used to distinguish lysosomes based upon cathepsin-C content (62), reinforced these findings. When applied to intact sea urchin eggs, GPN abolished NAADP-induced Ca^{2+} release, whilst IP_3 and cADPR Ca^{2+} signals remained undisrupted (44). Furthermore, GPN eliminated fluorescent acidic organelles identified by the proton-driven dye LysoTracker (44), confirming that acidic organelles are the target Ca^{2+} stores for NAADP.

However, recent findings question the selectivity of GPN in distinguishing lysosomal Ca^{2+}. Re-examination of the mechanism of action of GPN suggests that GPN may not directly cause cathepsin-C-mediated lysosomal rupture and Ca^{2+} release. Atakpa *et al*. demonstrated that GPN instead increases cytosolic pH, which directly stimulates Ca^{2+} release from the ER through a mechanism independent of IP_3Rs and RyRs (63). Given the prevailing view that GPN also acts at acidic organelles (64,65), further work is required to unravel the precise mechanism of GPN action at lysosomal and/or ER Ca^{2+} stores. Despite the uncertainty of GPN selectivity, NAADP-evoked Ca^{2+} release from acidic stores has since been observed within numerous mammalian cells and tissues, ranging from pancreatic acinar cells to skeletal and smooth muscle (49,66–70), confirming the aforementioned GPN-conclusive findings (44).

1.2.3 NAADP-mediated Ca^{2+} signalling

As briefly mentioned, NAADP is an extremely potent second messenger, able to elicit Ca^{2+} responses within the picomolar region in sea urchin egg homogenate (66). A remarkable feature of NAADP signalling within the sea urchin egg system is the phenomenon of NAADP desensitisation. Following the application of submaximal concentrations of NAADP, the Ca^{2+} release mechanism becomes desensitised, preventing subsequent NAADP-induced Ca^{2+} release at normally effective concentrations for up to 20 minutes (71–73). This desensitisation is also apparent in mammalian cells, where NAADP exhibits a bell-shaped concentration-response relationship (67,68,70,74,75), with nanomolar and micromolar concentrations activating or inhibiting acidic organelle Ca^{2+} release respectively. Although not entirely understood, evidence suggests that these responses correspond to either low- (activation) or high-affinity (inhibition) channel binding (76).

Following the realisation that acidic organelles represented the target Ca^{2+} store of NAADP, several 'NAADP receptor' candidates were postulated, including transient receptor potential mucolipin (TRPMLs) channels and RyRs. However, these Ca^{2+}/cation channels crucially lacked NAADP-sensitivity (77,78), disregarding themselves as candidates. Despite this, experimental evidence in specific cell lines has led to the suggestion for the involvement of RyRs in NAADP-mediated Ca^{2+} signalling. Within Jurkat T-cells, NAADP-evoked Ca^{2+} release appears to originate from the ER and remains unaffected by bafilomycin-A1 pretreatment (74,79), presenting a striking contrast to numerous other cell lines (44,80–82). However, this is not conclusive, since Ca^{2+} signals originating from acidic organelles have been observed in Jurkat T-cells where endogenous RyRs were absent (75). The sensitivity of RyRs to NAADP could potentially be explained by CICR mechanisms, whereby NAADP-induced Ca^{2+} release activates ER Ca^{2+}-sensitive channels (33,67,83). Prompted by the finding that two-pore channels (TPCs) form the dominant Ca^{2+}/cation channels in plant vacuoles, the lysosome equivalent in plants (84), TPCs were proposed as a target channel for NAADP. Three simultaneous publications from individual groups converged on the finding that TPCs were the acidic organelle channel responsible for NAADP-evoked Ca^{2+} release. Collectively, deletion of *Tpcn2* in mice (80), gene silencing of *TPCN1* in SKBR3 cells (85), and pharmacological manipulation of acidic Ca^{2+} stores (80,85,86) validated and confirmed these conclusions. The physiological significance and mechanistic action of NAADP-induced TPC-mediated Ca^{2+} release will be discussed in subsequent sections.

1.2.4 NAADP-binding proteins

A significant outcome from early NAADP photoaffinity labelling studies was that NAADP binding still occurred in TPC-deficient mice tissue (87,88), implying that

NAADP regulation is mediated by an accessory protein. Indeed, two unrelated proteins, named Lsm12 (Like-Sm protein 12) and JPT2 (Jupiter microtubule-associated homolog 2), were reported by separate groups to bind NAADP and interact with TPCs. The RNA-binding protein Lsm12 (89) was identified through affinity purification and immunoprecipitation as an interacting protein shared by NAADP, TPC1, and TPC2 (90). Functional Ca^{2+} imaging and channel current recordings in Lsm12-deficient HEK293 cells confirmed the essential requirement of Lsm12 for NAADP-induced TPC activation, whereby Lsm12 interacts with both NAADP and TPCs through its N-terminal Lsm domain (90). Alongside Lsm12, the intrinsically disordered protein JPT2 was simultaneously reported to also interact and regulate NAADP-mediated Ca^{2+} sensitivity (91–93). JPT2 appears to associate more strongly with TPC1 than TPC2 (91,92,94), tentatively linking NAADP-dependent signalling to endosomal Ca^{2+} stores. Finally, Lsm12 and JPT2 have become increasingly associated with Ca^{2+}-dependent processes, analogous to processes for which NAADP-evoked TPC Ca^{2+} release is crucial (92,95), reaffirming the role of these accessory proteins in regulating NAADP signalling.

1.3 Two-pore channels

At the end of the 20th century, the first TPC gene was successfully cloned from rat kidney tissue whilst attempting to identify new members of the voltage-activated cation channel family (96). Subsequent sequence screening revealed that TPCs share structural similarities with voltage-gated Ca^{2+} and Na^{+} channels, a finding since confirmed by TPC phylogenetic trees (97). Following this landmark discovery, TPCs were characterised within *Arabidopsis thaliana* plant cell vacuoles, where electrophysiological and luminescent assays indicated voltage-dependent Ca^{2+} channel activity (84,98,99), suggesting that TPCs act as Ca^{2+}-conducting transporters.

1.3.1 Structure and homology

As previously mentioned, TPCs share structural similarities with voltage-gated Ca^{2+} and Na^{+} channels and are considered a part of the voltage-gated ion channel superfamily (97). Evidence suggests that TPCs form dimers, acting as evolutionary intermediates between single-domain tetrameric channels, such as voltage-gated K^{+} channels, and four-domain monomeric voltage-gated Ca^{2+} and Na^{+} channels (100–103). Despite having been identified in 2000, it was not until 16 years later when the first structural insights into TPCs from *Arabidopsis thaliana* were provided through the use of protein X-ray crystallography (104,105).

Although sequence alignment analysis indicates a lack of conservation between mammalian and plant TPCs, both classes share an overarching structure (104–107). As implied by their name, TPCs possess two homologous 'shaker-like' six transmembrane (TM) domains, 6-TMI and 6-TMII, resulting in a dimeric subunit consisting of 12-TM helices (IS1-6 & IIS1-6) (96,104,106,108). The topological structure of TPCs is shown in Figure 1.1. 6-TMI and 6-TMII are connected by a central cytosolic EF-hand domain, which in plant TPCs contains Ca^{2+}-binding motifs that share an approximate 30% sequence identity with calmodulin (105,109). The overall structure of each TPC monomer contains two putative voltage-sensing domains (VSDs) on the S4 segment, in addition to two pore-forming domains comprised of helices S5-6, with S6 representing the pore-lining helix (96,104–106,108). Furthermore, evidence implies that both the C-terminus and N-terminus of TPCs are essential for channel activation and trafficking. Upon either deletion, mutagenesis, or fluorescence tagging of TPCs N-terminus, experimental findings indicate plasma-membrane channel mistrafficking and decreased channel sensitivity to NAADP (110–112).

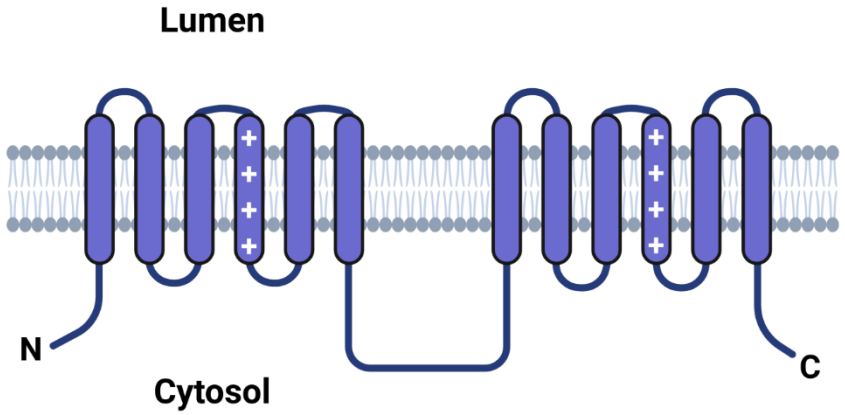

Figure 1.1: Structure of TPCs. Topology of a TPC monomer containing two homologous 'shaker-like' six transmembrane repeats connected by a central cytosolic EF-hand domain. Charged arginine residues (++++) in the S4 domains comprise the voltage-sensing domain which is active in TPC1.

The TPC family is comprised of three isoforms, TPC1-3, which are diverse across eukaryotic organisms but lack expression in prokaryotes (113). Despite this diversity, not every TPC variant is expressed across all classes. TPC3 expression is absent in humans (*Homo sapiens; Hs*), as well as in mice (*Mus musculus; Ms*) and rats (*Rattus rattus; Rr*), where it likely takes the form of a non-functional pseudogene (80). Furthermore, in plants, such as thale cress (*Arabidopsis thaliana; At*), barley (*Hordeum vulgare*), and rice (*Oryza sativa*), only TPC1 is present. Conversely, organisms of the deuterostome lineage have retained expression of all animal TPC isoforms, most notably sea urchins (*Lytechinus pictus*) and zebrafish (*Danio rerio; Dr*), which have been pivotal for demonstrating NAADP-induced Ca^{2+} release (44,114,115). Phylogenetic data suggests that TPCs are crucial for vertebrae survival; however, TPC biodiversity between genera and the need for multiple TPC isoforms remains unclear.

1.3.2 Isoforms

As previously discussed, animals express three different isoforms of TPCs, namely TPC1, TPC2 and TPC3, encoded by *TPCN1*, *TPCN2*, and *TPCN3* respectively. Despite sharing similar characteristics, each isoform exhibits distinct channel properties that contribute to specific physiological processes within cells. The various TPC isoforms, along with differences between human (*Hs*TPC), mouse (*Mm*TPC), and plant (*At*TPC1) species, are discussed below.

1.3.2.1 TPC1

Distribution and localisation

Screening of rat kidney cDNA identified TPC1 as the first channel within the TPC family, with an approximate transcript length of 5 kb. Early Northern blot analysis of *Rr*TPC1 mRNA suggested a restricted expression pattern, with increased exposure revealing additional tissue expression (96). Similar TPC1 expression patterns were reported in blots by Zong *et al*. (86) and Ruas *et al*. (116), suggesting that TPC1 shows widespread distribution, with greater expression in kidney, lung, liver, spleen, and adipose tissues. Reverse transcription PCR (RT-PCR) also revealed analogous broad tissue expression for an evolutionary conserved variant isoform of TPC1, termed TPC1B, which is transcribed from an alternative promoter (116).

TPCs have been well characterised in relation to their localisation, showing distribution across acidic organelles of the endo-lysosomal system (Figure 1.2). Colocalisation experiments have revealed a well-defined localisation of TPC1 to mildly acidic early and recycling endosomal vesicles (pH 5.7-6.9) (35,116), with marginal localisation to late

endosomes and lysosomes (80,85,116) (Figure 1.2). For reasons that are not yet fully understood, but likely related to function, recombinant *Hs*TPC1 shows only scarce colocalisation with *Hs*TPC2 (80). More recently, a large colocalisation and correlation analysis of TPC1 with nine intracellular markers was performed by Castonguay *et al*. confirming a predominant TPC1 localisation to early and recycling endosomes (117). Comparatively, *At*TPC1 is localised to vacuoles, analogous to mammalian lysosomes (84,109). However, the current evidence for TPC1 localisation is based solely on channel overexpression; it remains to be determined whether endogenous TPC1 likewise localises to early and recycling endosomes.

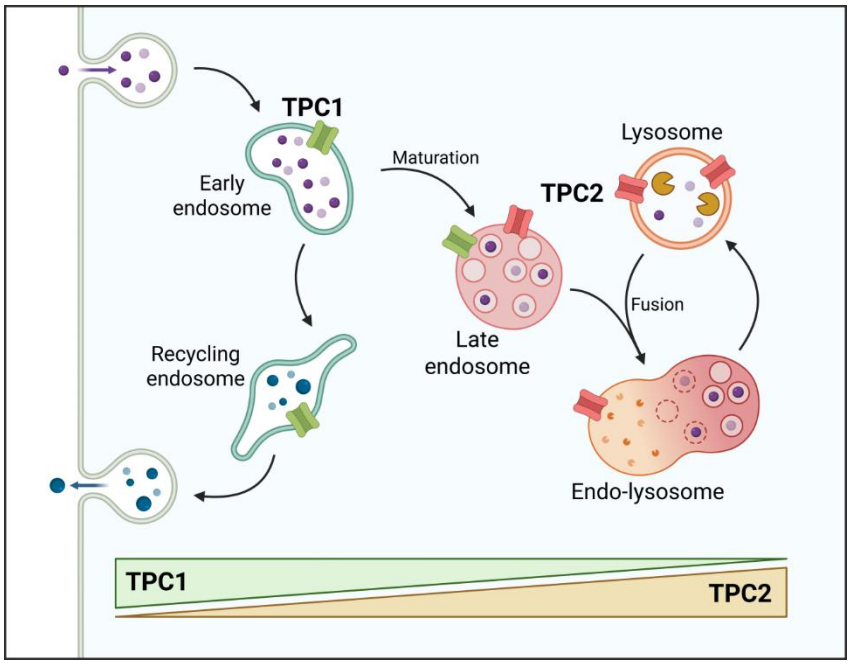

Figure 1.2: Cellular distribution of mammalian TPCs. TPC1 localises to mildly acidic early and recycling endosomes, whilst TPC2 localises to acidic late endosomes and lysosomes. Adapted from Morgan *et al*. (118).

Through site-directed mutagenesis studies, N-terminal dileucine-based motifs have been proposed as responsible for TPC channel targeting and localisation. Although the N-terminus of *Hs*TPC2 appears important for compartmental targeting (discussed in section 1.3.2.2), the removal of the N-terminus, mutation of dileucine motifs, or combination, fail to elicit a change in the endo-lysosomal distribution of *Hs*TPC1 (111,116). TPC1 targeting to the plasma membrane has only been successfully performed with *Mm*TPC1 and *At*TPC1, where expression of the *Mm*TPC1 N-terminal dileucine mutation L11A/I12A in HEK293 cells (106), or the analogous *At*TPC1 L5A/I6A mutation (119), resulted in *some* plasma membrane distribution. This suggests that *Hs*TPC1 targeting may not require its conserved dileucine motifs, but instead other motifs such as tyrosine-based sorting signals (120), present elsewhere in the *Hs*TPC1 sequence.

Structure and key residues

Currently, only *At*TPC1 and *Mm*TPC1 structures have been determined to a resolution of 2.9 and 3.2 Å respectively (105,106). Despite no definite structure of *Hs*TPC1, a high sequence conservation between *Mm*TPC1 and *Hs*TPC1 (90% sequence identity; Figure 1.3) allows generalisations to be made surrounding key structural residues of *Hs*TPC1. Positioning of voltage-sensing arginine residues throughout VSD1 and VSD2 provide TPC1 with unique voltage-dependent gating (121). Although containing three IS4 arginine residues, Arg200, Arg203 and Arg206 positioned at R2, R3 and R4 respectively, *Mm*TPC1 structural analysis indicates that VSD1 does not contribute to voltage-dependent gating (106), as also observed in *At*TPC1 (104,105). This deficit in VSD1 voltage-sensing likely reflects a lack of the key voltage-sensor features, including an absent arginine from the gating-charge transfer centre of IS4 (106,121). TPC1 voltage-dependent gating is instead reliant on the canonical voltage sensor, VSD2. Two arginine residues positioned at R3

(Arg540) and R5 (Arg546) on IIS4 are responsible for *Mm*TPC1 voltage gating. Additionally, unlike VSD1, IIS4 conserves its gating-charge transfer centre, along with the formation of a 3_{10}-helix (106). Likewise, the IIS4 helix of *At*TPC1 contains four arginine residues, Arg531 (R1), Arg537 (R3), Arg540 (R4) and Arg543 (R5), with the latter three residues (R3-5) required for *At*TPC1 voltage-sensing (104,105).

Mutations to the voltage-sensing region of *Mm*TPC1 has a unique, experimentally beneficial effect on the voltage dependence of the channel. In particular, mutation of R3 (R540Q) abolishes *Mm*TPC1 voltage-sensing, rendering a voltage-independent channel sustained in a VSD2 active state which can be activated exclusively by the phosphoinositide phosphatidylinositol-3,5-bisphosphate ($PI(3,5)P_2$; see section 1.3.3.1) (106). Similarly, the homologous R3 mutation in *Hs*TPC1 (R539I) results in a loss of voltage sensitivity (122). Interestingly, mutation of Arg546 (R5) in *Mm*TPC1 yields a channel which even at high concentrations of $PI(3,5)P_2$, is only marginally activated by voltage, suggesting that the voltage-sensor is locked in a resting state (106). In contrast to *At*TPC1 and *Mm*TPC1, mutation of VSD *Hs*TPC1 arginine residues (R219Q, R220Q, R223Q, and R539I) results in a loss of voltage sensitivity (122), suggesting that both VSD1 and VSD2 might contribute to *Hs*TPC1 voltage-sensitivity. Although Cang *et al.* detail that Arg219, Arg220, and Arg223 are located on the VSD1 TM-IS4 domain of *Hs*TPC1 (122), based on sequence alignment with *Mm*TPC1 (Figure 1.3), these residues more likely reside on the cytosolic IS4-S5 linker (123). Additionally, more recent studies have shown that these three arginine residues and their conserved *Mm*TPC1 equivalents appear crucial for $PI(3,5)P_2$- and NAADP-induced activation of TPC1 (106,123). As $PI(3,5)P_2$ was present during the channel recordings of the *Hs*TPC1 'IS4' mutants (R219Q, R220Q, and R223Q) (122), the authors likely misinterpreted these findings as voltage-dependent effects; these observed effects are better explained by the impairment of indirect

$PI(3,5)P_2$ TPC1 interactions. Together with the cytosolic positioning of these residue on the IS4-S5 linker, this implies that the VSD1 of *Hs*TPC1 is not voltage-sensing.

Interestingly, in both the holo $PI(3,5)P_2$-bound and apo confirmation, *Mm*TPC1 VSD2 remains in an activated state (106), suggesting that the voltage-sensor can be activated without channel opening. As the VSD2 of *At*TPC1 is in the resting state (104), this can be extrapolated to *Mm*TPC1 to understand the confirmational change the VSD2 undergoes when transitioning from its active to resting state. Thus, upon *Mm*TPC1 hyperpolarisation, downward sliding of IIS4 by roughly two helical turns positions the R3 arginine (Arg540) at the gating-charge transfer centre. This consequently obstructs the space required for the movement of the IIS4-S5 linker and IIS6, which are associated with $PI(3,5)P_2$-mediated channel activation (106,108). Therefore, rather than directly activating *Mm*TPC1, endo-lysosomal membrane depolarisation instead removes inhibition caused by the IIS4-5 linker, enabling $PI(3,5)P_2$-induced channel opening.

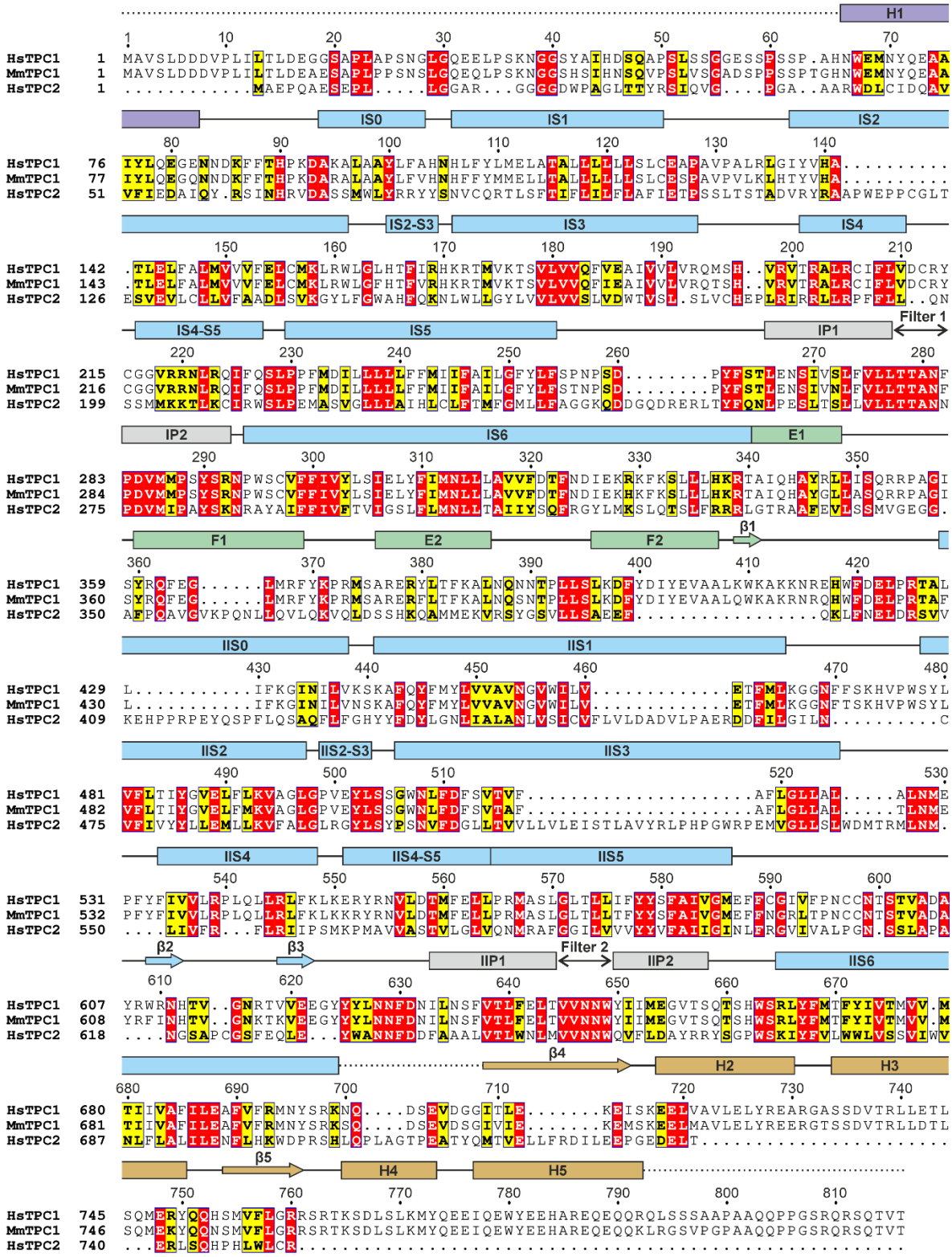

Figure 1.3: Multiple sequence alignment of *Hs*TPC1, *Mm*TPC1, and *Hs*TPC2. Sequences were aligned using MAFFT (v7) and the alignment visualised using ESPript 3.2 (124). Strictly conserved residues are highlighted in red, whilst similar residues are highlighted in yellow. Secondary structure elements of *Mm*TPC1 derived from She *et al*. (106) are shown above the alignment, with blue, grey, and green elements representing transmembrane, pore, and EF-hand domains respectively.

PI(3,5)P_2 binding

By virtue of structural insights, we know that PI(3,5)P_2 binds directly to *Mm*TPC1, positioning itself on the junction formed by the IS3, IS4, and IS4-S5 linker region (106). PI(3,5)P_2 predominantly interacts with *Mm*TPC1 basic residues upon binding, including Lys331 on IS6, in addition to the IS4-S5 linker arginines Arg220, Arg221 and Arg224 (Figure 1.3). These residues are predicted to interact with the C3 phosphate head of PI(3,5)P_2, and upon mutation, have a significant effect on PI(3,5)P_2 activation (106), demonstrating their importance for ligand binding. In particular, Lys331 appears to be especially critical for PI(3,5)P_2 activation, as demonstrated by the major confirmational change overseen by the lysine, drawing IS6 towards the ligand binding pocket and whose mutation completely abolishes PI(3,5)P_2-evoked channel currents (106). As a consequence of the IS6 movement, IIS6 helices also undergo rotational movements away from the central axis, which are accompanied by opening and widening of the intracellular gate. Under hyperpolarisation, PI(3,5)P_2 may still bind to *Mm*TPC1; however, as the space for IIS6 movement is occluded, the channel remains closed. Therefore, TPC1 VSD2 depolarisation and PI(3,5)P_2-induced IIS6 movement can be interpreted as complementary prerequisites for TPC1 channel opening and activation.

*At*TPC1 permeability and selectivity

Before the discovery of TPCs, reports detailed a vacuole voltage-dependent K^+ channel within plants, termed the slow vacuole channel (125–127). Since this observation, *At*TPC1 is now recognised as responsible for generating slow vacuole channel currents and contributing towards Ca^{2+} signalling within plants (104). Although first assumed to act as a K^+-selective channel (125), subsequent findings revealed that *At*TPC1 is in fact a non-

selective cation channel, able to conduct various monovalent cations (113). Unlike typical K^+ channels, *At*TPC1 contains a spatially wider, yet shorter residue selectivity filter, consisting of residues $_{264}TS_{265}$ from filter 1 and $_{629}MGN_{631}$ from filter 2, which assist the permeability of both hydrated and partially hydrated ions (104).

Studies have reported that *At*TPC1 is a non-selective ion channel, exhibiting almost equal permeability to K^+ and Na^+ (107,128), as well as permeability to the cations Li^+, Rb^+ and Cs^+ (107,129). In addition to representing a permeable ion, Ca^{2+} acts as an *At*TPC1 modulator, with channel activation or inhibition dependent upon the presence of cytosolic or luminal Ca^{2+} respectively (126,127,130,131). The fatty acid oxygenation upregulated 2 (*fou2*) point mutation in *At*TPC1 (D454N) alters the luminal Ca^{2+} recognition site, thereby reducing the channel's sensitivity to luminal Ca^{2+} inhibition (132). Cytosolic Ca^{2+} activation is mediated via the EF-hand domain between 6-TMI and 6-TMII, with the EF2-hand motif appearing vital for cytoplasmic Ca^{2+} sensing (104,109). Despite a high K^+ physiological concentration gradient across the vacuole membrane compared to Ca^{2+} (133,134), *At*TPC1 has been shown to have a greater selectivity for Ca^{2+} over both K^+ and Na^+, yielding a permeability ratio ($P_{Ca/Na}$ and $P_{Ca/K}$) of approximately 5.0 (107,135). Based on these permeability ratios and those of other cations, the relative permeability sequence for *At*TPC1 is suggested to be $Ca^{2+} > Na^+ \sim Li^+ \sim K^+ > Rb^+ > Cs^+$ (107,127,129,135).

Mammalian TPC1 permeability and selectivity

Whole-endo-lysosome patch-clamping of vacuolin-1 enlarged endo-lysosomes expressing TPCs have assisted in the electrophysiological characterisation of previously inaccessible mammalian TPCs (136). Unlike the non-selective *At*TPC1, evidence suggests a more specific cation selectivity for mammalian TPC1. This selectivity can likely be attributed to

the unique filter residues present in *Mm*TPC1. In particular, the filter 2 asparagine residues Asn648 and Asn649 form a narrow constriction point along the filter pathway (Figure 1.3), optimally positioned to stabilise the passage of Na^+ cations, with their mutation (N648A) abolishing Na^+ selectivity (106).

Numerous whole-endo-lysosome electrophysiology studies have validated TPC1 Na^+ permeability (122,137–139), typically utilising asymmetric or bi-ionic conditions comprised of high Na^+ (~140 mM) or high K^+ (~145 mM) solutions, to mimic the lumen of endo-lysosomes and the cytosol respectively (136). Elimination of $PI(3,5)P_2$-induced (1 μM) *Hs*TPC1 current has been observed when substituting luminal cations with N-methyl-D-glucamine (NMDG) or K^+. Additionally, *Hs*TPC1 current is abolished following the removal and replacement of cytosolic Na^+ with cations, including K^+, Ca^{2+}, or NMDG (137), suggesting that Na^+ represents the major permeant ion. Relative permeability ratios between Na^+ and Ca^{2+} ($P_{Na/Ca}$ ~212), or Na^+ and K^+ ($P_{Na/K}$ ~78) (122), further demonstrate the Na^+-selective nature of *Hs*TPC1.

As mentioned, TPC1 is predominantly localised to mildly acidic endosomes, which themselves are positioned within the initial sorting element of the progressively acidic endo-lysosomal system (45). Through manipulation of *Hs*TPC1 luminal recording solutions, increasing the pH by two units from 4.6 to 6.6 resulted in an 88.6 mV negative shift of the membrane potential conductance relationship towards hyperpolarisation (122). This implies that at an increased pH representative of the physiological lumen of TPC1-positive endosomes, *Hs*TPC1 remains open and is activated over wider, increasingly negative membrane voltages. Similarly, TPC1 exhibits increased affinity for NAADP by approximately 10 nM/mV of membrane hyperpolarisation (140). In addition to a shift in channel open probability, a report by Pitt *et al.* details an observed reduction in TPC1

current at luminal pH 7.2 compared to 4.8, implying proton conductance (141). Subsequent symmetrical and bi-ionic HCl solutions revealed positive reversal potentials (E_{rev}) with increased luminal acidity (-47 mV, 10 mM HCl pH 2; compared to +43 mV, 100 mM HCl pH 1), alongside a 67-fold and 500-fold increase in H^+ selectivity over Na^+ and Ca^{2+} respectively. However, these experimental findings, which were obtained from artificial lipid bilayers, are yet to be reproduced in a native lipid environment representative of endosomes. Therefore, further evidence is required to conclude whether TPC1 exclusively acts as an endosomal pH sensor, or if TPC1 is also a proton permeable channel.

Despite Na^+ representing the major permeant cation following $PI(3,5)P_2$ activation, reports detail that like its homologous paralog TPC2, TPC1 maintains Ca^{2+} permeability. Electrophysiological characterisation of reconstituted TPC1 in planar lipid bilayers indicate that TPC1 is Ca^{2+} permeable when activated by NAADP, whilst also regulated by luminal and cytosolic Ca^{2+} concentrations (140,141). Dispute within the literature regarding the relative Ca^{2+} permeability of *Hs*TPC1 makes interpretation challenging. The variety of reported permeability ratios between Ca^{2+} and Na^+ ($P_{Ca/Na}$) include 0.98 (141), 0.051 (0.114 prior to protocol correction) (139), and 0.005 (122), discrepancies likely attributable to different methodological procedures, such as isolated endo-lysosome recordings, artificial lipid bilayers, or transient expression in *Arabidopsis thaliana* vacuoles.

Alongside Ca^{2+} permeability, TPC1 demonstrates minor K^+ conductance, as shown by small detectable tail currents (137,139). TPC1 K^+ permeability is supported by the presence of inward tail currents, but not outward currents, following cytosolic Na^+ substitution with K^+ (luminal Na^+ solution), together with a large E_{rev} of +90 mV (139).

This strongly suggests that *Hs*TPC1 elicits a modest K^+ permeability compared to Na^+ ($P_{K/Na}$ ~0.03), yet is marginally more permeable than Ca^{2+} ($P_{K/Ca}$ ~9) when assessed in K^+ cytosolic and Ca^{2+} luminal solutions (139,141).

Unfortunately, due to varying results and methodologies, the permeability sequence for mammalian TPC1 is not straight forward. However, an educated approximation would consist of (H^+?) > Na^+ > Ca^{2+} ≥ K^+ (Figure 1.4), with emphasis on the uncertainty of H^+ permeability or sensitivity. It is evident that the permeability of TPC1 towards Na^+ exceeds that of Ca^{2+}. This difference could explain and predict the key roles of TPC1 in Na^+-related cellular functions, including endo-lysosomal excitability, osmolarity, and membrane tension (118).

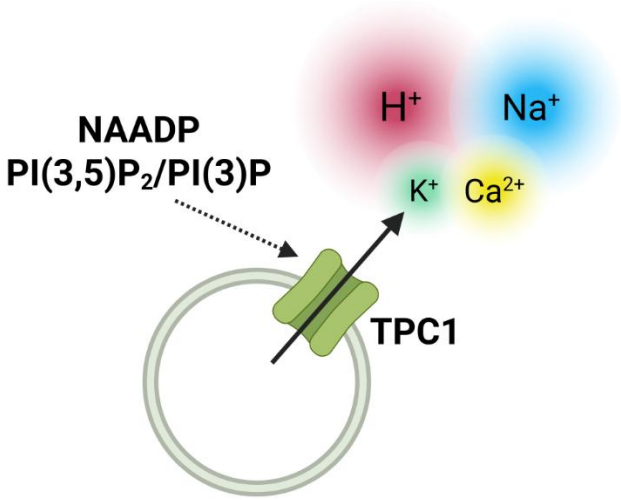

Figure 1.4: Ionic permeabilities of TPC1. Schematic of the relative permeability of TPC1 to Na^+, Ca^{2+}, H^+, and K^+, activated by NAADP or the phosphoinositides $PI(3,5)P_2$ and PI(3)P. Adapted from Morgan *et al*. (118).

1.3.2.2 TPC2

Distribution and localisation

Similar to the widespread expression of TPC1 mRNA, *TPCN2* transcripts are expressed in the majority of tissues, with increased detectable levels in the kidney and liver (80,86). Additionally, TPC2 shows comparable localisation to the intracellular endo-lysosomal system, although boasting a more explicit confinement. TPC2 exhibits colocalisation with the lysosome-associated membrane protein (LAMP) 1 and 2, as well as the proton-driven fluorescent dye LysoTracker, symbiotic to the highly acidic compartments of late endosomes and lysosomes (pH 4.0-5.6) (35,80,86). In contrast to TPC1, TPC2 shows little to no localisation with early or recycling endosomes (80), indicating specific targeting to lysosomal and late endosomal membranes.

TPC2 is targeted to lysosomes and late endosomes via dileucine-based signal motifs (120). Specifically, the N-terminal dileucine motif Leu11 and Leu12 of *Hs*TPC2 represent vital signal residues for precise lysosomal targeting. Deletion or mutation of these residues (L11A/L12A) disrupts channel trafficking, instead redirecting TPC2 to the plasma membrane (111). Both whole-lysosome and conventional patch-clamp recordings of either native lysosomal *Hs*TPC2 or rerouted plasma membrane *Hs*TPC2$^{L11A/L12A}$ establish similar current recordings (111,142), signifying a valid, convenient methodology for TPC2 patch-clamp recordings.

Structure and key residues

Although a similar overarching protein structure, *Hs*TPC2 shares only a ~23% amino acid identity with *Hs*TPC1 (Figure 1.3). Fortunately, the cryo-EM structure of *Hs*TPC2 has been reported at a resolution of 3.7 Å (108), revealing key structural differences consistent

with isoform-specific functions. The most striking difference to TPC1 is that *Hs*TPC2 lacks voltage-sensitivity despite sharing characteristic traits of a voltage-sensing channel, including conserved VSD2 arginine residues at positions R4 (Arg554) and R5 (Arg557), as well as a gating-charge transfer centre on IIS4 (108). The loss of voltage-dependent gating in TPC2 can largely be attributed to the presence of an isoleucine (Ile551) at the R3 position of IIS4 rather than an arginine (Figure 1.3). She *et al*. hypothesise that in the place of an R3 arginine, Ile551 prevents the downward sliding motion of the IIS4 domain upon membrane hyperpolarisation, thereby preventing the sequential outward movement of the IIS4-S5 linker that is required for pore opening (108). Similar to how mutation of the R3 arginine of *Mm*TPC1 (R540Q) renders the channel voltage-independent (106,122), the opposite holds true for *Hs*TPC2. Accordingly, a substitution of the R3 isoleucine for an arginine residue (I551R) yields a voltage-sensitive TPC2 channel requiring both voltage and $PI(3,5)P_2$ for channel activation (108).

$PI(3,5)P_2$ binding

Much like its interaction with *Mm*TPC1, $PI(3,5)P_2$ interacts with residues located on the IS3, IS4, and the IS4–S5 linker transmembrane domains of *Hs*TPC2. The majority of these residues are lysines located on the IS4-S5 linker, including Lys203, Lys204, and Lys207 (Figure 1.3). All three of these lysine residues stringently mediate $PI(3,5)P_2$ binding, as shown by an abolishment of current density following alanine substitution (108). Alongside IS4-S5 linker residues, the IS6 residues Arg329 and Ser322 interact with the phosphate groups of $PI(3,5)P_2$ to assist with the IS6 conformational change necessary for channel pore opening and closing. These interactions occur in a ligand-bound state-dependent manner, with Arg329 portraying a more prominent role in open state channel gating compared to Ser322, as indicated by alanine mutant recordings (108). This contrasts

to *Mm*TPC1, in which a single lysine IS6 residue (Lys331) occupying the position of Ser322 on *Hs*TPC2 (Figure 1.3) is responsible for $PI(3,5)P_2$-dependent channel gating (106). In addition to mediating $PI(3,5)P_2$ activation, TPC2 current and Ca^{2+} measurements from the Patel group suggest that several *Hs*TPC2 $PI(3,5)P_2$ binding site residues (Lys204, Lys207, Arg329, and Ser322) also facilitate NAADP-mediated activation (143). Whilst these findings demonstrate that caution should be taken when interpreting results from mutational studies, they more critically suggest that the endogenous activators of TPC2, $PI(3,5)P_2$ and NAADP, might share an analogous binding site.

As previously mentioned, $PI(3,5)P_2$ triggers channel pore opening through manipulation of the IS6 helix. In the case of TPC2, the interaction between $PI(3,5)P_2$ and Arg329 extends the IS6 helix outward into a straight open configuration exposing the IS6 gating residues Thr308 and Tyr312, stabilised by hydrogen bonds surrounding Ser322 (108). Simultaneously, IIS6 performs a parallel motion to open the channel pore, resulting in the outward rotation of the IIS4-S5 linker and IIS6 gating residues Leu690 and Leu694 (108). Similar to *Mm*TPC1, this movement of the IS6, IIS6 and the IIS4-S5 linker provides the necessary space for $PI(3,5)P_2$-induced channel opening and cation permeation.

Permeability, dual-regulation and selectivity

Homologous to TPCs, the channel pore contains two sets of filter residues which define the diameter of the central ion conductance pathway and cation permeability. TPC2 filter 1 and filter 2 consist of the residues $_{270}$TTANN$_{274}$, and $_{651}$VVNNW$_{655}$ respectively (107,108). The selectivity filters of *Hs*TPC2 are near-identical to that of *Hs*TPC1 (Figure 1.3), with the exception of Asn274 which is changed to a phenylalanine in TPC1 (106). As expected, given their near-identical filter sequence and structural similarities, mammalian

TPC1 and TPC2 have been shown to share the same structural mechanism to achieve Na^+ selectivity (106,107). In relation to this mechanism, molecular dynamic simulations of the *Hs*TPC2 PI(3,5)P_2-open conformation have identified that rotation and separation of the filter 2 residues Asn653 and Asn654 widen the channel pore radius, thereby increasing Na^+ permeation (144,145). To further understand which filter residues define TPC ion selectivity, Guo *et al.* reproduced the selectivity properties of *Hs*TPC2 within the non-selective isoform *At*TPC1 (107). Conversion of the *At*TPC1 filter 1/2 residues, including the critical central glycine residue of filter 2 (104), with those filter residues of *Hs*TPC2, yielded a *At*TPC1 mutant (*At*TPC1$^{S265A/M629V/G630N}$) that displayed high Na^+-selectivity and a loss of Ca^{2+} selectivity. Comparably, reversely swapping the identified key filter residues of *Hs*TPC2 with those of *At*TPC1 (*Hs*TPC2$^{A272S/V652M/N653G}$), resulted in a near-complete loss of *Hs*TPC2 Na^+ selectivity, whilst enhancing Ca^{2+} selectivity – the importance and impact of which will be discussed and extrapolated to *Hs*TPC1 in Chapter 4.

Following its discovery, strong debates and opinions arose surrounding the *true* ion selectivity of TPC2, in particular, the discrepancy between a Na^+ or Ca^{2+} permeation. Despite early Ca^{2+} imaging experiments demonstrating an essential requirement for TPCs in NAADP-dependent Ca^{2+} release (80,85–87) (discussed in section 1.2.3), whole-endo-lysosomal patch-clamp experiments suggested that TPC2 was rather a Na^+-selective channel (107,108,137,138). Specifically, when activated by PI(3,5)P_2 under bi-ionic conditions, TPC2 exhibited a high selectivity for Na^+ over other monovalent and divalent cations, notably K^+ ($P_{Na/K}$ ~23.8-33.3) and Ca^{2+} ($P_{Na/Ca}$ ~10.0-16.8) (107,138). These findings contrasted from previous TPC2 NAADP lipid-bilayer electrophysiological recordings, which reported TPC2 as a highly selective Ca^{2+} channel that exhibits an NAADP-evoked E_{rev} of +44.4 mV, comparable to that of the calculated E_{rev} for Ca^{2+} (+42.5 mV) (146,147). A plausible explanation for these differences could lie with the

electrophysiological technique used, as with whole-endo-lysosomal patch-clamp recordings, accessory proteins important for NAADP-evoked Ca^{2+} currents may be lost during endo-lysosome isolation (136,138). Although contentious, the conflict between an explicit Ca^{2+} or Na^{+} permeability has now been resolved by the emergence of a ligand-dependent permeability model.

It is now acknowledged that TPC2 maintains a biased permeability to either Na^{+} or Ca^{2+}, dependent on the endogenous activation molecule. These traits are unique, with only a few other Ca^{2+} channels, such as the P2X receptor isoforms P2X5/7 (148), displaying similar ligand- or time-dependent Ca^{2+} selectivity bias. Intriguingly, NAADP renders TPC2 more Ca^{2+}-permeable, whilst $PI(3,5)P_2$ preferentially increases Na^{+} conductance (149,150), an occurrence which correlates with the aforementioned electrophysiology studies. As such, the relative Ca^{2+} permeability ($P_{Ca/Na}$) and conductance of TPC2 increases 9-fold from 0.08 to 0.73 when activated by NAADP (149). Furthermore, it is speculated that cells can enhance the Ca^{2+} permeability of TPC2 through co-activation and synergy of NAADP and $PI(3,5)P_2$ (83,143,150), a requirement to enhance Ca^{2+} signalling. Based on the ligand-dependent selectivity of TPC2, it is challenging to place a definite rank for cation permeability. Nevertheless, as Na^{+} appears to represent the dominant flux regardless of the endogenous activator, the permeability sequence for TPC2 is likely $Na^{+} > Ca^{2+} > K^{+}$.

1.3.2.3 TPC3

In comparison to TPC1 and TPC2, TPC3 lacks extensive research. A functional TPC3 gene is absent in both humans and mice (80), existing only as a pseudogene in primitive mammals (151,152). Sequence homology demonstrates that TPC3 shares an approximate 30% conserved amino acid identity with mammalian TPC1/2 and *At*TPC1 in

transmembrane regions, making it an analogue of all TPCs (80,151). TPC3 is the only isoform which endogenously localises to both acidic endo-lysosomal organelles and the plasma membrane (151,153,154). Similar to mammalian TPC1, zebra fish *Dr*TPC3 is voltage-sensitive due to the presence of three IIS4 VSD2 arginine gating residues (Arg522, Arg525 and Arg528) (155,156). Perhaps more striking is that endo-lysosomal *Dr*TPC3 exhibits an extremely high current activation threshold of approximately +70 mV (153) in comparison to the activation threshold of *Hs*TPC1 (~0 mV) (122). Even when expressed on the plasma membrane, *Dr*TPC3 maintains a persistent elevated activation threshold (~0 mV) relative to other cell-surface voltage-sensitive channels (153). Furthermore, upon reaching the activation threshold, TPC3 remains activated for several minutes, enabling the generation of ultra-long action potentials (153). This phenomenon likely relates to the functionality of TPC3, enabling cells to maintain prolonged depolarised states, which is crucial for neuronal control.

TPC3 demonstrates less stringent modulation by phosphoinositides in contrast to TPC1 and TPC2. The H1-IS0 loop of TPC3 appears critical for phosphoinositide selectivity, in particular, Asn54, which contributes to $PI(3,4)P_2$ recognition (157). Analogous to other isoforms, phosphoinositide binding induces the movement of IS6, which simultaneously couples to the voltage-dependent movement of IIS6 to enable pore opening (157). Relative permeability estimations suggest that *Dr*TPC3 is a Na^+-selective channel, showing negligible permeability for Cs^+ ($P_{Na/Cs}$ ~88.1) and K^+ ($P_{Na/K}$ ~117.3) (153). Unlike TPC1 and TPC2, mammalian cells expressing sea urchin TPC3 exhibit small inconsistent NAADP-dependent Ca^{2+} signals (151,154), suggesting that TPC isoforms contribute to NAADP-evoked Ca^{2+} release in distinct ways. Whether all polymorphic sea urchin TPC3 sequence variants respond to NAADP in this way, remains to be determined (154).

1.3.3 Pharmacology

The various activators and inhibitors of TPCs together with their respective potency are listed in Table 1.1 and discussed in-depth below.

Table 1.1 Activators and inhibitors of TPCs

Compound	Original use	Action	Approx isoform EC_{50} or IC_{50}	Reference
Amitriptyline	Tricyclic antidepressant	Activator	TPC2 EC_{50}: 102 μM	(158)
ATP	Endogenous molecule	Inhibitor	TPC1 IC_{50}: ~1 mM TPC2 IC_{50}: 0.92 mM	(137)
Chlomipramine	Tricyclic antidepressant	Activator	TPC1 EC_{50}: 27 μM TPC2 EC_{50}: 43 μM	(158)
Chlorpromazine	Tricyclic antidepressant	Activator	TPC2 EC_{50}: 60 μM	(158)
Chlorpromazine	Tricyclic antidepressant	Inhibitor	TPC1 IC_{50}: 77 μM	(158)
Desipramine	Tricyclic antidepressant	Activator	TPC1 EC_{50}: 10 μM TPC2 EC_{50}: 87 μM	(158)
Diltiazem	Ca^{2+} channel blocker	Inhibitor	IC_{50}: 7.41 μM	(159)
Duartin	Plant flavonoid	Inhibitor	TPC2 IC_{50}: 9.50 μM	(160)
MASTER-NAADP*	New entity	Activator	TPC EC_{50}: ~100 nM	(161)
Mg^{2+}	Cation	Inhibitor	TPC2 IC_{50}: ?	(142)
NAADP*	Endogenous messenger	Activator and inhibitor	EC_{50}: nM IC_{50}: nM to μM	(66,67,71)
NAADP-AM*	New entity	Activator	TPC EC_{50}: ~200 nM	(87,162)
Naringenin	Plant flavonoid	Inhibitor	TPC1 IC_{50}: ? TPC2 IC_{50}: 74-200 μM	(160,163)
Nifedipine	Ca^{2+} channel blocker	Inhibitor	TPC2 IC_{50}: ~10 μM TPC3 IC_{50}: 3.35 μM	(153,159,164)

Ned-K*	New entity	Inhibitor	TPC IC_{50}: 1-100 μM	(165)
Ned-19*	New entity	Inhibitor	TPC IC_{50}: 1-100 μM	(76,166)
Pratensein	Plant flavonoid	Inhibitor	TPC2 IC_{50}: 2.6 μM	(160)
PI(3)P	Endogenous endosomal lipid	Activator	TPC1 EC_{50}: ? TPC3 EC_{50}: ?	(156)
$PI(3,4)P_2$	Endogenous plasma membrane lipid	Activator	TPC3 EC_{50}: ?	(156,157)
$PI(3,4,5)P_3$	Endogenous plasma membrane lipid	Activator	TPC3 EC_{50}: ?	(156)
$PI(3,5)P_2$	Endogenous endo-lysosomal lipid	Activator	TPC1 EC_{50}: 145 nM TPC2 EC_{50}: 390 nM TPC3 EC_{50}: ~142 nM	(106,108,138,156)
Rapamycin*	mTOR inhibitor	Activator	TPC2 EC_{50}: ~30 μM	(164)
Riluzole	GluR antagonist	Activator and inhibitor	TPC1 IC_{50}: 150 μM TPC2 EC_{50}: 182 μM	(158)
SG-005	Tetrandrine analogue	Inhibitor	TPC1 IC_{50}: ~10 μM TPC2 IC_{50}: 2.5-7.6 μM	(167)
SG-094	Tetrandrine analogue	Inhibitor	TPC1 IC_{50}: ~10 μM TPC2 IC_{50}: 8.3-24 μM	(167)
Sphingosine	Endogenous lipid	Activator	TPC1 EC_{50}: <2 μM	(168)
Tetrandrine	Ca^{2+} channel blocker	Inhibitor	TPC IC_{50}: 10 μM	(169)
TPC2-A1-N	New entity	Activator	TPC2 EC_{50}: 7.8 μM	(149)
TPC2-A1-P	New entity	Activator	TPC2 EC_{50}: 10.5 μM	(149)
Verapamil	Ca^{2+} channel blocker	Inhibitor	TPC1 IC_{50}: 23.1 μM TPC2 IC_{50}: 10 μM TPC3 IC_{50}: 600 nM	(122,138,153)
YM201636	PIKfyve inhibitor	Inhibitor	TPC2 IC_{50}: 160 nM	(170)

Note. EC_{50} and IC_{50} values are given for mammalian TPC isoforms. A '*' denotes indirect TPC activation or inhibition. A '?' denotes confirmed modulation with no reported EC_{50} or IC_{50} value. EC_{50}, half-maximal effective concentration; IC_{50}, half-maximal inhibitory concentration. Table is an updated version from Galione *et al*. (171).

1.3.3.1 Activators

To date, NAADP and phosphoinositides are recognised as the endogenous activating molecules of TPCs. As mentioned in section 1.2.3, NAADP exhibits the unique property of channel desensitisation upon the application of micromolar concentrations, making NAADP both an activator and inhibitor of TPCs. Studying NAADP-mediated Ca^{2+} signalling *in vitro* is challenging, since NAADP lacks membrane permeability because of its negative charge and hydrophilic nature. To resolve this issue, a membrane-permeant acetoxymethyl ester (AM) variant of NAADP, NAADP-AM, was synthesised (162,172); however, this compound presents its own difficulties owing to its instability. Recently, a stabilised, bio-reversibly protected precursor of NAADP, termed MASTER-NAADP (161), was synthesised to combat the instability of NAADP-AM. Although indirect agonists, both NAADP analogues evoked similar Ca^{2+} peak amplitudes in Jurkat T-cells, yet MASTER-NAADP increased the number of Ca^{2+} peaks and responding cells (161).

TPC isoforms demonstrate phosphoinositide selectivity, reflective of the compartmental distribution of phosphoinositides and TPCs. This selectivity likely enables TPC isoforms to discretely regulate ion fluxes and differentiate cellular processes. All three mammalian TPC isoforms display $PI(3,5)P_2$ sensitivity (106,108,122,138), with an approximate isoform sensitivity rank order of TPC1 > TPC3 > TPC2 (156). While $PI(3,5)P_2$ is the sole phosphoinositide activator of TPC2 (138), research suggests that TPC1 responds to both $PI(3,5)P_2$ and its precursor PI(3)P, albeit displaying a weaker PI(3)P response at equal concentrations (156). Due to its abundance in endosomal membranes compared to $PI(3,5)P_2$ (173), PI(3)P therefore represents a more relevant activator of the endosomal isoform TPC1. Similarly, mammalian TPC3 is activated by $PI(3,5)P_2$ and PI(3)P at

equipotent concentrations, also exhibiting weak sensitivity to $PI(3,4)P_2$ and $PI(3,4,5)P_3$ (156,157), on account of the plasma membrane localisation of TPC3 (151,153).

A key factor constraining progress in elucidating TPC signalling is the lack of TPC isoform-selective cell-permeant agonists. Small molecule screening identified tricyclic antidepressants, including amitriptyline, chlomipramine, and desipramine, which were able to activate TPC2, with the latter two tricyclics additionally activating TPC1 (158). Another screening performed by Gerndt *et al.* discovered two small molecule agonists of TPC2 through Ca^{2+} imaging and electrophysiology (149). Appropriately named TPC2-A1-N and TPC2-A1-P, these compounds are highly selective for TPC2 whilst also mimicking the ligand permeability bias observed with NAADP (TPC2-A1-N; Ca^{2+}) and $PI(3,5)P_2$ (TPC2-A1-P; Na^+). Although a mimetic of NAADP, deletion of the NAADP-accessory proteins Lsm12 and JPT2 in U2OS cells revealed that TPC2-A1-N mediates TPC2 activation independently of NAADP-binding proteins (143). These findings suggest that the action of TPC2-A1-N is different from NAADP, indicating that TPC2-A1-N directly binds to TPC2, interacting with IIS4 residues such as Arg557 on *Hs*TPC2 (143). Furthermore, recent research questions the specificity of TPC2-A1-N, pointing towards an additional Ca^{2+} channel target independent of TPCs and IP_3Rs (174).

In addition to direct agonists, TPC activity is modulated by several cytosolic and endo-lysosomal luminal molecules and proteins. Notably, rapamycin indirectly promotes TPC-mediated Ca^{2+} and Na^+ release through inhibition of the mechanistic target of rapamycin (mTOR), which forms a repressive complex with TPCs (137,164). Similarly, the lysosomal Rab7-GTPase has been shown through fluorescence resonance energy transfer and co-immunoprecipitation to physically interact with TPC2, with Rab7 strongly enhancing TPC2 channel activity (175–177). Whether the same can be said for endosomal

Rab5- or Rab11-GTPases enhancing the channel activity of TPC1 remains to be determined. Interestingly, photo-activation of caged sphingosine, a sphingolipid, acutely triggers exclusive Ca^{2+} signals from TPC1, but not TPC2 or TRPML1 (168,178). In addition to providing evidence of the first TPC1-selective agonist, these findings also postulate the suitability of sphingosine as a potential endogenous second messenger of TPCs, a critical area which requires further evaluation.

1.3.3.2 Inhibitors

The most prominent antagonists of TPCs are pore-blockers. Based on their structural similarities, L-type VGCC blockers, such as verapamil, nifedipine, and diltiazem, inhibit TPCs by preventing NAADP-evoked Ca^{2+} release (138,153,159,164,169). In particular, the alkaloid Ca^{2+} channel blocker tetrandrine, represents a potent inhibitor of TPC1 and TPC2 (137,149,169). Evidence suggests that tetrandrine and its analogues SG-005 and SG-094 directly bind to the VSD2 of TPCs, stabilising the channel in an inactive state (167,178,179). However, recent findings indicate that tetrandrine may also suppress TPC-mediated Ca^{2+} release indirectly, by binding to the lysosomal integral membrane protein-2 (LIMP-2) lipid transporter and preventing lysosomal lipid (sphingosine and cholesterol) efflux, resulting in a loss of TPC sensitivity to NAADP stimulation (168,178). Additionally, the dietary flavonoid naringenin weakly inhibits TPC1 and TPC2 (160,163,180), whilst other flavonoids (duartin and pratensein) suppress TPC2-specific activation (160). Finally, intracellular factors strongly mediate TPCs, including both Mg^{2+} and ATP, whose electrostatic charge enables direct binding and inhibition of TPC1/2 NAADP- and $PI(3,5)P_2$-evoked channel currents (137,142).

In the context of antagonising endogenous activators of TPCs, the most widely used NAADP antagonist is Ned-19 and its analogues. Identified through NAADP-based virtual screening, Ned-19 selectively inhibits NAADP-mediated Ca^{2+} release, without affecting Ca^{2+} signals from IP_3 or cADPR secondary messengers (76,166). Simulated TPC1 Ned-19 binding models indicate two functional binding sites: a high-affinity allosteric site where Ned-19 blocks NAADP-accessory protein binding and prevents TPC activation by narrowing the channel pore, and a low-affinity orthosteric site, where low concentrations of Ned-19 stabilise the open configuration of TPCs, triggering channel activation and Ca^{2+} release (76,105). Although no specific inhibitors of the lipid activation site exist, high concentrations of Ned-19 have tentatively been shown to block the $PI(3,5)P_2$ activation site of TPC2 (169). It also remains possible to deplete endogenous $PI(3,5)P_2$ through inhibition of the lipid kinase PIKfyve. In particular, vacuolin-1, apilimod, and YM201636 are well-characterised PIKfyve inhibitors (181–183), with YM201636 also considered to directly inhibit TPC2 (170).

1.3.4 TPC Ca^{2+} transduction

Given the small size of acidic Ca^{2+} stores, endo-lysosomes generate local Ca^{2+} signals, rather than global Ca^{2+} signals. These local Ca^{2+} nanodomains ([Ca^{2+}] of 7-42 μM for TPC2 (184)) provide a discrete source of Ca^{2+} for processes such as phagocytosis (81), exocytosis (75), receptor internalisation and trafficking (185,186), for which other Ca^{2+} sources cannot substitute. Even more remarkable is recent evidence that indicates the Ca^{2+} nanodomains supplied from different channels (TPC2 and TRPML1) on the same lysosome, remain insulated from each other (184). By preventing cross-contamination of nanodomains, this enables autonomous Ca^{2+} channel signalling and helps explain how cells discretely decode Ca^{2+} from varying sources.

Although TPC-mediated Ca^{2+} release represents a common theme in the literature, exactly how TPC Ca^{2+} signals are decoded into downstream signalling responses is ambiguous. Based on TPCs role in membrane and protein trafficking and vesicle fusion (116,117,185,186), it can be assumed that several Ca^{2+}-dependent proteins within these processes are sensitive to TPC-mediated Ca^{2+} signals. Interactome studies have identified numerous Ca^{2+}-dependent proteins associated with membrane organisation, endo-lysosomal trafficking, and cargo sorting, which selectively interact with TPC1 and TPC2 (175,187). Notably, SNARE (soluble N-ethylmaleimide-sensitive factor attachment protein receptor) proteins, such as syntaxin-12, as well as the membrane-scission protein dynamin, mediated through the Ca^{2+}-binding protein calcineurin, represent endo-lysosomal Ca^{2+}-dependent proteins that interact with TPC1 to regulate toxin trafficking and phagocytosis respectively (81,117). Furthermore, downstream Ca^{2+} signalling via the NAADP/TPC axis has been shown to phosphorylate the kinases ERK (188), AMPK (189) and GSK3β (160,176), which regulate cell proliferation and metabolism.

Similar to the mechanism utilised by the ER through IP_3Rs and RyRs, endo-lysosomes maintain the ability to amplify local Ca^{2+} release into global Ca^{2+} signals using a form of CICR. Evidence indicates that through endosome-ER and lysosome-ER membrane contact sites (MCSs), the ER amplifies both TPC1- (190–193) and TPC2-mediated Ca^{2+} release (33,83,115) respectively. This crosstalk between TPCs and IP_3Rs enables cell-wide prolonged Ca^{2+} signals for physiological signalling, as well as the potential to supply ER Ca^{2+} for endo-lysosomal refilling (194,195).

1.4 TRPML ion channels

TRPML ion channels are the other major cation channel family present on endo-lysosomes. Encoded by *MCOLN* genes, TRPML1, TRPML2, and TRPML3 comprise the mammalian genome and are distributed across various endo-lysosomal membranes. Whilst TRPML1 shares a similar localisation to TPC2 (late endosomes and lysosomes) (196), TRPML2 is predominantly localised to endosomal membranes (Figure 1.5), in particular recycling endosomes where TRPML2 regulates the transport and trafficking of extracellular cargo and pathogens (197,198). In contrast, the distribution of TRPML3 is dynamic and appears contingent on its physiological interaction with other TRPML isoforms (199). When expressed alone, a small fraction of TRPML3 localises with the ER (199), likely due to ER retention in the absence of overexpressed TRPML1 or TRPML2.

TRPMLs represent non-selective cation channels and are therefore permeant to a variety of ions including Ca^{2+}, Na^{+}, Fe^{2+}, Zn^{2+}, Mg^{2+}, Ni^{2+}, Ba^{2+}, as well as several others (196). Activated by $PI(3,5)P_2$ (198,200), TRPMLs have specialised roles in physiological and cellular processes. Similar to TPCs, TRPML-mediated Ca^{2+} release acts as a source for downstream Ca^{2+} signalling, including the vesicular transport of fungal pathogens (198) and the maintenance of mitochondrial metabolism and structure through MCSs (201). Additionally, dysfunction of TRPML-mediated Fe^{2+} and Zn^{2+} release disrupts the homeostatic balance of endo-lysosomes, leading to the accumulation of iron and zinc within endo-lysosomes which affects cytosolic levels, causing cytotoxicity, and inevitably cell-programmed death in cells (196,202). Accompanying TRPML1 dysfunction is the rare autosomal lysosomal storage disorder mucolipidosis type IV (MLIV), where the lysosomal accumulation of ions, lipids and substances, translates to neurodegeneration, motor impairment, vision loss, and intellectual disabilities in MLIV patients (203).

1.5 Endo-lysosomal trafficking

The endo-lysosomal system exists as an intracellular network of membrane-bound organelles that dynamically interconvert to transport cargo substrates for cellular processes. This pathway functions as the central trafficking hub for macromolecules and pathogens, where cells precisely regulate the rates of substrate internalisation, recycling, and degradation. Various vesicular compartments comprise the endo-lysosomal system (Figure 1.5), all of which are identified by specific Rab-GTPase membrane proteins. These compartments include early endosomes (Rab5), recycling endosomes (Rab11 and Rab4), and late endosomes and lysosomes (Rab7) (204,205). Additionally, autophagosomes traffic intracellular debris to lysosomes for degradation via the process of autophagy (45). Dysfunction of membrane trafficking within the endo-lysosomal system can be disastrous for cells and organisms, cascading into severe consequences and diseases, as described in section 1.6.

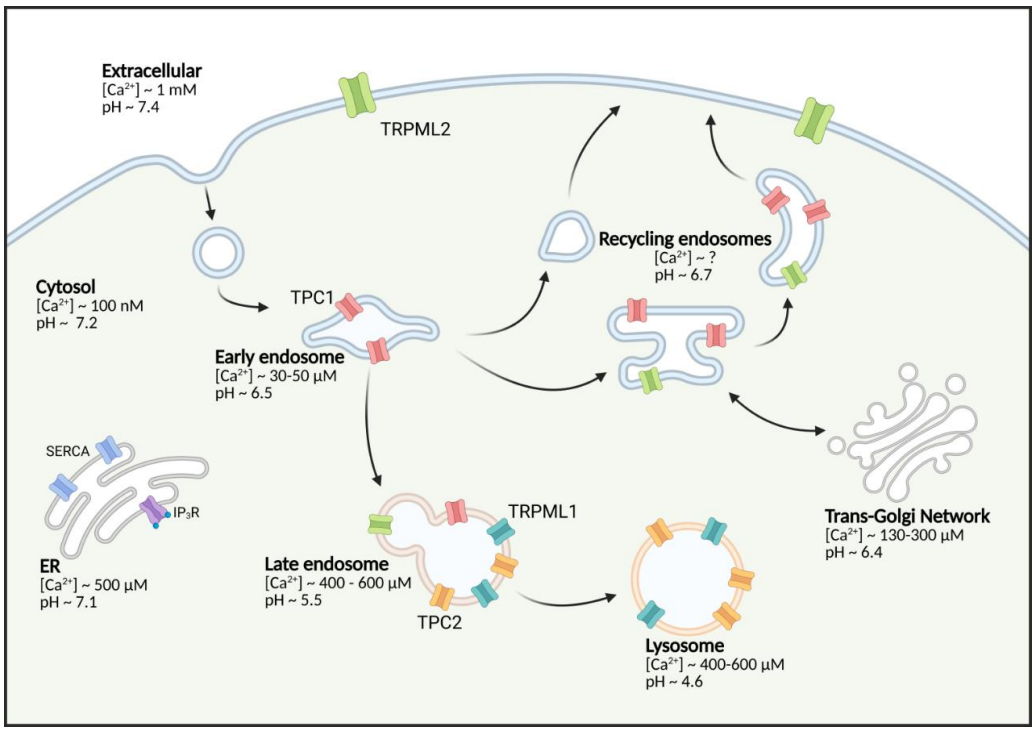

Figure 1.5: The endo-lysosomal system. Following endocytosis, internalised cargo enters early endosomes, the primary sorting vesicle. Cargo is sorted based on its fate, either sent for degradation in lysosomes, retrograde transport to the trans-Golgi network, or recycled back to the cell surface via recycling endosomes. The endo-lysosomal system displays an inverse relationship between luminal pH and [Ca^{2+}]. The distribution of the endo-lysosomal channels TPC1, TPC2, TRPML1 and TRPML2, alongside luminal [Ca^{2+}] and pH approximations are shown for each compartment.

To enter the endo-lysosomal system, cells must first internalise extracellular molecules through the process of endocytosis. Clathrin-mediated endocytosis represents the classical fundamental endocytic mechanism. Numerous cell surface receptors are internalised through clathrin-mediated endocytosis in response to nutrient or hormone binding, including low-density lipoprotein (LDLR), transferrin (TfR), EGFR, and β2-adrenergic receptors (206–208). Additionally, several viruses and bacterial toxins, such as SARS-CoV-2 and cholera toxin, hijack endocytosis to enter a cells endo-lysosomal system, where the pathogen is then trafficked to the lysosome for viral uncoating (209). Following initiation of clathrin-mediated endocytosis, endocytic machinery are recruited to and

surround the endocytic site, assisting with membrane bending and invagination. Notable recruitment proteins include clathrin and the adapter protein 2 complex, which assemble together to form a clathrin lattice coat that covers the endocytic pit to trigger membrane bending (207,210,211). The recruitment and polymerisation of actin filaments at the endocytic site further invaginates the clathrin pit, where the vesicle is then constricted by the membrane fission protein dynamin, inevitably resulting in membrane scission and the formation of a clathrin-coated vesicle (210,212). Finally, the endocytic machinery is released from the vesicle and the clathrin coat disassembled, enabling the vesicle to fuse with nearby early endosomes.

In addition to clathrin-mediated endocytosis, cells maintain the ability to internalise extracellular substances through clathrin-independent mechanisms. Examples of clathrin-independent processes include phagocytosis, where cells engulf pathogens and cellular debris for degradation (213,214), as well as pinocytosis, an endocytic process described in more detail within Chapter 5, whereby small particles and extracellular fluid are engulfed by cells (213,215). Several different clathrin-independent pathways exist, each regulated by specific endocytic machinery. The best-characterised is caveolae-mediated endocytosis, in which extracellular material, such as albumin and bacterial toxins, are internalised through 50-100 nm caveolae membrane invaginations (216). Caveolae are cholesterol-rich membrane curvatures comprised of caveolin proteins, which in response to ligand binding, trigger membrane budding through kinase-regulated caveolae phosphorylation (216,217). Similar to clathrin-dependent endocytosis, dynamin facilitates the scission of intracellular caveolar vesicles, which then fuse with early endosomes. Alternatively, extracellular cargo can be internalised through dynamin- and clathrin-independent pathways. This includes the clathrin-independent carriers/glycosylphosphatidylinositol (GPI)-anchored protein-enriched endosomal compartment (CLIC/GEEC) endocytic pathway, in which the majority

of fluid-phase extracellular material are internalised (213). Representing a constitutive pathway, membrane bending is driven by the Rho-GTPase Cdc42, which activates actin polymerisation pathways, contributing to membrane curvature and facilitating scission through actin-generated mechanical forces (213,218).

Early endosomes exist as the cells major sorting compartment, where the fate of internalised material is determined. Cargo is sorted based on its geometry, sequence-specific sorting motifs, and substrate-protein interactions (219). For the majority of internalised material, their fate is to remain in the early endosome, awaiting compartment maturation into late endosomes and their eventual fusion with lysosomes for degradation and the release of nutrients. In contrast, vesicles containing material destined for cellular retrieval will bud off the early endosome, transported directly back to the cell surface by fast recycling, or first fusing with the endocytic recycling compartment. The latter follows the slow recycling pathway, a longer more stringently regulated route where material is further sorted or modified before being recycling back to the cell surface (220,221). Whilst it is not explicitly clear what determines the choice of either recycling route, material abundance or stimulus strength could dictate whether recycling occurs through fast or slow pathways – a similar phenomenon utilised by synapses for the immediate retrieval (fast) or replenishment (slow) of synaptic vesicles (222).

The endo-lysosomal pathway is characterised by the gradual acidification of compartments, as shown by the reduction in luminal pH between early endosomes (pH ~6.5) and lysosomes (pH ~4.6) (35,45). The mechanism responsible for endo-lysosome acidification are specialised proton pumps known as V-ATPases, which couple ATP hydrolysis to H^+ influx across endo-lysosome membranes (223,224). The strong driving force of H^+ into endo-lysosomes by V-ATPase pumps generates and maintains a lumen-

positive endo-lysosomal membrane potential (~ +10-150 mV) relative to the cytosol (48,225,226). To offset the lumen-positive membrane potential, endo-lysosomal chloride channels, such as ClC-7, provide counter-ion influx, thereby maintaining the driving force for proton accumulation and lumen acidification (227,228). The acidic luminal environment of endo-lysosomes is essential for various functions (45); first, acidic conditions are required to dissociate substrates from internalised cell surface receptors (229,230); second, luminal degradation hydrolases, such as cathepsins, are pH-dependent (231); likewise, the low pH facilitates the hydrolysis of other macromolecules (223); fourth, the acidic environment benefits oxidation reactions which are critical for cell signalling and sensing (232,233).

1.5.1 Phosphoinositides

Phosphoinositides represent a family of phosphorylated phosphatidylinositol derivatives. Comprised of a cytosolic inositol head and non-polar fatty acid tails that extend into the lipid bilayer, phosphoinositides are modifiable phospholipids whose inositol ring can be phosphorylated at either the 3, 4, or 5 inositol positions (234). Distinct cellular compartments are enriched with specific phosphoinositides, which benefits membrane trafficking and signalling by providing membrane identity. PI(4,5)P_2 (PIP_2) represents the residential cell-surface membrane phosphoinositide, which is synthesised from PI(4)P, catalysed by PI(4)P-5-kinases (234). Additional cell surface phosphoinositides include PI(3,4)P_2 and PI(3,4,5)P_3, although both exist in low abundance, representing <0.15% of all phosphoinositides in human cells (234). Within the endo-lysosome system, PI(3)P is situated on early endosomal membranes, as shown by colocalisation with early endosome antigen 1 (EEA1)-positive vesicles (235). The majority of PI(3)P is synthesised following the phosphorylation of phosphatidylinositol at the 3-position of the inositol ring, catalysed

by class 3 PI(3)P kinase (PI3K) Vps34, alongside contributions from class 1 and 2 PI3Ks (236,237). PI(3)P is also the precursor for $PI(3,5)P_2$, the hallmark phosphoinositide of late endosomal and lysosomal membranes, the synthesis of which is catalysed by PIKfyve (182,238).

Phosphoinositide identity is reinforced through interactions with proteins containing unique lipid binding domains, ensuring the correct targeting of proteins to the appropriate intracellular compartment (238). Through these specific interactions, phosphoinositides elicit their specialised cellular functions. In relation to endocytosis, $PI(4,5)P_2$ provides a critical role in stabilising the clathrin lattice coat and the positioning of dynamin in preparation for membrane scission (210,212). Likewise, PI(3)P associates with endocytic vesicles prior to engulfment during pinocytosis (239), whilst also regulating the fusion and fission of endosomes during membrane trafficking and sorting (240). $PI(3,5)P_2$ regulates lysosomal pH by controlling ClC-7 activity (227), alongside endo-lysosomal trafficking and osmoregulation (200,241). Finally, phosphoinositides directly interact and modulate intracellular ion channels and signalling cascades, a trending topic which forms the basis of this thesis.

1.5.2 The transferrin cycle and cellular iron homeostasis

Iron represents an essential mineral for all cells because of its fundamental role in numerous biological processes, including, but not limited to, oxygen transport, DNA biosynthesis, and energy production (242). Most of these processes rely on cells tightly regulating iron redox cycling between Fe^{2+} (ferrous iron) and Fe^{3+} (ferric iron). If uncontrolled, free Fe^{2+} accumulates, acting as a catalyst for the Fenton reaction and the production of reactive oxygen species (ROS), which induces oxidative stress including

DNA damage, lipid peroxidation, and cell death (232,242). To prevent the accumulation of free Fe^{2+}, iron is stored in the cytoplasm as ferritin, a spherical nanocage that retains ferroxidase activity, converting Fe^{2+} into Fe^{3+} for safer long-term storage (232). When required, Fe^{2+} can be released from ferritin through the lysosome-dependent degradation pathway known as ferritinophagy (243), where Fe^{2+} can be utilised by mitochondria for haem and Fe-S biosynthesis (244). However, excessive ferritinophagy can result in large amounts of Fe^{2+} accumulating in the lysosomal lumen and cytosolic labile Fe^{2+} pool, increasing the likelihood of ROS formation and susceptibility to iron-dependent cell-programmed death known as ferroptosis (243,245).

Very little free iron is present in blood plasma. Instead, iron is transported bound to the plasma glycoprotein transferrin. Each monomeric molecule of transferrin (~80 kDa) is able to bind two Fe^{3+} ions very strongly (K_d ~10^{-20} M at pH 7.4) (246,247), to which transferrin delivers to cells through the established constitutive homeostatic process known as the transferrin cycle (illustrated in Figure 1.6). The transferrin cycle utilises the TfR, a ubiquitous cell surface protein critical for cellular iron delivery. Two TfR isoforms are known: the well-characterised TfR1, which is responsible for cellular Fe^{2+} delivery and is regulated by intracellular iron levels; and TfR2, which is restricted to hepatocytes and exhibits a 25-fold reduction in transferrin affinity, instead interacting with the HFE (high-Fe^{2+}) protein to control hepcidin levels and iron absorption (246,248,249).

During the transferrin cycle, Fe^{3+}-bound transferrin (holo-transferrin) binds to the cell surface TfR1, triggering receptor-mediated clathrin-dependent endocytosis and the internalisation of the transferrin/TfR complex into the endo-lysosome system. The mild acidity within the early endosome lumen triggers an exponential decrease in the affinity of transferrin for Fe^{3+}, resulting in Fe^{3+} dissociation. Fe^{3+} is subsequently reduced into Fe^{2+} by

the endosomal luminal protein STEAP3 (six-transmembrane epithelial antigen of the prostate 3) before being transported across the endosomal membrane into the cytosolic labile Fe^{2+} pool by the divalent metal transporter 1 (DMT1). Finally, the apo-transferrin-TfR complex is recycled back to the cell surface for subsequent cycles of Fe^{3+} uptake (Figure 1.6). As briefly mentioned, the transferrin cycle is a constitutive yet rapid cycle, with estimations suggesting a prompt internalisation into early endosomes ($t_{1/2}$ ~5-10 minutes) and transit through the cell back to the cell surface ($t_{1/2}$ ~20 minutes) (220,250). Alternatively, during iron-overload, non-transferrin-bound Fe^{2+} can enter cells directly through cell surface DMT1 or ZRT/IRT-like protein transporters, prior to Fe^{3+} reduction by cell membrane ferrireductases (246,251).

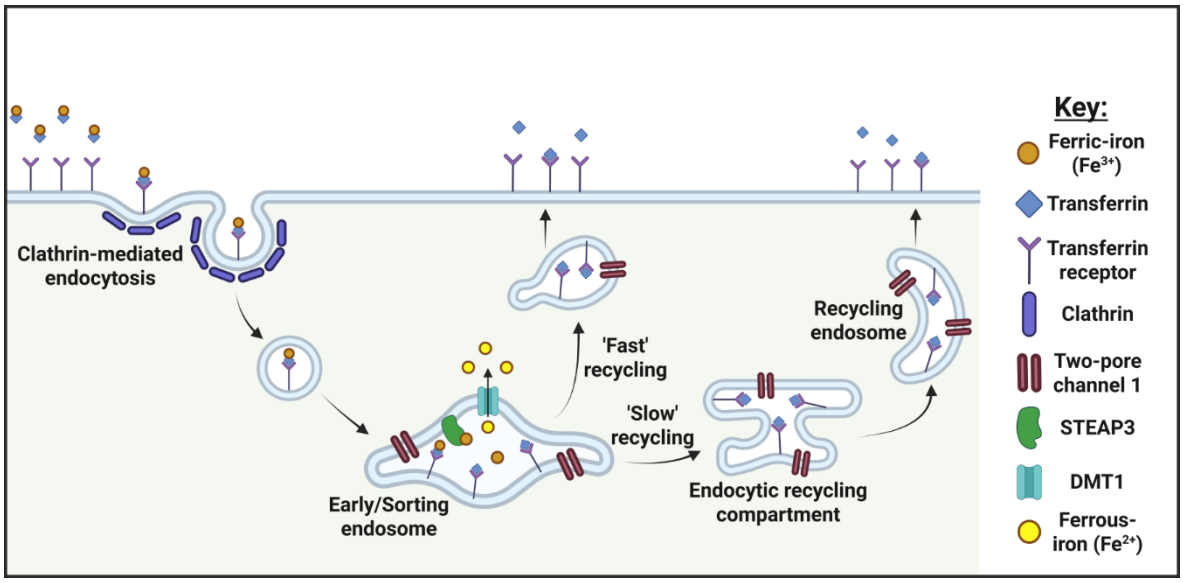

Figure 1.6: The transferrin cycle. Illustration depicting the trafficking and recycling pathway of the transferrin receptor (TfR) complex. Fe^{3+}-bound transferrin (holo-transferrin) binds to cell surface TfRs triggering clathrin-mediated endocytosis. A fall in pH (~6.5) in early endosomes prompts the release of Fe^{3+}, where Fe^{3+} is reduced into Fe^{2+} by STEAP3. Fe^{2+} is transported into the cytosol via DMT1, whereas iron-free transferrin (apo-transferrin) is recycled back to the plasma membrane by recycling endosomes, where it disassociates from the TfR to make it available again for subsequent cycles.

1.6 TPCs in health and disease

Considering their localisation at the intersection of cell membrane- and protein-trafficking, numerous diseases and health conditions are affiliated with TPCs. Neurodegenerative diseases and their link to TPCs represents an area of increasing significance. Within Alzheimer's disease, inhibition of TPC2 prevents the accumulation of β-amyloid plaque through maintenance of endogenous lysosomal pH and Ca^{2+} homeostasis (252,253). Likewise, enhanced TPC2 activity has been observed in fibroblasts derived from Parkinson's disease patients containing the G2019S mutation in leucine-rich repeat kinase 2 (LRRK2), with inhibition of TPC2 correcting lysosomal pH and morphology (254–256). In relation to neuroendocrine signalling, oxytocin secretion and social behavioural disorders also appear to be influenced by TPC-mediated Ca^{2+} release (257).

Genome-wide association studies have revealed several *Hs*TPC2 polymorphisms (M484L, G734E, R210C) associated with hypopigmentation, characterised by blonde hair colour and albinism (258,259). These TPC2 polymorphisms were identified as gain of function (GOF) mutations, with $TPC2^{M484L}$ and $TPC2^{R210C}$ exhibiting increased basal activity and efficacy towards $PI(3,5)P_2$ (259,260), whilst $TPC2^{G734E}$ displayed reduced sensitivity to ATP channel inhibition (260). Given their affiliation with light skin and hair colour phenotypes, these TPC2 GOF variants establish a role for TPC2 in melanin production and pigmentation within melanocytes and melanoma cells. Indeed, genetic ablation or inhibition of TPC1 or TPC2 in melanoma cells and other cancer cell lines results in reduced cell proliferation, metastasis, invasiveness, migration, and tumour growth (160,167,176,261–264). Interestingly, transcription factor EB (TFEB) is upregulated and displays a nuclear localisation in TPC-deficient HeLa cells (262,265), linking TPCs to

lysosomal autophagy and potentially signifying upregulation of tumour-suppressor genes in TPC-deficient cells (266).

As previously mentioned, pathogens and toxins enter host cells through the endocytic pathway, discretely hijacking the endo-lysosomal system to infect and multiply. Given TPCs endo-lysosomal distribution and their importance in regulating endocytic pathways (81,117,184) and membrane trafficking (116,185,186), their involvement in viral and bacterial infectivity is unsurprising. Inhibition of TPCs reduces the infectivity of *Mycobacterium tuberculosis* (Mtb) (267), in addition to severe viruses, including the Ebola virus (169,268) and coronaviruses MERS-CoV (269) and SARS-CoV-2 (COVID-19) (180,270). Similarly, the internalisation and transport of cholera, diphtheria, and *Pasteurella multocida* bacterial toxins are dependent on TPC1 expression (116,117,154).

1.7 Aims of this thesis

This thesis aims to contribute to current perceptions of TPCs involvement in cell-membrane protein trafficking, including the necessity for multiple TPC isoforms and ion fluxes. In particular, the lesser understood isoform, TPC1, is explored by addressing the following research questions:

How is TPC1 involved in mediating cell-membrane protein trafficking? The localisation of TPC1 positions itself at the forefront of membrane fusion and trafficking events. Despite this, little is known of the physiological role of TPC1, nor its involvement in regulating endo-lysosomal processes. This research question aims to assess if and how TPCs are involved in the internalisation, trafficking, and recycling of the TfR.

How do the different ion modalities of TPC1 contribute to cell-membrane protein trafficking? Although an established Na^+-permeable channel, ambiguity surrounds the Ca^{2+} permeability of TPC1. In view of this uncertainty, whole-endosomal electrophysiology will be used to determine the relative Na^+/Ca^{2+} permeability of TPC1, with the value compared to other estimations. Furthermore, TPC1 cation selectivity will be probed *in vitro* to establish if endosomal Ca^{2+} is essential in mediating TfR trafficking.

Does TPC1 have a pathway-specific, or generic role in regulating endo-lysosomal trafficking pathways? The role of TPC1 in endo-lysosomal trafficking will be extrapolated to alternative analogous pathways through the use of high-throughput assays. Likewise, the TPC1 modality required for these pathways will be probed and discussed through re-expression of previously validated TPC1 mutant channels. The specificity or generality for TPC1 or TPC2 in the context of cell membrane trafficking will be discussed.

Which upstream messenger(s) is responsible for initiating TPC1 cation release during cell-membrane protein trafficking? It remains unclear if TPC1 exhibits ligand-dependent cation permeability changes in response to either NAADP or PI(3,5)P2, similar to TPC2. Through manipulation of phosphoinositide production and messenger binding sites, this research question aims to identify which second messenger molecule is likely responsible for relaying cell-membrane protein trafficking signals to TPC1.

Overall, this thesis combines elements of molecular biology, electrophysiology, and microscopy, to characterise native TPC1 within physiologically relevant trafficking pathways.

Chapter 2 – Materials and methods

2.1 Materials

All chemicals were purchased from Sigma-Aldrich unless stated otherwise. All reagents were of analytical grade and stored accordingly based on their recommended storage instructions.

2.2 Cell culture

The human cell lines used in this thesis consisted of the HeLa cell line, derived from an epithelioid cervical carcinoma, and HAP1 cells, a near-haploid cell line derived from KBM-7 chronic myeloid leukaemia cells. Mouse cell lines included macrophage RAW264.7 cells derived from BALB/c mice, as well as mouse embryonic fibroblast (MEF) cells. HeLa, macrophage RAW264.7 and mouse embryonic fibroblast (MEF) cells were maintained in Dulbecco's modified Eagle medium (DMEM), whilst HAP1 cells were maintained in Iscove's modified Dulbecco's medium (IMDM). Both media contained 4500 mg/L glucose and phenol red, supplemented with 10% (v/v) foetal bovine serum (FBS), 2 mM L-glutamine, 100 U/ml penicillin, and 0.1 mg/ml streptomycin. Cells were kept in a humidified incubator at 37ºC supplied with 5% (v/v) CO_2. Upon resurrection from long-term storage, cells were treated with 0.5 μM mycoplasma removal agent (Bio-Rad Laboratories; cat: BUF035) for three passages.

2.2.1 TPC knockout cell lines

HeLa *TPNC1* and *TPCN2* knockout cells were generated by Dr Julie Xiao from the Townsend group (University of Oxford) through CRISPR/Cas9 genome editing using double single guide (sg) RNA, as detailed in Dr Xiao's DPhil thesis (268). In summary, exon 7 from the *TPCN1* transcript variant 1 (NCBI code: NM_001143819.2) and exon 2 from the *TPCN2* transcript (NCBI code: NM_139075.4) were chosen for sgRNA-targeted deletion. Deletion of exon 7 and exon 2 from *TPCN1* and *TPCN2* respectively, resulted in a frameshift in transcription, followed by nonsense translocation and a premature STOP codon. Any residual protein translated lacked transmembrane and pore-forming helices, rendering the protein non-functional. All clones generated (*TPCN1* KO: A17 and D149, *TPCN2* KO: E64 and E182) were screened for genomic DNA (PCR) and mRNA (reverse transcription (RT)-PCR), as detailed in Dr Xiao's DPhil thesis (268), to validate and confirm the complete knockout of either gene.

Knockout macrophage RAW264.7 cells were custom engineered by Abcam using the CRISPR/Cas9 system. *Tpcn1*$^{-/-}$ cells were generated by guide RNA (gRNA)-targeted deletion of exon 3 from *MmTpcn1* (ENSMUSG00000048677), using the following targeted gRNA sequences: 5'-ATCTCCCAGTTGTGTCCGGT-3' and 5'-AGAGGCGGCAATCTACCTCC3'. This resulted in a 43 bp deletion of the splicing donor site on exon 3 and a frameshift knockout. Similarly, for *Tpcn2*$^{-/-}$ cells, exon 4 and intron 4 from *MmTpcn2* (ENSMUSG00000048677) were targeted using the gRNA sequences: 5'-TGGCCTGACCGAGACGATCG-3' and 5'-GACGATACCAAGAGCTCTGT-3'. This resulted in a 79 bp deletion, removal of the splicing donor site and a frameshift of the open reading frame. RT-PCR reactions using mRNA were performed 'in-house' by Dr Lianne Davis to confirm the deletion of TPC1 or TPC2 in RAW264.7 cells.

MEF wildtype, *Tpcn1*$^{-/-}$, *Tpcn2*$^{-/-}$, and *Tpcn1/2*$^{-/-}$ double knockout cells were obtained from primary mouse embryos. The generation of these mice and the extraction and verification of these cells have been extensively detailed previously (87,116).

2.2.2 TPC stable cell lines

Stable clones of HeLa cells overexpressing *Hs*TPC1-mNeonGreen or *Hs*TPC1-ALFA-tag were generated for experimental use. Following transient transfection with the respective plasmid DNA (see section 2.5), 10 μg/ml blasticidin (InvivoGen) was added to the cell culture media to enforce the selection of expressing cells.

Single-cell sorting was performed for *Hs*TPC1-mNeonGreen stable cells at the Flow Cytometry Facility within the Sir William Dunn School of Pathology (University of Oxford). Cells were gated by size and granularity to exclude cell debris and ensure doublet/triplet cells were excluded (Appendix Figure A.1A). Furthermore, cells were gated according to protein expression which was determined by the fluorescence of their fluorescent protein tag. Three gates were chosen for TPC1 expression resulting in specified single-cell sorting based on either low (P3), moderate (P5) or high (P4) TPC1 overexpression (Appendix Figure A.1B). Single cells overexpressing TPC1 were sorted into 96-well plates, then grown and cultured as described above in cell culture media containing 10 μg/ml blasticidin to maintain selectivity.

2.2.3 JPT2 and Lsm12 knockout cell lines

The targeted deletion of either *LSM12* (NM_152344) or *HN1L* (JPT2; NM_144570) in HAP1 cells was performed using gRNA CRISPR/Cas9 genome editing by Horizon

Discovery. For *LSM12* knockout cells, the gRNA sequence 5'-CATTTTGGATTGGTAGTCAA-3' was used to target exon 2, resulting in a 7 bp deletion and a frameshift of the open reading frame. *JPT2* knockout cells were generated following a 1 bp insertion in exon 3 using the gRNA sequence 5'-CGGAGACCCAAAAATGTCGC-3'. This insertion similarly resulted in a frameshift and the altered translation of JPT2. Successful deletion of *LSM12* and *JPT2* was verified by Western blotting performed by Dr Liane Davis (see section 2.7.1).

2.2.4 Long-term cell storage

Stocks of each cell line were maintained at -196ºC in a liquid nitrogen cell storage bank. Cells were preserved in aliquoted suspensions consisting of FBS with 10% (v/v) dimethyl sulfoxide (DMSO), which were slowly frozen to -80ºC before transfer to the cell bank.

2.3 Whole-endo-lysosome electrophysiology

Electrophysiological experiments were performed in collaboration with Professor Cheng-Chang Chen and Alice Lin (National Taiwan University, Taiwan) in both Oxford and Taiwan laboratories. Whole-endo-lysosome patch-clamp enables direct voltage and current measurements of isolated endo-lysosomal channels situated on their native membrane within an experimentally controlled physiological environment. The procedure of whole-endo-lysosome patch-clamping is based on previously established protocols (136,271), as detailed below.

2.3.1 Swelling of endo-lysosomes

Stable HeLa cells overexpressing *Hs*TPC1-mNeonGreen were seeded into 6-well plates containing 25 mm glass coverslips. Alternatively, HeLa cells were transfected with either *Hs*TPC1$^{A280S/V646M/N647G}$-mNeonGreen (TPC1-mut3), or *Hs*TPC1^{K330A}-mNeonGreen, as described below in section 2.5. To promote cell adhesion and prevent the detachment of cells during endo-lysosome isolation, 25 mm glass coverslips were autoclaved and coated with 0.1 mg/ml poly-D-lysine (Gibco, cat: A3890401) overnight at room temperature, then washed and stored in sterile-filtered water (cat: W3500).

Owing to their size, endo-lysosomes must first be enlarged to a diameter of approximately 3-5 μm (136) to enable isolation and ion channel measurement. For endo-lysosome vesicle enlargement, the PIKfyve inhibitor vacuolin-1 was used to non-selectively enlarge TPC1-positive endosomes, through inhibition of endo-lysosomal exocytosis and membrane fusion (183,272). HeLa cells were incubated with 2 μM vacuolin-1 overnight at 37^{o}C supplied with 5% (v/v) CO_2 to enlarge TPC1-positive endosomes.

2.3.2 Design and fabrication of glass pipettes

Due to the size and morphology of endo-lysosomes, the fabrication of glass pipette electrodes is crucial for successful endo-lysosome patch-clamping. Patch-clamp electrodes were produced using a Sutter P-97 micropipette puller (Sutter Instrument, USA) equipped with a 3.0 mm wide trough filament (World Precision Instruments, cat: FT330B). Borosilicate glass capillaries (Sutter Instrument, cat: BF150-75-10) were pulled into patch-clamp pipettes following a 6-cycle pulling program (Appendix Table A.1), with the heat value predetermined by a ramp protocol. Patch-clamp pipettes were inspected and fire-polished by applying brief heat pulses to the pipette tip using an MF-830 microforge

(Narishige, Japan). Optimal recording pipettes which had a resistance of 5-8 MΩ, tip opening diameter of <0.3 μm, and parallel inner pipette >2 μm following fire-polishing, were used for subsequent whole-endo-lysosome patch-clamp recordings. Pipettes which did not meet this criteria were used as isolation pipettes for the dissection and isolation of endo-lysosomes.

2.3.3 Bath and pipette recording solutions

Unless stated otherwise, bath and pipette recording solutions were designed to mimic the physiological environment of the endosome lumen (pipette solution) and cytosol (bath solution). Thus, the luminal solution used for patching TPC1-positive endosomes was buffered at a mildly acidic luminal pH (6.15), in an effort to mirror the reported endogenous pH of early and recycling endosomes (35). For standard recordings, the pipette solution contained in mM: 140 Na-methanesuphonic acid (MSA), 5 K-MSA, 2 Ca-MSA, 1 $CaCl_2$, 10 MES pH 6.15. The standard bath solution contained in mM: 140 K-MSA, 5 KOH, 4 NaCl, 0.39 $CaCl_2$, 1 EGTA and 10 HEPES pH 7.2; the bath solution was buffered to a free Ca^{2+} concentration of 110 nM.

For bi-ionic recordings, solutions were comprised of a single permeant cation. The pipette solution contained (in mM): 105 $CaCl_2$ and 5 MES (pH 6.15 adjusted with $Ca(OH)_2$), whilst the bath solution contained (in mM): 160 NaCl and 5 HEPES (pH 7.2 adjusted with NaOH). For Na^+ gradient recordings, the pipette solution contained (in mM): 145 Na-MSA, 5 NaCl and 10 HEPES pH 7.2, whilst the bath solution contained (in mM): 3 NaOH, 2 NaCl, 145, 125 or 0 K-MSA, 0, 20 or 145 Na-MSA and 10 MES pH 6.15. All solutions were sterilised by passing them through a 0.2 μm filter and stored at 4°C for 2-4 weeks.

2.3.4 Isolation of endo-lysosomes

A single coverslip from the 6-well plate containing cells with enlarged vesicles was removed and transferred to a microscope imaging chamber (Warner Instruments, cat: 641943) containing 1 ml of bath solution. Isolation pipettes were back-filled with pipette solution using a self-made Eppendorf plastic filling needle and mounted onto the patch-clamp headstage. Cells were inspected using a Nikon Eclipse Ti inverted microscope equipped with a 40x (NA 0.55) Achro objective to ensure vesicle enlargement and that the enlarged vesicle was overexpressing an mNeonGreen-tagged TPC1. The isolation pipette, controlled by an MPC-200 micromanipulator (Sutter Instruments, USA), was used to isolate TPC1-positive endosomes from cells by rapidly tearing the plasma membrane, then gently pushing the enlarged endo-lysosome out through the incision away from the cell.

2.3.5 Whole-endo-lysosome patch-clamp protocol

Whole-endo-lysosome patch-clamp recordings were collected using a Multiclamp 700B amplifier, a Digidata 1440A data acquisition system and pCLAMP software (Molecular Device, USA). Fire-polished glass patch pipettes were used for TPC1 channel recordings. Briefly, a negative pressure was applied to the pipette to suck the isolated endosome into the pipette tip, in an effort to form a gigaseal (>1 GΩ). To facilitate seal formation, a series of fast-ramp protocols (−100 mV to +100 mV in 100 ms; 10-100 times; 1 second interval) were applied to facilitate gigaseal formation. To rupture the endosomal membrane and establish the whole-endo-lysosome configuration, a series of fast high-voltage ‘ZAP’ pulses (-700 mV in 0.5 ms) were applied until the capacitive transients suddenly increased, indicating access to the interior of the endosome. Capacitance compensation was then applied to cancel capacity transients and the endosome membrane capacitance (1-3 pF)

recorded. To activate TPC1, water-soluble PI(3,5)P_2-diC8 (Echelon Biosciences, cat: P-3508) was directly applied to the recording bath at a final concentration of either 0.1 μM (lipid-binding mutant and Na^+ gradient recordings) or 1 μM (bi-ionic recordings). TPC1 current recordings were collected using 500 ms voltage ramps from -100 to +100 mV, applied every 5 seconds. All electrophysiological recordings were performed at room temperature (22°C). For analysis under bi-ionic conditions, the permeability ratio ($P_{Ca/Na}$) was calculated as described below. Data was analysed and plotted using Clampfit (Molecular Device).

2.3.6 Calculations

Permeability ratios of *Hs*TPC1 and *Hs*TPC1$^{A280S/V646M/N647G}$ (TPC1-mut3) under bi-ionic conditions were calculated according to the Goldman Hodgkin Katz equation, Eq. III.3 from Chen *et al*. (273):

$$(1) \quad \frac{P_{Ca}}{P_{Na}} = \frac{[Na]_i}{4[Ca]_o} * e^{\frac{VF}{RT}}\left(e^{\frac{VF}{RT}} + 1\right)$$

Where: P_{Ca} = Ca^{2+} permeability; P_{Na} = Na^+ permeability; $[Na]_i$ = concentration of Na^+ in the cytosol (bath solution); $[Ca]_o$ = concentration of Ca^{2+} in the lumen (pipette solution); V = reversal potential (V); F = Faraday constant; R = gas constant; T = room temperature (K).

2.4 Molecular cloning techniques

Unless specified, plasmid DNA constructs were generated in-house, either by restriction cloning, Gibson Assembly cloning, or site-directed mutagenesis. The primers and individual plasmid constructs used in this thesis are listed in section 2.13 Table 2.2 and section 2.14 Table 2.3 respectively, alongside protein accession numbers and the cloning

technique used to generate each construct. Constructs encoding human TPC1, TRPML1, and TRPML2, were engineered with a C-terminal ER export sequence (ERES: FCYENEV), fused to the upstream protein by a TG amino acid linker, to minimise ER retention and encourage compartmental targeting. For visualisation, fluorescent proteins were fused to either the C- or N-terminus of proteins by a short flexible amino acid linker (Table 2.3).

2.4.1 Primer design

To clone DNA from template plasmid constructs, primers were designed within the SnapGene software against the 5' and 3' ends of each template DNA, with a target annealing temperature (T_m) of 55^{o}C. To optimise downstream DNA assembly efficiency, overlapping primers were designed to contain 20-25 base overlaps relative to adjacent DNA fragments. In an effort to assist future cloning projects, restriction enzyme sites were incorporated into primers to recreate the restriction site after amplification and assembly. Primers were synthesised by Invitrogen and reconstituted at 200 µM. A full list of primers are shown in section 2.13 Table 2.2, alongside the specific plasmid construct each primer helped generate.

2.4.2 Synthesis and annealing of oligonucleotides

Oligonucleotides containing the ER export amino acid sequence FCYENEV were designed within the SnapGene software, alongside up- or downstream unique restriction enzyme sites to assist future cloning projects. The oligonucleotides were synthesised by Invitrogen as 5' phosphorylated primers, thereby allowing direct insertion into the vector. Complementary oligonucleotides were prepared at 20 µM in annealing buffer (10 mM Tris

pH 7.5, 50 mM NaCl, 1 mM EDTA) and annealed together during a temperature ramp, starting at 95°C for 2 minutes, then decreasing 1°C every 1 minute until 25°C.

2.4.3 DNA amplification – PCR

Polymerase chain reaction (PCR) was performed using the Q5 Hot Start High-Fidelity kit (NEB) following the manufacturer's instructions. Briefly, forward and reverse primers were mixed with nuclease-free water to 500 nM together with 1 ng of template DNA, followed by the addition of the NEB master mix. The master mix buffer contained the Q5 DNA polymerase, Mg^{2+}, and free deoxynucleotide triphosphates. The thermocycling conditions for routine PCR reactions is summarised in Appendix Table A.2.

PCR products were analysed by gel electrophoresis (section 2.4.5), with successfully amplified PCR fragments purified using the Monarch PCR and DNA Cleanup kit (NEB) following the manufacturer's instructions. In summary, DNA fragments were mixed with binding buffer and loaded onto a DNA cleanup column. The column was centrifuged and washed twice with an ethanol-based buffer to remove enzymes, primers, and impurities, while the negatively-charged DNA fragment remained bound to the silica-gel membrane. Washed DNA was eluted in the supplied DNA elution buffer and stored at -20°C for future use.

2.4.4 Restriction enzyme digestion

Plasmid constructs were digested using the appropriate FastDigest restriction enzymes dependent upon the sites incorporated in the assembled PCR product. In summary, plasmid DNA was digested by FastDigest restriction enzymes (1 U enzyme / 1 μg DNA,

ThermoFisher Scientific) at 37ºC for 30 minutes in the appropriate restriction enzyme buffer as stated by the manufacturer. Successful double restriction enzyme digest reactions were confirmed by gel electrophoresis (section 2.4.5) and the digested vector extracted and gel purified (section 2.4.6). In comparison, single restriction enzyme digest reactions were DNA purified after incubation following the same purification method used for PCR products (see section 2.4.3).

2.4.5 Agarose gel electrophoresis

Digested DNA and PCR-amplified products were mixed with DNA gel-loading dye (2.5% Ficoll-400, 3.3 mM Tris-HCl pH 8, 10 mM EDTA and 0.08% SDS; NEB, cat: B7024) and loaded onto 1% (w/v) agarose gels in Tris-acetate-EDTA (TAE) buffer (40 mM Tris-acetate pH 7.5 and 1 mM EDTA; Fisher, cat: 10490264) containing ethidium bromide (0.5 μg/ml). Digest reactions performed with FastDigest Green buffer (ThermoFisher Scientific) were loaded directly onto the agarose gel. A DNA ladder ranging from 100 to 10,000 bp (GeneRuler 1 kb DNA ladder, ThermoFisher Scientific) was loaded alongside DNA to provide size markers. Loaded agarose gels were electrophoresed at 100 mV in TAE buffer, followed by visualisation using an ultraviolet (UV) transilluminator.

2.4.6 Agarose DNA purification

Initially, electrophoresed DNA fragments were carefully excised from the agarose gel in preparation for purification. The Monarch DNA extraction kit (NEB) was used according to the manufacturer's guidelines in order to purify DNA fragments from the agarose gel. In summary, excised gel slices were solubilised in gel dissolving buffer (guanidine thiocyanate and sodium iodide-based) at a ratio of 400 μl buffer per 100 mg agarose, then

loaded onto a silica-gel DNA collection column and centrifuged. Bound DNA was washed to remove contaminants and then eluted in DNA elution buffer.

2.4.7 Dephosphorylation of vector DNA

To prevent re-ligation of digested linearised DNA, vector DNA was dephosphorylated prior to ligation by removal of the 5' phosphate. Dephosphorylation of DNA was performed using Quick CIP (NEB, cat: M0525) following the manufacturer's instructions. Briefly, 1 pmol of vector DNA was incubated with 1 µl Quick CIP enzyme diluted in rCutSmart buffer (20 mM Tris-acetate pH 7.9, 50 mM potassium acetate, 10 mM magnesium acetate and 100 µg/ml recombinant albumin) and incubated for 10 minutes at 37^{o}C, followed by heat-inactivation at 80^{o}C for 2 minutes.

2.4.8 DNA ligation

Vector and insert DNA fragments containing cohesive or blunt ends were annealed together using the Quick Ligation kit (NEB, cat: M2200) following the manufacturer's instructions. Briefly, insert DNA was ligated into 100 ng of digested dephosphorylated vector DNA at a 3:1 insert to vector molar ratio, diluted in Quick Ligase reaction buffer (66 mM Tris-HCl pH 7.6, 10 mM $MgCl_2$, 1 mM dithiothreitol, 1 mM ATP and 7.5% polyethylene glycol). The vector and insert DNA mixture was then incubated with 0.5 µl Quick Ligase for 5 minutes at room temperature, directly followed by transformation into Z-Competent bacteria (see section 2.4.11), or stored at -20^{o}C long-term.

2.4.9 Gibson Assembly

Gibson Assembly was utilised as an alternative cloning technique for the assembly of multiple linear DNA fragments and to overcome restriction site requirements. The NEBuilder HiFi Assembly Master mix (NEB) was used following the manufacturer's instructions. The contents of the enzyme master mix were as follows: exonucleases to create 3' overhangs which enable complementary single stranded regions to anneal, DNA polymerase to fill in any gaps within each annealed fragment, DNA ligase to seal nicks in the assembled DNA.

Initially, DNA fragments containing sequence homology between neighbouring fragments were amplified by PCR (section 2.4.3) using custom primers that included the appropriate homologous sequences within an approximate 20-25 bp overlap (detailed in section 2.4.1). Restriction enzyme-digested vector DNA and PCR-amplified DNA fragments were mixed together at a DNA molar ratio of 1:2, to a total of 0.1-0.2 pmol DNA per Gibson Assembly reaction. Assembled reactions were incubated with the enzyme master mix for 15 minutes at 50^{o}C, then stored on ice for subsequent heat-shock transformation (see section 2.4.12), or at -20^{o}C long-term.

2.4.10 Site-directed mutagenesis

Targeted mutations (including substitutions, insertions and deletions) were introduced into DNA constructs by means of entire plasmid amplification using back-to-back non-overlapping primers containing the desired mutation. Primers specific for mutagenesis were designed using the NEBaseChanger tool (https://nebasechanger.neb.com), then synthesised by Invitrogen and reconstituted at 200 μM (Table 2.2). Plasmid DNA

constructs were amplified by PCR as described in section 2.4.3. Routine site-directed mutagenesis PCR reactions are summarised in Appendix Table A.2.

Following amplification, a KLD (kinase, ligase and DpnI) enzyme mix (NEB, cat: M0554) was added to the mutagenesis PCR product. This reaction simultaneously phosphorylates PCR-amplified linear DNA (kinase), creates a circular DNA construct through ligation of phosphorylated ends (ligase), and specifically degrades methylated template DNA to ensure the exclusive transformation of mutated plasmid DNA (DpnI). A reaction containing 1 µl of mutagenesis PCR product and 1 µl KLD enzyme mix, diluted in KLD reaction buffer, was incubated for 5 minutes at room temperature. Reactions were then transformed into Z-Competent bacteria (described in section 2.4.11), or stored at -20ºC long-term.

2.4.11 Preparation and transformation of Z-Competent bacteria

Escherichia coli (*E. coli*) were used to transform and propagate plasmid DNA constructs. To increase the speed, reliability and efficiency of DNA transformation, Z-Competent *E. coli* were generated using the Z-Competent *E. coli* transformation kit (Zymo Research, cat: T3001) according to the manufacturer's guidelines. Initially, a single colony of either DH5α or Top-10 *E. coli* was picked from an agar plate and cultured in 5 ml Luria broth (LB: 10 g/L tryptone, 5 g/L yeast extract and 10 g/L NaCl) overnight at 37ºC with shaking (190-210 rpm). From this pre-culture, 0.5 ml was used to inoculate 50 ml of the provided ZymoBroth, which was shaken (150-250 rpm) at 28ºC until the *E. coli* culture had reached an optical density ($OD_{600\ nm}$) of 0.4. Pre-chilled *E. coli* cultures were then pelleted by centrifugation at 2000g for 10 minutes at 4ºC, the pellet washed by resuspension in the

provided wash buffer, followed by centrifugation once again. After washing, pelleted *E. coli* were resuspended in 5 ml of the provided competent buffer and divided into 100 µl aliquots which were stored at -80ºC.

For bacterial transformation, 10 µl of plasmid DNA generated by restriction cloning or site-directed mutagenesis was added to 100 µl of thawed DH5α Z-Competent *E. coli* and incubated on ice for 10 minutes. Transformed Z-Competent *E. coli* were then spread onto surface-dried LB agar plates containing either 50 µg/ml kanamycin or 100 µg/ml ampicillin, dependent upon the plasmids respective antibiotic resistance. Prior to plating kanamycin-resistant plasmids, transformed *E. coli* were pre-incubated in SOC outgrowth medium (2% vegetable peptone, 0.5% yeast extract, 10 mM NaCl, 2.5 mM KCl, 10 mM $MgCl_2$, 10 mM $MgSO_4$ and 20 mM glucose; NEB, cat: B9020) at 37ºC with rotation for 1 hour, to allow the bacteria time to multiply and express the kanamycin-resistant gene. Agar plates were incubated overnight at 37ºC to promote colony growth.

2.4.12 Bacteria transformation by heat-shock

Plasmid DNA constructs generated using HiFi Gibson Assembly were transformed into NEB DH5α-competent *E. coli* (NEB, cat: C2987) according to the manufacturer's instructions. Briefly, 50 µl of competent cells were thawed on ice and mixed with 2 µl of the assembled Gibson reaction, followed by incubation on ice for 30 minutes. Assembled DNA was introduced into bacteria through temporary cell membrane pores created by heat-shock. This involved placing the DNA mixture in a 42ºC water bath for 30 seconds, then immediately transferring onto ice for 2 minutes. Transformed bacteria were pre-incubated with SOC outgrowth medium for either 15 minutes (ampicillin-selective) or

45 minutes (kanamycin-selective), then plated onto surface-dried agar plates containing the respective antibiotic and incubated overnight at 37ºC.

2.4.13 Small scale plasmid DNA preparation (miniprep)

Plasmid DNA was prepared using the GeneJET Plasmid miniprep kit (ThermoFisher Scientific, cat: K0503) and provided solutions according to the manufacturer's instructions. Initially, single bacterial colonies were propagated overnight at 37ºC (with shaking) in 5 ml LB containing the selective antibiotic. The bacteria was centrifuged at 6800g for 2 minutes and the resultant pellet resuspended in a Tris-HCl/EDTA buffer containing RNase-A. The bacterial suspension was subsequently lysed in an alkaline (NaOH) solution containing SDS to separate DNA and denature proteins, then neutralised using an acidic high-salt buffer containing potassium acetate, in order to precipitate lipids, proteins, and genomic DNA. Bacterial lysates were centrifuged at 12,000g for 5 minutes and the supernatant passed through a silica-gel spin column by centrifugation. Silica membrane-bound DNA was then washed twice using a high-salt ethanol concentrated buffer to remove contaminants, with the presence of ethanol ensuring only pure DNA remained bound to the membrane. Purified plasmid DNA was then eluted from the silica membrane using 50 µl of elution buffer (10 mM Tris-HCl pH 8.5 and 0.1 mM EDTA) and stored at -20ºC.

2.4.14 Large scale plasmid DNA preparation (midiprep)

Large scale plasmid DNA preparation and the purification of endotoxin-free DNA was performed using the ZymoPURE II Plasmid midiprep kit (Zymo Research, cat: D4200) according to the manufacturer's instructions. Briefly, 50 ml of bacteria culture grown

overnight in LB, was pelleted by centrifugation and then resuspended and lysed in the provided buffers. The bacterial lysate was subsequently neutralised and loaded into a ZymoPURE syringe filter, where the lysate was manually pushed through the filter using the syringe. The recovered filtered lysate was mixed with the supplied DNA binding buffer to dehydrate DNA and provide the optimal conditions for silica membrane binding, then transferred to a Zymo spin column. Plasmid DNA was absorbed onto the membrane using a filtration vacuum manifold, followed by three ethanol-based washes to remove any contaminants. DNA was eluted from the silica membrane using 200 µl of elution buffer, then transferred into an EndoZero-II spin column and centrifuged at 10,000g for 1 minute to remove endotoxins from the DNA. Purified plasmid DNA was stored at -20^{o}C.

2.4.15 DNA quantification

Plasmid DNA concentrations were determined on a NanoDrop One spectrophotometer (ThermoFisher Scientific), which measures the absorbance of DNA under a 260 nm UV light. Alongside concentrations, the purity of plasmid DNA was assessed through comparison of the 260 nm absorbance peak, in contrast to 230 nm and 280 nm absorbance, to detect salt or protein contaminants respectively.

2.4.16 DNA sequencing

All newly generated plasmid constructs were sequenced by Source BioScience (Cambridge, UK) to confirm successful DNA insertion or mutagenesis. For small insertions (≤1200 bp), Sanger sequencing was performed using 100 ng/µl of plasmid DNA and 3.2 pmol/µl of primer either upstream or downstream of the desired sequencing region. For large insertions (≥1200 bp) or site-directed mutagenesis, whole-plasmid DNA was

sequenced using Nanopore sequencing technology, by quantifying changes in the electrical current of DNA. All returned sequences and chromatograms were aligned against their predicted DNA sequences within the SnapGene software, then visually inspected to check for non-intentional mutations, or changes to the open reading frame.

2.5 Transient transfection with JetPEI

Cells were seeded one or two days before transfection at a predetermined density to ensure an approximate 50-70% cell confluency on the day of transfection. The commercial transfection reagent JetPEI (Polyplus) was used according to the manufacturer's instructions. Acting as a cationic polymer, JetPEI binds to DNA, compacting DNA into positively-charged complexes which are internalised into cells by endocytosis. Within endosomes, JetPEI buffers the luminal pH, leading to the influx of water and Cl^- ions which causes endosomes to swell and rupture, releasing DNA into the cytoplasm where it is then transported to the nucleus for protein expression. Purified plasmid DNA and JetPEI were diluted in separate equal volumes of 150 mM NaCl at a ratio of 1:2 plasmid DNA to JetPEI reagent (w/v). The diluted JetPEI was then added to the DNA solution, vortexed, and incubated at room temperature for 15 minutes before the mixture was added to cells. Cells were incubated for at least 24 hours before experimental use, while cell media was replaced after 4-6 hours to avoid cellular toxicity.

2.6 Ca^{2+} imaging

Ca^{2+} imaging experiments were performed using a ZEISS LSM510-META laser-scanning confocal microscope equipped with a 40x (NA 1.3) Fluar objective. Ca^{2+} imaging experiments were performed in extracellular medium (ECM) to mimic the extracellular

milieu, containing (in mM): 121 NaCl, 5.4 KCl, 0.8 $MgCl_2$, 6 $NaHCO_3$, 1.8 $CaCl_2$, 10 glucose, 25 HEPES pH 7.2, and RPMI 1640 essential amino acids (cat: R7131). For experiments performed in Ca^{2+}-free medium, cells were washed three times in Ca^{2+}-free ECM supplemented with 100 μM EGTA and experiments conducted in this same medium.

To measure intracellular Ca^{2+} responses, cells were loaded with the cytosolic Ca^{2+}-sensitive dye Fluo-8H-AM (AAT Bioquest, cat: 21090), or transfected (as described in section 2.5) with the genetically encoded Ca^{2+} indicator (GECI) G-GECO1.2, GCaMP6s, or NEMOs fused to the C-terminus of the desired protein. For dye loading, cells were incubated with 2 μM Fluo-8H-AM in ECM for 45 minutes at room temperature, with or without the presence of the cytosolic Ca^{2+} chelators EGTA-AM or BAPTA-AM, followed by a 15 minute de-esterification period. Ca^{2+} responses were determined via excitation at 488 nm and emission fluorescence captured at 525 nm, with images collected every 2-5 seconds. To ensure GECI transfection or Ca^{2+} dye loading, as well as to normalise single-cell Ca^{2+} responses to the F_{max}, 1 μM ionomycin plus 10 mM $CaCl_2$ was added post-run to saturate the reporter. Images were analysed on a single cell basis using a custom-written Magipix software (Ron Jacob, King's College London, UK).

2.6.1 Determination of Ca^{2+} reporter affinities

To determine the Ca^{2+} affinity of Fluo-3 (ThermoFisher Scientific, cat: F3715) and 10 kDa Cal-520 dextran (AAT Bioquest, cat: 20601) *in situ* at endosomal pH 6.7, fluorescence was measured in 96-well black-walled μCLEAR microplates (Greiner Bio) on a BMG Labtech CLARIOstar plate reader. Fluorophores were excited at 470 ± 27 nm and emission collected at 560 ± 37.5 nm. Fluo-3 and Cal-520 dextran (1 μM) were diluted in an intracellular-like medium (ICM, in mM: 140 KCl, 10 NaCl, and 20 MES pH 6.7)

containing varying ratios of Ca^{2+} and the Ca^{2+} chelators EGTA (cat: E4378) or HEDTA (cat: H8126). The Ca^{2+} chelators were prepared at 5 mM in ICM in the presence or absence of 5 mM $CaCl_2$, then mixed in different ratios to obtain a range (nM to mM) of free Ca^{2+} concentrations. The free Ca^{2+} concentration was determined from total Ca^{2+} in the presence of 5 mM chelator at pH 6.7, using the MaxChelator calculator (C. Patton, Stanford, USA). Fluorescence was normalised to the F_{min} and F_{max} and the data fitted using a non-linear curve, to which the K_d was determined against.

2.6.2 Calculation of endosomal luminal Ca^{2+}

HeLa wildtype cells were pre-incubated with 0.5 mg/ml Cal-520 dx and 0.5 mg/ml 10 kDa Texas-Red-conjugated dextran (ThermoFisher Scientific, cat: D1863) and chased to early endosomes for 5, 10, or 20 minutes at 37ºC in ECM. Cells were then washed three times with ECM and imaged in ECM. Fluorescence was measured ratiometrically at resting (F: Ca^{2+}-containing), saturated (F_{max}: 2 μM ionomycin + 10 mM $CaCl_2$), and free (F_{min}: 2 μM ionomycin + 5 mM EGTA) Ca^{2+}-binding states. Secondary basal measurements were performed after an additional 10 min incubation at 4ºC in Ca^{2+}-free medium (supplemented with 100 μM EGTA), the same methodology used when assessing the effect of extracellular Ca^{2+} removal on transferrin trafficking. To account for uneven dye loading, Cal-520 dextran Ca^{2+} measurements were performed ratiometrically against a co-loaded Ca^{2+}-insensitive Texas-Red-conjugated dextran (488/561), excited at 488 and 561 nm, and emission centred at 525 and 595 nm respectively. The endosomal luminal Ca^{2+} concentration was calculated according to equation 6 from Grynkiewicz *et al*. (274) below:

$$(2) \qquad [Ca^{2+}] = K_d * \frac{F - F_{min}}{F_{max} - F}$$

Where: $[Ca^{2+}]$ = Ca^{2+} concentration; K_d = Ca^{2+} binding affinity of reporter; F = measured fluorescence ratio (488/561); F_{min} = measured fluorescence ratio (488/561) following Ca^{2+} chelation; F_{max} = measured fluorescence ratio (488/561) of the reporter when saturated with Ca^{2+}.

2.7 Immunological techniques

2.7.1 Western blotting

Cells were seeded onto 100 mm petri dishes (Greiner Bio-One) at a predetermined density to ensure an approximate 90% confluency and sufficient protein extraction on the day of use. Cells were washed in phosphate buffered saline (PBS) four times to remove dead cells and serum proteins which could interfere with downstream protein detection, then solubilised for 1 hour on ice in Pierce IP lysis buffer (25 mM Tris-HCl pH 7.4, 150 mM NaCl, 1 mM EDTA, 1% NP-40 and 5% glycerol; ThermoFisher Scientific, cat: 87787) supplemented with cOmplete EDTA-free protease inhibitors (Roche, cat: 11836153001). Subsequently, cells were centrifuged at 13,000g for 10 minutes at 4°C to pellet and remove nuclear DNA and the solubilised protein supernatant collected. Total protein concentrations were quantified using the Pierce bicinchoninic acid (BCA) protein kit (ThermoFisher Scientific, cat: A55864) according to the manufacturer's instructions. Briefly, a working range of 10-1000 µg/ml albumin (BSA) standards were prepared by diluting BSA at different ratios in 100 mM NaOH. Protein lysates were similarly diluted 1:5 or 1:10 in 100 mM NaOH and 10 ul of each diluted protein sample or BSA standard pipetted in triplicate into a separate well of a 96-well plate. To each well, 200 µl of an alkaline $CuSO_4$ BCA solution was added and the plate incubated at 50°C for 30 minutes.

In the presence of proteins, Cu^{2+} is reduced to Cu^{+}, which is subsequently chelated by BCA to form a purple-coloured complex. The absorption of this complex was measured at 562 nm on a BMG Labtech CLARIOstar plate reader and a standard curve plotted using the known BSA standards. The measured absorption of the diluted protein sample was interpolated against this curve to determine the total protein concentration of each unknown sample.

For immunoblotting, 15 µg of solubilised protein lysate was denatured and reduced in a protein loading buffer (125 mM Tris-HCl pH 6.8, 50% glycerol, 4% (v/v) SDS and 0.2% orange G; LI-COR, cat: 928-40004) and 20 mM dithiothreitol (ThermoFisher Scientific, cat: 707265ML) mixture at 85°C for 5 minutes. Subsequently, denatured proteins were loaded onto an mPAGE 8% Bis-Tris precast gel (Millipore, cat: MP8W10) immersed in MOPS SDS running buffer (Millipore, cat: MPM0PS) and separated according to their molecular weight by electrophoresis at 150 mV. The resolved proteins were then transferred onto a methanol-activated low background Immobilon-FL polyvinylidene fluoride membrane (0.45 µm pore size; Millipore, cat: IPFL00010) in cold transfer buffer (25 mM Tris pH 8.2, 25 mM bicine, 10% methanol; Millipore, cat: MPTRB) at a fixed 300 mA current for 1 hour. Afterwards, protein blots were dried at 37°C for 10 minutes to fix proteins to the membrane.

For quantitative Western blots, the signal intensities of proteins of interest were normalised to total protein levels, to ensure any observations were due to biological differences. Protein membranes were stained in Revert 520 total protein stain (LI-COR, cat: 926-10010) for 10 minutes at room temperature, followed by two washes using the supplied Revert wash solution (6.7% v/v glacial acetic acid). Stained membranes were immediately imaged at 520 nm using a LI-COR Odyssey M imaging system, with water added onto the

surface of membranes to prevent drying. Following a brief rinse in water, membranes were incubated with the provided Revert destaining solution (0.1 M sodium hydroxide, 30% v/v methanol) for 10 minutes at room temperature to remove the total protein stain, then rinsed a final time in water before proceeding with blocking and immunodetection.

The membrane was blocked with Intercept (PBS) blocking buffer (LI-COR, cat: 927-70000) for 1 hour at room temperature. Primary antibodies (listed in Table 2.4) were diluted in Intercept T20 (PBS) antibody diluent (0.05% v/v Tween 20; LI-COR, cat: 927-75001) and incubated with the membrane overnight at 4ºC with gentle agitation. Membranes were washed three times for 5 minutes with PBS and 0.2% v/v Tween 20 to remove unbound primary antibodies. Protein blots were incubated for 1 hour at room temperature with an IRDye 800CW secondary antibody (listed in Table 2.5) corresponding to the species the primary antibody was raised in, diluted with Intercept T20 (PBS) antibody diluent. The membrane was washed as above before a final wash in PBS prior to drying. Membranes were scanned at 800 nm using an Odyssey M imager (LI-COR) to visualise specific bands and Empiria Studio software (LI-COR) was used for analysis.

2.7.2 Co-immunoprecipitation

HeLa cells were transfected to stably express TPC1 tagged with the small, high affinity peptide epitope ‘ALFA-tag’ (275). Cells were lysed and the total protein was extracted and quantified as described previously in section 2.7.1. ALFA Selector magnetic agarose resin (NanoTag Biotech, cat: N1511) was washed twice for 10 minutes at room temperature in Pierce IP lysis buffer supplemented with cOmplete EDTA-free protease inhibitors, then transferred into low-protein-binding tubes to prevent proteins from adhering to the plastic surface. To allow the sufficient detection of any low-abundant protein interactions, 1

mg/ml (in 1 ml) of total protein lysate was incubated with 20 µl of ALFA resin overnight at 4ºC with rotation. Following protein binding, the resin was washed three times as above, then transferred to new low-protein-binding tubes and washed twice more. The immunoprecipitated protein complexes were simultaneously eluted from the beads, denatured, and reduced in a mixture of the aforementioned protein loading buffer and 20 mM dithiothreitol at 85ºC for 5 minutes. Eluates were then subjected to SDS-PAGE and immunoblotting, as described in section 2.7.1.

2.7.3 Cell surface protein biotinylation

To exclusively label cell-surface membrane proteins, cells were washed three times in PBS then incubated with 0.5 µg/ml of biotin-XX sulfosuccinimidyl ester, provided as part of the FluoReporter cell surface biotinylation kit (ThermoFisher Scientific, cat: F20650), for 30 minutes at 4ºC to prevent endocytosis. Following ice-cold PBS washes to remove excess biotin, cells were lysed and pelleted, as described for whole-cell protein lysates in section 2.7.1. To isolate surface biotinylated proteins, protein lysates were incubated with 40 µl of washed streptavidin magnetic Dynabeads (ThermoFisher Scientific, cat: 65001) for 30 minutes at room temperature, then washed, as detailed above for ALFA resin beads. Biotin-labelled proteins were eluted from streptavidin beads, denatured, and reduced in a mixture of the aforementioned protein loading buffer and 20 mM dithiothreitol at 95ºC for 5 minutes. Eluates were then subjected to SDS-PAGE and immunoblotting, as described in section 2.7.1.

2.7.4 Immunofluorescence staining

To observe and localise endogenous proteins, immunofluorescence staining was performed. Cells were washed in PBS to remove dead cells and serum proteins, then fixed in 4% paraformaldehyde (PFA; cat: P6148) diluted in PBS for 15 minutes at room temperature. To preserve cellular integrity, the milder detergent saponin (cat: 47036) was used for permeabilisation. Cells were simultaneously permeabilised and blocked in a mixture of 0.1% saponin and 5% goat serum (cat: G6767) diluted in PBS for 30 minutes at room temperature with gentle shaking. Primary antibodies (listed in Table 2.4) were diluted in PBS containing 0.01% saponin and 5% goat serum and then incubated with cells overnight at 4^{o}C. Following incubation, cells were washed three times with 0.01% saponin/PBS for 5 minutes to remove residual antibodies. To visualise proteins of interest, species-specific secondary antibodies (listed in Table 2.5) conjugated to an Alexa Fluor fluorescent dye were diluted in PBS containing 0.01% saponin and 5% goat serum, then incubated with cells for 1 hour at room temperature. Finally, cells were washed as above, followed by two brief washes in PBS, covered in foil, and stored at 4^{o}C for a maximum of 1 week prior to imaging.

2.7.5 In-cell Western

Cells were seeded into a 96-well black-walled μCLEAR microplate in preparation for immunofluorescent assays, to improve signal-to-noise ratios. Cells were washed in PBS and then fixed in 4% PFA in PBS for 15 minutes at room temperature. In-cell Western assays were then performed, as detailed below, with either fixed non-permeabilised cells in order to quantify cell surface protein expression (on-cell Western), or with fixed permeabilised cells to quantify total cell protein expression (in-cell Western).

To determine cell surface expression (on-cell Western), cells were blocked in Intercept (PBS) blocking buffer for 30 minutes at room temperature, then incubated overnight at 4ºC with the desired primary antibody (listed in Table 2.4) diluted in Intercept (PBS) blocking buffer. Alternatively, for total cell protein detection, cells were permeabilised immediately after fixation with 0.1% Triton X-100 (cat: T9284) in PBS for 10 minutes at room temperature, blocked, and then incubated with the desired primary antibody diluted in Intercept T20 (PBS) antibody diluent, as described above. Following washes in either PBS (on-cell Western) or 0.01% Triton X-100/PBS (in-cell Western), cells were incubated with species-specific IRDye 800CW secondary antibodies (listed in Table 2.5) for 1 hour at room temperature, diluted in Intercept (PBS) blocking buffer (on-cell Western) or Intercept T20 (PBS) antibody diluent (in-cell Western). To account for the variability in cell number, cells were stained with CellTag 520 (LI-COR, cat: 926-41094) diluted in Intercept T20 (PBS) antibody dilutant. CellTag 520 was co-incubated alongside secondary antibodies in permeabilised cells (in-cell Western). For non-permeabilised cells (on-cell Western), permeabilisation was first performed with 0.1% Triton in PBS (as described above), followed by incubation with CellTag 520 for 1 hour at room temperature. Plates were scanned using an Odyssey M imager and Empiria Studio software was used for analysis where TfR signals were normalised to cell number (CellTag 520 stain).

2.8 TfR trafficking experiments

For transferrin uptake and recycling experiments, cells were initially washed in Ca^{2+}-containing ECM and synchronised by incubation on ice in the same medium for 10 minutes. Unless otherwise stated, cells were incubated with Alexa Fluor 647-conjugated human transferrin (Jackson ImmunoResearch, cat: 009-600-050) for 2.5 minutes at 37ºC. Subsequently, cells were placed on ice to arrest transferrin trafficking and washed twice in

PBS to remove residual and surface-bound transferrin, followed by fixation in 4% PFA in PBS for 15 minutes. A pulse-chase experiment was utilised to monitor transferrin recycling back to the cell surface. Briefly, cells were incubated with transferrin for 10 minutes following the aforementioned conditions, then washed and transferrin chased in room temperature ECM for the specified duration before fixation. To account for differences in the rate of transferrin internalisation between wildtype and TPC1-deficient cells, pulse-chase experimental results were normalised to $t = 0$ following the initial 10 minute incubation. For experiments involving endo-lysosomal channel overexpression, cells were transfected (see section 2.5) with the specified channel fused to an mScarlet-I fluorescent tag (Table 2.3). Transferrin trafficking was assessed in relation to the degree of channel rescue observed in *TPCN1* or *TPCN2* knockout cells, compared with wildtype overexpressing cells; TPC overexpression in wildtype cells does not affect TfR trafficking relative to endogenous TPC levels. Only cells overexpressing TPCs with similar mScarlet-I fluorescence were included for the analysis of TPC rescue experiments.

Table 2.1 depicts the various compounds used within transferrin trafficking experiments, alongside their respective experimental concentrations and treatment periods. Cells remained in the presence of compounds throughout transferrin experiments. Ca^{2+}-free transferrin trafficking experiments were performed as detailed for Ca^{2+}-free imaging experiments in section 2.6, with drug and transferrin incubation conducted in Ca^{2+}-free ECM (supplemented with 100 µM EGTA) following the aforementioned transferrin experimental procedure. Images were collected using a Nikon A1R confocal laser-scanning microscope equipped with a 60x (NA 1.49) Apochromatic objective, excited at 640 nm and Alexa Fluor 647 emission fluorescence centred at 667 nm. Transferrin trafficking analysis was performed using ImageJ/Fiji on a single-cell basis by either calculating the corrected total cell fluorescence (CTCF; equation 3 below), which accounts

for background fluorescence and cell size variation, or by counting the number of transferrin-positive vesicles per cell. To enhance the detection of fluorescent puncta for vesicle counting, a Difference of Gaussians filter was applied to images, followed by either MaxEntropy or Otsu thresholding (276) and particle analysis within defined single-cell regions of interests (ROIs).

(3) $CTCF = Integrated\ density - (Area\ of\ cell * Mean\ background\ fluorescence)$

Table 2.1 List of compounds used in transferrin trafficking experiments

Compound name	Concentration	Incubation period	Manufacturer
Apilimod	1 μM	Overnight in DMEM – 37ºC/5% CO_2	Cayman Chemical (cat: 19094)
Bafilomycin-A1	1 μM	4 hours in DMEM – 37ºC/5% CO_2	Sigma-Aldrich (cat: B1793)
BAPTA-AM	25 μM	45 minutes	AAT Bioquest (cat: 126150-97-8)
Cyclopiazonic acid	30 μM	5 minutes or simultaneous with transferrin	Sigma-Aldrich (cat: C1530)
EGTA-AM	100 μM	45 minutes	AAT Bioquest (cat: 99590-86-0)
Histamine dihydrochloride	50 μM	Simultaneous with transferrin	Sigma-Aldrich (cat: H7250)
Ionomycin free acid	1 μM	Simultaneous with transferrin	Sigma-Aldrich (cat: 407950)
ML2-SA1	30 μM	Simultaneous with transferrin	Axon Medchem (cat: EVP-22)
Rapalog AP21967	250 nM	30 minutes	Takara Bio (cat: 635055)
Tetrandrine	10 μM	1 hour	ApexBio (cat: N1798)
TF-BAPTA-AM	25 μM	45 minutes	Santa Cruz Biotechnology (cat: sc-271696)

Thapsigargin	1 μM	5 minutes or simultaneous with transferrin	Sigma-Aldrich (cat: T124)
trans-Ned-19	100 μM	1 hour	Cayman Chemical (cat: 1752)
Vacuolin-1	2 μM	Overnight in DMEM – 37ºC/5% CO_2	Sigma-Aldrich (cat: 673000)
Vps34-IN-1	1 μM	1 hour	Cayman Chemical (cat: 17392)
Wortmannin	0.5 μM	1 hour	Santa Cruz Biotech (cat: sc-3505)
YM201636	0.5 μM	Overnight in DMEM – 37ºC/5% CO_2	Cayman Chemical (cat: 13576)

Note. Incubations were performed at 37ºC in extracellular imaging medium (ECM) unless stated otherwise. All drugs were dissolved in DMSO except for rapalog AP21967 which was dissolved in ethanol.

2.9 Endosomal pH measurements

Early endosomal pH measurements were performed by ratiometric imaging within HeLa wildtype and *TPCN1* knockout cells. To detect changes in the luminal pH of early endosomes, cells were incubated with 10 μg/ml of the pH-sensitive pHrodo-Red human transferrin conjugate (ThermoFisher Scientific, cat: P35376) and 10 μg/ml of the pH-insensitive Alexa Fluor 488 transferrin conjugate (Jackson ImmunoResearch, cat: 009-540-050) in ECM + 1% bovine serum albumin (BSA; Roche, cat: 735086) for 30 minutes at 37ºC. Cells were then washed twice in ECM. Localisation of transferrin to early endosomal compartments was confirmed by colocalisation with a transiently expressed (see section 2.5) mScarlet-I-Rab5 marker protein. Ratiometric imaging was performed using a Nikon A1R confocal laser-scanning microscope equipped with a 60x (NA 1.49) Apochromatic objective, with Alexa Fluor 488 and pHrodo-Red fluorophores excited at 488 and 561 nm, and emission captured at 525 and 585 nm respectively in channel series.

Alongside endogenous measurements, a pH calibration was performed for both genotypes by incubating cells in high K^+-based ECM solutions (containing in mM; 145 KCl, 5 NaCl, 1 $MgCl_2$, 1 $CaCl_2$, 10 glucose, and 10 of either acetate, MES, HEPES, or Tris) with the pH ranging from 4.38 to 8.65. Cells were washed three times in this solution and then incubated for 10 minutes in the same solution containing 10 μM of the ionophores nigericin and valinomycin, in order to equilibrate the endosomal luminal pH to the extracellular medium. The resultant 561/488 fluorescence intensity ratios were plotted within GraphPad Prism and a log (inhibitor) vs response (three parameters) sigmodal curve fitted, to which measurements obtained under standard ECM were interpolated to acquire an absolute pH value.

2.10 Iron measurements

Ferrous-iron (Fe^{2+}) was detected in HeLa cells using the *N*-oxide-based Fe^{2+}-selective fluorescent probe RhoNox-1 (277). To determine intracellular Fe^{2+} levels, cells were first washed in ECM to remove any residual iron from cell culture medium, then incubated with 10 μM RhoNox-1 (ApexBio, cat: C8199) in Ca^{2+}-containing ECM for 1 hour at 37ºC. RhoNox-1 Fe^{2+} detection was confirmed by enhancing RhoNox-1 fluorescence with 100 μM $FeCl_2$ (cat: 215406) 30 minutes prior to RhoNox-1 incubation, or by chelating Fe^{2+} with 1 mM 2,2'-bipyridyl (cat: D216305) alongside the incubation of RhoNox-1. To determine the compartmental accumulation of RhoNox-1, cells were incubated with 300 nM LysoTracker Green DND-26 (ThermoFisher Scientific, cat: L7526) post RhoNox-1 for 5 minutes at 37ºC. Cells were washed three times in ECM and immediately imaged using a Nikon A1R confocal laser-scanning microscope equipped with a 60x (NA 1.49) Apochromatic objective, excited at 561 nm and emission fluorescence captured at 575 nm.

Data analysis was performed multifariously, either by calculating the number of Fe^{2+} vesicles per cell (as described in section 2.8 for transferrin vesicles, together with manual inspection), the mean fluorescence of Fe^{2+} vesicles, or the labile cytoplasmic Fe^{2+} (excluding Fe^{2+} vesicles) using ImageJ/Fiji. ROIs for labile cytoplasmic Fe^{2+} measurements were generated by first creating separate binary masks for the whole-cell (using manually defined thresholds) and for Fe^{2+} vesicles (as described in section 2.8 for transferrin vesicles). The vesicle mask was then subtracted from the whole-cell mask to create a new mask representing only cytoplasmic fluorescence, which was subsequently converted into a cytoplasmic ROI for analysis.

2.10.1 Haem quantification

Total haem content in HeLa wildtype and *TPCN1* knockout cell lysates was assessed using porphyrin fluorometrics, whereby Fe^{2+} is liberated from haem, converting haem into its fluorescent precursor protoporphyrin-IX (PPIX) (278). Following solubilisation (as described in section 2.7.1), cell lysate protein samples were mixed in a 1:1 volume ratio with 2 M oxalic acid to chelate Fe^{2+} from haem, covered in foil, and then incubated at 95ºC, or room temperature for 1 hour. Subsequently, samples were cooled to room temperature, pelleted at 12,000g and the supernatant transferred to a 96-well black μCLEAR microplate. PPIX was excited at 405 nm and emission fluorescence captured at 620 nm using a BMG Labtech CLARIOstar plate reader. Measurements were adjusted for endogenous background PPIX fluorescence by subtracting room temperature PPIX fluorescence from all heated sample readings. Cellular PPIX/haem was standardised to the protein mass present in each reaction and normalised to the wildtype control for semi-quantitative analysis.

2.11 High-throughput trafficking assays

Cells were seeded into 96-well black-walled μCLEAR microplates and grown until approximately 90% confluent. Transferrin trafficking assays were performed as described previously in section 2.8 using 10 μg/ml Alexa Fluor 555-conjugated human transferrin (ThermoFisher Scientific, cat: T35352) diluted in ECM supplemented with 1% BSA. For dextran trafficking assays, cells were incubated with 0.5 mg/ml Texas-Red-conjugated dextran 10 kDa in ECM for different time intervals at 37ºC. Following incubation, cells were washed three times in PBS and fixed in 4% PFA in PBS for 15 minutes, then washed twice again in PBS. For LDL trafficking assays, cells were serum starved overnight to synchronise cells and promote LDLR transcription. Cells were then incubated with 3 μg/ml of Dil-conjugated LDL (ThermoFisher Scientific, cat: L3482) in ECM for various time periods, washed three time in PBS, then fixed in 4% PFA in PBS for 15 minutes followed by final PBS washes. Transferrin Alexa Fluor 555 and Dil LDL fluorescence was excited at 532.5 ± 12.5 nm with the emission centred at 580 ± 10 nm, whilst Texas-Red dextran fluorescence was excited and emission captured at 565 ± 15 nm and 612.5 ± 12.5 nm respectively. To account for differences in cell number, cells were incubated with 2 μM of the nuclear stain DRAQ5 (Biostatus, cat: DR50050) for 20 minutes at room temperature, followed by PBS washes to remove excess dye. A BMG Labtech CLARIOstar plate reader was used to assess transferrin, dextran, or LDL fluorescence, with these values normalised to DRAQ5 fluorescence excited at 640 ± 20 nm and emission captured at 705 ± 20 nm.

2.12 Statistical analysis

Experiments were performed a minimum of three times over multiple days. All data are presented as mean ± SEM unless stated otherwise, with results normalised to the daily control. Data analysis was conducted within GraphPad Prism 10. For multiple conditions, a one-way ANOVA or two-way ANOVA were used. An unpaired two-tailed student's t-test was used for comparison between two groups. Where possible, exact *P* values are provided. *P* values < 0.05 were considered statistically significant, whilst *P* values > 0.9999 are denoted in figures as 'ns'. Normality tests were performed using the Shapiro-Wilk and Kolmogorov-Smirnov tests to confirm a Gaussian or lognormal data distribution. Normally distributed data were analysed using the Dunnett post-hoc test, otherwise a Kruskal–Wallis non-parametric post-hoc test was used.

2.13 List of primers

Table 2.2 Primers used for plasmid DNA construct generation

Primer name	Sequence (5' - 3')	PCR Template	Plasmid Construct
WB01	GTACAAGACCGGTTTCTGCTACGAGAACGAGGTGTAAT	ERES (38 bp)	*Hs*TPC1-mCherry-ERES
WB02	GTACATTACACCTCGTTCTCGTAGCAGAAACCGGTCTT		
WB03	CGCTCCCAGACCGTTACCGCGGCCGCCATGGTGAGCAA	mScarlet-I (748 bp)	*Hs*TPC1-mScarlet-I-ERES
WB04	CCTCGTTCTCGTAGCAGAAACCGGTCTTGTACAGCTCGTCC		
WB05	GCTCCCAGACCGTTACCCAGTCGACCATGGTGTCTACA	mStayGold (729 bp)	*Hs*TPC1-mStayGold-ERES
WB06	CCTCGTTCTCGTAGCAGAAACCGGTCAGGTGGGCCTCCAGG		
WB07	GCTCCCAGACCGTTACCCAGTCGACGGTACC	G-GECO1.2 (1332 bp)	*Hs*TPC1-G-GECO1.2-ERES
WB08	CCTCGTTCTCGTAGCAGAAACCGGTCTTCGCTGTCATCATTT		
WB09	GCTCCCAGACCGTTACCCAGTCGACGGTACCG	GCaMP6s (1431 bp)	*Hs*TPC1-GCaMP6s-ERES
WB10	CCTCGTTCTCGTAGCAGAAACCGGTCTTCGCTGTCATCATTTGTACA		
WB11	TACCGCGGGCCCGGGATCCACCGGTCATGCTGCAGAACGAGCTTG	NEMOs (1410 bp)	*Hs*TPC1-NEMOs-ERES
WB12	CCTCGTTCTCGTAGCAGAAACCGGTCTTGTACAGCTCGTCCATGCCC		
WB13	AGATCTCGAGCTCAAGCTACCATGGCTGTGAG	*Hs*TPC1-mScarlet-I-ERES (3218 bp)	*Hs*TPC1-mScarlet-I-ERES-FRB*
WB14	AGGATTCCACTTGCTCCCACCTCGTTCTCGT		

WB15	GGACTCTAGCGTTTAAACTTAA GCTTACCATGGCTGTG	*Hs*TPC1^{L273P}Δ (2112 bp)	*Hs*TPC1^{L273P}-mScarlet-I-ERES
WB16	TCATTCGGAAGACGAAGGCCTC GAGGATAAAGGCGAC		
WB17	GCTCCCAGACCGTTACCCAGTC GACCATGGTGAGCAAGGGC	mScarlet-I (747 bp)	*Hs*TPC1$^{A280S/V646M/N647G}$ -mScarlet-I-ERES
WB03	CCTCGTTCTCGTAGCAGAAACC GGTCTTGTACAGCTCGTCC		
WB18	GGACTCAGATCTCGAGCTCAAG CTTACCATGGCTGTGAG	Δ*Hs*TPC1 (875 bp)	*Hs*TPC1$^{A280S/V646M/N647G}$ -mNeonGreen-ERES
WB19	GGAAATTGCTTGTGGTCAGAAG		
WB20	TCTGACCACAAGCAATTTCCCA	Δ*HsTPC1*Δ (1118 bp)	
WB21	AGTTGCCCATAACTGTGAGCTC		
WB22	GCTCACAGTTATGGGCAACTGG TACATC	*HsTPC1*Δ (550 bp)	
WB23	TTCGCCCTTGGACACCATGGTC GACTGGGTAACGGTC		
WB05	GCTCCCAGACCGTTACCCAGTC GACCATGGTGTCTACA	mStayGold (729 bp)	*Hs*TPC1$^{A280S/V646M/N647G}$ -mStayGold-ERES
WB06	CCTCGTTCTCGTAGCAGAAACC GGTCAGGTGGGCCTCCAGG		
WB17	GCTCCCAGACCGTTACCCAGTC GACCATGGTGAGCAAGGGC	mScarlet-I (747 bp)	*Hs*TPC1^{K330A}- mScarlet-I-ERES
WB03	CCTCGTTCTCGTAGCAGAAACC GGTCTTGTACAGCTCGTCC		
WB18	GGACTCAGATCTCGAGCTCAAG CTTACCATGGCTGTGAG	Δ*Hs*TPC1 (1025 bp)	*Hs*TPC1^{K330A}- mNeonGreen-ERES
WB24	ACTTGAACGCGCGTTTCTCAAT		
WB25	TGAGAAACGCGCGTTCAAGTCT	*Hs*TPC1Δ (560 bp)	
WB26	AGAAGTCAAACAAGTTCCATCC GGAAGACAAGTACTC		
WB05	GCTCCCAGACCGTTACCCAGTC GACCATGGTGTCTACA	mStayGold (729 bp)	*Hs*TPC1^{K330A}- mStayGold-ERES
WB06	CCTCGTTCTCGTAGCAGAAACC GGTCAGGTGGGCCTCCAGG		

WB27	TACCGCGGGCCCGGGATCCACC GGTTTATCCCTATGACGTGCCT GATTACGCCG	3xHA-mScarlet-I (3602 bp)	*Hs*TPC2-3xHA-mScarlet-I
WB28	CTGATTATGATCTAGAGTCGCG GCCGCTTACTTGTACAG		
WB29	TACCGCGGGCCCGGGATCCACC GGTCGCCATGGTGAG	mScarlet-I-ERES (782 bp)	*Hs*TRPML1-mScarlet-I-ERES
WB30	CTGATTATGATCTAGAGTCGCG GCCGCTTACACCTCGTTCTCGT		
WB31	ATACCTATTAGCCGGTCGACGG CCGCCATGGTGAG	mScarlet-I-ERES (773 bp)	*Hs*TRPML2-mScarlet-I-ERES
WB32	TGATCTAGAGTCGCGGCCGCTT ACACCTCGTTCTCGT		
WB33	ACTTGATACCTATTAGCCGGCA GTCGACGGTAC	G-GECO1.2-ERES (1361 bp)	*Hs*TRPML2-G-GECO1.2-ERES
WB34	CTGATTATGATCTAGAGTCGCG GCCGCTTACACCTCGTT		
WB35	AGGGCCTTCATCAAGCACCCC	FRB* (344 bp)	FRB*-mScarlet-I-*Hs*EEA1
WB36	GGAGCCGTACATGAACTGAGG		
WB37	GGAGAACATGCACATGAAGCT GTACATGGTGTCTACAGGCG	mStayGold (735 bp)	FKBP12-CB_{wt}x2-mStayGold
WB38	GGCTGATTATGATCTAGAGTCG CGGCCGCTTACAGGTGGGC		
WB39	GGGGGATCCTAAACCGGTACC CATGGTGTCTACAGGCG	mStayGold (731 bp)	FKBP12-CB_{mut}x2-mStayGold
WB40	CAGGCACATCGTAAGGGTAATT AAGCTTTTACAGGTGGGCCTCC		

Note: *Hs*, *Homo sapiens*; CB, Calbindin-2. Δ denotes a partial PCR of TPC1. For each PCR template, primers are listed in the order: forward primer followed by reverse primer.

2.14 List of plasmids

Table 2.3 Plasmid DNA constructs utilised

Plasmid name	Vector backbone	Cloning technique	Linker(s)* (amino acids)	Insert accession number
*Hs*TPC1-mCherry	pcDNA5TO	Restriction cloning	AAA	NM_001143819.3
*Hs*TPC1-mCherry-ERES	pcDNA5TO	Oligo-nucleotide insertion	AAA	NM_001143819.3
*Hs*TPC1-mScarlet-I-ERES	pcDNA5TO	Gibson cloning	AAA	NM_001143819.3
*Hs*TPC1-mNeonGreen-ERES	pDendra2-N	Restriction cloning	QST	NM_001143819.3
*Hs*TPC1-mStayGold-ERES	pcDNA5TO	Gibson cloning	QST	NM_001143819.3
*Hs*TPC1-G-GECO1.2-ERES	pDendra2-N	Gibson cloning	QSTVPRARDPPV	NM_001143819.3
*Hs*TPC1-GCaMP6s-ERES	pDendra2-N	Gibson cloning	QSTVPRARDPPVT	NM_001143819.3
*Hs*TPC1-NEMOs-ERES	pDendra2-N	Gibson cloning	QSTVPRARDPPV	NM_001143819.3
*Hs*TPC1-mScarlet-I-ERES-FRB*	pEGFP	Gibson cloning	AAA; GASG	NM_001143819.3
*Hs*TPC1^{L273P}-mScarlet-I-ERES	pcDNA5TO	Gibson cloning	AAA	NM_001143819.3 mutation
*Hs*TPC1$^{A280S/V646M/N647G}$-mScarlet-I-ERES	pDendra2-N	Gibson cloning	QST	NM_001143819.3 mutation
*Hs*TPC1$^{A280S/V646M/N647G}$-mNeonGreen-I-ERES	pDendra2-N	Gibson cloning	QST	NM_001143819.3 mutation
*Hs*TPC1$^{A280S/V646M/N647G}$-mStayGold-ERES	pDendra2-N	Gibson cloning	QST	NM_001143819.3 mutation
*Hs*TPC1^{K330A}-mScarlet-I-ERES	pDendra2-N	Gibson cloning	QST	NM_001143819.3 mutation
*Hs*TPC1^{K330A}-mNeonGreen-ERES	pDendra2-N	Gibson cloning	QST	NM_001143819.3 mutation

*Hs*TPC1^{K330A}-mStayGold-ERES	pDendra2-N	Gibson cloning	QST	NM_001143819.3 mutation
*Hs*TPC2-3xHA-mScarlet-I	pDendra2-N	Gibson cloning	QSTVPRARDPPV; GGSGARDPPVAT	NM_139075.4
*Hs*TRPML1-mScarlet-I-ERES	pDendra2-N	Gibson cloning	QSTVPRARDPPVA	NM_020533.3
*Hs*TRPML2-mScarlet-I-ERES	pDendra2-N	Gibson cloning	RSTAA	NM_153259.4
*Hs*TRPML2-G-GECO1.2-ERES	pDendra2-N	Gibson cloning	RQSTVPRARDPPV	NM_153259.4
mScarlet-I-*Hs*Rab5	pAcGFP1	Restriction cloning	SGLRSRA	NM_002868.4
mScarlet-I-*Hs*Rab11	pEGFP	Restriction cloning	SGLRSRA	NM_004663.5
FRB*-mScarlet-I-*Hs*EEA1	pEGFP	Gibson cloning	GAGAGALPVGSG; SGGGGGSTGLRSRA	NM_003566.4
FKBP12-CB$_{wt}$x2-mStayGold	pEGFP	Gibson cloning	ARGAAAGAGGAAS; GDPPVATMSELIKENMHMKLY	NM_001740.5
FKBP12-CB$_{mut}$x2-mStayGold	pEGFP	Gibson cloning	ARGARGAAAGAGGAAS; GDPKPVP	NM_001740.5 mutation
Cyto-NEMOs	pcDNA3.1	Addgene (279)	-	-
KDEL-mCherry	pcDNA5TO	From the Grinstein laboratory	-	-

Note: *, Linkers are listed in N- to C-terminal protein order. All constructs incorporating a C-terminal ERES sequence contained a TG amino acid linker at the protein-ERES fusion. *Hs*, *Homo sapiens*; CB, Calbindin-2. KDEL represents the ER retention amino acid sequence.

2.15 List of antibodies

Table 2.4 Primary antibodies used for immunological techniques

Antibody	Specificity	Epitope	Manufacturer	Application & dilution
FluoTag-X2 α-ALFA 680RD	Alpaca single-domain antibody	Full ALFA-tag sequence	NanoTag Biotechnologies (cat: N1502)	- Co-IP (1:2000)
α-FTH1 (D1D4)	Rabbit monoclonal	C-terminal residues	Cell Signaling Technology (cat: 4393)	- WB (1:1000) - IF (1:200)
α-HN1L (JPT2)	Rabbit polyclonal	Residues 50-100	Bethyl Laboratories (cat: A304-663A)	- WB (1:1000)
α-LAMP1 (H4A3)	Mouse monoclonal	Luminal residues	Developmental Studies Hybridoma Bank (cat: H4A3)	- IF (1:200)
α-Lsm12 (EPR12282)	Rabbit monoclonal	Proprietary information	Abcam (cat: ab173291)	- WB (1:1000)
α-NCOA4 (E8H8Z)	Rabbit monoclonal	Residues ~213	Cell Signaling Technology (cat: 66849)	- WB (1:1000) - IF (1:200)
α-Rab5 (C8B1)	Rabbit monoclonal	Residues ~190	Cell Signaling Technology (cat: 3547)	- IF (1:200)
α-TfR (H68.4)	Mouse monoclonal	Residues 3-28	Santa Cruz Biotechnology (cat: sc-65877)	- WB (1:1000) - Co-IP (1:1000) - In-cell Western (1:200)
α-TfR (G-8)	Mouse monoclonal	Residues 708-737	Santa Cruz Biotechnology (cat: sc-393719)	- In/On-cell Western (1:50) - IF (1:50)

Note: Epitope residues provided where possible, ~ denotes surrounding residues. WB, Western blotting; Co-IP, Co-immunoprecipitation; IF, Immunofluorescence.

Table 2.5 Secondary antibodies used for immunological techniques

Antibody	Conjugation	Manufacturer	Application & dilution
Donkey α-mouse	IRDye 680RD	LI-COR Bio (cat: 926-68072)	- WB (1:10,000)
Goat α-mouse	Alexa Fluor 488	ThermoFisher Scientific (cat: A-11001)	- IF (5 µg/ml)
Goat α-mouse	IRDye 800CW	LI-COR Bio (cat: 926-32210)	- WB (1:10,000) - In/On-cell Western (1:800)
Goat α-rabbit	VRDye 549	LI-COR Bio (cat: 926-54020)	- IF (5 µg/ml)
Goat α-rabbit	IRDye 800CW	LI-COR Bio (cat: 926-32211)	- WB (1:10,000)
α-streptavidin	IRDye 800CW	LI-COR Bio (cat: 926-32230)	- WB (1:5000)

Note: WB, Western blotting; IF, Immunofluorescence.

Chapter 3 – Results

The involvement of TPC1 in the transferrin cycle and iron homeostasis

3.1 Summary

Positioned on endo-lysosomal organelles, TPCs are required for an assortment of membrane trafficking processes, from homeostatic to pathogenic pathways (81,116,169,185,186). However, many of these previous studies predominantly focus on which endo-lysosomal channels are important, without necessarily addressing the precise mechanisms by which TPCs regulate trafficking. Regarding cell-membrane protein trafficking, TPCs have been shown to govern the internalisation and trafficking of the EGFR, PDGFRβ, and LDLR (116,185,186), surface receptors critical for growth factor signalling (EGFR and PDGFRβ) and cholesterol homeostasis (LDLR) (208,280). Although important, *how* TPCs precisely modulate endo-lysosomal trafficking is poorly understood. Therefore, to address this gap in knowledge, the trafficking of the TfR, a cell surface protein, was investigated as an analogous receptor-mediated trafficking pathway.

As detailed in section 1.5.2 and illustrated in Figure 1.6, the transferrin cycle is a constitutive pathway whereby Fe^{3+}-bound transferrin binds to cell surface TfRs, initiating internalisation and trafficking into endosomes to maintain iron homeostasis (246,281). As TPC1 expression is restricted to TfR-positive early and recycling endosomes (116,117), it was hypothesised that TPC1 likely regulates the transferrin cycle to some extent. In this chapter, recombinant human transferrin conjugated to the fluorophore Alexa Fluor 647 is

used to monitor TfR trafficking in TPC-deficient HeLa cells. As will be shown, TPCs, especially TPC1, are required for the functional uptake, trafficking, and recycling of the transferrin-TfR complex. The specificity of TPC1 regulation within the transferrin cycle will be discussed, as other endo-lysosomal channels fail to restore trafficking in TPC1-deficient cells.

Previous evidence has proposed that for clathrin-dependent receptor-mediated endocytic pathways, such as EGFR internalisation (186), TPCs mediate receptor uptake by regulating protein synthesis and expression. Thus, understanding how TPC1 regulates TfR trafficking represents a key focal point of this chapter. As will be shown, TPC1 does not regulate cellular TfR expression, but instead controls cell surface TfR levels by regulating the efficiency of TfR trafficking and recycling. The possibility that TPC1 forms a complex with the TfR and how this may affect transferrin trafficking will be discussed.

In the final parts of this chapter, the implications of altered transferrin-mediated iron uptake will be explored. Consistent with a reduction in iron-bound transferrin internalisation, basal cytosolic Fe^{2+} was substantially reduced following TPC1 deletion. The consequence of diminished labile Fe^{2+} revealed several downstream detriments, including impaired mitochondrial-dependent haem synthesis and enhanced iron-regulated autophagy. How these findings from cellular systems translate to *in vivo* mouse models will also be discussed, particularly how they relate to the iron-deficiency phenotype of microcytic anaemia.

The following chapter contains figures and content from Burton *et al*. (282).

3.2 Establishment of transferrin assay

3.2.1 Generation of TPC-deficient HeLa cells

To investigate TPCs within the transferrin cycle, an appropriate cell line was first selected which exhibits endogenous expression of the TfR, in addition to being amenable to genetic manipulation. HeLa cells represent an immortal cancer-derived cell line, whose comprehensive characterisation and endogenous expression of the TfR establish them as a potential model system. Owing to their cancerous origin, HeLa cells express several-fold higher levels of the TfR to facilitate enhanced iron uptake to support DNA synthesis and cell proliferation (283,284). Specifically, HeLa cells are extensively detailed within the literature, with early experiments involving HeLa cells presenting initial evidence of the properties and regulation of TfR trafficking and recycling (250,285,286). Thus, HeLa cells were chosen as the appropriate system for investigating the role of TPC1 within the transferrin cycle and are used extensively throughout this thesis.

Through genetic ablation of either TPC1 or TPC2, the effects of TPC loss of function can be assessed to determine the role of TPCs in TfR trafficking. TPC1- and TPC2-deficient HeLa cells were generated by Dr Julie Xiao and generously gifted to the Galione laboratory. The complete generation, characterisation and experimental implementation of these cell lines is thoroughly detailed in Dr Xiao's DPhil thesis (268) and briefly described in section 2.2.1. Figure 3.1 summarises the results presented in Dr Xiao's thesis regarding the RT-PCR analysis of CRISPR/Cas9-edited *TPCN1* and *TPCN2* knockout HeLa cells (268). In summary, for *TPCN1* knockout cells, band excision and DNA fragment sequencing revealed deletion of exon 7 for clone D149. In contrast, the A17 clone contained two bands corresponding to either exon 7 deletion (upper band), or exon 6 and 7 deletion (lower band). For *TPCN2* knockout cells, exon 2 and part of exon 3 was deleted

from both E64 and E182 clones. All deletions introduced a frameshift resulting in a premature STOP codon which lead to altered translation, thereby confirming successful TPC knockout (268).

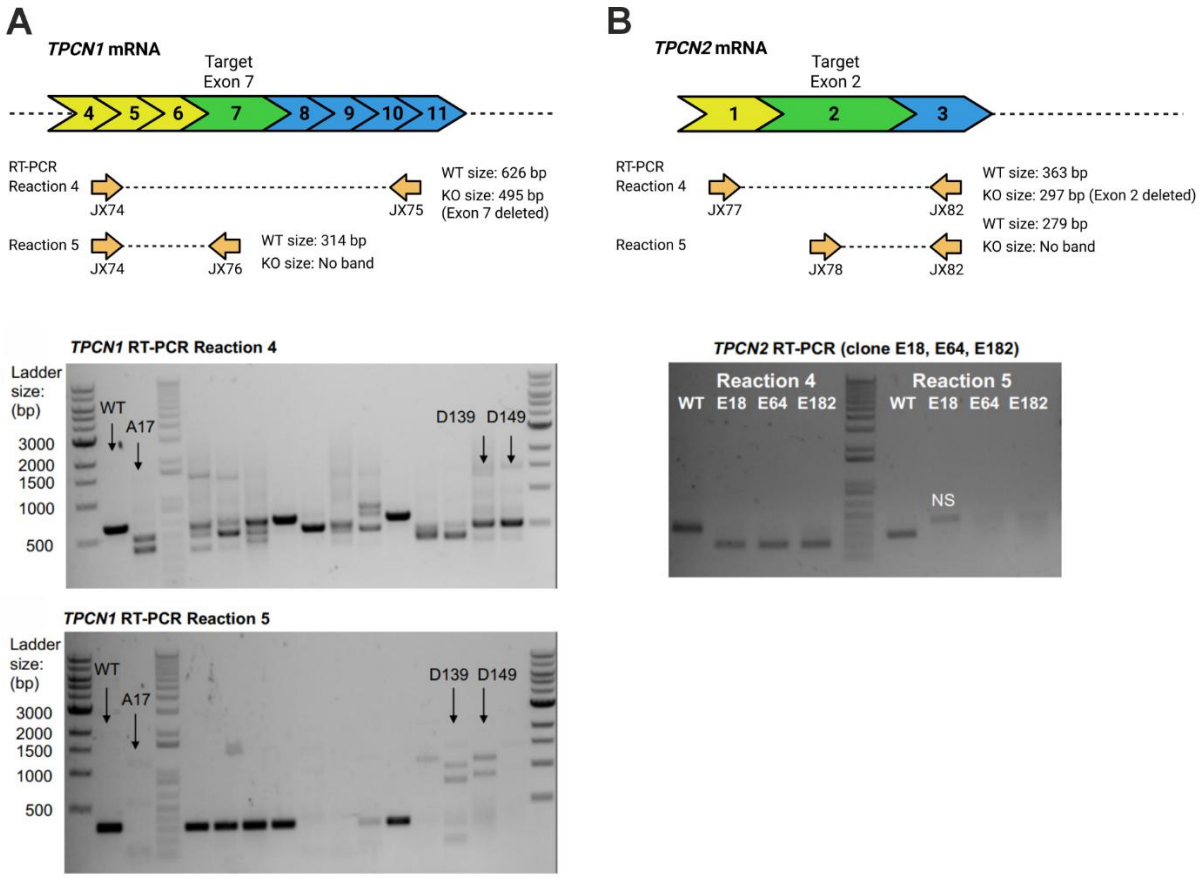

Figure 3.1: RT-PCR analysis confirms *TPCN1* and *TPCN2* knockout in CRISPR-edited HeLa cells. Reproduced from Julie Xiao's thesis deposited on the University of Oxford's research archive (268). **(A)** Schematic diagram of *TPCN1* HeLa mRNA showing the CRISPR-editing target exon 7 (in green) and exons up/downstream (yellow/blue) of the editing site. Agarose gel images showing the amplified mRNA products from RT-PCR reactions 4 and 5 from wildtype (WT) and *TPCN1* knockout (KO) clones (A17, D139, D149). **(B)** Schematic diagram of *TPCN2* HeLa mRNA. Agarose gel image showing the amplified mRNA products from RT-PCR reactions 4 and 5 from WT and *TPCN2* KO clones (E18, E64, E182). Successful deletion of *TPCN1* exon 7, or *TPCN2* exon 2 resulted in shorter sized bands in reaction 4 and no amplified product in reaction 5. Non-specific bands are labelled NS.

3.2.2 Defining experimental parameters

Investigating the internalisation and trafficking of the transferrin-TfR complex forms the foundation for numerous experiments within this thesis. Therefore, it was first pivotal to establish a procedure which could serve as a benchmark assay for future experiments. The transferrin cycle is remarkably fast to meet the cellular demands for iron metabolism and haemoglobin production; the TfR is recycled back to the cell surface after a full cycle with a half-time ($t_{1/2}$) of approximately 20 minutes (220,250). Thus, to combat the challenges of rapid endo-lysosomal trafficking, cells were initially placed on ice prior to the application of transferrin, to synchronise cells to the same trafficking state. Likewise, pre-warmed transferrin (37^{o}C) was applied to cells to ensure simultaneous reinitiation of trafficking across all conditions, whilst PFA was used to instantaneously arrest transferrin trafficking following incubation.

Due to the uncertain effect of TPC deletion on transferrin trafficking and to ensure a defect of any magnitude was not overlooked, concentration- and incubation-response curves were generated to ensure assay parameters fell within the dynamic range. As shown in Figure 3.2A and B respectively, a concentration-, time-dependent increase in transferrin internalisation was observed in HeLa cells. Specifically, transferrin uptake plateaued at concentrations greater than 20 µg/ml, and incubation periods longer than 10 minutes, suggestive of TfR saturation. Therefore, unless stated otherwise, for subsequent experiments investigating transferrin uptake and trafficking, a submaximal transferrin concentration of 10 µg/ml and approximate $t_{1/2}$ incubation time of 2.5 minutes were used. The benchmark transferrin assay and parameters are illustrated in Figure 3.2C.

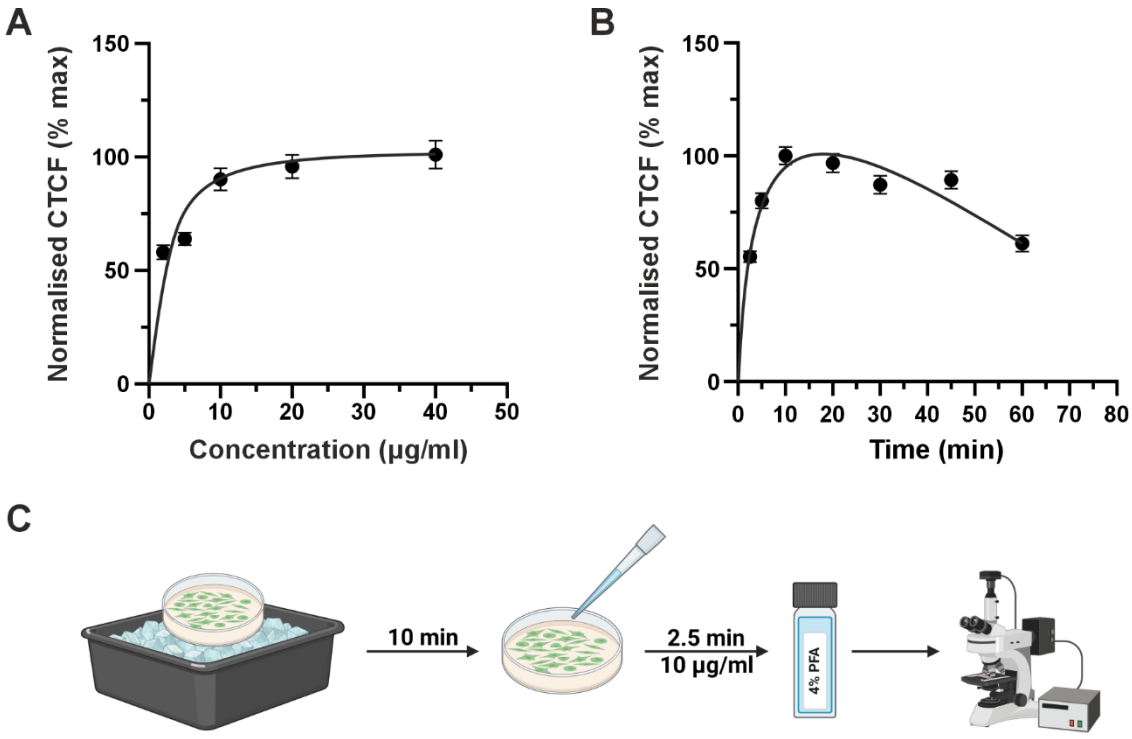

Figure 3.2: Establishment of transferrin assay parameters. (A) Concentration- and **(B)** incubation-response curves of 10 µg/ml Alexa Fluor 647 transferrin internalisation, used to determine transferrin assay experimental parameters. CTCF, corrected total cell fluorescence. Individual data points are presented as the mean ± SEM. **(C)** Visual depiction of the benchmark transferrin assay used throughout this thesis.

3.3 Transferrin uptake and recycling in TPC knockout HeLa cells

To first investigate the involvement of TPCs within the transferrin cycle, a pilot transferrin internalisation and trafficking assay was performed in CRISPR-generated HeLa cells from *TPCN1* or *TPCN2* knockout clones. To confirm reproducibility and reliability, transferrin trafficking was examined in two *TPCN1* (D149 and A17) and *TPCN2* (E64 and E182) knockout HeLa clones in parallel with wildtype cells. Following transferrin incubation, TPC deletion significantly impaired transferrin uptake and trafficking in both *TPCN1* and *TPCN2* knockout clones (Figure 3.3). To ensure the observed reduction in transferrin

trafficking was a direct consequence of TPC deletion, TPC1 or TPC2 were reconstituted by transfection in either *TPCN1* or *TPCN2* knockout cells respectively. As expected, re-expression of the respective missing isoform completely restored the trafficking defect (Figure 3.3), establishing a role for TPCs within the transferrin cycle. Although deletion of TPC2 did result in a reduction (~27% decrease in E182 clone) in transferrin uptake, Figure 3.3 indicates an increased trafficking defect of approximately 45% (A17 clone) occurred following TPC1 deletion, suggesting a more prominent role for TPC1, which was thus investigated further.

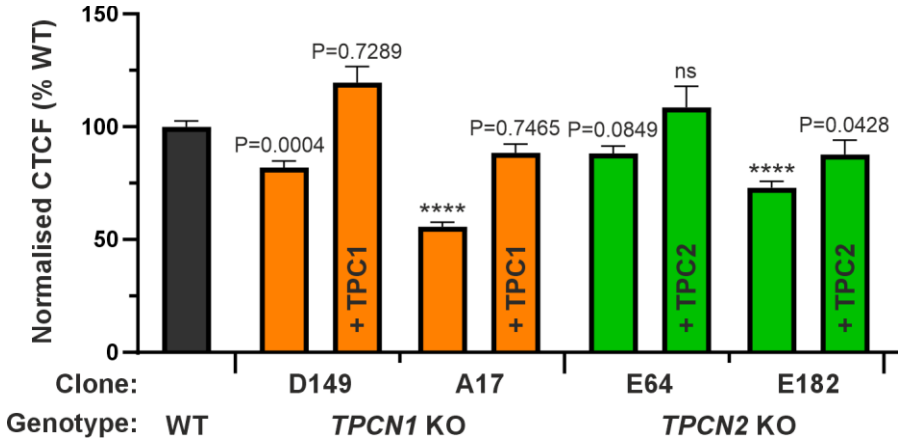

Figure 3.3: Deletion of TPC1 or TPC2 impairs transferrin trafficking. Transferrin uptake and trafficking is impaired in *TPCN1* (D149 and A17 clones) and *TPCN2* (E64 and E182 clones) knockout (KO) HeLa cells relative to wildtype (WT). Transient re-expression of the respective missing TPC isoform, tagged with mScarlet-I, restores transferrin uptake and trafficking in TPC-deficient cells, n = 42-153 cells. CTCF, corrected total cell fluorescence. Data are presented as the mean ± SEM, and probability determined using a one-way ANOVA (**** $P < 0.0001$, ns = no significance vs WT).

The finding that TPC1 may have a more significant role than TPC2 in the transferrin cycle, prompted further investigation. As an increased impairment was observed in the A17 *TPCN1* knockout clone compared to the D149 clone (discussed in section 3.8.1), clone A17 was chosen for all future experiments and will henceforth be referred to solely as

'*TPCN1* knockout'. To more precisely elucidate the role of TPC1 in the transferrin cycle, a transferrin uptake time-course was performed in HeLa wildtype and *TPCN1* knockout cells to quantify the rate of internalisation. As shown in Figure 3.4A, TPC1 deletion significantly slowed transferrin uptake, with TPC1-deficient cells unable to reach the maximum transferrin uptake of wildtype cells. Notably, the rate of transferrin uptake was substantially impaired in *TPCN1* knockout cells between the 1 and 2.5 minute time points, leading to lower overall transferrin internalisation compared with wildtype cells, despite similar uptake kinetics between timepoints thereafter (Figure 3.4A).

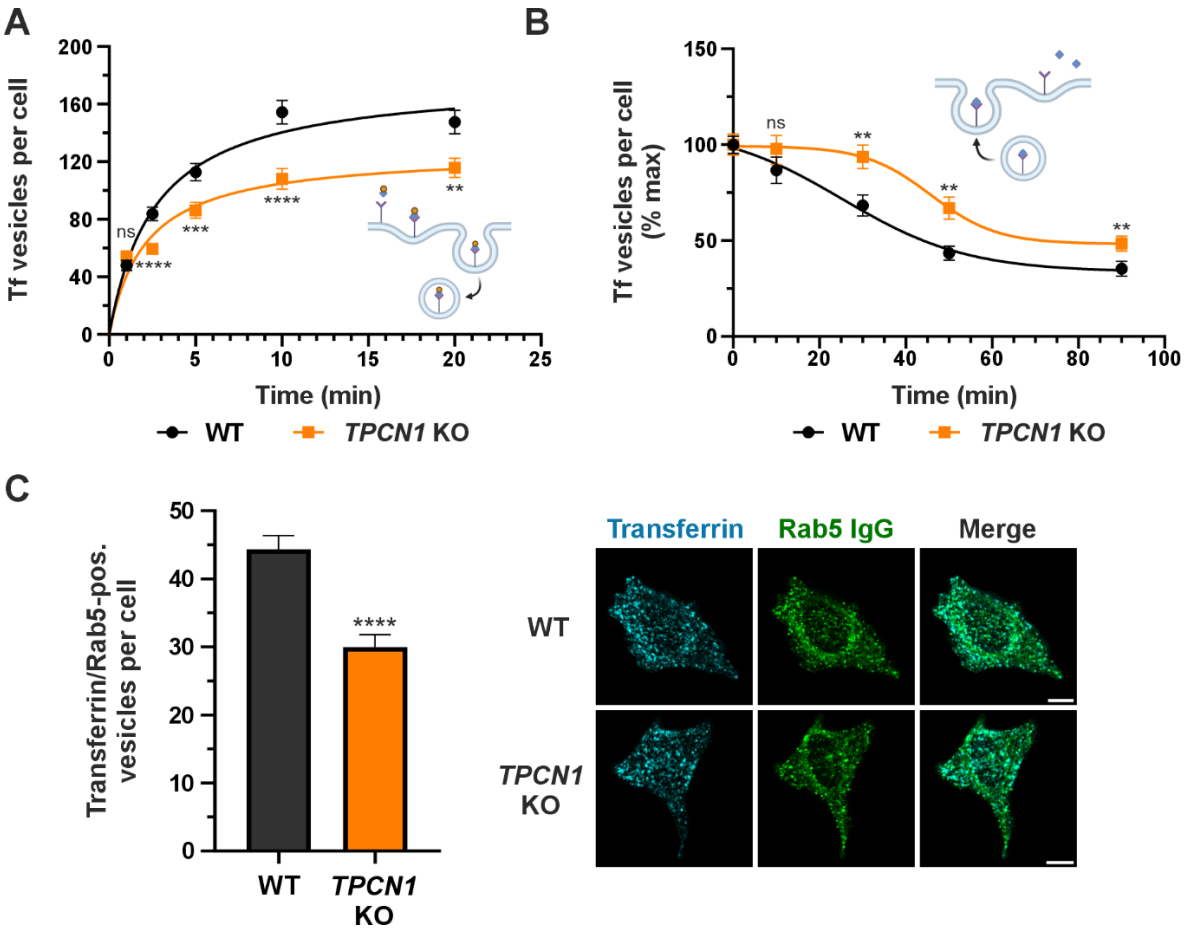

Figure 3.4: TPC1 regulates transferrin internalisation, trafficking, and recycling. Alexa Fluor 647 transferrin **(A)** uptake (n = 36-47 cells) and **(B)** recycling (n = 29-35 cells) assays performed in HeLa wildtype (WT) and *TPCN1* knockout (KO) cells. For recycling assays, data are normalised to t = 0. **(C)** The number of transferrin and anti-Rab5 IgG labelled-positive vesicles per cell following a 10 minute transferrin incubation is shown for WT and *TPCN1* KO HeLa cells, n = 68-69 cells. Representative images of transferrin and Rab5 colocalisation, scale bars = 10 µm. Data are presented as the mean ± SEM, and probability determined by a two-tailed t-test (**** $P < 0.0001$, *** $P < 0.001$, ** $P < 0.01$, ns = no significance vs WT).

A key feature of the transferrin cycle is the sorting and recycling of the apotransferrin-TfR complex back to the plasma membrane for subsequent iron uptake cycles (246,250). Therefore, transferrin recycling was investigated in parallel to internalisation using a pulse-chase approach, to establish if TPC1 is required for both transferrin-dependent processes. Similar to transferrin uptake, deletion of TPC1 significantly slowed the recycling of the apo-transferrin-TfR complex back to the cell surface (Figure 3.4B), as

shown by increased quantities of transferrin remaining intracellularly in *TPCN1* knockout compared to wildtype cells.

In view of the above finding of reduced transferrin uptake, a reduction in transferrin-vesicle fusion with early endosomal organelles would be expected. Indeed, as shown in Figure 3.4C, colocalisation revealed a reduction in the number of transferrin/Rab5-positive early endosomes following TPC1 deletion, confirming that this trafficking defect was associated with reduced uptake and transport of transferrin. These findings imply that TPC1 is essential for early endosomal membrane fusion following the internalisation of the transferrin-TfR complex. Taken together with time-course experiments, these findings support a role for TPCs, specifically TPC1, in mediating transferrin internalisation, trafficking, and recycling.

3.3.1 Overexpression of endo-lysosomal channels

Given that TPC1 re-expression successfully rescued transferrin trafficking (Figure 3.3), the requirement for TPC1 expression was further evaluated. The specificity of TPC1 within the transferrin cycle was investigated, to provide insight into the mechanisms regulating trafficking. To determine the specificity of TPC1, various endo-lysosomal channels were overexpressed in TPC1-deficient cells and assessed for their ability to rescue the TPC1 defect. In particular, the endosomal channel TRPML2 and lysosomal channels TPC2 and TRPML1 were chosen based on their similar cation permeability to TPC1 yet different compartmentalisation (80,122,138,196,198). Additionally, the pore-dead mutant channel $TPC1^{L273P}$ was overexpressed (85), to establish if the trafficking defect observed in TPC1-deficient cells was caused by the physical presence of the channel or by the cations that flow through it. As shown in Figure 3.5, of all the endo-lysosomal channels overexpressed,

only the endosomal wildtype TPC1 could restore transferrin trafficking, whilst all other channels failed to rescue the *TPCN1* knockout defect. Interestingly, overexpression of TRPML2 marginally restored transferrin trafficking by approximately 21%; however, this increase was small in contrast to TPC1 re-expression. Furthermore, despite restoring transferrin uptake in *TPCN2* knockout cells (Figure 3.3), TPC2 exhibited no effect when overexpressed in *TPCN1* knockout cells (Figure 3.5), hinting at possible endo-lysosomal organelle specificity for transferrin trafficking regulation. These findings establish TPCs, notably TPC1, as mediators of the transferrin cycle and reinforce a selective requirement for TPC1 over other endo-lysosomal channels.

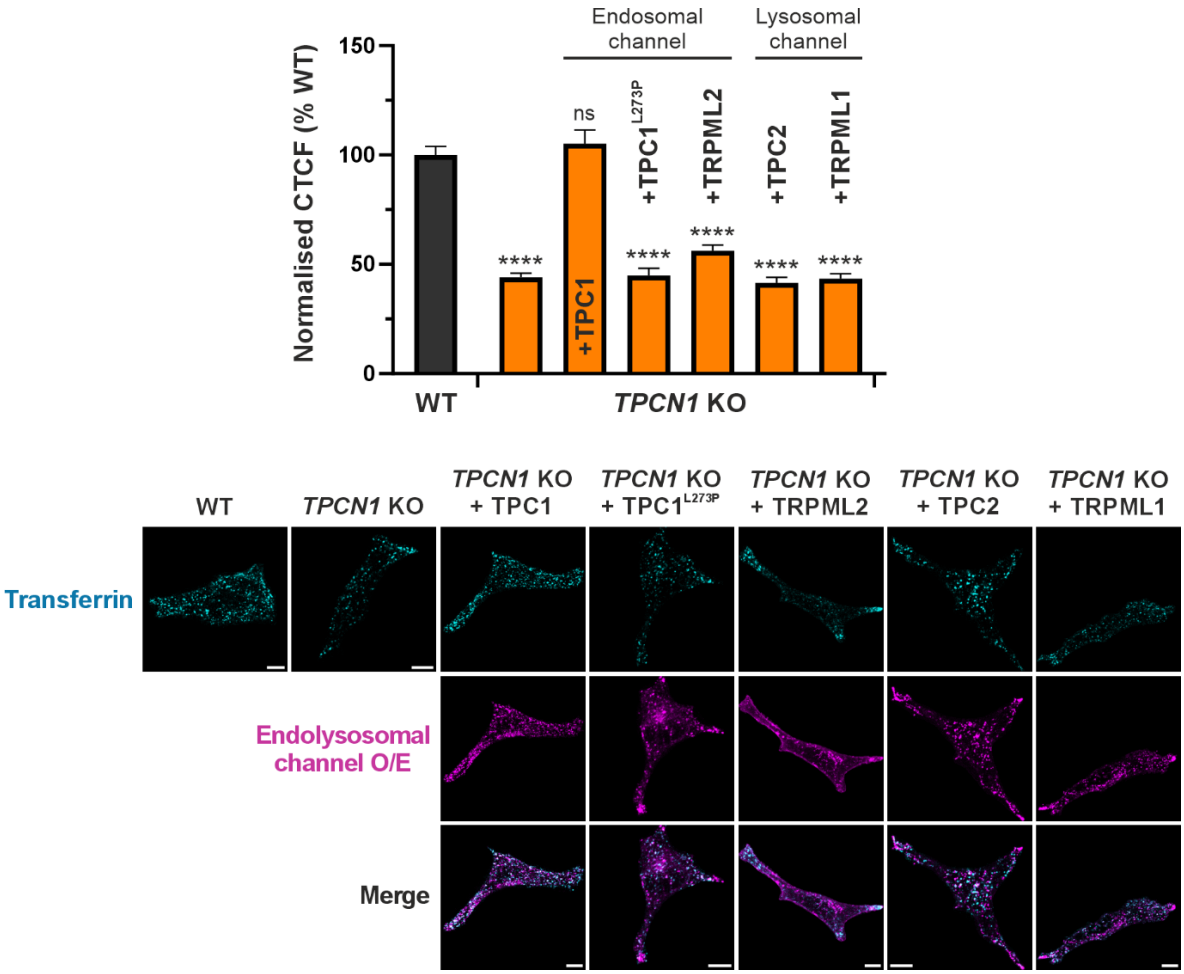

Figure 3.5: TPC1 is specifically required for transferrin internalisation and trafficking. Overexpression of mScarlet-I-tagged versions of endosomal (TRPML2), lysosomal (TPC2, TRPML1) channels, or a pore-dead TPC1 (TPC1^{L273P}) channel cannot restore efficient transferrin uptake and trafficking in TPC1-deficient cells relative to wildtype (WT) HeLa cells, n = 48-61 cells. Representative images of transferrin trafficking upon endo-lysosomal channel expression, scale bars = 10 µm. CTCF, corrected total cell fluorescence. Data are presented as the mean ± SEM, and probability determined using a one-way ANOVA (**** $P < 0.0001$ vs WT).

3.4 Small molecule inhibition of TPCs

To complement the genetic approach, the involvement of TPCs in the transferrin cycle was also investigated through pharmacological inhibition. Figure 3.6 shows the effect of either Ned-19 or tetrandrine preincubation on transferrin internalisation and trafficking. When applied to cells, 10 µM tetrandrine significantly reduced transferrin trafficking compared

to DMSO-treated cells, consistent with previous reports that tetrandrine suppresses endo-lysosomal viral trafficking (169,269). In striking contrast, Ned-19 elicited no effect on transferrin trafficking when applied at two different concentrations (10 and 100 µM) recognised to inhibit TPC activity (75,81,169,287). These experiments not only provide further evidence of TPCs involvement in mediating the transferrin trafficking, but also tentatively allude to the likely signalling molecule regulating channel activity – discussed further in section 3.8.1.

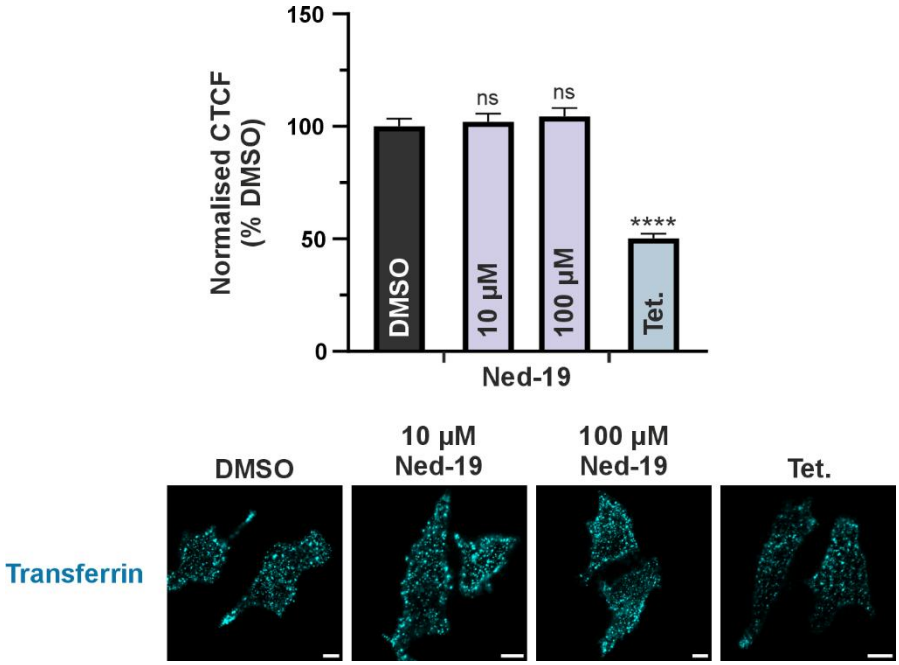

Figure 3.6: Pharmacological inhibition of TPCs reduces transferrin trafficking. Transferrin trafficking was inhibited following preincubation with 10 µM tetrandrine (Tet.), but not with 10 µM or 100 µM Ned-19, relative to 0.1% DMSO control, n = 75-90 cells. Representative images of transferrin following DMSO, Ned-19, or tetrandrine pretreatment, scale bars = 10 µm. CTCF, corrected total cell fluorescence. Data are presented as the mean ± SEM, and probability determined using a one-way ANOVA (**** $P < 0.0001$ vs DMSO).

3.5 Regulation of TfR expression by TPC1

Previous research has suggested that for cell-membrane receptor trafficking, TPC deletion affects the expression levels of cell membrane receptors, thereby regulating the quantity of ligand entering the cell (186). Therefore, by analogy, a reduction in TfR levels could offer a trivial explanation for the transferrin uptake phenotype observed in TPC1-deficient cells.

3.5.1 Whole-cell expression

To determine if TPC1 deletion affected cellular TfR synthesis and expression, Western blotting against the TfR was performed in both wildtype and *TPCN1* knockout HeLa whole-cell lysates. The resultant Western blot was probed using an anti-TfR antibody and band intensities normalised to the total protein content. Reassuringly, a dominant ~95 kDa band was visualised in both wildtype and *TPCN1* knockout cell lysates (Figure 3.7), closely matching the known molecular weight of the monomeric TfR (~90 kDa) (288,289). Alongside this band, two other pronounced bands of approximately 250 and 160 kDa were visualised (Appendix Figure A.2). Whilst the 160 kDa band could represent the homodimeric form of the TfR (289,290), the larger 250 kDa band may be the result of protein aggregation or non-specific antibody binding, as this unexpected band was also identified by the manufacturer Abcam (cat: ab269513). When normalised to total protein content, analysis of the ~95 kDa band revealed no alteration in the total protein levels of TfR protein in TPC1-deficient cells compared to wildtype (Figure 3.7). Although these findings suggest that TPC1 does not regulate TfR synthesis and total cell expression, TPC1 does mediate transferrin uptake and recycling, which could alter the distribution of the transferrin-TfR complex within the cell. This possibility was therefore investigated.

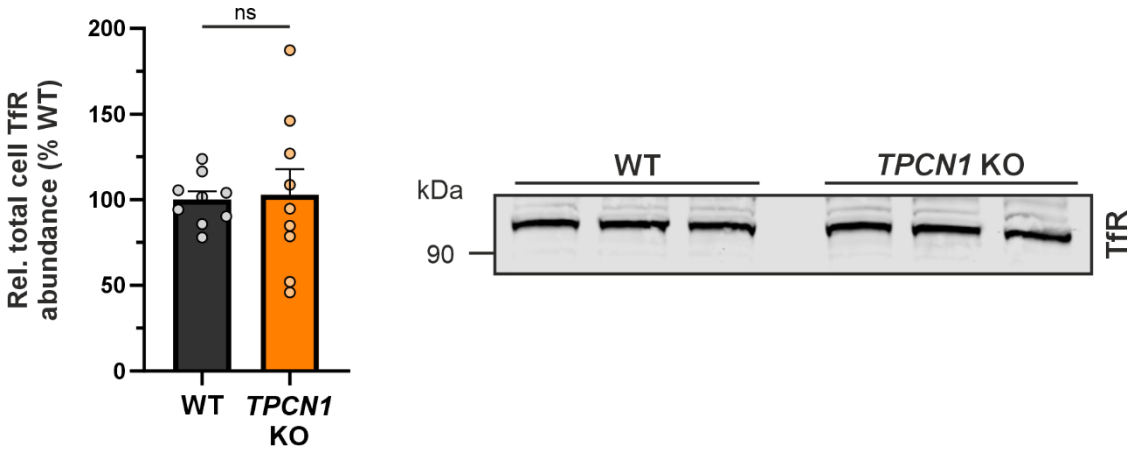

Figure 3.7: Whole-cell TfR expression is not altered following TPC1 deletion. Western blot analysis indicates that whole-cell TfR protein levels, normalised to total protein, are unchanged in *TPCN1* knockout (KO) cell lysates compared to wildtype (WT), $n = 9$ WT and *TPCN1* KO HeLa cell lysates. Blots were labelled using an anti-TfR antibody and detected using a secondary antibody labelled with a fluorescent near-infrared dye. Uncropped representative blot shown in Appendix Figure A.2. Data are presented as the mean ± SEM, and probability determined by a two-tailed t-test (ns = no significance vs WT).

3.5.2 Cell surface expression

Despite the observation that total TfR protein levels are unchanged in *TPCN1* knockout cells (Figure 3.7), this does not exclude the possibility that TPC1 regulates cell surface TfR levels by controlling the ratio of cell surface TfR to internalised TfR. To investigate this possibility, on-cell and in-cell Western assays were performed using non-permeabilised and permeabilised cells respectively, to assess the relative number of cell surface TfR and total cellular TfR respectively. To ensure the selective detection of cell surface TfR, an extracellular C-terminal specific anti-TfR (G-8) IgG was used when labelling non-permeabilised cells. As shown in Figure 3.8, cell surface levels of the TfR were significantly reduced by approximately 49% in TPC1-deficient cells compared to wildtype cells. Surprisingly, the TfR signal was slightly reduced by ~20% in *TPCN1*

knockout permeabilised cells (Figure 3.8), a reproducible finding across two different anti-TfR antibody clones (G-8 and H68.4).

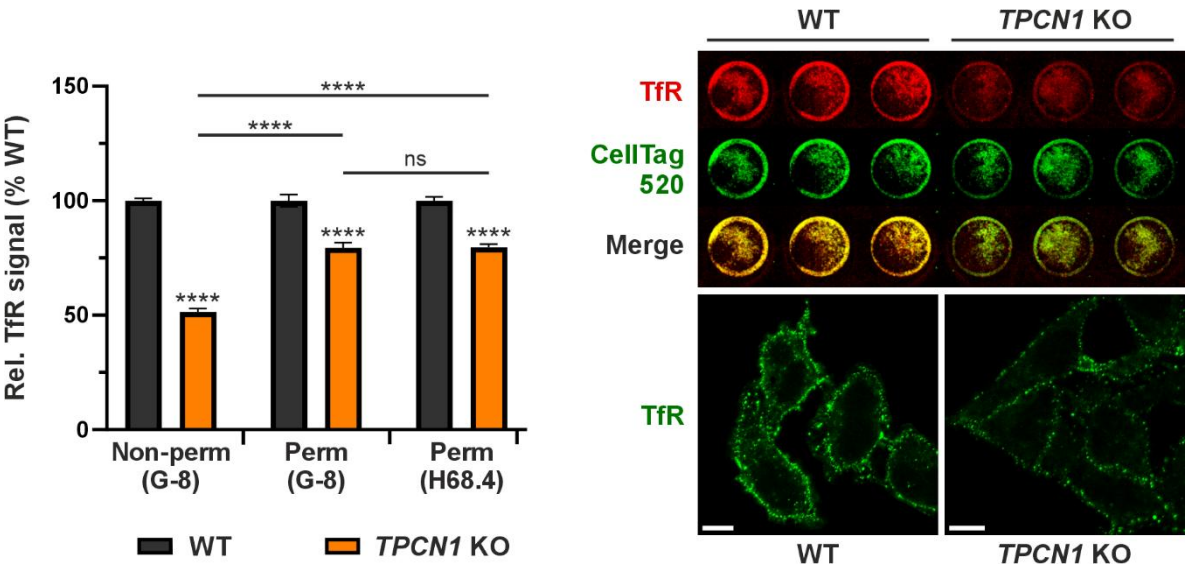

Figure 3.8: TPC1 controls TfR cell surface levels. On-cell and in-cell Western performed with fixed non-permeabilised (non-perm) and Triton X-100-permeabilised (perm) cells respectively. Summary data indicates a significant reduction in cell surface TfR levels (non-perm) in *TPCN1* knockout (KO) HeLa cells compared to wildtype, n = 30-46 wells. TfR protein was detected using either an anti-TfR H68.4, or extracellular C-terminal specific anti-TfR G-8 IgG and normalised to cell number using a CellTag 520 stain. Representative image of non-permeabilised wells labelled with anti-TfR G-8 and stained with CellTag 520, alongside single-cell images of non-permeabilised cells labelled with anti-TfR G-8, scale bars = 10 μm. Data are presented as the mean ± SEM, and probability determined using a one-way ANOVA (**** $P < 0.0001$, ns = no significance vs WT).

To complement the on-cell Western experiment, plasma membrane proteins were surface-biotinylated, solubilised, and then isolated from other proteins using streptavidin beads, to determine the abundance of the TfR at the plasma membrane. Western blotting of streptavidin purified proteins revealed a band size of approximately ~95 kDa (Figure 3.9) which represented the cell surface TfR. Unexpected bands were also observed at 30 kDa (Appendix Figure A.3). As the 30 kDa bands were consistent between wildtype and TPC1-deficient cells and were not observed in whole-cell protein lysates (Appendix Figure A.2),

it is likely that the 30 kDa band represents degradation products from sample preparation, rather than non-specific antibody binding. Comparison of the ~95 kDa TfR band between HeLa wildtype and *TPCN1* knockout conditions revealed a significant ~70% decrease in cell surface TfR levels in TPC1-deficient cells relative to wildtype (Figure 3.9), similar to that observed previously in non-permeabilised cells (Figure 3.8). Taken together with Western blot and in-cell Western experiments, these findings suggest that TPC1 does not regulate total TfR expression, but rather controls the levels of cell surface TfR through regulation of TfR trafficking and recycling back to the cell surface.

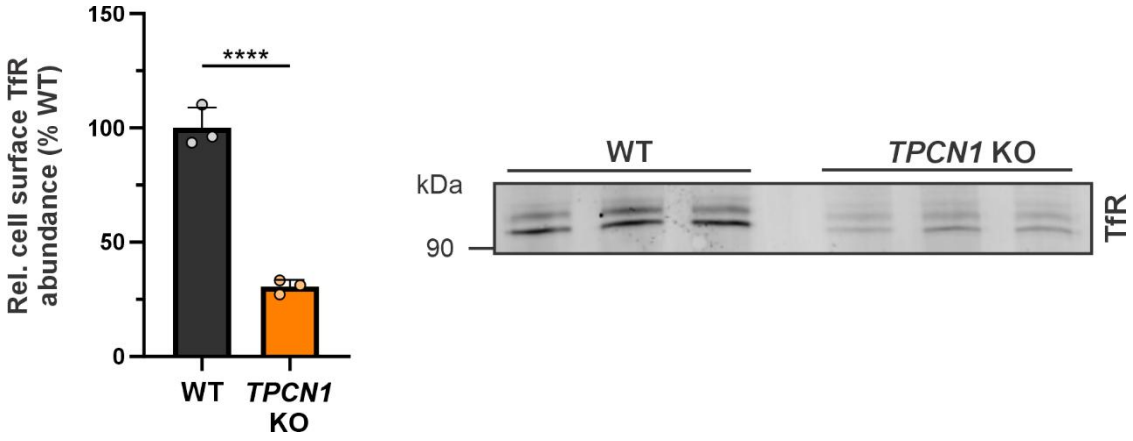

Figure 3.9: Cell-surface biotinylated TfR is reduced in TPC1-deficient cells. Western blot analysis indicates that biotinylated cell-surface TfR levels, normalised to cell surface biotin levels, are reduced in *TPCN1* knockout (KO) HeLa cells compared to wildtype (WT), $n = 3$ WT and *TPCN1* KO cell lysates. Blots were labelled using an anti-TfR antibody and detected using a secondary antibody labelled with a fluorescent near-infrared dye. Uncropped representative blot shown in Appendix Figure A.3. Data are presented as the mean ± SEM, and probability determined by a two-tailed t-test (**** $P \leq 0.0001$ vs WT).

3.6 TPC1 and TfR interaction

A plethora of endo-lysosomal trafficking, cargo-sorting, and membrane-associated proteins have been identified through mass spectrometry as TPC-interacting proteins (175,187), contributing to a deeper understanding of the cellular processes associated with TPCs. Given that the above evidence establishes a regulatory role for TPC1 within the transferrin cycle, the possibility that TPC1 regulates transferrin trafficking through TPC1-TfR protein interactions and complex formation was investigated. The technique chosen to examine a potential protein-protein interaction was co-immunoprecipitation. This procedure involved using antibody-coupled agarose to pull-down heterologous TPC1 tagged with the small peptide epitope -ALFA-tag (275), with the aim of simultaneously pulling down the TfR to confirm an interaction.

Indeed, co-immunoprecipitation of HeLa cell lysates heterologously expressing (+)TPC1-ALFA-tag revealed a protein-protein interaction between TPC1 and the TfR on endosomes (Figure 3.10). Co-labelling of blots using anti-ALFA-tag and anti-TfR antibodies exposed a thick dominant ~110 kDa band for TPC1, comparable to previously reported sizes (80,86,141), as well as smaller doublet bands of approximately 90 and 100 kDa which likely stem from *N*-glycosylation (117,291). Detection of the TfR revealed a standard ~95 kDa band, matching that observed earlier in Figure 3.7, alongside a larger ~110 kDa band, potentially signifying post-translational modifications (292). No bands or proteins were visible following antibody co-labelling in control cell lysates without (-)TPC1-ALFA-tag (Figure 3.10), confirming that the bands were not the result of non-specific binding. These findings point towards the first known interaction of TPC1 with a cell surface receptor. The reasoning why this interaction may be required for TfR trafficking will be discussed in section 3.8.2.

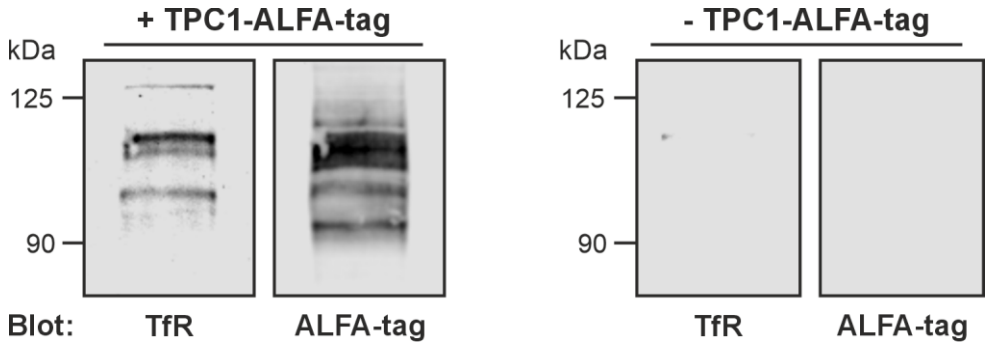

Figure 3.10: TPC1 forms a complex with the TfR. Co-immunoprecipitation of the TfR with TPC1 from HeLa cell lysates of heterologous expression of TPC1-ALFA-tag (+) or not (-), using anti-ALFA-tag coupled-agarose, $n = 3$. Blots were co-labelled using anti-ALFA-tag and anti-TfR antibodies and detected using secondary antibodies labelled with spectrally distinct NIR dyes (results shown as separate channel images for clarity). Uncropped representative blot shown in Appendix Figure A.4.

In order to visualise how TPC1 and the TfR may be interacting, the TPC1-TfR protein complex was predicted using amino acid sequences of the respective proteins within the AI-generated structural modelling program AlfaFold (293). Figure 3.11 shows the predicted structural arrangement of the TPC1-TfR complex. This model suggests that the TfR interacts with the pore region of TPC1. Considering that both of these proteins are transmembrane and would rarely, if ever, be orientated in this configuration, it is unlikely that the TfR and TPC1 interact as predicted in Figure 3.11.

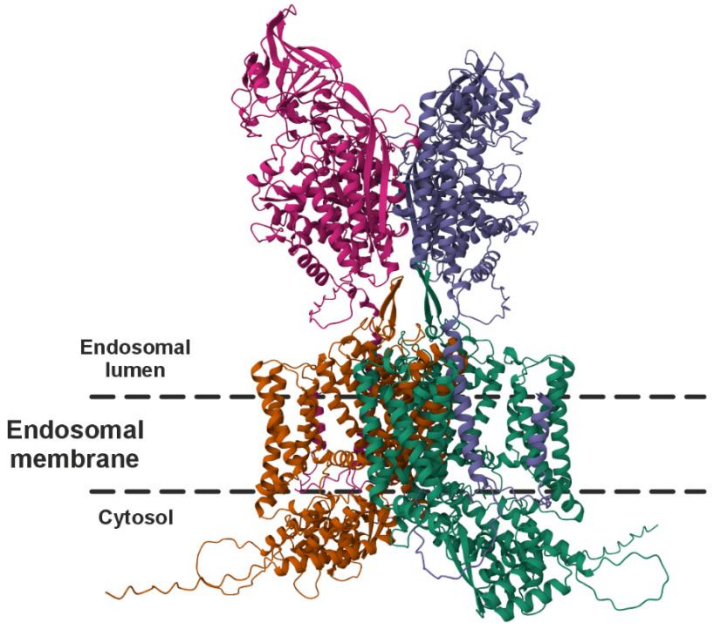

Figure 3.11: AlfaFold-predicted 3D structure of the TPC1-TfR protein complex. TPC1 and TfR protein interactions were predicted using AlfaFold (293) in their dimeric forms. The two homologous domains of TPC1 are coloured orange and green, and the TfR domains are coloured pink and blue. The dotted lines represent the endosomal membrane.

3.7 Iron homeostasis

Following internalisation of the transferrin-TfR complex, Fe^{3+} is released from transferrin and subsequently reduced to Fe^{2+} within endosomes. The reduced iron is then transported across the endosomal membrane into the labile cytosolic Fe^{2+} pool by DMT1, where it is available for storage or exhausted during cellular processes (242,246). As TPC1 is required for the internalisation of iron-bound transferrin, it was theorised that phenotypes of iron deficiency would also be present in cells where TPC1 function is disrupted. The following sections investigated if and how reduced iron-bound transferrin internalisation and trafficking impacts intracellular iron levels, translating these findings to iron-dependent biochemical processes in cellular and mouse models.

Despite representing the most abundant transition metal in the human body, Fe^{2+} is only found in trace amounts (294). Thus, to detect Fe^{2+}, a fluorescent probe must be used which is highly selective for Fe^{2+}, rather than Fe^{3+}, other transition metals, or biological molecules. To reduce such non-selectivity, the fluorescent 'turn-on' probe RhoNox-1 was chosen to directly monitor intracellular Fe^{2+} within living cells. As illustrated in Figure 3.12A, RhoNox-1 exists as a rhodamine scaffold containing a tertiary amine *N*-oxide. This functional group exploits the chemical reaction between Fe^{2+} and the *N*-oxide, exposing a rhodamine B fluorophore and yielding fluorescence in the presence of Fe^{2+} (277,295). The redox chemistry of this reaction establishes a high selectivity for Fe^{2+}, with RhoNox-1 fluorescence not enhanced by other metal ions (including Fe^{3+}), reductants, or ROS (277).

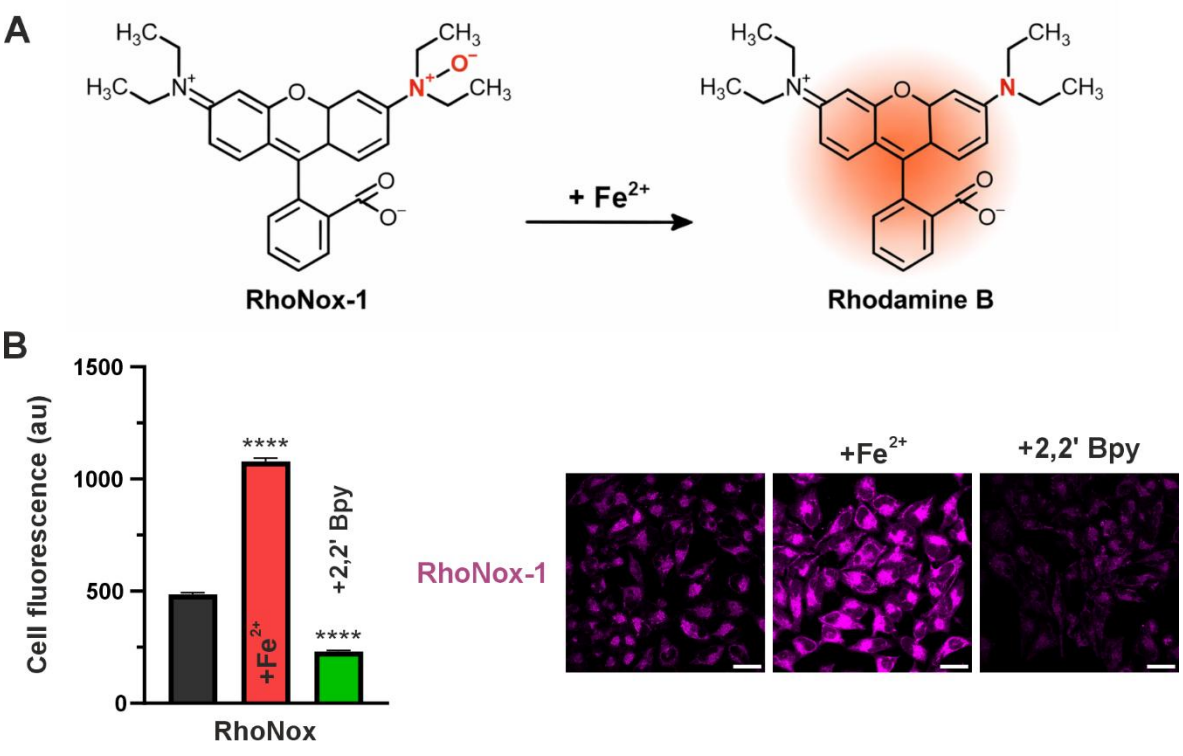

Figure 3.12: RhoNox-1 detects intracellular Fe^{2+}. (A) Structure and mechanism of RhoNox-1 Fe^{2+} detection, tertiary amine *N*-oxide highlighted in red. Adapted from Hirayama (295). **(B)** Confirmation of Fe^{2+} RhoNox-1 detection. HeLa wildtype cells were treated with either 100 µM $FeCl_2$ (Fe^{2+}) to stimulate RhoNox-1 detection, or 1 mM 2,2′-bipyridyl (2,2' Bpy) to chelate Fe^{2+}, n = 284-328 cells. Representative images of each condition, scale bars = 30 µm. Data are presented as the mean ± SEM, and probability determined using a one-way ANOVA (**** $P < 0.0001$).

Before the measurement of endogenous intracellular Fe^{2+} in TPC1-deficient cells, it was first important to confirm that RhoNox-1 detects Fe^{2+} within HeLa cells. As expected, RhoNox-1 displayed a bright cytosolic basal staining in cells, which was substantially enhanced following preincubation with 100 μM Fe^{2+} (Figure 3.12B). Conversely, RhoNox-1 fluorescence was quenched following preincubation with the Fe^{2+} transition metal chelator 2,2′-bipyridyl. These findings support the known application of RhoNox-1 (277), demonstrating its ability to detect changes in the cellular free Fe^{2+} in HeLa cells. Turning next to TPC1-deficient cells, results indicated a 39.7 ± 2.0% (mean ± SEM, n = 131 cells, $P < 0.0001$) decrease in the cytosolic RhoNox-1 fluorescence in *TPCN1* knockout cells relative to wildtype. These findings were consistent with a reduction in iron-bound transferrin internalisation in *TPCN1* knockout cells, thereby providing additional evidence of the criticality of TPC1 within the transferrin cycle for cellular iron homeostasis.

3.7.1 Endogenous iron (Fe^{2+}) accumulation

An intriguing observation was that alongside the anticipated reduction in cytoplasmic Fe^{2+}, RhoNox-1 labelling displayed an additional unexpected staining pattern. RhoNox-1 fluorescence noticeably displayed a prominent punctate distribution within *TPCN1* knockout cells. When quantified, the number of RhoNox-1 puncta was substantially greater in TPC1-deficient cells than in wildtype (Figure 3.13A), which in comparison, contained limited puncta per cell. As indicated in Figure 3.13A, re-expression of TPC1 in *TPCN1* knockout cells reduced the number of puncta back to wildtype levels, demonstrating that the accumulation of puncta was indeed TPC1-dependent.

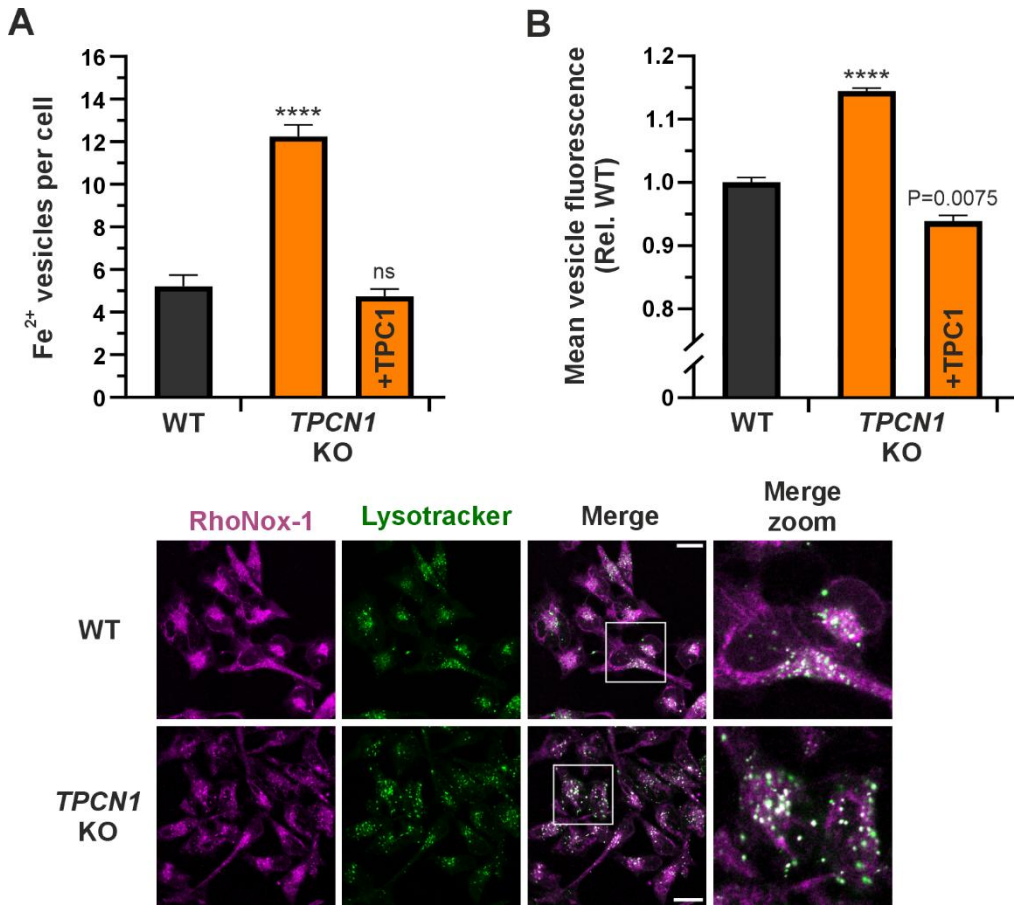

Figure 3.13: RhoNox-1 accumulates in lysosomes in TPC1-deficient cells. Measurement of endogenous iron (Fe^{2+}) using the Fe^{2+}-selective probe RhoNox-1 in HeLa wildtype (WT) and *TPCN1* knockout (KO) cells. **(A)** The number of RhoNox-1 Fe^{2+} vesicles per cell (n = 118-129 cells) and **(B)** calculated mean fluorescence of these vesicles (n = 566-1501 vesicles) relative to WT. Rescue experiments in *TPCN1* KO cells were performed by transient re-expression of TPC1 tagged with mNeonGreen. Representative images of RhoNox-1 in WT and *TPCN1* KO HeLa cells, alongside LysoTracker Green colocalisation, scale bars = 20 µm. Data are presented as the mean ± SEM, and probability determined using a one-way ANOVA (**** $P < 0.0001$ vs WT).

To confirm that these pronounced puncta were RhoNox-1 specific and represented Fe^{2+}-loaded vesicles, two methodologies were used. First, wildtype and *TPCN1* knockout cells were loaded with either RhoNox-1 or the Ca^{2+} indicator Fluo-8H, to determine if deletion of TPC1 affects the uptake or distribution of cytosolic fluorescent dyes. As shown in Figure 3.14A, Fluo-8H puncta formation did not manifest in either wildtype or TPC1-deficient cells, indicating that the accumulation of puncta was specific to RhoNox-1

labelling. Next, to investigate if these RhoNox-1-positive puncta represented Fe^{2+}-containing vesicles, wildtype and TPC1-deficient cells were pre-incubated with 2,2′-bipyridyl to chelate Fe^{2+}. Chelation of cellular Fe^{2+} substantially reduced the number of puncta in *TPCN1* knockout cells, restoring puncta number back to that observed in wildtype cells (Figure 3.14B), validating that the RhoNox-1 puncta were indeed Fe^{2+}-loaded vesicles.

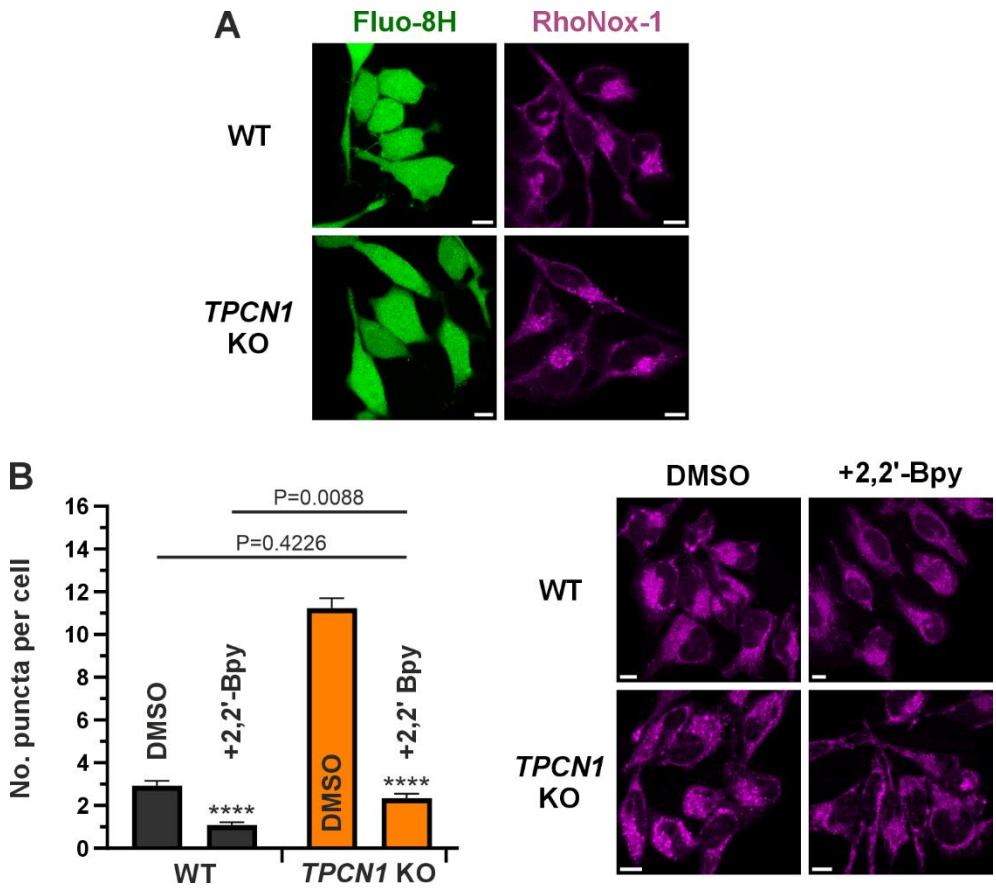

Figure 3.14: RhoNox-1 punctate staining represents Fe^{2+}-loaded vesicles. (A) RhoNox-1 punctate vesicles are specific to RhoNox-1 labelling. HeLa wildtype (WT) and *TPCN1* knockout (KO) cells were incubated with either RhoNox-1, or the cytosolic Ca^{2+} indicator Fluo-8H (2 μM). Representative images of RhoNox-1 (in magenta) or Fluo-8H (in green) cell dyes in WT and *TPCN1* KO HeLa cells. **(B)** Punctate vesicles detected with RhoNox-1 in *TPCN1* KO cells are Fe^{2+}-loaded vesicles, n = 88-102 cells. Representative images of RhoNox-1 staining in either DMSO control, or following Fe^{2+}-chelation by 2,2′-bipyridyl (2,2'-Bpy) conditions in WT and *TPCN1* KO HeLa cells. Scale bars = 10 μm. Data are presented as the mean ± SEM, and probability determined using a one-way ANOVA (**** $P < 0.0001$ vs DMSO).

The observed punctate staining of RhoNox-1 was surprising, especially considering the probes suggested cytosolic and Golgi distribution (277). To pinpoint the compartmental localisation of RhoNox-1 Fe^{2+} vesicles, cells were co-loaded with the proton-driven lysosomal organelle dye LysoTracker Green. As judged by spatial overlap in Figure 3.13, the RhoNox-1 puncta colocalised extensively with LysoTracker Green, indicating that these Fe^{2+}-concentrated vesicles represented lysosomes. In comparison, the RhoNox-1 puncta did not overlap with early or recycling endosome protein markers (Appendix Figure A.5). To understand if Fe^{2+} was accumulating in lysosomes, the brightness of RhoNox-1 puncta were measured as an indirect readout for lysosomal luminal Fe^{2+} levels. As shown in Figure 3.13B, deletion of TPC1 significantly enhanced the fluorescence intensity of RhoNox-1 lysosomal vesicles relative to RhoNox-1 vesicles measured in wildtype cells. Similar to how TPC1 re-expression normalised the vesicle number in *TPCN1* knockout cells, the fluorescence intensity of these vesicles was likewise restored following TPC1 reconstitution (Figure 3.13B). Taken together, these findings establish a role for TPC1 in iron homeostasis.

3.7.2 Ferritinophagy

Although the reduction in transferrin-bound iron internalisation could account for the perceived decrease in cytosolic Fe^{2+}, TPC1 deletion resulted in an unexpected, paradoxical increase in RhoNox-1 Fe^{2+} vesicle number and fluorescence. To understand why Fe^{2+} accumulates within lysosomes in TPC1-deficient cells, the iron homeostatic process of ferritinophagy was explored as a possible explanation.

The process of ferritinophagy is illustrated in Figure 3.15A and described in detail below. Ferritinophagy represents a specialised form of cellular autophagy, whereby the iron-

binding protein ferritin is selectively degraded to release Fe^{2+}. In response to low intracellular labile Fe^{2+} levels, the nuclear receptor coactivator 4 (NCOA4) directly binds to the ferritin heavy chain 1 (FTH1) subunit of ferritin, resulting in the recruitment of phagophore-associated proteins. The NCOA4-ferritin complex is then encapsulated into an autophagosome, which through maturation, inevitably fuses with lysosomes, ultimately leading to the degradation of ferritin and the release of Fe^{2+} to replenish the labile Fe^{2+} pool and restore homeostatic balance. In response to high labile Fe^{2+} levels, NCOA4 is degraded by the E3 ubiquitin protein ligase 2, preventing excessive ferritin degradation (243,296). As cytosolic labile Fe^{2+} levels stringently regulate the dynamic distribution of NCOA4 and ferritin (243), it was hypothesised that the excessive lysosomal Fe^{2+} puncta observed in *TPCN1* knockout cells stemmed from ferritin-NCOA4 lysosomal fusion.

To investigate if ferritin was targeted for lysosomal degradation in TPC1-deficient cells, the degree of colocalisation between either ferritin or NCOA4 and LAMP1 was quantitatively assessed. As depicted in Figure 3.15B, *TPCN1* knockout cells exhibited enhanced redistribution of both ferritin and NCOA4 to LAMP1-positive lysosomes, as demonstrated by a significant increase in the number of ferritin or NCOA4 LAMP1-positive vesicles compared to wildtype. Furthermore, within wildtype and *TPCN1* knockout cells the number of ferritin, and NCOA4 LAMP1-positive vesicles was the same (9 and 17 respectively; Figure 3.15B), consistent with NCOA4 and ferritin being in a complex together when targeted for lysosomal degradation. Taken together with RhoNox-1 findings (Figure 3.13), it can be theorised that TPC1 plays a central role in mediating iron homeostasis in two ways: (a) it regulates TfR (and iron) uptake across the plasma membrane; (b) a consequence of the aforementioned, TPC1 is important for the control of intracellular Fe^{2+} levels by indirectly influencing ferritin-NCOA4 lysosomal fusion, a finding consistent with increased ferritinophagy (243,297). This would explain why the

RhoNox-1 fluorescence becomes more punctate and intense, owing to enhanced ferritin degradation and subsequent Fe^{2+} accumulation/storage in lysosomes.

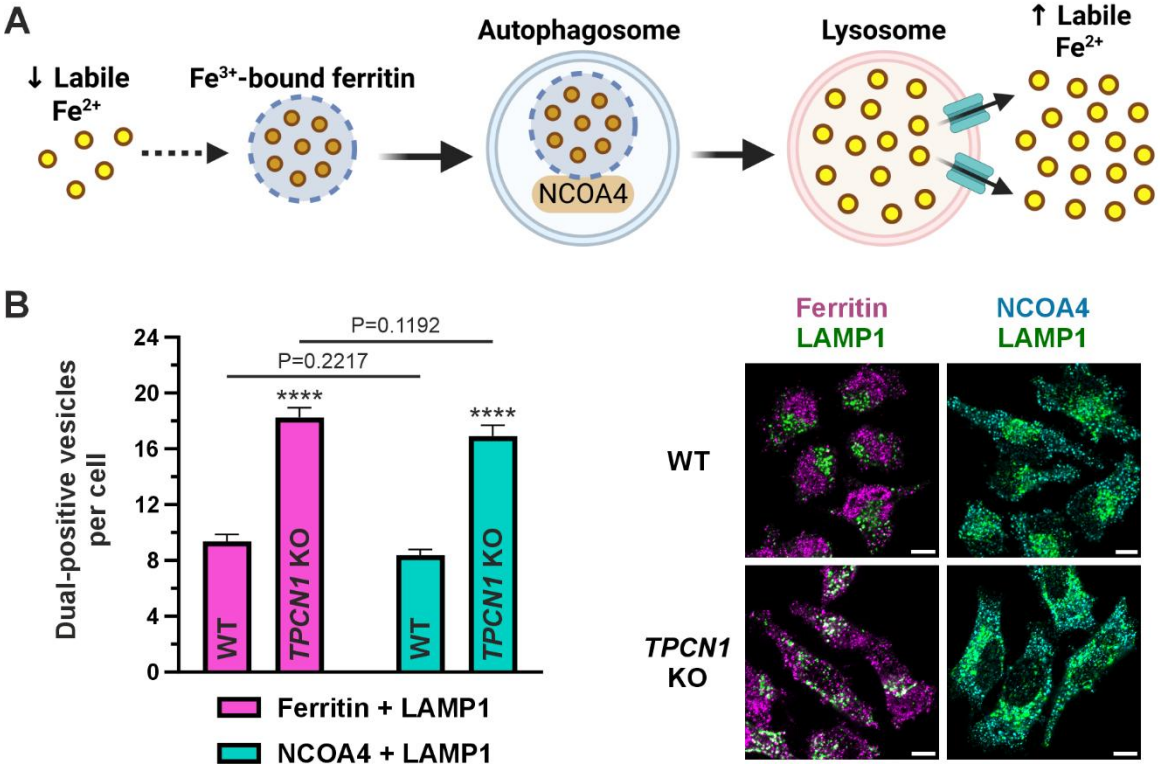

Figure 3.15: Loss of TPC1 triggers cellular ferritinophagy. (A) Illustration depicting the mechanism of ferritinophagy. In response to reduced labile Fe^{2+}, ferritin is selectively targeted for lysosomal degradation by the nuclear receptor coactivator 4 (NCOA4) to restore labile Fe^{2+} levels. **(B)** Colocalisation analysis of ferritin and NCOA4 with LAMP1 in HeLa wildtype (WT) and *TPCN1* knockout (KO) cells, n = 112-138 cells. The degree of colocalisation was determined by the number of ferritin, or NCOA4 LAMP1-positive vesicles per cell. Representative images of ferritin, NCOA4, and LAMP1 immunofluorescence staining, scale bars = 10 µm. Data are presented as the mean ± SEM, and probability determined using a two-way ANOVA (**** $P <$ 0.0001 vs WT).

3.7.3 Haem and haemoglobin synthesis

Having identified a defective transferrin and iron trafficking phenotype in TPC1-deficient cells, the consequence of TPC1 deletion was further investigated to establish how this defect correlates to a disease phenotype within cellular and animal models. The findings

from these experiments will assist in understanding the fundamental biological processes that TPC1 regulates. Imbalance of iron homeostasis can either cause iron deficiency or iron overload. Iron-deficiency anaemia represents the most prevalent iron-deficiency disorder worldwide, characterised by insufficient iron to support haemoglobin synthesis and red blood cell production (298). On the basis of this definition, it was examined whether haem synthesis, an essential prerequisite for haemoglobin production, was altered in TPC1-deficient cells as a downstream consequence of defective transferrin and iron trafficking. To quantify haem in HeLa cells, the metalloporphyrin properties of haem were exploited to liberate the central Fe^{2+} from the protoporphyrin ring of haem (244,278), converting haem into its fluorescent precursor protoporphyrin IX (PPIX) (Figure 3.16A), which could then be analysed by fluorescence spectroscopy. As shown in Figure 3.16B, a significant reduction in PPIX fluorescence, and subsequently haem content, was identified in *TPCN1* knockout HeLa cell lysates compared to wildtype, a decrease suggestive of iron-deficiency in TPC1-deficient cells.

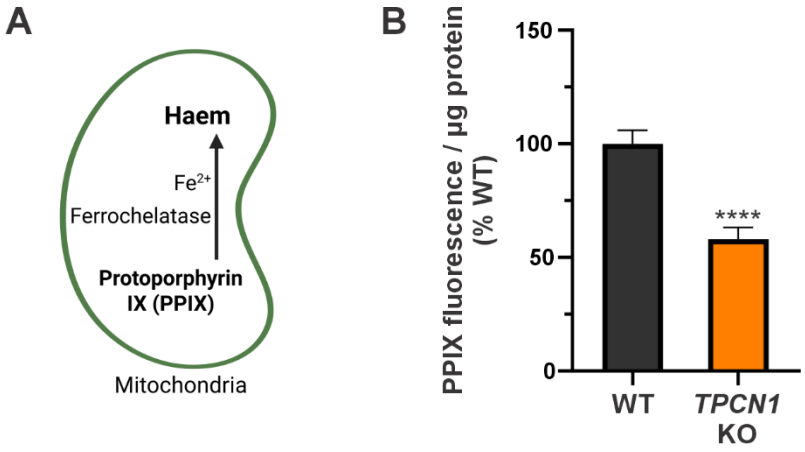

Figure 3.16: Iron dysfunction impairs haem synthesis in TPC1-deficient cells. (A) The final step of mitochondrial haem synthesis, where ferrochelatase catalyses the insertion of Fe^{2+} into protoporphyrin IX (PPIX) to yield haem. **(B)** Quantification of haem in HeLa wildtype (WT) and *TPCN1* knockout (KO) cells (n = 11-12 reactions), through chelation of Fe^{2+} from haem into its fluorescent precursor PPIX. Reactions were standardised to protein mass, and the data normalised to the daily control (WT). Data are presented as the mean ± SEM, and probability determined using a two-tailed t-test (**** $P < 0.0001$ vs WT).

To assess the consequences of impaired iron trafficking and haem synthesis, the above findings from cellular transferrin uptake and iron homeostasis were extrapolated to mice, as a systemic model for iron-deficiency anaemia. As the Galione laboratory lacks TPC mutagenic mice strains, open source phenotypic data from TPC1- and TPC2-deficient mice was obtained from the International Mouse Phenotyping Consortium (IMPC) (299). Intriguingly, analysis revealed that the haematopoietic system within TPC1-deficient mice was severely affected. Figure 3.17A displays phenotypic data from haematology assessments which indicate a reduction in both mean corpuscular volume and haemoglobin within early adult *Tpcn1*$^{-/-}$ mice, two common phenotypic markers associated with microcytic anaemia, for which iron deficiency is the primary cause (298). In comparison, the haematopoietic system within *Tpcn2*$^{-/-}$ mice appears unaffected (Figure 3.17B), signifying a specific requirement for TPC1 within iron homeostasis. These findings correlate with cellular Fe^{2+} and haem experiments, which position TPC1 at the centre of iron trafficking and homeostasis, where TPC1 dysfunction results in an iron-deficiency phenotype.

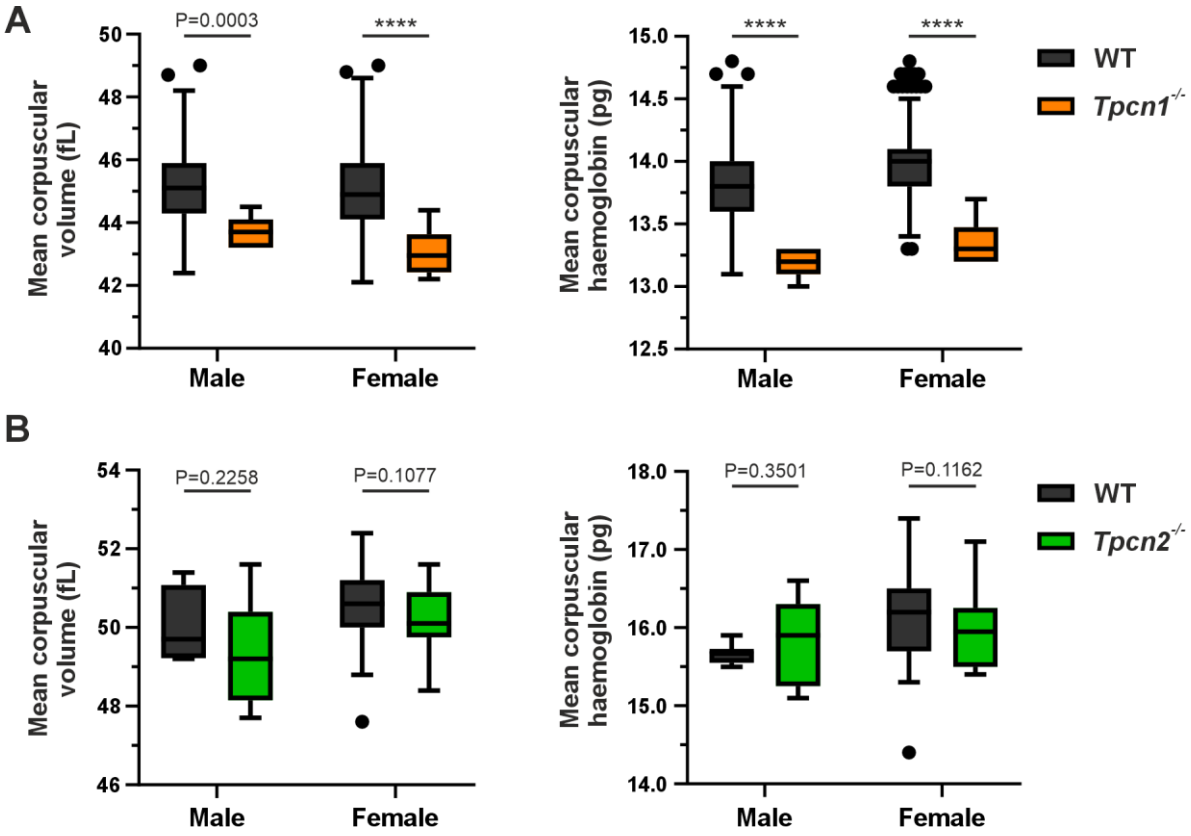

Figure 3.17: TPC1 is required for haematopoiesis in mice. Data obtained from the International Mouse Phenotyping Consortium (www.mousephenotype.org) (299). Haematology phenotypic assays performed in early adult wildtype (WT), **(A)** *Tpcn1*$^{-/-}$ (*Tpcn1*$^{tm1.1(KOMP)Vlcg}$; Jackson Laboratories, n = 7-8), and **(B)** *Tpcn2*$^{-/-}$ (*Tpcn2*$^{Gt(YHD437)Byg}$; BayGenomics, n = 9-14) male and female mice. Data are presented as a Tukey boxplot, and probability determined using a two-tailed t-test (**** $P < 0.0001$ vs WT).

3.8 Discussion

This chapter was preluded on three publications reporting the involvement of TPCs in mediating cell-membrane protein trafficking of the endocytic EGFR, PDGFRβ, and LDLR (116,185,186). The aim of this chapter was to investigate if TPCs likewise regulate the analogous process of TfR trafficking within the transferrin cycle. Taken together, the data here strongly suggests that TPC1 mediates the transferrin cycle and iron homeostasis, in addition to providing evidence regarding how TPC1 likely governs these processes.

3.8.1 TPC1 specificity in the transferrin cycle

The involvement of TPCs within the transferrin cycle was unsurprising, especially considering the variety of reports detailing a role for TPCs within similar ligand and pathogenic trafficking pathways (81,116,169,185,186). More intriguing was the finding that TPC1 appears to have a more prominent role than TPC2 in mediating TfR internalisation and trafficking (Figure 3.3). These findings contrast to results from analogous endocytic pathways, which demonstrate a near equal trafficking defect in both TPC1- and TPC2-deficient cells (81,92,116,186). A plausible explanation for the results observed in Figure 3.3 and Figure 3.5 is the exclusive compartmental use of TPC1-positive early and recycling endosomes within the transferrin cycle. Approximately 99% of transferrin-TfR complexes are recycled back to the cell surface, with negligible amounts entering the lysosomal lumen (220). In comparison, LDL, PDGFRβ, and EGFRs are transported to lysosomes for degradation, to release cholesterol and attenuate growth factor-mediated signalling (116,208,280). The position of TPC1 integrates itself at the forefront of endosomal TfR trafficking, enabling localised signals to be decoded by downstream endosomal machinery involved in mediating endosomal membrane trafficking. Furthermore, if TfR trafficking is truly regulated by a protein-protein interaction between TPC1 and the TfR (discussed in subsequent section), it could explain why deletion of TPC2 resulted in a smaller transferrin trafficking defect, as TPC2 is sparsely distributed across early and recycling endosomes (80).

An unexpected, yet explainable outcome, were the differences in transferrin internalisation between *TPCN1* and *TPCN2* knockout clones (Figure 3.3). Logically, within TPC1- and TPC2-deficient cells, a similar phenotype would be expected between cell clones of the same missing isoform. Although a consistent transferrin uptake defect was observed in

TPCN1 and *TPCN2* knockout cell clones (Figure 3.3), the magnitude of the defect was variable. These differences likely arise from the genetic mutations generated following CRISPR-editing. As demonstrated by Dr Xiao in Figure 3.1, allelic heterogeneity exists between clones, particularly the D149 and A17 *TPCN1* knockout clones, the latter containing an extra exon deletion (6 and 7) which will affect protein truncation and phenotypes differently. Although TfR trafficking was assessed within single TPC knockout cells, the effect of dual isoform deletion within *TPCN1/2* double knockout HeLa cells was not investigated, due to the unavailability of this cell line. The consequence of TPC1 and TPC2 deletion on transferrin trafficking was instead assessed in a different cell line and is presented in Chapter 5.

Another finding supporting the involvement of TPCs within the transferrin cycle was that observed following the pharmacological inhibition of TPCs. Due to the poor availability of TPC1-selective antagonists, it remains challenging to selectively inhibit TPC1 channel activity. Nonetheless, preincubation with tetrandrine severely impacted transferrin trafficking, similar to that observed in *TPCN1* knockout cells (Figure 3.6). In comparison, Ned-19 failed to affect transferrin trafficking, despite varying experimental conditions. Reports detail that the stereoisomerism of Ned-19 could account for tissue- and cell type-specific effects (166,300). This is exemplified in cancer cell lines, where tetrandrine, but not Ned-19, impairs the HLA-B45 presentation of Mtb antigens (267) and increases sorafenib-induced cell death (301). Therefore, the cancer-derived nature of HeLa cells, or the stereoisomer composition of Ned-19, could explain the results observed in Figure 3.6. Finally, recent evidence suggests that similar to Ned-19, tetrandrine inhibits NAADP-induced TPC activity, albeit perhaps indirectly through LIMP-2 modulation (178). Therefore, as well as linking TPCs to transferrin trafficking, these findings postulate the

potential upstream messenger regulating TPC activity, a topic which is investigated and discussed further in Chapter 5.

Taken together, the data shown here indicates that TPC1 expression is specifically required for mediating TfR internalisation and trafficking. This was particularly evident when overexpression of several endo-lysosomal channels failed to sufficiently restore the trafficking defect in *TPCN1* knockout cells (Figure 3.5). The endo-lysosomal channels chosen for overexpression included both Na^+- and Ca^{2+}-permeable channels which are expressed on a variety of endo-lysosomal compartments. In addition to channel specificity, this provided a basis to hypothesise which cation and compartment may mediate TfR trafficking. Interestingly, only overexpressed endosomal channels, TPC1 and TRPML2 (117,198), were able to elicit a change in transferrin trafficking in TPC1-deficient cells (Figure 3.5). Previously, TRPML2 has been tentatively linked to TfR recycling regulation, since the $PI(3,5)P_2$-insensitive channel mutant $TRPML2^{R310A}$ slowed the rate of transferrin recycling (198), a similar observation to TPC1 deletion in Figure 3.4B. These findings provide initial evidence that endosomal compartments mediate TfR trafficking, either through their luminal environment, or through localised cation efflux. The former is true for the transferrin cycle, where a mild endosomal luminal pH is required for Fe^{3+} release from transferrin (230), while the latter is vital for the analogous process of phagocytic internalisation (81). Deducing whether TPC1 mediates transferrin trafficking through maintenance of the endosomal luminal environment, or through localised endosomal channel cation release, forms the basis of Chapter 4.

3.8.2 An alternative mechanism to TfR expression

To address one of the main aims of this thesis, TPC1 was investigated for how it governs TfR internalisation, trafficking, and recycling. The data presented in this chapter indicates that TPC1 regulates the recycling of the apo-transferrin-TfR complex back to the cell surface, thereby controlling the plasma membrane, but not total cell, TfR levels (Figure 3.7 and Figure 3.8). This explains the reduction in transferrin uptake observed in TPC1-deficient cells, whereby deletion of TPC1 slows recycling, decreasing the levels of TfR protein at the cell surface and subsequently, the number of TfRs available to bind and internalise exogenous transferrin. Contrary to how the number of Rab5/transferrin-positive early endosomes were reduced in *TPCN1* knockout cells (Figure 3.4C), future experiments would expect to observe increased quantities of Rab11/transferrin-positive recycling endosomes in *TPCN1* knockout cells, attributable to a reduction in the rate of TfR recycling.

Despite sharing the same fundamental mechanism of receptor-mediated endocytosis and receptor recycling, how TPC1 regulates TfR trafficking contrasts to other receptor-mediated pathways. Müller *et al*. showed that TPC deletion rather enhances EGFR and c-Jun N-terminal kinase (JNK) signalling, subsequently increasing EGFR synthesis and cell surface levels (186). In comparison, cell surface levels of other endocytic receptors such as the FcR, which recognises pathogens and initiates phagocytosis, are unaltered in TPC-deficient macrophages (81). These differences between cell surface receptor levels highlight the intricate link between TPC function and protein trafficking and signalling. Thus, further efforts to decipher the mechanistic regulation and downstream signalling of TPC1 would be beneficial.

To investigate if TPC1 governs TfR expression, two approaches were used to quantify total TfR protein levels. Although quantitative analysis of TPC1-deficient HeLa cell lysates revealed no difference in total TfR protein expression (Figure 3.7), a significant reduction in the total TfR protein signal was observed in fixed permeabilised cells in an in-cell Western assay (Figure 3.8). This finding was reproduced using two different anti-TfR antibody clones (G-8 and H68.4), confirming the validity of the in-cell Western outcome (Figure 3.8). A caveat of in-cell Western assays are their inability to exclude truncated or modified forms of the detected protein, instead providing a bulk cellular protein signal per well. As several molecular weight bands were observed in both wildtype and *TPCN1* knockout cell lysates following TfR labelling, only the true ~95 kDa molecular band representing the monomeric TfR protein was quantified. This could explain the differences observed between methodologies, as truncated or non-specific anti-TfR IgG binding may be altered in TPC1-deficient cells, reducing the overall antibody signal. Thus, the findings from quantitative Western blotting depict a more specific, accurate representation of total cell TfR levels compared to the in-cell Western. Nonetheless, two discrete labelling techniques demonstrated that cell surface TfR protein levels were reduced in both non-permeabilised (Figure 3.8) and biotinylated *TPCN1* knockout cells (Figure 3.9). Therefore, it can be deduced that the cell surface levels of the TfR are indeed reduced in TPC1-deficient cells.

The observation that TPC1 and the TfR form a complex together was unexpected (Figure 3.10). Whether this interaction is essential for mediating TfR trafficking is not yet apparent and requires further investigation. In particular, it is not clear why TPC1 would need to complex with the TfR to govern trafficking and recycling. A more plausible interaction would be with membrane fusion proteins, such as SNARE or Rab-GTPase proteins, both of which have already been identified to interact with TPCs to modulate membrane

trafficking (117,176). As co-immunoprecipitation does not indicate the type of interaction, it is unclear if the TPC1-TfR complex is formed through either a direct, or indirect protein-protein interaction. Based on the structural AlphaFold (293) prediction and alignment of the TPC1-TfR interaction (Figure 3.11), it is unlikely that these proteins directly bind to one another, especially considering their transmembrane positioning on the endosomal membrane. An alternative explanation is that TPC1 interacts with the TfR through an intermediate protein, similar to the requirement of Lsm12/JPT2 accessory proteins for NAADP-induced TPC activation (92). Alternatively, the observed interaction could be attributed to the spatial distance between TPC1 and the TfR on the endosomal membrane, resulting in the TfR being precipitated alongside TPC1 (Figure 3.10).

3.8.3 TPC1 regulates iron homeostasis

Alterations in iron homeostasis, especially iron overload, have been suggested to contribute to endo-lysosomal dysfunction, potentially through enhanced activation of TPCs (302,303). To gain additional insights into the role of TPC1 in iron homeostasis, the downstream consequence of defective transferrin and iron trafficking was investigated within TPC1-deficient cells. TPC1 appears to regulate the dynamics of endogenous transferrin and iron transport, as shown by a reduction in cytosolic labile Fe^{2+} staining in *TPCN1* knockout cells by the Fe^{2+} reporter RhoNox-1. These findings complement results from previous studies, that show that the opposite dysfunctional phenotype, increased cytosolic labile Fe^{2+}, is present in cells overexpressing TPC1 (302). The consequence of reduced labile Fe^{2+} in TPC1-deficient cells was emphasised during haem synthesis (Figure 3.16), where the intracellular levels of Fe^{2+} acted as a rate limiting step for the biosynthesis of haem (244).

Not only do the above results establish TPC1 as a critical endo-lysosomal channel required for cellular iron homeostasis, but they also associate TPCs with mitochondrial function. TPC2-mediated Ca^{2+} release was recently shown to facilitate mitochondria Ca^{2+} uptake at MCSs (304), providing additional evidence that TPCs act as upstream regulators of mitochondrial-dependent processes. Reassuringly, the conclusions from cellular systems correlate with *in vivo* mouse models, further signifying the importance of TPC1 within iron-dependent haematopoietic pathways. *Tpcn1*$^{-/-}$ mice display a reduction in red blood cell volume and haemoglobin content, two clinical characteristics of the anaemic-related disorder microcytic anaemia (298). Based on the findings from this chapter, it is speculated that TPC1 indirectly influences red blood cell formation by regulating the trafficking of iron-bound transferrin, thereby controlling the availability of cytosolic labile Fe^{2+} available for haem synthesis and haemoglobin production.

Consistent with the above observation that *TPCN2* knockout does not impair TfR trafficking to the same degree as TPC1 deletion (Figure 3.3), data from the IMPC (299) indicated that the haematopoietic system within TPC2-deficient mice was unaffected (Figure 3.17). The IMPC contains phenotypic data from several *Tpcn1*$^{-/-}$ and *Tpcn2*$^{-/-}$ mouse strains; however, not all of these strains have been fully characterised to confirm absolute TPC knockout. The measurements reported in Figure 3.17 were obtained from *Tpcn1*$^{-/-}$ and *Tpcn2*$^{-/-}$ mice strains denoted as *Tpcn1*$^{tm1.1(KOMP)Vlcg}$ and *Tpcn2*$^{Gt(YHD437)Byg}$ respectively. *Tpcn2*$^{Gt(YHD437)Byg}$ represents a well-characterised mouse strain, successfully used in numerous studies (80,81,87,305–307) and confirmed by RT-PCR to express no wildtype transcripts across various tissues (80,87,307). Generated by the Knockout Mouse Project, minimal information is available regarding the *Tpcn1*$^{tm1.1(KOMP)Vlcg}$ mouse strain due to proprietary restrictions. Although the IMPC does contain data from the TPC1-deficient mouse strain *Tpcn1*$^{Gt(XG716)Byg}$, characterisation of homozygote mice carrying this

mutation indicated that *Tpcn1* expression was not abolished (116,308). Therefore, the insignificant results from haematology assessments using this mouse strain cannot be confidently interpreted.

Although a reduction in TfR uptake and subsequently intracellular Fe^{2+} was observed in *TPCN1* knockout cells, increased lysosomal Fe^{2+}-loaded vesicles were unexpectedly detected (Figure 3.13). Initially, the accumulation of these vesicles appeared paradoxical, as a reduction in both the number and fluorescence of Fe^{2+}-positive vesicles would be anticipated, given the decreased internalisation of iron-bound transferrin. These vesicles were confirmed to arise from lysosomal Fe^{2+} detection by RhoNox-1, as punctate labelling was not observed with other cytosolic dyes, and critically, chelation of iron abolished the Fe^{2+} puncta (Figure 3.14). Moreover, as RhoNox-1 is highly selective for Fe^{2+}, the non-specific detection of other metal ions, reductant, or ROS can be excluded (277). Previous measurements of endo-lysosomal Fe^{2+} using RhoNox-1 estimate that the luminal concentration of Fe^{2+} in LysoTracker-stained endo-lysosomes ranges from 32.7 ± 7.4 μM in primary rat cortical neurons, to 50.4 ± 6.4 μM in astrocytoma cells (309). Since RhoNox-1 fluorescence was enhanced by approximately 14% in LysoTracker-stained TPC1-deficient endo-lysosomes (Figure 3.13B), it is likely that the luminal Fe^{2+} concentration is also increased in these vesicles. To explain this paradoxical phenomenon, it is hypothesised that deletion of TPC1 decreases the internalisation of iron-bound transferrin, diminishing intracellular labile Fe^{2+}. This reduction results in the redistribution and fusion of the NCOA4-ferritin complex with lysosomes (Figure 3.15), a finding consistent with the process of ferritinophagy (243,297). Alternatively, deletion of TPC1 may interfere with Fe^{2+} egress from endo-lysosomes. Similar to the selectivity of TRPML1 and TRPML2 (196), TPC1 may retain permeability to Fe^{2+} and represent an additional endo-lysosomal Fe^{2+} efflux pathway alongside DMT1 (246,281).

Although essential for providing Fe^{2+} for biological processes and metabolism, excessive ferritinophagy can cause Fe^{2+} overload, leading to iron-dependent programmed cell death known as ferroptosis (245). Additionally, the accumulation of redox-active Fe^{2+} makes lysosomes vulnerable to the generation of ROS and oxidative stress-induced cell damage (232,242). The above findings provide provisional evidence that TPC1 indirectly mediates Fe^{2+}-dependent ROS generation in mammalian cells. In relation to this, future experiments would expect to observe increased lysosomal ROS production and impaired lysosomal membrane permeabilisation in cells where TPC1 dysfunction is apparent (232).

3.9 Conclusions

Together, the findings from this chapter indicate that TPCs are critical for cell-membrane protein trafficking. In the context of the transferrin cycle, a constitutive process necessary for cell iron delivery, TPC1 was identified as a crucial regulator of TfR internalisation, trafficking, and recycling. Unlike analogous trafficking pathways, the mechanism behind this regulation stems from cell surface TfR localisation, where TPC1 controls the rate of TfR recycling and hence the levels of cell surface TfR. This chapter also revealed a potential interaction between TPC1 and the TfR, an intriguing finding which requires further investigation to understand if formulation of this complex is necessary for mediating TfR trafficking. A downstream corollary of reduced iron-bound transferrin uptake in TPC1-deficient cells is diminished intracellular labile Fe^{2+}. This reduction consequently influences major iron homeostatic processes such as haem synthesis and potentially increases ferritinophagy. Finally, this work demonstrates that the dysfunction of endosomal membrane trafficking observed in TPC1-deficient cells translates to disease, particularly in relation to anaemic phenotypes associated with iron deficiency.

Establishment of TPC1 within TfR and iron trafficking acts as a foundation for further research into the molecular mechanism defining this regulation.

Chapter 4 – Results

TPC1 cation release in the transferrin cycle

4.1 Summary

As demonstrated in the previous chapter, the transferrin cycle is dependent upon endosomal TPC1 expression, without which iron-bound transferrin/TfR internalisation and trafficking is impaired, resulting in iron-deficiency phenotypes. Although a clear involvement of TPC1 was established, the exact TPC1 cation fluxes which regulate the transferrin cycle remained uncertain. The aim of this chapter was to elucidate which TPC1 cation modalities contribute to regulating the trafficking of the transferrin-TfR complex.

The transferrin cycle is a multiphasic pathway which contains different phases that have been shown to be regulated by Ca^{2+} and endo-lysosomal proteins. In particular, clathrin-mediated endocytosis (210,211), endosomal trafficking (185), and exocytosis (75,221), are all processes within the transferrin cycle which are dependent upon intracellular Ca^{2+} for normal function. Previous research has suggested that local intracellular Ca^{2+} is a critical driving factor for TfR internalisation and recycling (310,311), likely mediated by Ca^{2+}-dependent kinases such as the Ca^{2+}/calmodulin-dependent protein kinase kinase 2 (CaMKK2) (312,313). Through buffering of local Ca^{2+}, this chapter will evaluate whether localised endosomal Ca^{2+} nanodomains are required for efficient TfR internalisation and trafficking.

Despite the apparent role of Ca^{2+} within the transferrin cycle, the source of these Ca^{2+} domains remains unclear. The ER represents the largest intracellular Ca^{2+} store, initiating and amplifying global Ca^{2+} signals for signal transduction. Alongside the ER, endo-lysosomes are newly established Ca^{2+}-containing organelles, whose Ca^{2+} signals are crucial for localised signalling. Therefore, the main focus of this chapter is to define the cellular compartmental source of Ca^{2+} which likely drives TfR trafficking.

Whole-endosomal patch-clamp recordings will be shown, which characterise a new TPC1 channel mutant that exhibits a loss of Na^{+} selectivity, whilst maintaining Ca^{2+} permeability. Findings from TPC1-deficient cells expressing this mutant channel will be discussed, to establish which TPC1 cation flux regulates TfR trafficking. Furthermore, the possibility that the TfR itself functions as a signal transduction receptor, whereby transferrin initiates intracellular signal transduction and local TPC1-mediated Ca^{2+} efflux (311), will be explored using GECIs tethered to TPC1. The methodology used to attempt to detect these transferrin-induced TPC1-mediated Ca^{2+} signals will be discussed.

The following chapter contains figures and content from Burton *et al*. (282).

4.2 Intracellular Ca^{2+} chelation

4.2.1 Confirmation of cytosolic Ca^{2+} chelation

First, it was investigated whether the abnormal TfR trafficking defect observed in Chapter 3 was likely caused by impaired intracellular Ca^{2+} signalling as a consequence of TPC1 deletion. To confirm if the transferrin cycle was Ca^{2+}-dependent, intracellular cytosolic Ca^{2+} was chelated using two distinct Ca^{2+} buffers, EGTA and BAPTA. Although both chelators are highly specific for Ca^{2+}, their ability to differentially chelate cytosolic Ca^{2+} is

a function of their unique Ca^{2+}-binding kinetics (314). As illustrated in Figure 4.1A, EGTA (K_d ~151 nM) acts as a slower buffer of global Ca^{2+}, whilst BAPTA (K_d ~160 nM) binds Ca^{2+} approximately 100-fold faster, chelating both global and local cytosolic Ca^{2+} (81). The contrasting Ca^{2+}-binding kinetics of EGTA and BAPTA provide a diagnostic tool for determining cellular processes dependent on either global, or local Ca^{2+} domains respectively (81,314).

To confirm the chelation of intracellular Ca^{2+}, HeLa wildtype cells were pre-incubated with varying concentrations of either EGTA or BAPTA in their respective cell-permeant AM-ester precursors, alongside the Ca^{2+} indicator Fluo-8H. As a positive control, single-cell Ca^{2+} signals in response to 50 μM histamine were quantified, to assess the ability of EGTA and BAPTA to chelate histamine-induced H1 receptor G_q/PLC-β/IP_3R-coupled Ca^{2+} release. As shown in Figure 4.1B, in the absence of either EGTA or BAPTA, the addition of histamine resulted in an approximate 6-fold increase in Ca^{2+} signals within both Ca^{2+}-containing and Ca^{2+}-free conditions. In contrast, a concentration-dependent decrease in Ca^{2+} signals in response to histamine was observed following both EGTA and BAPTA preincubation. As expected, an increased buffering capacity was observed for BAPTA, with 25 μM BAPTA almost completely abolishing the Ca^{2+} response (~99% reduction in Ca^{2+} signals; Figure 4.1B).

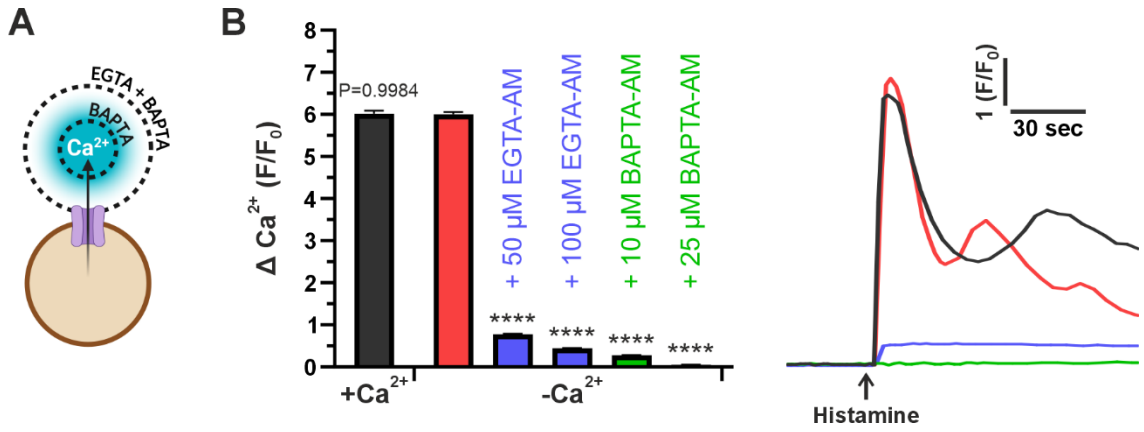

Figure 4.1: Intracellular EGTA and BAPTA Ca^{2+} buffering. (A) Cartoon depicting the range of action of the Ca^{2+} chelators BAPTA and EGTA. **(B)** The -AM ester variants of BAPTA and EGTA significantly chelate global IP_3R-induced Ca^{2+} signals by histamine (50 µM), n = 218-305 cells. Representative traces shown for Ca^{2+}-containing media (black), Ca^{2+}-free media (red), EGTA-AM (blue) and BAPTA-AM (green). Graph depicts the collated maximum Ca^{2+} peaks under the different conditions. Data are presented as the mean ± SEM, and probability determined using a one-way ANOVA (**** $P < 0.0001$ vs -Ca^{2+}).

4.2.2 Intracellular Ca^{2+} regulates TfR trafficking

Having verified the Ca^{2+}-buffering properties of EGTA and BAPTA within HeLa cells, these diagnostic compounds were subsequently used to chelate cytosolic Ca^{2+} prior to the exogenous application of transferrin. It was hypothesised that if the transferrin cycle is Ca^{2+}-dependent, TfR trafficking would be impaired following Ca^{2+} chelation with either EGTA or BAPTA. Although EGTA significantly buffered cytosolic Ca^{2+} (Figure 4.1B), surprisingly, it had no perceivable effect on TfR internalisation or trafficking (Figure 4.2). In contrast, chelation of local cytosolic Ca^{2+} with BAPTA significantly impaired transferrin trafficking by approximately 49% compared to DMSO-treated control cells (Figure 4.2). To control against off-site effects caused by BAPTA, the low Ca^{2+}-binding affinity variant, tetrafluoro-BAPTA (TF-BAPTA-AM, K_d ~160 µM), was incubated in parallel to BAPTA. Encouragingly, TF-BAPTA did not reduce TfR trafficking (Figure

4.2), confirming that the trafficking defect observed with BAPTA was a consequence of local Ca^{2+} chelation. These data suggest that TfR internalisation and trafficking is indeed regulated by Ca^{2+}. Furthermore, these findings indicate that this regulation is specifically at the level of a local Ca^{2+} domain and not a global Ca^{2+} signal, since BAPTA inhibited trafficking and the slower Ca^{2+} chelator EGTA did not.

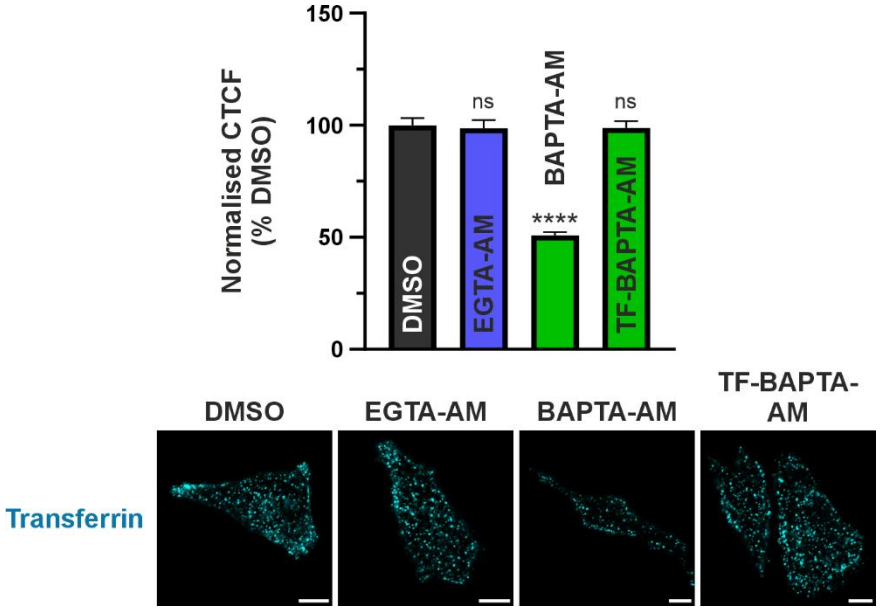

Figure 4.2: TfR trafficking is dependent on local intracellular Ca^{2+} domains. Trafficking is impaired by local Ca^{2+} chelation (BAPTA-AM, 25 µM), but not global Ca^{2+} chelation (EGTA-AM, 100 µM), n = 99-104 cells. Representative images of transferrin following EGTA-AM, BAPTA-AM, or TF-BAPTA-AM pretreatment, scale bars = 10 µm. Data are presented as the mean ± SEM, and probability determined using a one-way ANOVA (**** $P < 0.0001$ vs DMSO).

4.3 The contribution of endoplasmic Ca^{2+}

Although the BAPTA-dependent impairment of TfR trafficking implies that local Ca^{2+} is important for regulation, it does not specify where the local Ca^{2+} is generated. The following subsections detail the various approaches which were used to establish if the largest intracellular Ca^{2+} store, the ER, exits as the compartmental Ca^{2+} source which drives TfR trafficking.

4.3.1 Mechanistic demonstration of SERCA inhibition

The first approach used to investigate the involvement of the ER Ca^{2+} store in TfR trafficking was through depletion of luminal ER Ca^{2+}. SERCA pumps actively transport Ca^{2+} into the ER to replenish luminal Ca^{2+} stores and balance the passive leak of Ca^{2+} (5). SERCA-selective inhibitors, such as thapsigargin and cyclopiazonic acid (CPA) (315), disrupt the Ca^{2+} pump-leak equilibrium maintained by SERCA-mediated Ca^{2+} transport, resulting in net efflux and the eventual depletion of ER luminal Ca^{2+}. To assess the status of ER Ca^{2+} depletion following preincubation of SERCA inhibitors, the Ca^{2+} ionophore ionomycin was applied to HeLa cells to rapidly mobilise and release ER Ca^{2+} independently of channels (316). Following the addition of thapsigargin or CPA, a gradual rise in cytosolic Ca^{2+} was observed (Figure 4.3), representative of the passive leak of Ca^{2+} from the ER. In comparison to control cells, where ionomycin produced a large transient Ca^{2+} response, the Ca^{2+} response in cells pre-incubated with thapsigargin or CPA was essentially eliminated (Figure 4.3), indicating that ER Ca^{2+} stores were depleted.

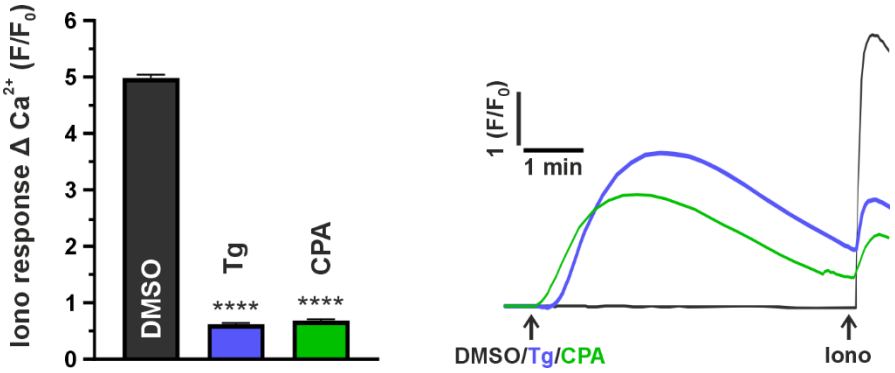

Figure 4.3: Confirmation of ER Ca^{2+} depletion. In Ca^{2+}-free medium, incubation with 1 µM thapsigargin (Tg) or 30 µM cyclopiazonic acid (CPA) depletes ER Ca^{2+} stores. Response summary data and representative Ca^{2+} traces measured using Fluo-8H are shown for ionomycin (iono) mobilisation of ER Ca^{2+} stores, n = 180-451 cells. Data are presented as the mean ± SEM, and probability determined using a one-way ANOVA (**** $P < 0.0001$ vs DMSO).

4.3.2 ER Ca^{2+} depletion

The preliminary investigation above offered insights into the rate of ER Ca^{2+} depletion within HeLa cells, providing a foundation which was subsequently used to investigate the importance of ER Ca^{2+} in the context of TfR trafficking. These experiments were conducted in Ca^{2+}-free medium (supplemented with 100 μM EGTA) to eliminate the complications of store-operated Ca^{2+} entry following ER Ca^{2+} emptying (15). Interestingly, depleting ER Ca^{2+} stores with either thapsigargin, or CPA, did not impair transferrin trafficking (Figure 4.4). Although a marginal (~10%) increase in transferrin trafficking was observed, this was insignificant relative to the DMSO control. Similarly, transferrin trafficking was unaffected following the removal of extracellular Ca^{2+} (Figure 4.4), suggesting a nonessential role for Ca^{2+} influx. Through emptying of ER Ca^{2+} stores, these results confirm that neither ER-mediated Ca^{2+} release, nor extracellular Ca^{2+} influx, are involved in mediating TfR internalisation and trafficking.

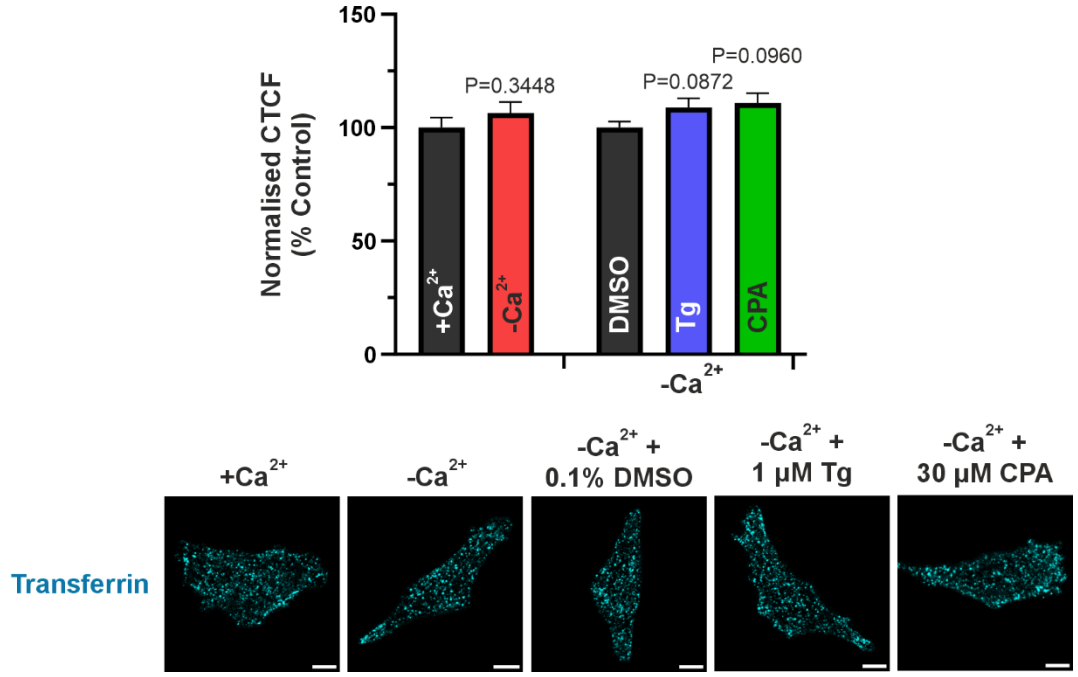

Figure 4.4: ER Ca^{2+} stores do not support TfR trafficking. The removal of extracellular Ca^{2+} ($-Ca^{2+}$), or depletion of ER Ca^{2+} using thapsigargin (Tg, 1 µM) or cyclopiazonic acid (CPA, 30 µM) does not affect transferrin trafficking, n = 49-116 cells. Representative images of transferrin in each condition, scale bars = 10 µm. Data are presented as the mean ± SEM, and probability determined using a one-way ANOVA (**** $P < 0.0001$ vs $+Ca^{2+}$ or DMSO).

4.3.3 ER-mediated Ca^{2+} release

Complimentary to ER Ca^{2+} depletion, the importance of ER Ca^{2+} in regulating TfR trafficking was also investigated using a second, more pharmacologically-driven approach. To explore the role of ER-mediated Ca^{2+} signals in the transferrin cycle, it was investigated whether experimentally-induced ER Ca^{2+} release could rescue the transferrin trafficking defect which occurs in *TPCN1* knockout cells (Figure 3.4). Pharmacological compounds were simultaneously applied to both HeLa wildtype and *TPCN1* knockout cells alongside transferrin and in the absence of extracellular Ca^{2+}, to stimulate ER-mediated Ca^{2+} release. ER Ca^{2+} efflux was induced in three different ways: activation of G_q-coupled H1 receptors using histamine to initiate CICR from IP_3Rs, through the mobilisation of ER Ca^{2+} using

ionomycin, or by increasing the passive leak of Ca^{2+} following the addition of thapsigargin or CPA. As shown in Figure 4.5, all four of the aforementioned compounds failed to restore transferrin internalisation and trafficking in *TPCN1* knockout cells, despite these compounds previously displaying substantial Ca^{2+} release or mobilisation from the ER (Figure 4.1B and Figure 4.3). These results further exclude a role for the ER Ca^{2+} store in TfR trafficking and also suggest that global Ca^{2+} signals initiated by ER-mediated Ca^{2+} release are insignificant.

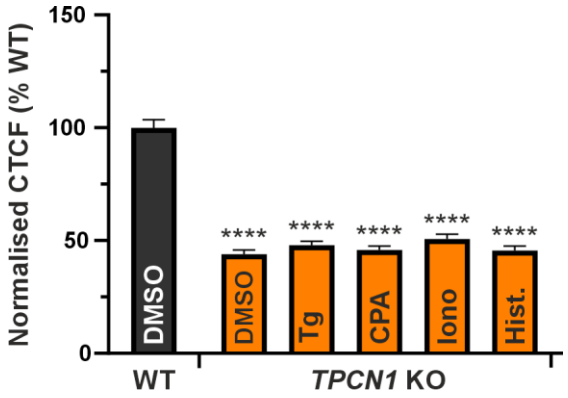

Figure 4.5: ER-induced Ca^{2+} release cannot restore TPC1-dependent TfR trafficking. Stimulation of ER Ca^{2+} release in Ca^{2+}-free medium (supplemented with 100 µM EGTA) using the small molecules thapsigargin (Tg, 1 µM), cyclopiazonic acid (CPA, 30 µM), ionomycin (iono, 1 µM), or histamine (Hist., 50 µM), alongside the simultaneous addition of transferrin, cannot restore the transferrin trafficking defect in HeLa *TPCN1* KO cells relative to WT stimulation, n = 70-80 cells. Data are presented as the mean ± SEM, and probability determined using a one-way ANOVA (**** $P < 0.0001$ vs WT).

In parallel experiments, the same methodology was used to investigate if Ca^{2+} efflux from endosomes could rescue the *TPCN1* knockout transferrin trafficking defect. Due to the unavailability of TPC1-selective activators, it was chosen to stimulate Ca^{2+} release from the recycling endosomal channel TRPML2 (198). TRPML2 was activated using the selective agonist ML2-SA1 (197), which was shown to evoke efficacious Ca^{2+} release from TRPML2-positive recycling endosomes (Figure 4.6A). Surprisingly, despite sharing

a similar compartmental localisation to TPC1, TRPML2-mediated Ca^{2+} release from recycling endosomes was unable to rescue transferrin trafficking in TPC1-deficient cells (Figure 4.6B). Only when ionomycin was applied to cells alongside transferrin in the presence of extracellular Ca^{2+}, to mobilise both ER and extracellular Ca^{2+}, and produce a supraphysiological cellular Ca^{2+} response, was the transferrin trafficking defect partly restored by approximately 40% (Figure 4.6B). Taken together, these findings provide strong evidence that ER Ca^{2+} does not regulate transferrin trafficking.

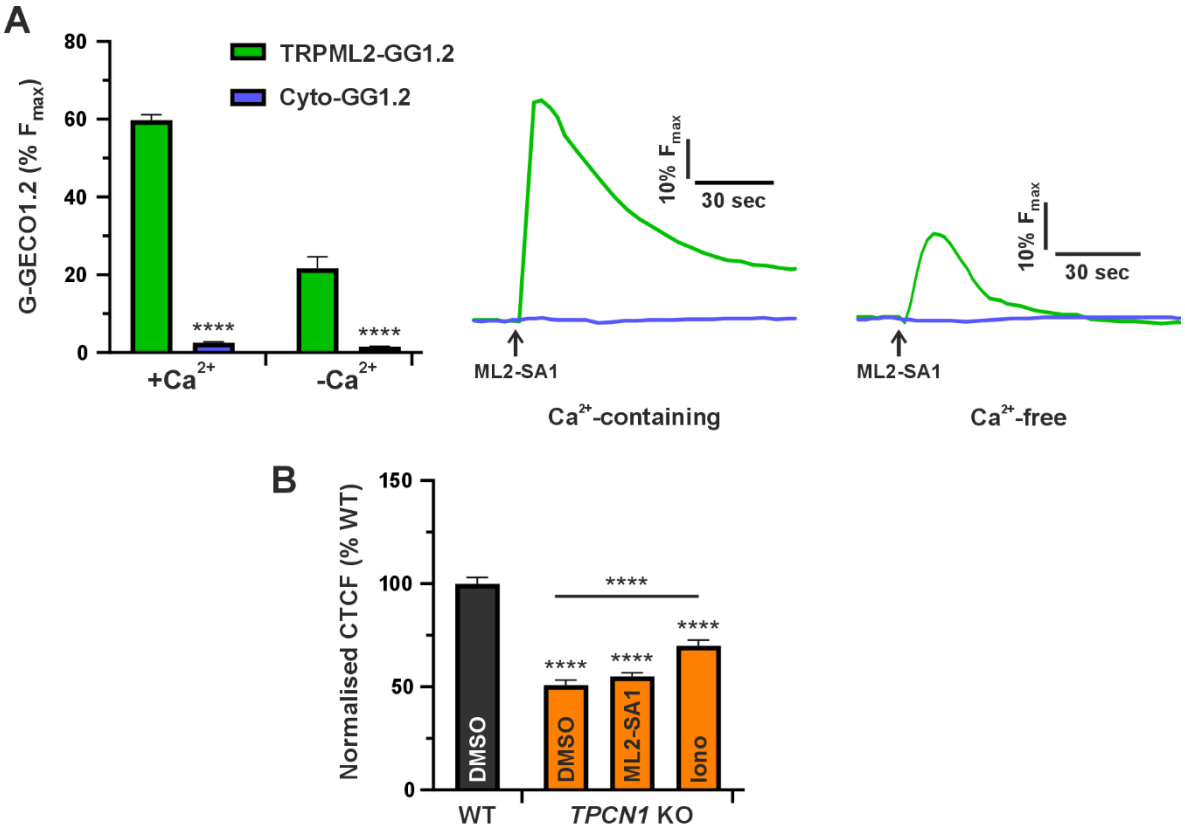

Figure 4.6: ML2-SA1 induced Ca^{2+} release via endosomal TRPML2. (A) Summary Ca^{2+} responses and representative Ca^{2+} traces from HeLa cells expressing either TRPML2 (in green) or cytosolic (cyto, in blue) G-GECO1.2 fusion proteins, in response to ML2-SA1 (30 µM). Experiments were conducted in either Ca^{2+}-containing, n = 101-158 cells, or Ca^{2+}-free media, n = 46-102 cells. **(B)** In Ca^{2+}-containing medium, only a strong global Ca^{2+} stimulus triggered using ionomycin (ER + Ca^{2+} influx) can partly restore transferrin trafficking in HeLa *TPCN1* knockout (KO) cells relative to the same stimulus in wildtype (WT) cells, whilst the TRPML2 (recycling endosomes) selective agonist ML2-SA1 (30 µM) does not, n = 59-76 cells. Data are presented as the mean ± SEM, and probability determined using a one-way ANOVA (**** $P < 0.0001$ vs TRPML2-GG1.2 or WT).

4.4 The contribution of endosomal Ca^{2+}

Whilst the above data implies that TfR trafficking is regulated by local Ca^{2+} signals, it also demonstrates that not all Ca^{2+} sources can support TfR trafficking. It appears that the transferrin cycle conveys selectivity for the source of Ca^{2+} required for efficient trafficking. Given that transferrin trafficking is dependent on TPC1 expression, it was hypothesised that the mildly acidic endosomal Ca^{2+} stores where TPC1 resides, represent the likely source of Ca^{2+} required for mediating transferrin trafficking.

4.4.1 Endo-lysosomal Ca^{2+} depletion

To initially evaluate whether endo-lysosomal Ca^{2+} is required for efficient transferrin trafficking, endo-lysosomal Ca^{2+} stores were depleted using the V-ATPase inhibitor bafilomycin-A1. As mentioned previously in section 1.1.3.2, bafilomycin-A1 inhibits the H^+-dependent mechanism of endo-lysosomal Ca^{2+} uptake, leading to net Ca^{2+} efflux and the depletion of endo-luminal Ca^{2+} (44,317). As a preliminary investigation to verify that endo-lysosomal Ca^{2+} stores were emptied following bafilomycin-A1 preincubation, endo-lysosomal alkalinisation was assessed using the proton-driven dye LysoTracker Green, as an indirect readout for Ca^{2+} depletion. Figure 4.7A shows that bafilomycin-A1 severely affected H^+ uptake within endo-lysosomes, as demonstrated by the disappearance of LysoTracker Green vesicles, an occurrence indicative of luminal alkalinisation (318). Based on the theorised H^+-dependent uptake of Ca^{2+}, these results tentatively suggest that bafilomycin-A1 preincubation depletes endo-lysosomal luminal Ca^{2+} stores. In the context of TfR trafficking, bafilomycin-A1 preincubation significantly reduced transferrin internalisation and trafficking compared to DMSO-treated control cells (Figure 4.7B). As

bafilomycin inhibits both the refilling of H^+ and Ca^{2+}, these results indicate that either the luminal pH, or Ca^{2+} of endo-lysosomes is vital for efficient TfR trafficking.

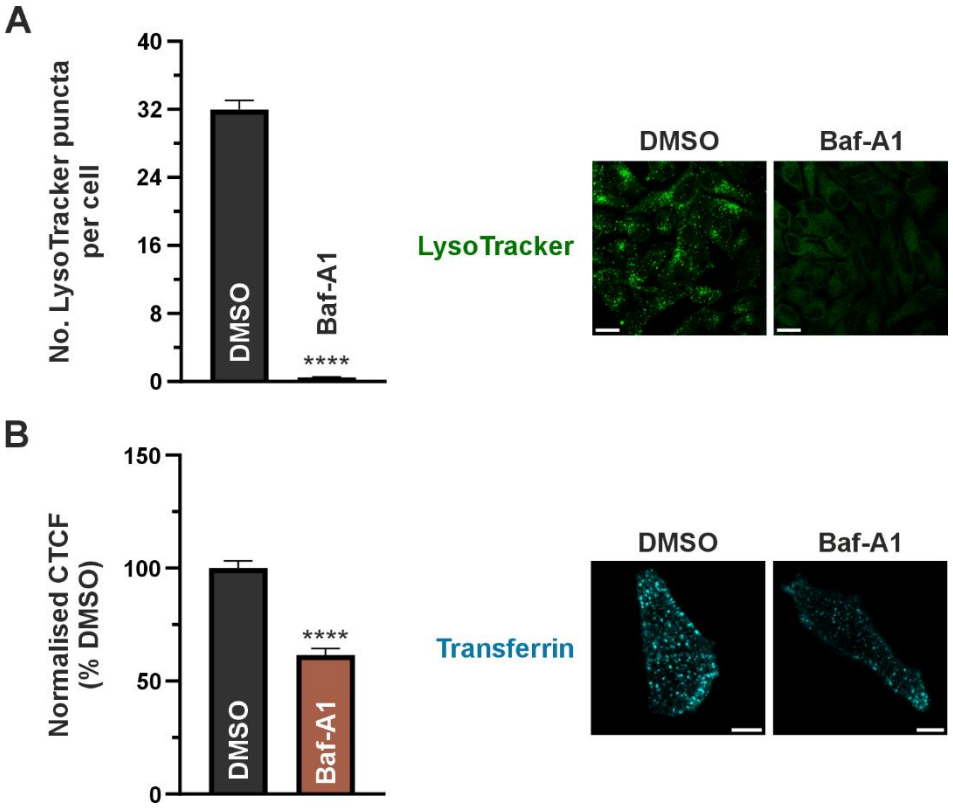

Figure 4.7: Depletion of endo-lysosomal Ca^{2+} stores. (A) Acidic organelle staining by LysoTracker Green (300 nM) is reduced following endo-lysosome alkalinisation by bafilomycin-A1 (Baf-A1, 1 µM), n = 235-245 cells. Representative images of LysoTracker Green staining following DMSO or Baf-A1 pretreatment, scale bars = 20 µm. **(B)** Emptying of endo-lysosomal Ca^{2+} stores using Baf-A1 impairs transferrin trafficking, n = 49-60 cells. Representative images of transferrin in each condition, scale bars = 10 µm. Data are presented as the mean ± SEM, and probability determined by a two-tailed t-test (**** $P < 0.0001$ vs DMSO).

4.4.2 Endosomal luminal Ca^{2+} chelation

To more definitively establish if endosomal Ca^{2+} stores are required for regulating TfR trafficking, a complementary strategy to Ca^{2+} depletion was adopted, which involved chelating Ca^{2+} within the lumen of endosomes. Ca^{2+} chelation was achieved using the Ca^{2+}-binding dextran Cal-520 dextran (K_d ~320 nM at pH 7.2), which was loaded in excess to

saturate the Ca^{2+}-reporter and ensure maximal luminal Ca^{2+} chelation. Figure 4.8A shows Pearson's colocalisation data from the dextran pulse experiment, which was performed to ensure dextran was accumulating in TPC1-positive endosomal compartments. Dextran displayed the greatest colocalisation with TPC1 following a 60 minute incubation, with longer incubation periods resulting in decreased colocalisation (Figure 4.8A), suggesting that dextran was being trafficked to late endosomal and/or lysosomal compartments. Therefore, a 60 minute dextran incubation time was chosen for subsequent endosomal Ca^{2+} chelation experiments.

As shown in Figure 4.8B, chelation of endosomal Ca^{2+} with Cal-520 dextran significantly impaired transferrin trafficking, reducing the number of transferrin vesicles per cell by approximately 26%. As a positive control, a non-Ca^{2+}-binding dextran (cyanine-based fluorescent dextran, CF dextran) was incubated in HeLa cells in parallel to Cal-520 dextran. Importantly, transferrin trafficking was unaffected in the presence of CF dextran (Figure 4.8B), indicating that the observed trafficking impairment was a direct consequence of Ca^{2+} chelation and providing further evidence that endosomal TPC1-positive Ca^{2+} stores regulate TfR trafficking.

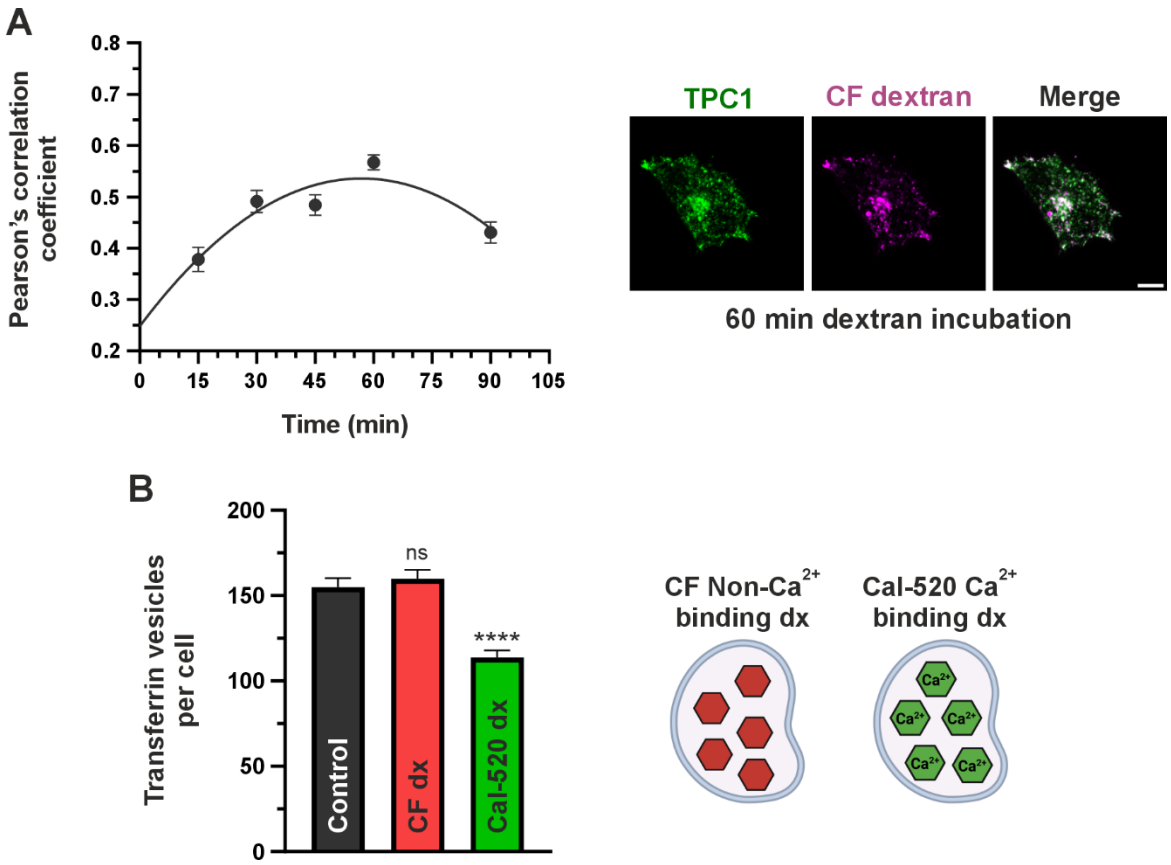

Figure 4.8: Endosomal luminal Ca^{2+} chelation. (A) Time-course incubation of 1 mg/ml CF dextran (cyanine-based fluorescent dextran) in wildtype HeLa cells overexpressing TPC1 tagged with mNeonGreen, n = 30-51 cells. Respective images shown for 60 minute dextran incubation, scale bar = 10 µm. **(B)** Chelating endosomal luminal Ca^{2+} using a Ca^{2+}-binding dextran (Cal-520 dx) chased to TPC1 compartments reduces TfR trafficking, whilst a non-Ca^{2+}-binding dextran (cyanine-based fluorescence, CF dx) does not, n = 75-77 cells. Cartoon depicting the two utilised dextran conjugates. Data are presented as the mean ± SEM, and probability determined using a one-way ANOVA (**** $P < 0.0001$, ns = not significant vs control).

4.4.3 Buffering of endosomal Ca^{2+} nanodomains

Although the findings above are independent sources of evidence that highlight the importance of local Ca^{2+} domains and endosomal luminal Ca^{2+} in regulating TfR trafficking, these experiments did not directly implicate local endosomal Ca^{2+}. Therefore, a targeted strategy was used to examine the plausible requirement of local endosomal Ca^{2+} domains within the transferrin cycle. To investigate the involvement of local peri-

endosomal Ca^{2+} in TfR trafficking, a custom-designed chemically-induced dimerization system was developed to selectively and acutely buffer endosomal Ca^{2+} nanodomains. This approach was an adaptation of the strategy utilised by Davis *et al*., which successfully buffered lysosomal Ca^{2+} nanodomains (81). The adapted strategy exploited the dimerization properties of the FK506-binding protein 12 (FKBP12) and the FKBP-rapamycin-binding (FRB*) domain, to which the Ca^{2+}-binding protein calbindin-2 (CB) and TPC1 were respectively fused. As illustrated in Figure 4.9A, it was hypothesised that the addition of the rapamycin-derived rapalog AP21967 would result in the acute translocation of two tandem copies of CB to the surface of TPC1-positive compartments, subsequently buffering local peri-endosomal Ca^{2+} nanodomains. Unlike rapamycin, AP21967 does not inhibit mTOR, which excludes the complication of mTOR effects on TPC activity (137,164).

To verify that the FKBP12-FRB* system was functional, rapamycin-induced dimerization was monitored in HeLa wildtype cells transiently co-expressing the FKBP12-CB and TPC1-FRB* fusion proteins. Application of rapamycin resulted in the immediate translocation of cytosolic CB to TPC1 puncta, as demonstrated by the acute increase in Pearson's correlation compared to the addition of DMSO (Figure 4.9B). Similarly, rapalog preincubation significantly increased the colocalisation of TPC1 and CB by approximately 3.5-fold (Figure 4.9C), confirming the successful dimerization of FKBP12-FRB* and CB translocation to the surface of TPC1-positive endosomes.

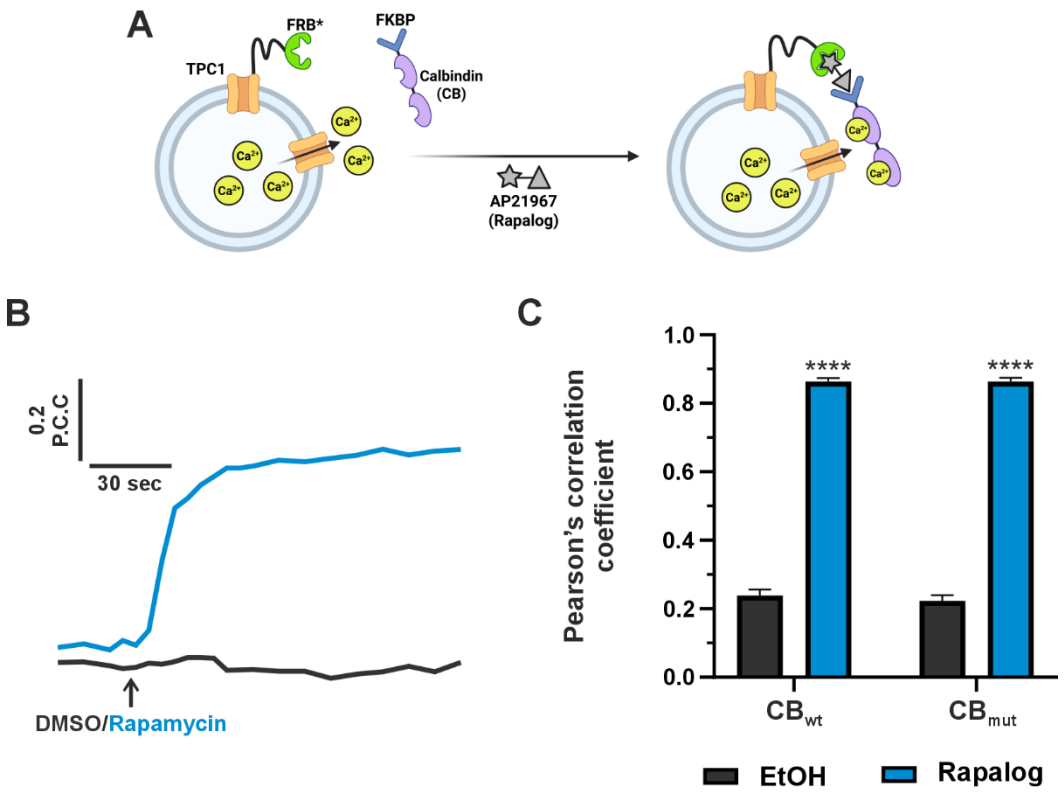

Figure 4.9: Calbindin translocation to TPC1-positive endosomes. (A) Illustration of the rapalog dimerization system (FKBP12/FRB*) used to acutely translocate two tandem copies of the calbindin-2 (CB) Ca^{2+}-binding protein to TPC1 compartments to buffer peri-endosomal Ca^{2+} domains. **(B)** Representative Pearson's correlation coefficient (P.C.C) traces of rapamycin-induced (1 µM) CB translocation to TPC1-positive endosomes. **(C)** Translocation of wildtype CB (CB_{wt}) or a non-Ca^{2+}-binding CB mutant (CB_{mut}) tagged with FKBP12-mStayGold to the surface of TPC1 mScarlet-I-FRB*-tagged compartments following preincubation with 250 nM rapalog was confirmed by an increase in the P.C.C compared to ethanol (EtOH)-treated cells, n = 42-54 cells. Data are presented as the mean ± SEM, and probability determined by a two-tailed t-test (**** $P <$ 0.0001 vs EtOH).

When this system was implemented into the established transferrin trafficking assay, trafficking was unaffected when CB_{wt} remained in the cytosol during the EtOH control. However, when CB_{wt} was translocated to TPC1-positive endosomes by AP21967 pretreatment, transferrin trafficking was severely impaired (Figure 4.10A). To control for potential steric effects caused by protein overcrowding, a non-Ca^{2+}-binding mutant of CB (CB_{mut}), in which all five EF-hand motifs were rendered non-functional (319), was

expressed in parallel experiments alongside CB_{wt}. In contrast, translocation of CB_{mut} to TPC1-positive endosomes showed no apparent effect on transferrin trafficking (Figure 4.10A), indicating that the observed CB_{wt} trafficking impairment was attributable to Ca^{2+} buffering. To complement these data, transferrin internalisation and trafficking was monitored across several time intervals to assess the kinetics of trafficking during peri-endosomal Ca^{2+} buffering. Figure 4.10B indicates that TPC1 peri-endosomal Ca^{2+} buffering reduces the rate of internalisation and trafficking, as shown by a decrease in the number of transferrin vesicles across all incubation periods. These experimental outcomes strongly suggest that local endosomal Ca^{2+} nanodomains, likely generated by TPC1-mediated Ca^{2+} efflux, are crucial for TfR internalisation and trafficking.

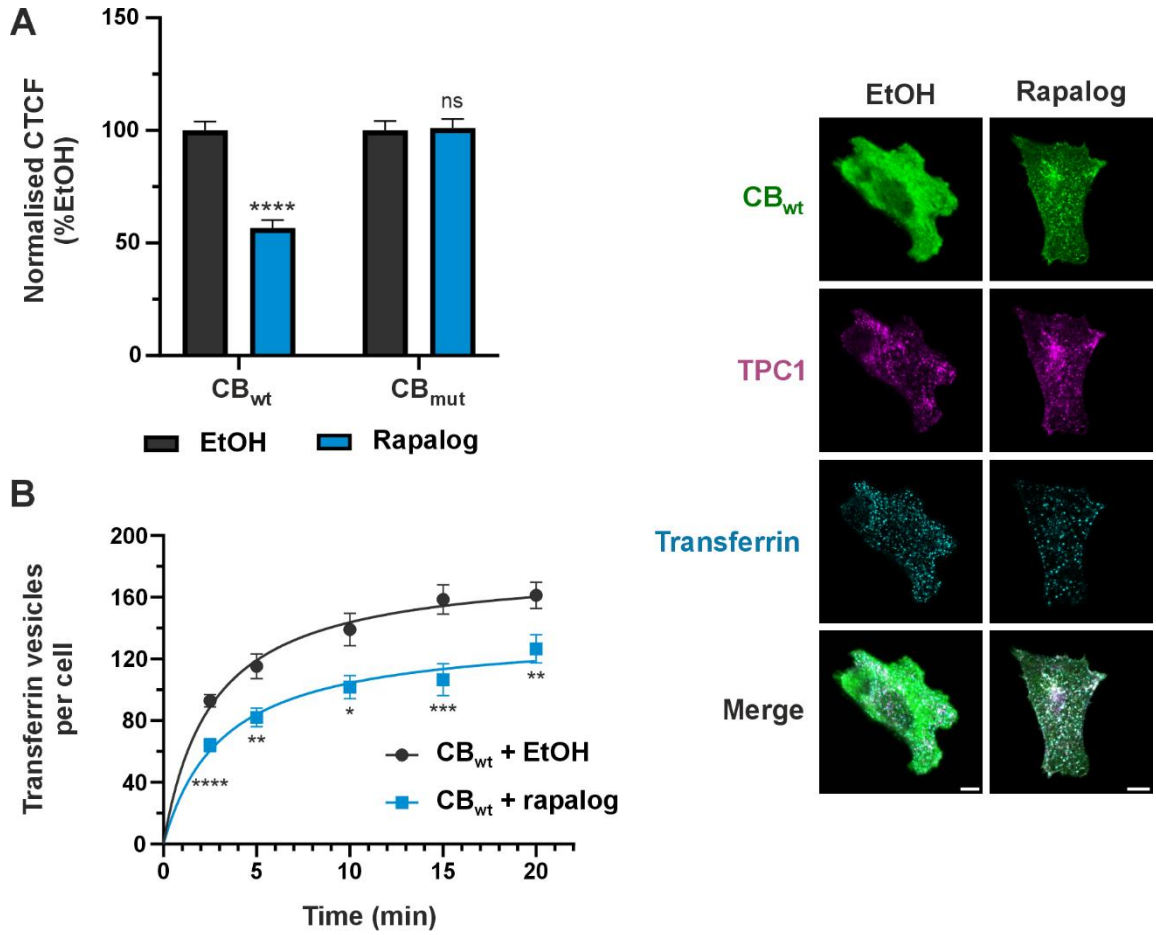

Figure 4.10: Peri-endosomal Ca^{2+} buffering impairs TfR trafficking. (A) Rapalog-induced translocation of calbindin (CB_{wt}) tagged with FKBP12-mStayGold (in green) to the surface of TPC1 mScarlet-I-FRB*-tagged compartments (in magenta) inhibits transferrin trafficking. Cytosolic CB_{wt} or translocation of a non-Ca^{2+}-binding CB mutant (CB_{mut}) does not impair trafficking, n = 70-76 cells. Representative images of the CB_{wt} condition, scale bars = 10 µm. **(B)** Time course of transferrin uptake and trafficking during acute TPC1 compartmental Ca^{2+} buffering by CB_{wt}, n = 24-31 cells. Data are presented as the mean ± SEM, and probability determined using a one-way ANOVA or two-tailed t-test (**** $P < 0.0001$, *** $P < 0.001$, ** $P < 0.01$, * $P < 0.05$, ns = not significant vs EtOH).

4.5 Estimation of early endosomal Ca^{2+} concentration

Whilst acidic organelles represent established Ca^{2+}-containing organelles, the Ca^{2+} concentration of mildly acidic endosomes is uncertain and has only been assessed in limited cell types. Given the apparent requirement of endosomal Ca^{2+} nanodomains for TfR trafficking, it was considered appropriate to estimate the luminal [Ca^{2+}] of endosomes

in HeLa cells. To cover a wide range of possible Ca^{2+} concentrations, HeLa cells were loaded with the Ca^{2+} indicator Cal-520, conjugated to dextran as a high affinity (K_d ~320 nM) or low affinity (Cal-520L, K_d ~90 μM) variant. Unfortunately, Cal-520L dextran was not internalised into cells, instead accumulating on the plasma membrane, as shown in Figure 4.11. This distribution was not a consequence of the loading procedure, since both Cal-520 dextran and Texas-Red dextran, the latter co-loaded with Cal-520L dextran, was readily internalised (Figure 4.11). As the Cal-520L dextran background labelling made quantifying the endosomal luminal $[Ca^{2+}]$ impossible, subsequent measurements were performed using Cal-520 dextran.

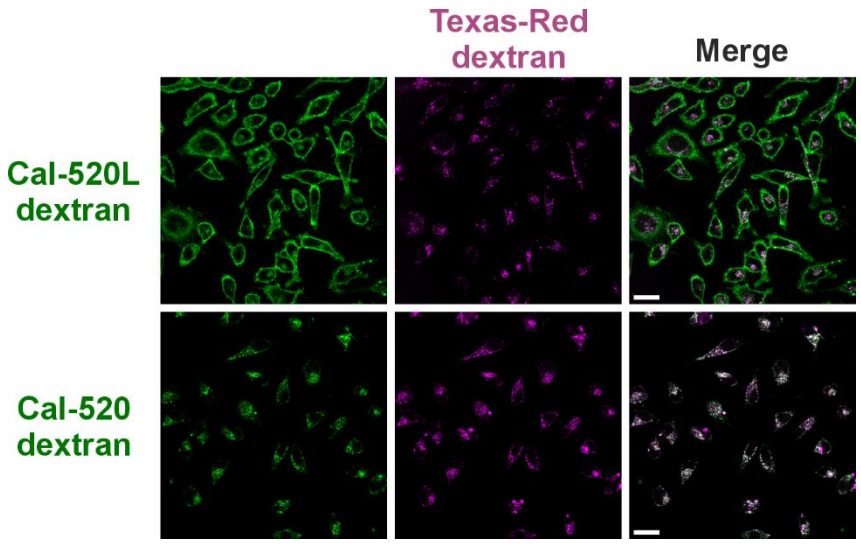

Figure 4.11: Images of Cal-520L dextran and Cal-520 dextran vesicle labelling. Cal-520L dextran, or Cal-520 dextran (0.5 mg/ml) co-loaded with Texas-Red dextran (0.5 mg/ml) in HeLa cells, scale bars = 30 μm.

Since the calculation used to determine the $[Ca^{2+}]$ is a direct function of the Ca^{2+} reporter K_d (see equation 2, section 2.6.2), it was first important to assess if the pH of endosomes, or the conjugation to dextran, affected the K_d of Cal-520. The Ca^{2+} affinity of Cal-520 dextran was determined at endosomal pH 6.7 by clamping the free $[Ca^{2+}]$ to a range of

values using different ratios of total Ca^{2+} and Ca^{2+} chelators. Specifically, the Ca^{2+} chelators EGTA or HEDTA were used to cover the nM, or μM range of free [Ca^{2+}] respectively. Figure 4.12A shows the Ca^{2+} dissociation curves for Cal-520 dextran obtained from EGTA, or HEDTA Ca^{2+} buffering in pH 6.7 medium. Astonishingly, the determined K_d of Cal-520 dextran was 1.36 μM and 8.31 μM for EGTA and HEDTA conditions respectively, drastically lower than the manufacturer's reported K_d value of 320 nM at pH 7.2. As a positive control to verify the accuracy of solutions, the same experiment was performed using the free acid form of Fluo-3 (K_d ~390 nM). When Ca^{2+} was buffered with EGTA, a K_d of 571 nM was determined for Fluo-3 (Figure 4.12B), marginally lower than manufacturer estimations. This small reduction likely reflects the lower pH (6.7) used when obtaining these measurements. These findings reassure that the above Ca^{2+} affinities determined for Cal-520 dextran were genuine. As the Cal-520 dextran K_d values fall within the effective μM buffering range of HEDTA, the predetermined K_d value of 8.31 μM (Figure 4.12A) was used for the future calculation of endosomal luminal Ca^{2+} concentrations.

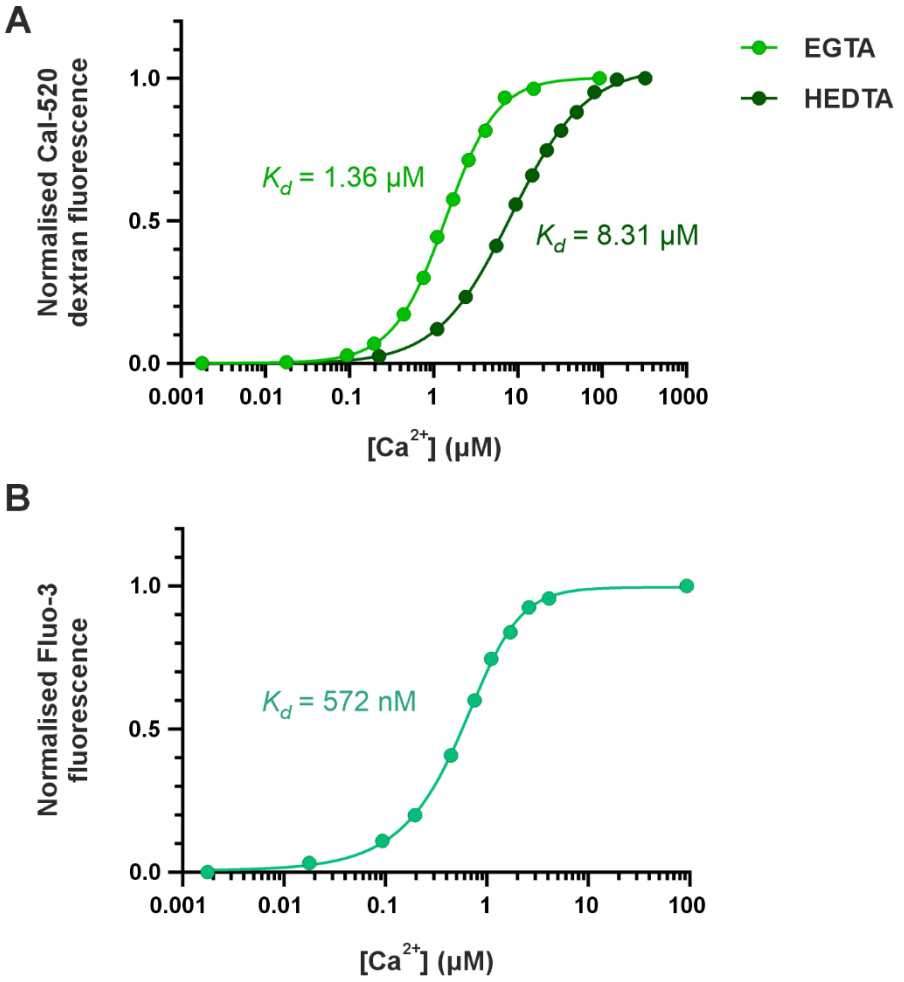

Figure 4.12: Ca^{2+}-binding affinity of Cal-520 dextran and Fluo-3. (A) The Ca^{2+} affinity (K_d) of Cal-520 dextran (1 μM) at endosomal pH 6.7, determined using different ratios of total Ca^{2+} and the Ca^{2+} chelators EGTA (5 mM) or HEDTA (5 mM). **(B)** The affinity of Fluo-3 (1 μM, free acid) at endosomal pH 6.7 determined using EGTA. Data are presented as the mean ± SEM.

To estimate the early endosomal luminal [Ca^{2+}], Cal-520 dextran was incubated in HeLa wildtype cells for varying time intervals. To account for uneven dextran loading, Cal-520 dextran signals were normalised to a Ca^{2+}-insensitive fluorescent dextran. As shown in Figure 4.13, the calculated endosomal luminal [Ca^{2+}] was 10.29 ± 0.42 μM and 12.35 ± 3.49 μM after a 5 or 10 minute dextran incubation respectively. After a longer 20 minute incubation, the endosomal Ca^{2+} concentration had decreased to 3.77 ± 1.01 μM, a reduction that supports the premise that early endosomal acidification facilitates the rapid

loss of luminal Ca^{2+} (320). Alongside basal measurements, endosomal luminal [Ca^{2+}] was quantified in the absence of extracellular Ca^{2+} (Ca^{2+}-free medium + 100 µM EGTA) after an additional 10 minute incubation, the same protocol used to investigate the requirement of extracellular Ca^{2+} for TfR trafficking (Figure 4.4). Removal of extracellular Ca^{2+} significantly reduced endosomal luminal [Ca^{2+}] across all dextran incubation times (Figure 4.13), indicating that endosomal Ca^{2+} stores were starting to deplete after the additional 10 minutes. Taken together, these findings show that early endosomes represent a small but critical compartmental source of intracellular Ca^{2+}.

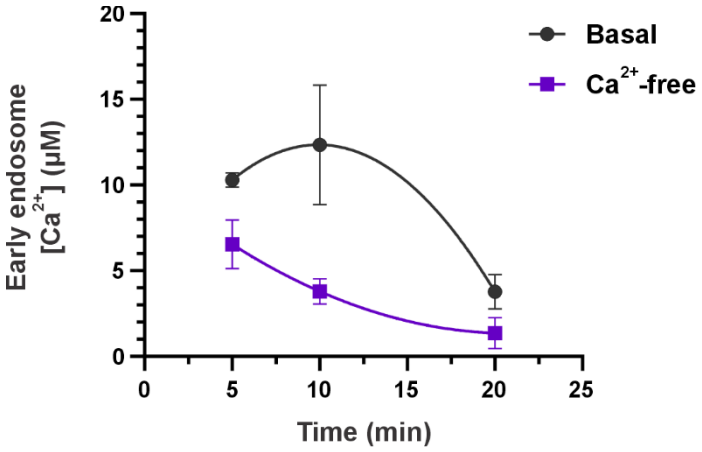

Figure 4.13: Early endosomal luminal Ca^{2+} concentration. Calculation of the early endosomal free [Ca^{2+}] using the Ca^{2+}-sensitive Cal-520 dextran (0.5 mg/ml), normalised to the Ca^{2+}-insensitive Texas-Red dextran (0.5 mg/ml), under basal conditions or after an additional 10 minute incubation at 4ºC in Ca^{2+}-free medium, $N = 4$ replicates, $n = 237$-422 cells. Data presented as the mean ± SEM.

4.6 Early endosomal pH

Ligand release from receptors is dependent on the acidity of the endosomal lumen, the pH of which is primarily determined by the activity of V-ATPase transmembrane pumps (224). Given the criticality of the early endosome pH for iron release from transferrin, it was investigated whether the resting endosomal luminal pH was altered in TPC1-deficient

cells, as this could provide a logical explanation as to why TfR trafficking was impaired in *TPCN1* knockout cells (Figure 3.4). The absolute luminal pH of early endosomes was quantified using the pH-sensitive reporter pHrodo-Red, which was conjugated to human transferrin. To ensure the precise measurement of early endosome pH, prior to pH measurements, transferrin was incubated for variable periods and colocalised with the early endosomal-associated protein Rab5. As judged by Pearson's correlation, a longer transferrin incubation period increased the colocalisation between transferrin and Rab5 (Figure 4.14). After 30 minutes, the degree of colocalisation tapered towards a plateau, indicating the maximal accumulation of transferrin in early endosomes. Thus, a 30 minute transferrin incubation period was chosen to proceed with, for measuring early endosome pH.

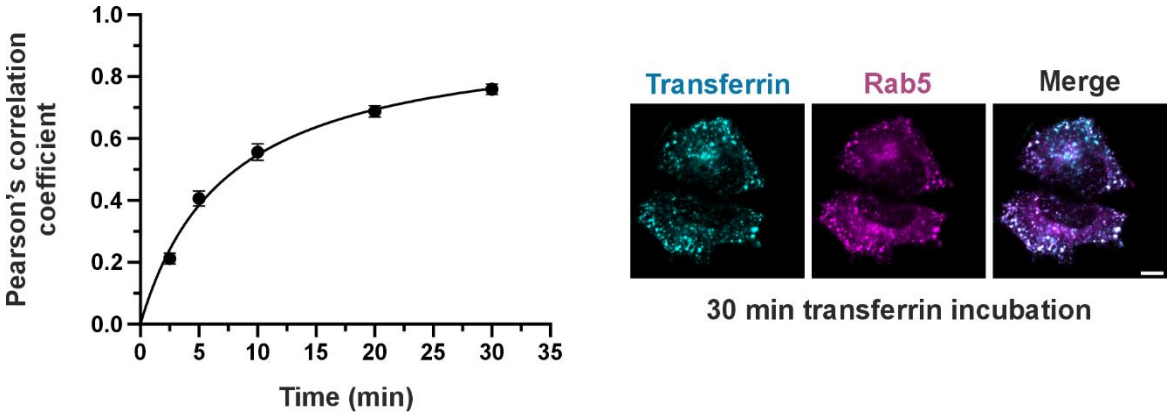

Figure 4.14: Time course of transferrin uptake into early endosomes. Varying incubation periods of transferrin in HeLa cells, colocalised to an mScarlet-I-tagged Rab5 protein. Representative images shown for transferrin (in cyan) and Rab5 (in magenta), following a 30 minute transferrin incubation, scale bar = 10 μm. Data are presented as the mean ± SEM.

To mitigate against misinterpreting altered pHrodo-Red transferrin signals simply as a function of reduced transferrin uptake and trafficking in TPC1-deficient cells, pH measurements were performed ratiometrically against the pH-insensitive Alexa 488

transferrin conjugate. As the effect of TPC1 deletion on the composition and buffering capacity of early endosomes is unknown, individual calibration curves were produced for both wildtype and *TPCN1* knockout cells from known pH standards (Figure 4.15A). Interpolation of fluorescence ratio signals indicated that deletion of TPC1 did not affect the resting pH of early endosomes, as shown by the recorded pH values of 6.69 ± 0.03 and 6.71 ± 0.02 for wildtype and *TPCN1* knockout early endosomes respectively (Figure 4.15B). These results suggest that TPC1 does not contribute to early endosomal pH regulation, at least not in the HeLa cell system.

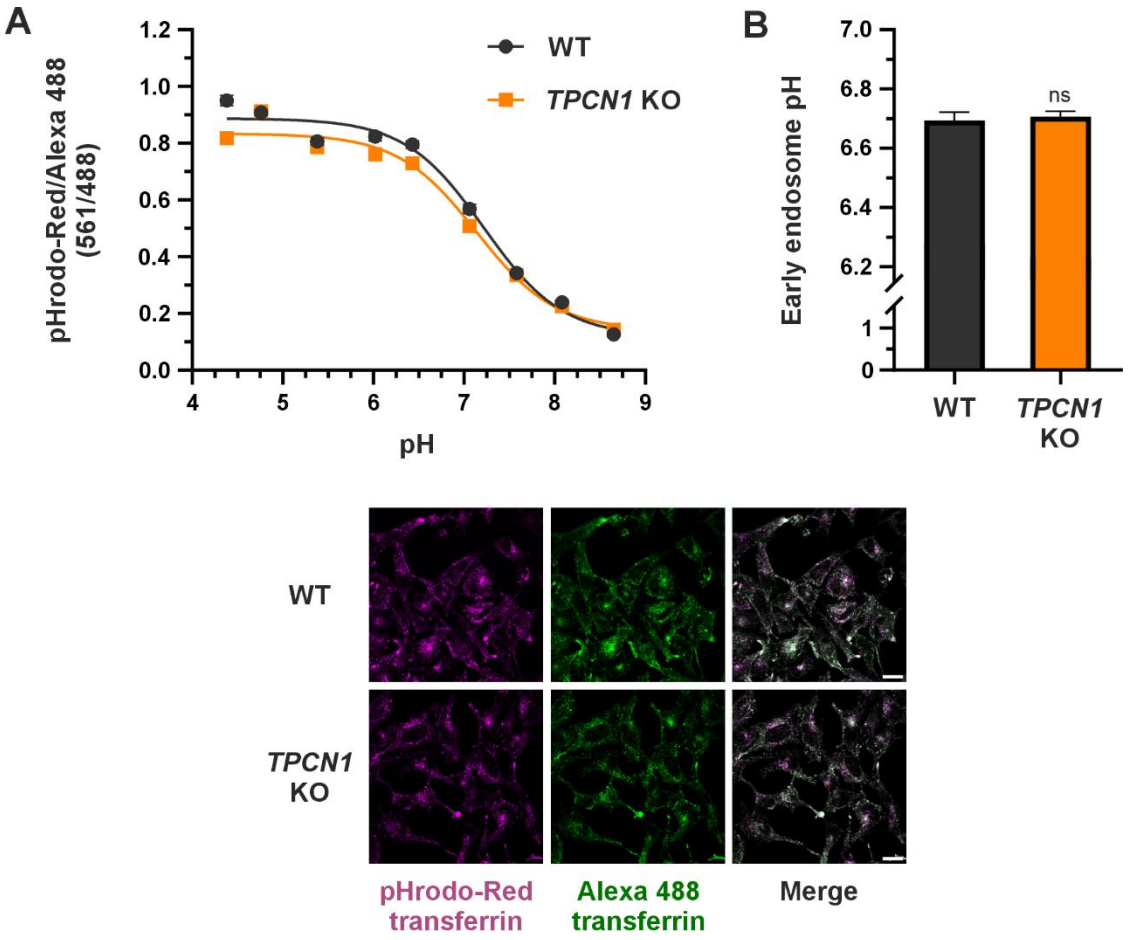

Figure 4.15: Early endosomal pH in TPC1-deficient cells. (A) Early endosomal pH sigmodal calibration curves for pH measurements performed in HeLa wildtype (WT) and *TPCN1* knockout (KO) cells. Luminal endosomal pH was equilibrated with the extracellular pH using a panel of high-K^+ pH solutions, each at a different pH in the presence of the H^+/K^+ ionophore nigericin (10 µM) and the K^+-ionophore, valinomycin (10 µM). Curves were fitted to transferrin pHrodo-Red fluorescence values normalised to transferrin Alexa 488 fluorescence. R^2 for WT cells is 0.927, R^2 for *TPCN1* KO cells is 0.948. **(B)** Early endosomal pH values in WT and *TPCN1* KO HeLa cells were determined by interpolation of endogenous pHrodo-Red/Alexa 488 fluorescence ratios against the respective calibration curves in A, *n* = 165-186 cells. Respective images of transferrin pHrodo-Red (in magenta) and transferrin Alexa 488 (in green) are shown for WT and *TPCN1* KO cells, scale bars = 20 µm. Data are presented as the mean ± SEM, and probability determined by a two-tailed t-test (ns = not significant vs WT).

4.7 TPC1 cation selectivity

4.7.1 Design of Na^+-deficient mutant

Until now, the experiments in this chapter have focused on establishing if local endosomal Ca^{2+} is an essential mediator of the TPC1-dependent transferrin cycle. Although Ca^{2+} appears to have a dominant role within the transferrin cycle, the accumulated evidence does not directly certify the need for TPC1-mediated Ca^{2+} signals. Additionally, it is unclear if dominant TPC1-mediated Na^+ fluxes contribute to the regulation of TfR trafficking (106,122). To address these uncertainties and more directly determine which TPC1 cation is required for mediating TfR trafficking, the selectivity filter of TPC1 was examined as a possible means of manipulating TPC1 permeability.

As displayed in Figure 1.3, the selectivity filter of *Hs*TPC1 and *Hs*TPC2 is functionally identical, with both isoforms achieving Na^+-selectivity using the same structural mechanism (106,107). Mutation of *Hs*TPC2 filter residues to the equivalent filter residues essential for determining the Ca^{2+}-selectivity of *At*TPC1 (*Hs*TPC2$^{A272S/V652M/N653G}$) abolishes *Hs*TPC2 Na^+-selectivity, whilst enhancing Ca^{2+}-selectivity (107). As both the filter region and key residues which determine cation selectivity are conserved between TPC isoforms, it was hypothesised that a TPC1 channel with the equivalent mutations (*Hs*TPC1$^{A280S/V646M/N647G}$) would also be Na^+-deficient. This mutant channel was named TPC1-mut3.

To verify that genetic modification did not affect the compartmental targeting of TPC1-mut3, the localisation of TPC1-mut3 was assessed against the known localisation of wildtype TPC1. Additionally, established markers of early and recycling endosomes (Rab5 and Rab11 respectively (204,205)), as well as the fluorescent protein mCherry targeted to the ER lumen by the C-terminal amino sequence KDEL, were co-transfected with TPC1-

mut3 in HeLa cells to determine the mutants localisation. As anticipated, TPC1-mut3 localised to TPC1-positive vesicles, as demonstrated by a strong Pearson's correlation with wildtype TPC1, Rab5, and Rab11 (Figure 4.16). Reassuringly, no correlation was observed between TPC1-mut3 and the ER, indicating that TPC1-mut3 was folded correctly and transported to early and recycling endosomes similar to wildtype TPC1 (116,117).

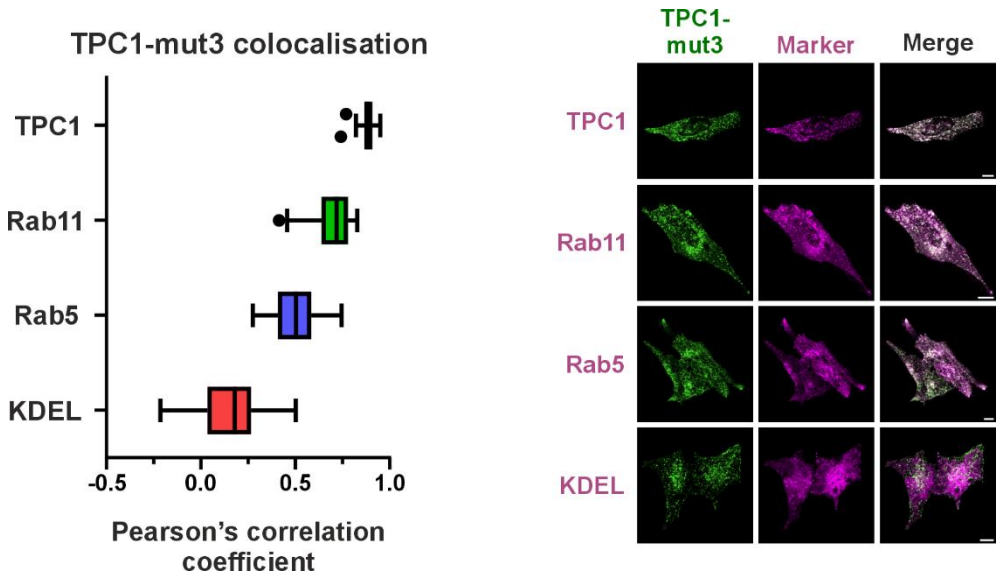

Figure 4.16: TPC1-mut3 colocalisation. Colocalisation of TPC1$^{A280S/V646M/N647G}$ (TPC1-mut3) tagged with mNeonGreen (in green), in respect to wildtype TPC1, recycling endosome marker Rab11, early endosome marker Rab5, all tagged with mScarlet-I (in magenta), and the fluorescent protein mCherry targeted to the ER lumen by the C-terminal endoplasmic reticulum retention amino sequence KDEL (in magenta). Colocalisation determined via Pearson's correlation coefficient, n = 30-42 cells. Representative images of each condition, scale bars = 10 µm.

4.7.2 TPC1-mut3 patch-clamp recordings

The following electrophysiology experiments were collaboratively performed by Alice Lin, of Prof. Cheng-Chang Chen's laboratory in Taiwan, and I. Whole-endosome patch-clamp experiments using vacuolin-enlarged endosomes isolated from either wildtype or TPC1-mut3 overexpressing HeLa cells were conducted to establish the cation selectivity of

TPC1-mut3. To directly determine the relative channel permeability to Na^+ and Ca^{2+}, the cation conductance evoked by $PI(3,5)P_2$ was measured under bi-ionic conditions (160 mM Na^+ in the cytosolic bath solution, pH 7.2; 105 mM Ca^{2+} in the luminal pipette solution, pH 6.15). As expected, wildtype TPC1 exhibited higher selectivity for Na^+ over Ca^{2+}, with an E_{rev} of approximately -49.3 mV, corresponding to a $P_{Na/Ca}$ permeability ratio of 16.2 (Figure 4.17). In marked contrast, TPC1-mut3 displayed a large reduction in Na^+ currents and a shift of the E_{rev} towards more positive values (E_{rev} approximately +53.3 mV), indicating a loss of Na^+-selectivity. Furthermore, this loss of Na^+-selectivity was also accompanied by a by an approximate 500-fold increase in Ca^{2+} permeability, as shown by the calculated $P_{Ca/Na}$ permeability ratio of 32.2 (Figure 4.17). These calculated permeability ratios provide evidence of a near complete loss of Na^+ permeability for TPC1-mut3, whilst retaining its Ca^{2+} fluxes.

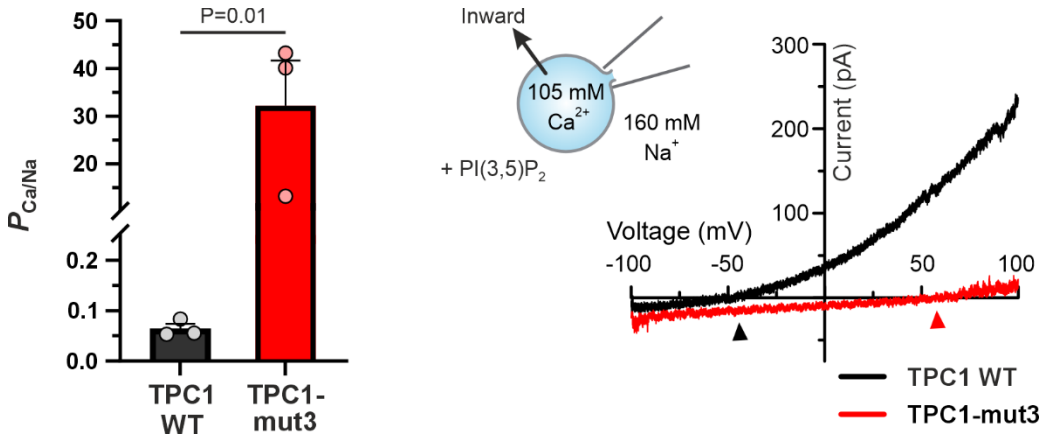

Figure 4.17: Bi-ionic characterisation of TPC1. Electrophysiological characterisation of $TPC1^{A280S/V646M/N647G}$ (TPC1-mut3) under bi-ionic conditions. The pipette solution contained 105 mM Ca^{2+} and the bath solution contained 160 mM Na^+. Permeability ratio ($P_{Ca/Na}$) of TPC1 wildtype (WT) and TPC1-mut3, $n = 3$ recordings. Representative I-V relationships of mNeonGreen-tagged TPC1 WT and TPC1-mut3 channels activated with 1 µM $PI(3,5)P_2$. Data are presented as the mean ± SEM, and probability determined by a two-tailed t-test.

As the magnitude of the TPC1-mut3-evoked currents in Figure 4.17 were small, one interpretation was that these residual recorded currents may have arisen from endogenous PI(3,5)P_2-sensitive endosomal channels, rather than from TPC1-mut3 itself. To investigate this possibility, additional endosomal patch-clamp recordings from enlarged endo-lysosomes of non-transfected HeLa cells were performed. At 1 μM PI(3,5)P_2, non-transfected cells showed negligible current responses (Figure 4.18A), indicating that endogenous background activity was minimal in this system at the concentration used. Additionally, in the presence of the TPC inhibitor tetrandrine, the residual PI(3,5)P_2-evoked TPC1-mut3 currents were strongly suppressed by approximately 2-fold (Figure 4.18B), indicating that these currents were TPC-dependent. Taken together, these findings strongly suggest that the small but reproducible recorded TPC1-mut3 current represents TPC1-mut3 channel activity rather than endogenous endosomal channel conductance.

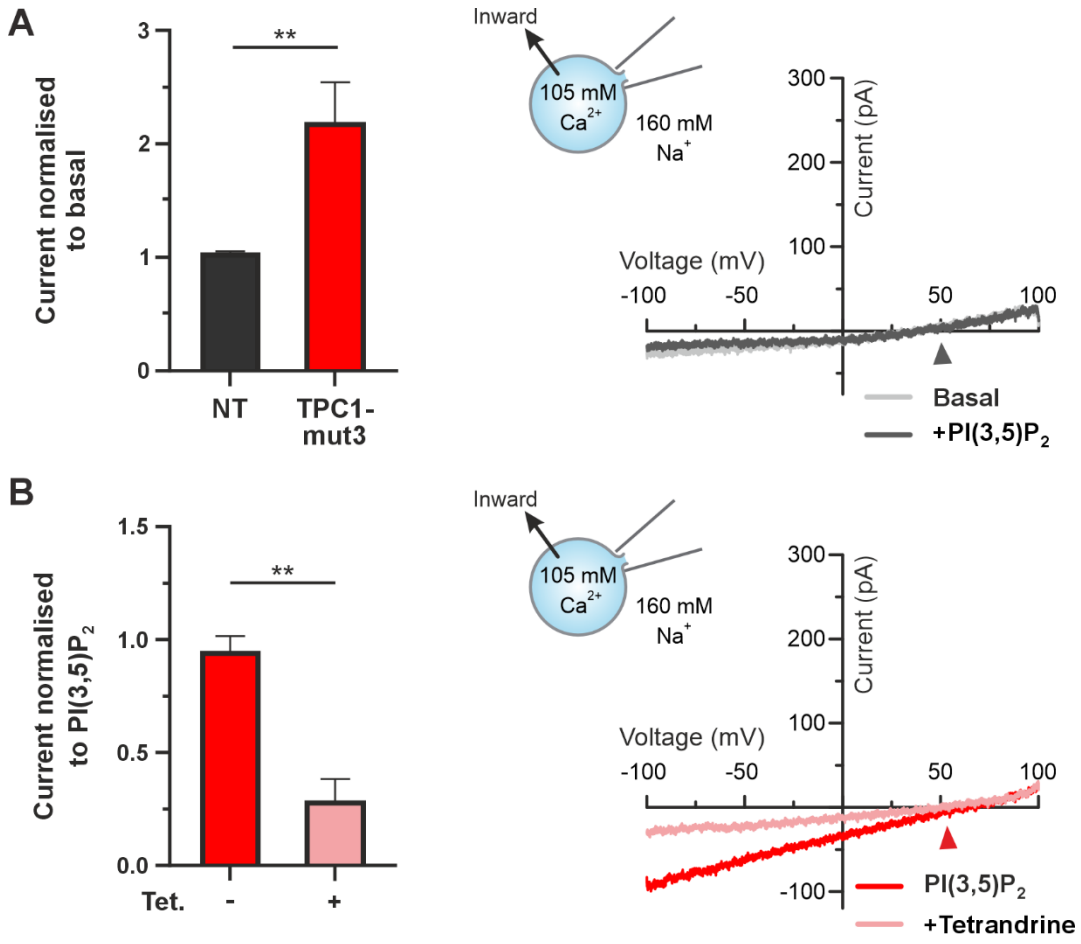

Figure 4.18: TPC1-mut3 channel currents. (A) Endogenous $PI(3,5)P_2$-sensitive currents are negligible in non-transfected HeLa endo-lysosomes. Quantification of current normalised to basal levels in non-transfected (NT) and TPC1-mut3-mNeonGreen-expressing vesicles, $n = 3$ recordings. Representative I–V relationships recorded from vacuolin-enlarged endo-lysosomes of non-transfected HeLa cells under basal conditions and after application of 1 µM $PI(3,5)P_2$. **(B)** Quantification of TPC1-mut3 currents normalised to $PI(3,5)P_2$-induced responses in the absence or presence of 100 µM tetrandrine (Tet.), $n = 3$ recordings. Representative I–V relationships recorded from TPC1-mut3-mNeonGreen-expressing endosomes in the presence of 1 µM $PI(3,5)P_2$, with or without 100 µM tetrandrine. Data are presented as the mean ± SEM and probability determined by a two-tailed t-test (** $P \leq 0.01$ vs control).

Although the permeability ratios from bi-ionic patch-clamp experiments indicate that TPC1-mut3 is indeed Na^+-deficient, they do not confirm an absolute loss of Na^+ permeability. To quantitatively and directly demonstrate the near-zero Na^+ permeability of TPC1-mut3, E_{rev}-shifts were measured across varying cytosolic [Na^+] gradients, in order to

estimate the Nernst slope for TPC1-mut3 versus wildtype TPC1. Whilst wildtype TPC1 displayed a linear slope of approximately -58 mV per decade, TPC1-mut3 channels exhibited negligible Na^+-dependent shifts across increasing cytosolic Na^+ concentrations (Figure 4.19), indicating impaired Na^+-selectivity. Taken together, these electrophysiology findings strongly support the hypothesis that $TPC1^{A280S/V646M/N647G}$ (TPC1-mut3) is a Na^+-deficient, yet Ca^{2+}-permeable endosomal channel.

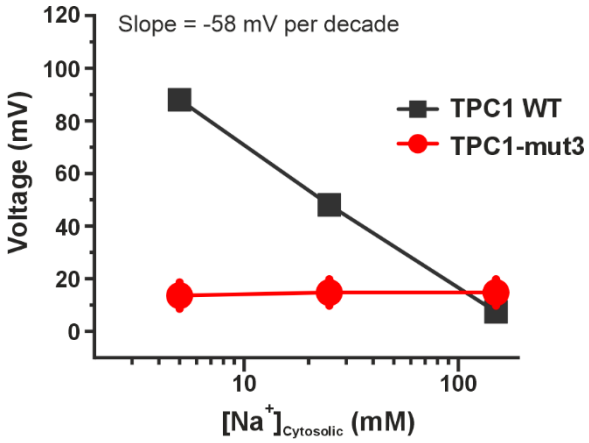

Figure 4.19: Na^+-dependence of TPC1. Reversal potentials of TPC1 wildtype (WT) and TPC1-mut3 mNeonGreen-tagged channels as a function of cytosolic Na^+ concentrations, with 0.1 µM $PI(3,5)P_2$ present in the bath, $n = 3$ recordings. TPC1 WT shows a slope of -58 mV per decade consistent with Na^+ selectivity, whereas TPC1-mut3 does not exhibit a Na^+-dependent shift. Data presented as the mean ± SEM.

4.7.3 Overexpression of Na^+-deficient mutant

Having established that TPC1-mut3 (*Hs*$TPC1^{A280S/V646M/N647G}$) was indeed Na^+-deficient, this mutant channel provides an invaluable tool to investigate the criticality of TPC1-mediated Na^+ fluxes for cell-membrane protein trafficking. In terms of transferrin trafficking, transient expression of TPC1-mut3 fully restored transferrin trafficking in *TPCN1* knockout HeLa cells to the same degree as re-expressed wildtype TPC1 (Figure 4.20). This remarkable finding strongly implies that the dominant Na^+ flux component of

TPC1 does not contribute to driving transferrin trafficking, instead, it is the considerably smaller Ca^{2+} flux that is the major ionic signal driving TfR internalisation and trafficking.

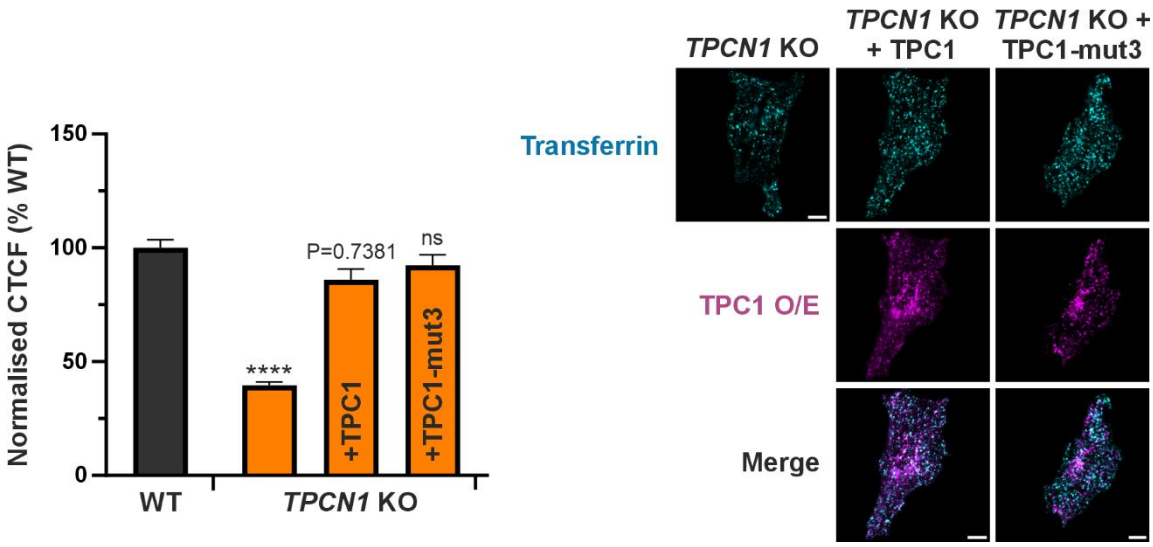

Figure 4.20: TPC1-mediated Ca^{2+} fluxes, but not Na^{+} fluxes, are essential for TfR trafficking. Expression of an mScarlet-I-tagged TPC1-mut3 restores TfR trafficking in *TPCN1* knockout (KO) HeLa cells to the same degree as re-expressed wildtype (WT) TPC1, n = 41-69 cells. Representative images of each condition, scale bars = 10 µm. Data are presented as the mean ± SEM, and probability determined using a one-way ANOVA (**** $P < 0.0001$, ns = not significant vs WT).

4.8 Transferrin-induced TPC1-mediated Ca^{2+} signals

Although the above findings emphasise the critical requirement of TPC1-mediated Ca^{2+} nanodomains for TfR trafficking, they do not directly demonstrate the magnitude of the Ca^{2+} efflux required. In an attempt to visualise TPC1-mediated Ca^{2+} release during TfR trafficking, a pilot study was conducted whereby transferrin was applied to cells and the resultant Ca^{2+} signals in response to transferrin binding and TfR internalisation measured. As the nanodomain Ca^{2+} concentration is unknown for TPC1, different GECIs of varying Ca^{2+} affinities were tethered to the C-terminus of TPC1, to determine the appropriate Ca^{2+} reporter for selectively detecting transferrin-induced TPC1-mediated Ca^{2+} release.

Specifically, TPC1 was fused to either the moderate affinity G-GECO1.2 (K_d ~1.2 µM), or high affinity GCaMP6s (K_d ~148 nM). Although no transferrin-induced Ca^{2+} responses were detected when TPC1 was tethered to G-GECO1.2, a small signal was observed in a subpopulation of cells with the higher affinity GECI GCaMP6s (Figure 4.21), suggesting that a small localised Ca^{2+} signal may be required.

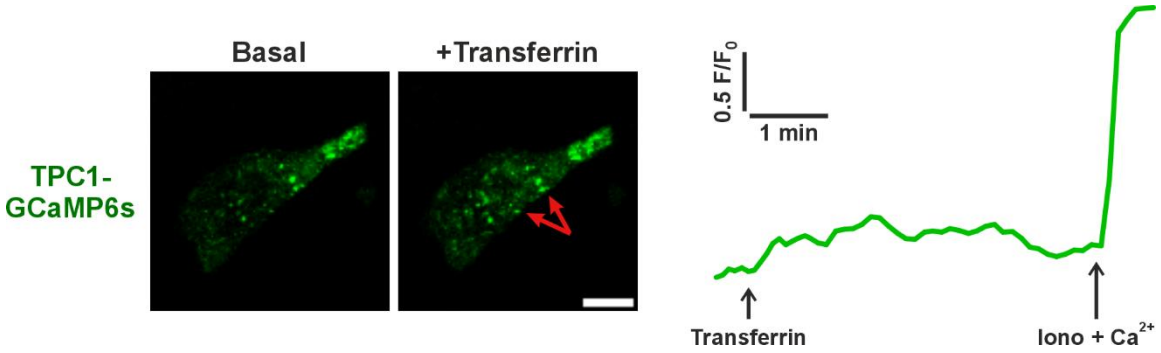

Figure 4.21: TPC1-GCaMP6s transferrin-induced Ca^{2+} signals. Transferrin-induced Ca^{2+} signals were detected by a transiently-expressed TPC1-GCaMP6s fusion protein. Red arrows show localised endosomal Ca^{2+} signals, scale bar = 15 µm. Corresponding single-cell Ca^{2+} trace displaying 40 µg/ml unconjugated transferrin and 1 µM ionomycin (iono) + 10 mM Ca^{2+} additions.

To enhance the chances of detecting transferrin-induced Ca^{2+} signals, GCaMP6s was exchanged for NEMOs, a GECI with comparable sensitivity (K_d ~157 nM) yet increased dynamic range (>100 fold) in response to Ca^{2+} (279). To ensure that any observed signals were not a consequence of focal changes, Ca^{2+} measurements were performed ratiometrically against the Ca^{2+}-insensitive cytosolic fluorescent protein mScarlet-I. As shown in Figure 4.22, the application of transferrin to cells induced a small, yet significant TPC1-mediated Ca^{2+} signal, approximately 0.17 $\Delta F/F_0$ above cytosolic background recordings. No Ca^{2+} responses were observed following the administration of a vehicle control relative to cytosolic-NEMOs, confirming that these signals arose from transferrin and not the delivery method or solvent. It is important to highlight that only a small

fraction of cells responded to transferrin (~15%) and in those that did, the TPC1-mediated Ca^{2+} response was small and highly localised, as demonstrated by individual fluorescent puncta representing individual TPC1-positive endosomes (Figure 4.22B). These findings provide visual evidence that TPC1-mediated Ca^{2+} fluxes are required for TfR internalisation and trafficking.

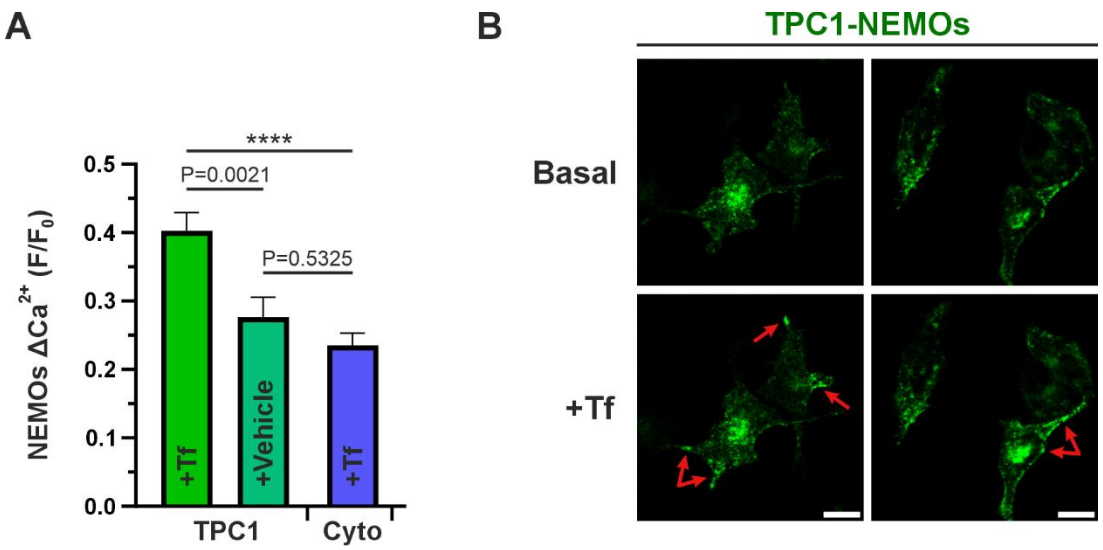

Figure 4.22: Quantification of transferrin-induced TPC1-mediated Ca^{2+} release. (A) Summary data of NEMOs Ca^{2+} measurements following the bath application of unconjugated transferrin (40 µg/ml) or a vehicle (PBS) control. Ca^{2+} signals were detected using a TPC1-, or cytosolic (cyto)-tethered NEMOs GECI, n = 86-145 cells. **(B)** Representative images of responding cells prior to (basal) and following the addition of transferrin (+Tf). Red arrows highlight regions of localised endosomal TPC1-mediated Ca^{2+} release, scale bars = 20 µm. Data are presented as the mean ± SEM, and probability determined using a one-way ANOVA (**** $P < 0.0001$)

4.9 Discussion

This chapter builds upon the findings from Chapter 3, where an exclusive requirement for TPC1 was identified for the regulation of the transferrin cycle and cellular iron homeostasis. The aim of this chapter was to investigate how the different cation modalities of TPC1 contribute to regulating TfR internalisation and trafficking. Specifically, the three major cation fluxes of TPC1 (Na^+, H^+, and Ca^{2+}) were investigated in the context of TfR trafficking.

4.9.1 A necessity for local Ca^{2+} domains

Ca^{2+} is recognised as a key mediator of vesicular membrane and protein transport, regulating endo-lysosomal trafficking pathways through both local compartmentalised and widespread Ca^{2+} domains. As the transferrin cycle is contingent on membrane-protein transport and the fusion/fission of endosomal vesicles (246,281), it is unsurprising that the transferrin cycle is Ca^{2+}-dependent. The data presented above builds upon pre-existing research that highlights a crucial role for local intracellular Ca^{2+} in mediating the vesicular transport of the TfR complex (310,311). While the findings in Figure 4.2 show that Ca^{2+} is critical for TfR internalisation and trafficking, they more importantly revealed which Ca^{2+} signalling domain is required. Accounting for the differential Ca^{2+}-binding kinetics of EGTA and BAPTA, these findings suggest that a local Ca^{2+} domain, which is chelated by BAPTA but not the slower Ca^{2+} buffer EGTA, is required for efficient TfR trafficking (Figure 4.2). These findings correlate with previous reports that describe a role for local intracellular Ca^{2+} in mediating analogous trafficking pathways, including EGFR, bacterial toxin, and viral internalisation and trafficking (81,117,185,269).

It is important to consider the off-target effects of chelator compounds such as BAPTA. In addition to Ca^{2+} chelation, BAPTA has been shown to inhibit various enzymes and ion channels, as well as chelate transition metals with high affinity (321). BAPTA variants which exhibit varying Ca^{2+} affinities are extremely useful to control for potential Ca^{2+}-independent effects. In particular, TF-BAPTA (K_d ~65 μM) exhibits an approximate 400-fold lower affinity for Ca^{2+} compared to BAPTA (K_d ~160 nM) (321). If TfR trafficking truly depends on local Ca^{2+} domains, TF-BAPTA should have no effect on trafficking in contrast to BAPTA. Indeed, as demonstrated in Figure 4.2, TF-BAPTA did not impair TfR trafficking, indicating that the BAPTA-induced trafficking impairment was a direct consequence of Ca^{2+} chelation. Additionally, EGTA was used as a control to differentiate between the requirement for local or global intracellular Ca^{2+} domains. Although EGTA- and BAPTA-mediated intracellular Ca^{2+} chelation was confirmed in Ca^{2+}-free medium (Figure 4.1B), the TfR trafficking experiments were performed in Ca^{2+}-containing medium (Figure 4.2). Therefore, EGTA and BAPTA may not have achieved the same extent of Ca^{2+} chelation during the TfR trafficking experiment as was observed under the Ca^{2+}-free conditions used for validation. Nevertheless, EGTA and BAPTA exhibited a similar ability to chelate histamine-induced H1 G_q/PLC/IP_3R-coupled Ca^{2+} release in Ca^{2+}-free medium (Figure 4.1B); however, EGTA did not impair TfR trafficking (Figure 4.2), implying that local, but not global, intracellular Ca^{2+} domains drive TfR trafficking. This highlights the importance of control experiments, to confirm intracellular Ca^{2+} chelation, pinpoint the domain of intracellular Ca^{2+}, and to ensure that any defects mediated by BAPTA are indeed a consequence of acute local Ca^{2+} chelation.

4.9.2 Endosomal Ca^{2+} drives TfR trafficking

Although acidic lysosomal compartments are recognised as major Ca^{2+} stores, the possibility that early and recycling endosomal compartments co-exist as essential Ca^{2+} stores has received relatively little attention. Estimating the free Ca^{2+} concentration in endosomes is challenging, predominantly because the acidic luminal pH directly interferes with the binding affinity of conventional Ca^{2+} indicators, as demonstrated by the lower K_d of Fluo-3 at endosomal pH 6.7 (Figure 4.12B). More outstanding was the substantial reduction in Ca^{2+} affinity upon Cal-520 dextran conjugation, reducing the K_d of Cal-520 dextran ~26-fold from 320 nM (manufacture's value) to 8.31 μM (Figure 4.12A). This is not specific to Cal-520, since conjugation has been shown to similarly reduce the K_d of Fluo-4 dextran (322), as well as the pKa of pH-sensitive reports such as pHrodo-Red. This highlights the importance of calibrating such probes *in situ*, as the K_d will be system specific.

Studies which have measured endo-lysosomal Ca^{2+} report a considerably lower endosomal luminal [Ca^{2+}] (2-50 μM) (36,320,323) compared to lysosomes (~500 μM) (37,317). The majority of endosomal measurements were performed using endocytosed low Ca^{2+}-affinity free acid variants such as Oregon-Green BAPTA-5N (K_d ~20 μM) (36,320), which exhibit poor sensitivity and dynamic range in response to Ca^{2+}. Alternatively, endosomal luminal [Ca^{2+}] has been estimated using Ca^{2+}-sensitive genetic reporters such as GEM-GECO1.2 (323). However, these genetic measurements were obtained at the lower limit of this reporters linear range (GEM-GECO1.2, K_d ~680 μM at pH 6.5 (323)), meaning the data should be interpreted with caution.

In an endeavour to accurately measure endosomal Ca^{2+} levels, endosomal luminal Ca^{2+} measurements were performed using a Cal-520-conjugated dextran (K_d = 8.31 μM at pH

6.7; Figure 4.12A). The calculated early endosomal luminal [Ca^{2+}] within HeLa cells was approximately 10-12 μM at basal conditions (Figure 4.13). Logically, nascent endosomes would be expected to contain millimolar Ca^{2+} engulfed from the extracellular milieu (5); however, this was not the case in Figure 4.13, even after a short 5 minute Cal-520 dextran incubation. Estimates suggest that the extracellular Ca^{2+} internalised during endocytosis is rapidly removed from endosomes ($t_{1/2}$ ~15 minutes in Swiss 3T3 cells), in response to the progressive acidification of endosomes by V-ATPase pumps (320). The findings in Figure 4.13 support this observation, since the endosomal luminal [Ca^{2+}] was drastically lowered after 20 minutes. The exact transporter which facilitates the removal of internalised Ca^{2+} from the endosomal lumen in response to the proton gradient is not clear, potential candidates include resident endosomal Ca^{2+} channels such as TRPML2/3 and TPC1. A potential limitation of the Ca^{2+} measurements performed in this chapter is that endosomal luminal Ca^{2+} was not quantified in TPC1-deficient cells in parallel to wildtype cells. Quantitative comparison requires identical image acquisition settings across wildtype and *TPCN1* knockout cells; however, enhanced fluid-phase uptake of fluorescent dextran conjugates in *TPCN1* knockout cells resulted in substantially stronger fluorescence than in wildtype cells (as shown in Chapter 5). Consequently, the signal-to-noise ratio in wildtype cells was insufficient for reliable early endosomal [Ca^{2+}] comparisons between genotypes. Future quantification of endosomal luminal Ca^{2+} levels in TPC1-deficient cells would help establish a role for TPC1 in early endosomal Ca^{2+} homeostasis, whilst also assisting to distinguish whether the Ca^{2+}-dependent TfR trafficking defect is a consequence of impaired TPC1-mediated Ca^{2+} signalling, or dysregulation of endosomal Ca^{2+} storage and availability.

An important consideration was if the low luminal [Ca^{2+}] of endosomes would be sufficient to initiate the local Ca^{2+} signal required for TfR trafficking. Based on the 10 μM

endosomal luminal [Ca^{2+}] estimation in Figure 4.13, this would provide a ~100-fold (electro)chemical Ca^{2+} gradient relative to the cytosol (100 nM). Given that plasma membrane Na^+ transport proteins, such as Na^+/H^+ exchangers (NHEs), facilitate Na^+ influx into the cytosol with only a ~10-fold (electro)chemical Na^+ gradient (324), it is theorised that the 100-fold endosomal Ca^{2+} concentration gradient would be more than sufficient to support the Ca^{2+} efflux required for local Ca^{2+} nanodomains. Low nanomolar Ca^{2+} concentrations are sufficient to maintain Ca^{2+} signals required for cell processes such as T-cell proliferation and astrocyte signalling (325,326). The findings presented in this chapter provide strong evidence that endosomes are Ca^{2+}-containing organelles, whose Ca^{2+} fluxes through TPC1 and localised Ca^{2+} nanodomains are crucial for regulating TfR internalisation and trafficking.

The criticality of endosomal Ca^{2+} for TfR trafficking was exemplified using several methodologies, including the effects of depleting endo-lysosomal Ca^{2+} stores and chelation of Ca^{2+} in the endosome lumen (Figure 4.7B and Figure 4.8B). In the instance of luminal Ca^{2+} chelation, TfR trafficking was unaffected by a non-Ca^{2+}-binding dextran chased to early endosomes, confirming that this effect was indeed Ca^{2+}-dependent. Ca^{2+} depletion was indirectly verified through the effects of endo-lysosomal alkalinisation caused by the inhibition of H^+-dependent Ca^{2+} uptake (Figure 4.7A). Although the effect of bafilomycin-A1 on TfR trafficking correlates with previous findings, the authors of these findings concluded that this effect was a consequence of endosomal pH dysfunction (327,328), rather than endo-luminal Ca^{2+} depletion. As will be discussed in section 4.9.4, although endosomal alkalinisation would impair Fe^{3+} release from transferrin and subsequently the rate of TfR trafficking, the findings from Figure 4.15 indicate that the TfR trafficking defect observed in TPC1-deficient cells was not a direct consequence of early endosomal alkalinisation. Whilst it was not determined whether bafilomycin-A1 affects TfR

trafficking through either Ca^{2+}- or H^{+}-dependent effects, taken together with endosomal luminal Ca^{2+} chelation (Figure 4.8B), the data presented in this chapter suggests that endosomal Ca^{2+} stores are the likely source of Ca^{2+} required for mediating TfR trafficking. Future experiments which target other endo-lysosomal Ca^{2+} uptake mechanisms, such as TMEM165-mediated Ca^{2+} uptake (46), would strengthen the conclusion that depletion of endosomal Ca^{2+} stores impairs TfR trafficking.

To further strengthen the claims that local endosomal Ca^{2+} domains are required for TfR internalisation and trafficking, peri-endosomal Ca^{2+} nanodomains were buffered using a chemically-induced FKBP12/FRB* dimerization system (Figure 4.9). The finding that local endosomal Ca^{2+} buffering severely impairs TfR trafficking (Figure 4.10) supports and strengthens the results from endosomal Ca^{2+} depletion and chelation experiments (Figure 4.7B and Figure 4.8B), providing clear evidence that local endosomal Ca^{2+} nanodomains are essential for driving TfR trafficking. An important consideration when buffering peri-endosomal Ca^{2+} was if the stoichiometry provided by TPC1 would enable enough buffering of local endosomal Ca^{2+} to elicit an effect in TfR trafficking. Davis *et al.* targeted calbindin to the surface of lysosomes by LAMP1, a surface protein which is expressed in superior quantities in relation to TPC2 expression (81). Whilst the endosomal tethering factor EEA1 would perhaps have been a more suitable target to increase the ratio, rapamycin-induced calbindin translocation to EEA1-positive endosomes was not observed (Appendix Figure A.6A). This was possibly because the tethered FRB* protein was concealed by the coiled structure of EEA1 (Appendix Figure A.6B), impacting the ability of the calbindin-tethered FKBP12 to bind to FRB*-EEA1.

Whilst the findings in Figure 4.10 demonstrate the importance of local endosomal Ca^{2+} for TfR trafficking, they also support the possibility that these endosomal nanodomains are

generated by TPC1-mediated Ca^{2+} efflux. Estimates suggest that TPC2 generates Ca^{2+} nanodomains of approximately 7-42 μM, which surround the channel in a radius of up to 50 nm (184). As will be discussed in section 4.9.5, TPC1 and TPC2 exhibit a similar Ca^{2+} permeability in response to $PI(3,5)P_2$ (Figure 4.17). Based on the assumption that the nanodomain concentration and radius is the same for both TPC2 and TPC1, the approximate number of Ca^{2+} ions within this nanosphere can be calculated by multiplying the nanodomain volume and concentration by Avogadro's number using the equation below.

$$N = C * \frac{4}{3}\pi r^3 * N_A$$

Where: N = number of ions; C = concentration of nanodomain (mol/L); r = radius of nanodomain (m); N_A = Avogadro's constant.

This calculation indicates that a single 50 nm TPC1 Ca^{2+} nanodomain of 7-42 μM contains approximately 0.3-1.7 Ca^{2+} ions. Since both the literature and the findings from Figure 4.17 suggest a substantial reduction in TPC1 Ca^{2+} conductance compared to TPC2 (122,139,141), it is appropriate to suggest that the number of Ca^{2+} ions which comprise the TPC1 nanodomain is towards the lower end of the above estimate. In relation to the peri-endosomal TPC1 Ca^{2+} buffering in Figure 4.10, since calbindin was targeted to the surface of endosomes by TPC1-FRB* fusion, endosomal Ca^{2+} was likely buffered from the mouth of the TPC1 channel pore. As the Ca^{2+}-binding capacity of a tandem-pair of calbindin is 10 Ca^{2+} ions, this is sufficient to buffer TPC1-mediated Ca^{2+} fluxes and the entire nanodomain. This therefore explains how the acute translocation of calbindin was capable of impairing TfR trafficking.

4.9.3 The role of ER and extracellular Ca^{2+}

Local compartmental Ca^{2+} release is often concealed behind global ER-mediated Ca^{2+} signals. To ensure the absolute measurement of endo-lysosomal Ca^{2+} efflux, appropriate controls, such as thapsigargin and CPA, must be performed to account for global Ca^{2+} propagation. In the context of endo-lysosomal Ca^{2+} release, local Ca^{2+} signals are often globalised by CICR, a critical source of intracellular Ca^{2+} signal propagation (4,5). The process of secondary endo-lysosomal Ca^{2+} amplification has been verified across numerous cell lines (80,188,329,330), indicating that for certain cellular processes, endo-lysosomal Ca^{2+} stores are insufficient by themselves to trigger global Ca^{2+} spikes. In contrast, the findings from this chapter indicate that the transferrin cycle is not dependent upon ER Ca^{2+}, since depletion of ER Ca^{2+} stores using thapsigargin and CPA did not affect TfR trafficking (Figure 4.4). Since TfR trafficking was similarly unaffected by global Ca^{2+} chelation (Figure 4.2), the conclusions from this chapter instead imply that a small, local, non-ER compartmental Ca^{2+} nanodomain is required to drive TfR trafficking. Localised Ca^{2+} domains are not limited to TfR trafficking, as a number of other cellular processes also require localised, non-ER-derived Ca^{2+} signals for precise control. Examples include synaptic transmission and gene transcription in neurones. These are two discrete processes that require localised Ca^{2+} microdomains for synaptic vesicle fusion and neurotransmitter release (331,332), as well as to regulate Ca^{2+}-dependent kinases and nuclear transcription factors, such as cAMP response element-binding protein (CREB), which are required for neuroplasticity and long-term memory (333,334).

In relation to endo-lysosomal-ER crosstalk, emerging evidence suggests that endo-lysosomes form MCSs with the ER, dynamically positioning themselves within a 30 nm proximity of the ER membrane to enable CICR (307). Alongside lysosomes (83,115,307),

early and recycling endosomal organelles have been shown to form MCSs with the ER, whose local confinement promotes Ca^{2+} amplification for cell autophagy, apoptosis, and proliferation (190–193). Whilst these studies support the basis of this chapter, that endosomes are Ca^{2+}-containing organelles whose Ca^{2+} efflux is essential for regulating cellular activity, the findings presented in section 4.3.3 suggest that Ca^{2+} signalling at endosome-ER MCSs is not required for TfR trafficking, a striking difference to EGFR trafficking and signalling (193). Despite exhibiting large global Ca^{2+} fluxes, stimulation of ER Ca^{2+} stores using a variety of pharmacological compounds did not restore TfR trafficking in TPC1-deficient cells (Figure 4.5). This implies that regardless of the proximity to the ER, local endosomal Ca^{2+} nanodomains remain largely insulated from global intracellular Ca^{2+} signals, in order to regulate transferrin trafficking. In this way, Ca^{2+}-decoding pathways remain spatially segregated from one another, restricting crosstalk and enabling the recruitment of specific Ca^{2+}-dependent regulatory proteins. The TPC1 Ca^{2+} decoding proteins potentially responsible for mediating cell membrane trafficking are explored in Chapter 6.

The extracellular Ca^{2+} milieu provides an approximate 10,000-fold chemical gradient relative to intracellular [Ca^{2+}] (5). A noteworthy finding was that the removal of extracellular Ca^{2+} did not impair TfR internalisation and trafficking (Figure 4.4). This contrasts to analogous transport pathways such as vesicle exocytosis, which rely on extracellular Ca^{2+} influx to activate Ca^{2+}-dependent trafficking proteins such as synaptotagmin (335). There are inconsistencies across studies when reporting the necessity of extracellular Ca^{2+} for the transferrin cycle. In particular, certain studies imply that extracellular Ca^{2+} is crucial for the internalisation and recycling of the transferrin-TfR complex, with these processes substantially impaired following extracellular Ca^{2+} chelation by 5 mM EDTA, EGTA, or BAPTA free acids (311,336). However, an important partially

unexplained finding from these studies was that transferrin uptake was only impaired at temperatures greater than 20ºC. This is surprising, as given that the Ca^{2+} chelators were in 5-fold excess compared to the extracellular Ca^{2+} environment (~1 mM), it suggests that the reduction in transferrin trafficking is attributed to a biological effect, such as increased membrane fluidity as a result of membrane phase-transition (336), rather than extracellular Ca^{2+} chelation. In relation to early endosomes, an additional 10 minute incubation at 4ºC in Ca^{2+}-free medium (supplemented with 100 μM EGTA) reduced the endosomal lumen [Ca^{2+}] 2-fold to approximately 5 μM (Figure 4.13). Whilst this concentration is low, the (electro)chemical Ca^{2+} gradient between the endosomal lumen and the cytosol is still 50-fold. Considering that only 1-2 Ca^{2+} ions comprise a Ca^{2+} nanodomain, it is reasonable to suggest that this 2-fold reduction would not substantially reduce TPC1-mediated Ca^{2+} fluxes. Therefore, this explains why the removal of extracellular Ca^{2+} did not impair transferrin trafficking in Figure 4.4, despite the minor depletion of endosomal luminal Ca^{2+}.

4.9.4 Early endosomal pH homeostasis

The compartmental pH of endo-lysosomes is diverse, ranging from ~6.5 in recycling endosomes to ~4.6 in the lysosomal lumen (Figure 1.5) (35). These specific pH levels drive the maturation of vesicles along the endo-lysosomal pathway, in addition to mediating trafficking through cargo substrate release and degradation. In terms of the transferrin cycle, a mild acidic early endosomal pH is essential for the release of Fe^{3+} from transferrin, as well as Fe^{2+} egress into the cytoplasm through the Fe^{2+}/H^{+} DMT1 symporter (230,246). Similarly, the LDLR and EGFR both exhibit ligand binding pH sensitivity (337,338), which determines the fate of receptor degradation or recycling. Indeed, bafilomycin-A1-induced alkalinisation of endo-lysosomes impairs TfR trafficking and

recycling (327,328), highlighting the importance of maintaining endogenous pH levels for trafficking.

To quantify early endosomal pH, the pH-sensitive dye pHrodo-Red was chosen based on its appropriate pKa (~6.5), which aligns well with the known pH of early endosomes (35). The wildtype early endosome pH calibration curve indicates an approximate pHrodo-Red pKa of 7.2 (Figure 4.15A), differing slightly to the reported pKa of pHrodo-Red. These differences could reflect the composition of the cell media, with the ions and tonicity of the medium shifting the curve slightly. As pHrodo-Red was conjugated to transferrin, ratiometric measurement ensured that any differences in luminal pH directly correlated with TPC1 deletion and were not a consequence of reduced transferrin internalisation in TPC1-deficient cells. Without ratiometric analysis, any results obtained cannot be reliably interpreted, as reduced transferrin uptake in TPC1-deficient cells would decrease the quantity and brightness of pHrodo-Red conjugated-transferrin in early endosomes. This reduction in pHrodo-Red fluorescence may be mistaken for early endosomal alkalinisation, when it is actually attributed to impaired transferrin internalisation. In this instance, normalising to wildtype fluorescence would not account for impaired transferrin internalisation, as this method only corrects day-to-day variability and not condition-dependent variability.

As TfR trafficking is highly dependent upon both TPC1 expression and the acidity of endosomes, the pH of the early endosomal lumen was measured in wildtype and TPC1-deficient HeLa cells. As shown in Figure 4.15B, the resting luminal pH of early endosomes was unchanged between wildtype (pH 6.69) and TPC1-deficient (pH 6.71) cells. The wildtype pH value fell within the expected physiological range for early endosomes (pH 6-6.8) (45), verifying the reliability of these early endosomal pH

measurements. These findings indicate that the TfR trafficking defect observed in TPC1-deficient cells, is likely not related to early endosomal pH dysfunction. Previous studies have reported that in addition to Na^+ and Ca^{2+}, TPC1 is permeable to H^+, functioning as a H^+ sensor on endosomal membranes (122,141). It therefore remains possible that deletion of TPC1 could disrupt TPC1-mediated H^+ efflux, without affecting the resting pH of early endosomes. Alternatively, TPC1-mediated Na^+ efflux could act as an electrochemical driving force for H^+ uptake through V-ATPase pumps (45,224). In this context, TPC1 deletion would abolish Na^+ efflux and increase the lumen-positive membrane potential of endosomes, reducing the efficiency of V-ATPase-dependent H^+ uptake (224). However, this is unlikely to account for the transferrin trafficking defect in TPC1-deficient cells, given that TPC1-mediated Na^+ fluxes are not required for trafficking (Figure 4.20).

Although the consequence of TPC deletion has been assessed in relation to endo-lysosomal pH, the majority of these studies did not directly assess early endosomal pH. Similar to the findings presented in Figure 4.15B, the acidic luminal pH of late endosomes and lysosomes appears to be unaffected in TPC1- and TPC2-deficient MEF cells, despite the presence of other trafficking defects (116,185). Fluctuations in endo-lysosomal pH could be tissue-dependent, as TPC2-deficient skeletal muscle cells exhibit increased lysosomal alkalinisation (339), whilst in other tissues, lysosomal pH is unaltered (116,185). A critical consideration is how much of a deviation in luminal pH is required to affect biological systems and trafficking. For example, an elevation of 0.2 pH units affects cathepsin degradation efficiency (340), whilst a shift from pH 6 to pH 5.5 substantially increases Fe^{3+} release from transferrin (230). A limitation of the pH measurements presented in this chapter, is that only the pH of early endosomes and not recycling endosomes were measured in TPC1-deficient HeLa cells. In addition to expressing TPC1 (103,116), recycling endosomes are crucial for the return of the apo-transferrin/TfR

complex back to the cell surface, a process shown as TPC1-dependent (Figure 3.4B). Therefore, future experiments should also quantify recycling endosomal luminal pH in wildtype and TPC1-deficient cells. Nevertheless, as TPC deletion did not affect the pH of early endosomes, it is unlikely that pH is the main driving factor behind the TfR internalisation and trafficking defect observed in *TPCN1* knockout cells.

4.9.5 TPC1-mediated Na^+ and Ca^{2+} release

TPC1 and its lysosomal counterpart, TPC2, are permeable to both Ca^{2+} and Na^+ cations. Unlike other endo-lysosomal channels, the relative permeability ratio of TPCs to Ca^{2+}/Na^+ is not a fixed property of the channel. Instead, the mode of TPC activation biases either a more Ca^{2+}-selective (NAADP), or Na^+-selective (phosphoinositide) permeability (149,150). Although this has been clearly demonstrated for TPC2, it is unclear if the permeability of TPC1 likewise exhibits 'biased agonism' (141).

Recent findings propose that TPC1 is predominantly associated with cellular mechanisms governing endosomal membrane tension and potential, and osmolality, processes fundamentally driven by Na^+ fluxes (122,341). The patch-clamp recordings presented in Figure 4.17 are consistent with the existing literature (106,122,141), demonstrating that wildtype TPC1 is a Na^+-selective channel ($P_{Na/Ca}$ = 16.2). In relation to the Ca^{2+}-selectivity of TPC1, the calculated $P_{Ca/Na}$ value of 0.06 indicates a significantly smaller Ca^{2+} permeability relative to Na^+ following $PI(3,5)P_2$ activation, which correlates with analogous bi-ionic experiments performed by Lagostena *et al*. ($P_{Ca/Na}$ ~0.05 to 0.1) (139). Upon $PI(3,5)P_2$ activation, TPC1 exhibits a similar Na^+-selectivity relative to TPC2 ($P_{Na/Ca}$ ~10 to 16.8) (107,138,149). This similarity is likely associated with analogous structural rearrangements upon $PI(3,5)P_2$-induced activation (106,108), as well as the near-identical

selectivity filters (Figure 1.3), both of which are conserved between TPC isoforms. If the permeability of TPC1 is indeed governed by the activating ligand, it would be expected that NAADP activation would enhance the relative Ca^{2+} selectivity of TPC1, as is the case with NAADP activation of TPC2 ($P_{Na/Ca}$ ~1.37) (149). As shown in Figure 4.19, the Na^+ dependence of the E_{rev} for TPC1 exhibited a Nernstian slope of -58 mV per decade. This value corresponds to the predicted Nernstian behaviour of TPC1 and is comparable to the previously reported slopes of wildtype TPC1 (-56 mV (122)) and TPC2 (-57 mV (138)).

In order to address which TPC1 cation modality drives TfR trafficking, a new mutant channel ($TPC1^{A280S/V646M/N647G}$, TPC1-mut3) was generated and characterised through TPC1 patch-clamp experiments. Although Ca^{2+} imaging was not performed to confirm that TPC1-mut3 retained Ca^{2+} permeability, the E_{rev} of TPC1-mut3 (+53.3 mV) was within the range anticipated for Ca^{2+} channels (E_{rev} +40 to +70 mV) (342,343). Taken together with the negligible Na^+-dependent Nernst shifts (Figure 4.19) and the calculated $P_{Ca/Na}$ value of 32.2 (Figure 4.17), these results strengthen the conclusion that TPC1-mut3 is indeed Na^+-deficient, yet retains its Ca^{2+} permeability. A drawback of the bi-ionic experiments was that the permeability of TPC1 was only evaluated in relation to Na^+ and Ca^{2+} cations. As mentioned previously, TPC1 is pH-sensitive and is potentially permeant to H^+ cations (122,141). Due to the current unavailability of TPC1-selective cell-permeant agonists, precisely measuring TPC1-mediated Ca^{2+} and H^+ fluxes *in vitro* with genetically-encoded fluorescent indicators, such as G-GECO1.2 and pHluorin, will form the basis of future work.

Expression of TPC1-mut3 in TPC1-deficient cells confirmed that the observed TfR trafficking defect was a direct consequence of the ablation of TPC1-dependent Ca^{2+} fluxes, with little requirement for TPC1-mediated Na^+ fluxes (Figure 4.20). This necessity for

TPC1 Ca^{2+} domains was established in early experiments, where local endosomal Ca^{2+} buffering around the mouth of TPC1 also impaired TfR trafficking (Figure 4.10). Given that TPC1 is one of several Ca^{2+}-permeable channels present on endosomes, it was expected that Ca^{2+} efflux from the endosomal channel TRPML2 might compensate for the lack of TPC1 (198). On the contrary, ML2-SA1-induced TRPML2-mediated Ca^{2+} release did not restore TfR trafficking in TPC1-deficient cells (Figure 4.6B), affirming the specificity of TPC1-mediated Ca^{2+} fluxes within the transferrin cycle. These findings support the concept of extreme compartmentalisation, where TPC1 and TRPML2 autonomous local Ca^{2+} nanodomains are segregated from one another even on the same vesicle population, enabling TPC1 to selectively regulate TfR trafficking. This phenomenon has similarly been observed in phagocytosis, where discrete TPC2- and TRPML1-mediated Ca^{2+} release drives the internalisation of different size pathogens (81,184).

To directly visualise TPC1-mediated Ca^{2+} release during TfR trafficking, the NEMOs response to exogenous transferrin was monitored. This approach was analogous to the methodology used by Davis *et al.* to monitor local TPC Ca^{2+} signals during the phagocytosis of IgG-coated beads (81). Although only a small signal was detected in a subpopulation of cells, control experiments assured this was a true signal attributed to the application of exogenous transferrin (Figure 4.22). Interestingly, Ca^{2+} signals were only observed when TPC1 was fused to high affinity GECIs including GCaMP6s or NEMOs, suggesting that a confined, low-amplitude Ca^{2+} signal regulates TfR trafficking. Although these reporters substantially enhance the sensitivity of Ca^{2+} detection, they simultaneously increase background and basal Ca^{2+} detection. Calibration of numerous GECIs identified G-GECO1.2 as the most appropriate reporter for detecting TPC2 Ca^{2+} nanodomains above global (cytosolic) Ca^{2+} signals (184). However, in the case of transferrin-induced Ca^{2+}

signals, none were detected when G-GECO1.2 was fused to TPC1, indicating that the TfR-stimulated Ca^{2+} signals must be of a lower concentration in comparison to FcR-stimulated TPC2-mediated Ca^{2+} signals (81,184). This correlates with the electrophysiological characterisation of wildtype TPC1 in Figure 4.17, which shows that Ca^{2+} is less permeant than Na^{+} ($P_{Ca/Na}$ ~0.06). In the future, TPC1 Ca^{2+} imaging experiments could be performed with moderate Ca^{2+} affinity GECIs such as NEMOc (K_d ~557 nM) (279), as such experiments may enhance the TPC1-Ca^{2+} response relative to global Ca^{2+} measurements.

The findings in Figure 4.22 tentatively suggest that the TfR may function as more than just an endocytic receptor, but also as a cell-surface signal transduction protein, whose circuitry with TPC1 mediates endosomal Ca^{2+} release and signalling for the transferrin cycle. Although the transferrin cycle is recognised as a constitutive process, in the absence of transferrin, TfR internalisation and recycling diminishes (344,345), implying that the formation of the transferrin-TfR complex must initiate downstream signalling. A potential role for the TfR in initiating signalling cascades has been reported in previous studies, in which the transferrin-TfR complex regulates ROS formation and subsequently ferroptosis through the JNK signalling pathway (346), as well as facilitating cytokine growth factor signalling for mouse embryonic cranial development (347). It has previously been suggested that extracellular Ca^{2+} could drive TfR-dependent signalling, since preincubation with extracellular Ca^{2+} chelators impaired transferrin and iron internalisation in reticulocytes (336), as well as recycling in Jurkat and L2C cells (311). However, as shown in Figure 4.4, TfR uptake and trafficking was unaffected in the presence of Ca^{2+}-free medium (supplemented with EGTA), indicating that the extracellular Ca^{2+} milieu does not drive the transferrin signalling cascade in the HeLa system.

Although a modest global (cytosolic) Ca^{2+} response was detected following the application of exogenous transferrin, the localised TPC1 Ca^{2+} response was significantly larger (Figure 4.22). This correlates with the experimental findings presented in Figure 4.2 and Figure 4.5, which show that a global/ER Ca^{2+} stimulus is not required for transferrin internalisation and trafficking. Instead, local endosomal Ca^{2+} events driven by TPC1 were observed. These localised Ca^{2+} events were similar to those which were observed following ML2-SA1-induced activation of the PI(3,5)P_2-insensitive mutant channel TRPML2^{R310A} (198). These findings contrast to EGFR stimulation, which is coupled to global PLC/IP_3-mediated Ca^{2+} release from ER stores and is negatively regulated by localised TPC1-mediated Ca^{2+} signalling at endosome-ER MCSs (185,193). Although future experiments are required to understand the TfR signal transduction mechanism behind this phenomenon (subsequent chapter), the findings in this chapter provide new evidence that establishes endosomes as Ca^{2+}-containing organelles (Figure 4.13), and whose TPC1-mediated Ca^{2+} efflux is required for TfR internalisation and trafficking (Figure 4.20 and Figure 4.22).

4.10 Conclusions

In summary, this chapter addresses the cation selectivity of TPC1 in the context of cell-membrane protein trafficking. Despite representing the lesser permeant cation, TPC1-mediated Ca^{2+} fluxes appear vital for the regulation of the transferrin cycle. These conclusions were supported by Ca^{2+} chelators and buffers targeted to TPC1-positive endosomes, providing evidence that endosomes are Ca^{2+}-containing organelles that generate localised Ca^{2+} nanodomains. In this chapter, the absolute early endosomal luminal [Ca^{2+}] and pH was quantified using new sensitive fluorescent reporters which outdate previous measurements. This study explicitly shows that endosomal protein trafficking is

dependent on endosomal Ca^{2+} fluxes through TPC1, rather than TPC1-mediated changes in endosomal pH. In the context of TfR trafficking, global Ca^{2+} signals initiated by ER-mediated Ca^{2+} release do not support trafficking and are segregated from endosomes, thereby supporting the hypothesis of extreme compartmentalisation between intraorganellar Ca^{2+} signals. Within this chapter, a new Na^{+}-deficient, Ca^{2+}-permeable TPC1 channel mutant was developed and validated by electrophysiology. This molecular tool helped demonstrate that the TPC1 Na^{+} signalling pathway is not required for TfR trafficking. It is envisioned that this mutant channel will equally act as an invaluable tool for future studies that likewise wish to investigate the dual-cation fluxes of TPC1. Finally, GECIs were used to visualise TPC1-mediated Ca^{2+} release during the transferrin cycle. Whilst these signals were inconsistent, they provide initial evidence of a new cell-surface signal transduction Ca^{2+} signalling pathway, which is initiated upon the interaction of transferrin and the TfR.

Chapter 5 – Results

Regulation and specificity of TPC1 in endo-lysosomal trafficking

5.1 Summary

The previous two chapters have established that TPC1 is a fundamental regulator of cell-membrane protein trafficking, whose expression is required for the efficient delivery of transferrin-bound iron to cells in order to maintain cellular iron homeostasis. Although the transferrin cycle is a ubiquitous cellular process, the involvement of TPC1 in tissues where iron absorption and trafficking is physiologically relevant has not been shown. Using a high-throughput trafficking assay and gene silencing, this chapter evaluates the biological specificity of TPC1 for TfR trafficking across various cell lines.

Membrane trafficking is a diverse cellular process which ensures the efficient transport of extracellular cargo between the cell surface and intracellular organelles. Without the stringent regulation of fusion/fission machinery by endo-lysosomal channels, endocytic and secretory pathways become dysfunctional, leading to cargo accumulation and storage disorders (37,45,203). The localisation of TPC1 at the crossroads of intracellular cargo sorting for cell recycling or degradation, situates TPC1 at an opportune position to regulate numerous vesicular pathways. The first aim of this chapter was to determine whether TPC1 regulates specific membrane trafficking pathways, or whose expression and constitutive activity governs generic cell membrane- and protein-trafficking.

TPCs are recognised to be gated by the second messenger NAADP and phosphoinositide lipids such as $PI(3,5)P_2$. Although NAADP and $PI(3,5)P_2$ are established activators of TPCs, few studies have assessed how these molecular messengers regulate TPCs in the context of TPC-dependent physiological processes. The second aim of this chapter focuses on defining which upstream messenger(s) gates TPC1 to evoke cation efflux during cell-membrane protein trafficking. In particular, knockout of NAADP-binding proteins, mutation of messenger binding sites, and depletion of phosphoinositide levels, all assist in understanding the involvement of NAADP and phosphoinositides within cell membrane protein trafficking.

The following chapter contains figures and content from Burton *et al*. (282).

5.2 Establishment of high-throughput trafficking assay

The previously detailed TfR trafficking experiments were performed by microscopy at a single-cell resolution. Although this enables precise detailed analysis of protein cellular distribution and morphology, the imaging procedure and analysis is time consuming. In order to evaluate endo-lysosomal trafficking across various cell lines and pathways, the previous TfR trafficking methodology was adapted to be performed in a plate reader to enable high-throughput screening and analysis. Figure 5.1 shows a time course for transferrin internalisation and trafficking in HeLa wildtype and *TPCN1* knockout cells performed using a plate reader. To ensure any observed differences were not a consequence of cell seeding density, fluorescence measurements were normalised to nuclear DNA content (DRAQ5 stain), as a direct correlation to cell number. Expectedly, TfR trafficking was significantly impaired in TPC1-deficient HeLa cells across the majority of incubation periods (Figure 5.1), closely matching the transferrin trafficking

kinetics observed in Figure 3.4A at a single-cell resolution. In addition to validating previously reported findings, these results demonstrate that a high-throughput approach to investigate endo-lysosomal trafficking is a valid, reproducible methodology, and is therefore utilised throughout this chapter.

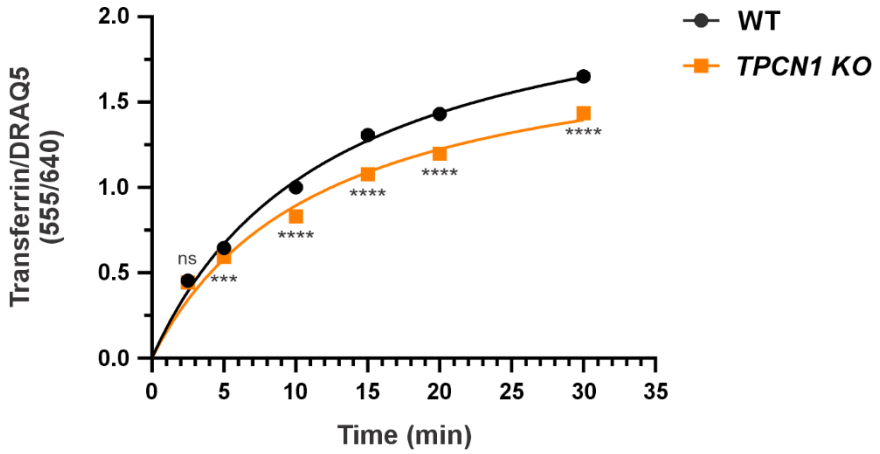

Figure 5.1: Plate reader analysis of TfR trafficking in HeLa cells. Time course of transferrin internalisation and trafficking in wildtype (WT) and *TPCN1* knockout (KO) HeLa cells, n = 7-12 wells. Transferrin fluorescence normalised to cell number (DRAQ5) and the data fitted using a non-linear regression model. Data are presented as the mean ± SEM, and probability determined by a two-tailed t-test (**** $P < 0.0001$, *** $P < 0.001$, ns = no significance vs WT).

5.3 Cell line-dependent TfR trafficking

Until now, all experiments detailed in this thesis were performed using HeLa cells. To grasp a broader understanding of the biological importance of TPC1 for iron trafficking and homeostasis, TfR trafficking was investigated in two additional tissue-specific cell lines where TPC expression had been disrupted.

5.3.1 TfR trafficking in RAW264.7 macrophage cells

To investigate if TPCs were likewise important for TfR trafficking in mouse macrophage cells, fluorescently-conjugated transferrin was incubated in wildtype, TPC1-, and TPC2-deficient RAW264.7 cells for varying incubation periods. Whilst wildtype cells displayed a rapid increase in TfR internalisation and trafficking, gradually plateauing after 20 minutes, trafficking was significantly, albeit modestly, impaired in *Tpcn1*$^{-/-}$ and *Tpcn2*$^{-/-}$ cells by approximately 13-20% across early time intervals (2.5, 5, and 10 minutes; Figure 5.2). Additionally, transferrin trafficking was further impaired in *Tpcn1*$^{-/-}$ cells compared to *Tpcn2*$^{-/-}$ cells at these time intervals. Interestingly, following prolonged incubation with transferrin after 30 minutes, an increased transferrin signal was quantified in *Tpcn1*$^{-/-}$ and *Tpcn2*$^{-/-}$ cells relative to wildtype cells (Figure 5.2). This could suggest that TPC-deficient RAW264.7 cells continue to internalise the transferrin-TfR complex beyond the maximal uptake of wildtype cells, resulting in an increased accumulation of transferrin in TPC knockout cells.

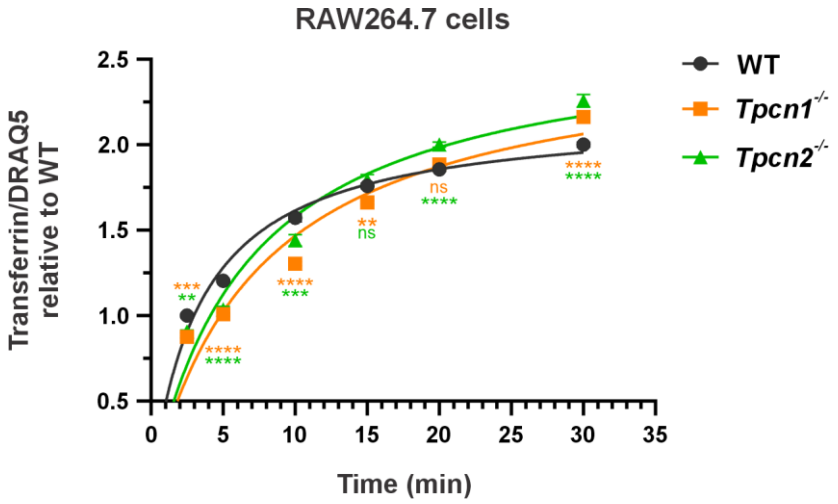

Figure 5.2: TfR trafficking in TPC-deficient RAW264.7 cells. Time course of transferrin internalisation and trafficking in wildtype (WT), *Tpcn1*$^{-/-}$, and *Tpcn2*$^{-/-}$ RAW264.7 macrophage cells, n = 9-12 wells. Transferrin fluorescence normalised to cell number (DRAQ5) and the data fitted using a non-linear regression model. Data are presented as the mean ± SEM, and probability determined using a two-way ANOVA (**** $P < 0.0001$, *** $P < 0.001$, ** $P < 0.01$, ns = no significance vs WT).

5.3.2 TfR trafficking in mouse embryonic fibroblast (MEF) cells

The second cell line in which TfR trafficking was investigated was within MEF cells. These cells were extracted from TPC-deficient mouse embryos and verified by Dr Margarida Ruas during her time as a post-doctoral researcher in the Galione laboratory (87,116). To evaluate the importance of both TPC1 and TPC2 within the transferrin cycle, transferrin trafficking experiments were performed using wildtype, *Tpcn1*$^{-/-}$, *Tpcn2*$^{-/-}$, and *Tpcn1/2*$^{-/-}$ double knockout MEF cells. As shown in Figure 5.3, TfR internalisation and trafficking was significantly reduced in both *Tpcn1*$^{-/-}$ and *Tpcn2*$^{-/-}$ MEF cells relative to wildtype cells. The magnitude of this trafficking defect was approximately 10% greater in TPC1-deficent cells compared to TPC2-deficient, a finding consistent with previous observations in HeLa and RAW264.7 cells. Remarkably, transferrin trafficking was almost

completely inhibited in *Tpcn1/2*$^{-/-}$ double knockout MEF cells. The linear regression gradient indicated that the rate of TfR trafficking was reduced by ~73% in *Tpcn1/2*$^{-/-}$ double knockout MEF cells and by ~45% in *Tpcn1*$^{-/-}$ cells relative to wildtype. This finding further indicates that both TPC1 and TPC2 are required for the efficient trafficking of the transferrin-TfR complex. Taken together, the findings from HeLa, RAW264.7, and MEF cells strongly suggest that TPCs mediate the transport of transferrin-bound Fe^{2+} for cellular iron homeostasis in a variety of tissue types.

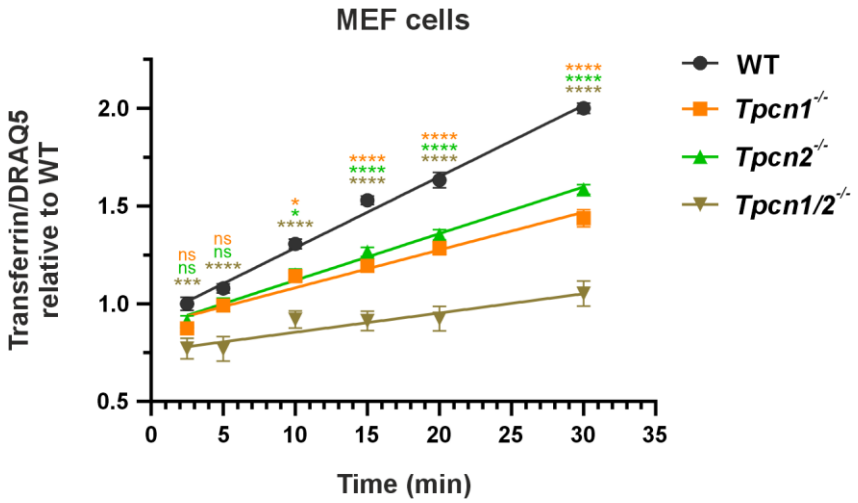

Figure 5.3: TfR trafficking in TPC-deficient MEF cells. Time course of transferrin internalisation and trafficking in wildtype (WT), *Tpcn1*$^{-/-}$, *Tpcn2*$^{-/-}$, and *Tpcn1/2*$^{-/-}$ double knockout MEF cells, n = 9-12 wells. Transferrin fluorescence normalised to cell number (DRAQ5) and the data fitted using a linear regression model. Data are presented as the mean ± SEM, and probability determined using a two-way ANOVA (**** $P < 0.0001$, *** $P < 0.001$, * $P < 0.05$, ns = no significance vs WT).

5.4 LDLR trafficking

Although the previous experiments establish a regulatory role for TPC1 in TfR trafficking, it remained uncertain whether the impairment of TfR cell membrane trafficking in TPC1-deficient cells was a general perturbation caused by TPC1 knockout. To address this, the effect of TPC deletion was monitored in a different trafficking system, with LDL

cholesterol acting as the transport particle. Cholesterol represents a critical component of cell membranes, where it stabilises the membrane and modulates its fluidity (208). The cellular levels of cholesterol are tightly regulated by the lysosomal degradation of LDL, which itself is internalised into cells by receptor-mediated endocytosis of the LDL-LDLR complex (208,348). LDL-degraded cholesterol is subsequently used by cells for the production of steroid hormones, vitamins, and bile acid (208). Both the transferrin and LDL cycles utilise similar endocytic mechanisms and machinery for receptor trafficking and recycling (210,220). As this pathway is parallel to the transferrin cycle, it was hypothesised that TPC1 would likewise be important for the trafficking and homeostasis of LDL cholesterol.

To evaluate the importance of TPCs for LDL-LDLR trafficking, the internalisation and transport of fluorescent non-acetylated LDL was monitored in HeLa wildtype, *TPCN1*, and *TPCN2* knockout HeLa cells. Figure 5.4 shows the acquired time course for LDL internalisation and trafficking in HeLa cells. A standout feature of the LDL time course was how slowly LDL was internalised in wildtype cells, an observation which correlates to the slower kinetics of LDL uptake and lysosomal degradation. A spike in wildtype LDL trafficking was observed at 45 minutes (Figure 5.4). As this increase was observed across multiple experimental replicates it is unlikely to represent an anomaly; however, as this data point did not fit the gradual increase trend in LDL trafficking in wildtype cells, it was not included in the generation of the non-linear regression. Although essential for receptor-mediated TfR endocytosis, deletion of TPC1 did not significantly alter the rate of LDL internalisation or trafficking relative to wildtype cells, with only a modest insignificant reduction in trafficking observed at longer incubations. In comparison, TPC2-deficient cells displayed a significant increase in LDL internalisation and trafficking, approximately 1.5-fold greater than wildtype cells (Figure 5.4). These findings importantly demonstrate

that TPC1 and TPC2 exhibit specificity for the endo-lysosomal pathways they regulate – the possible reasoning for which is discussed in 5.8.2.

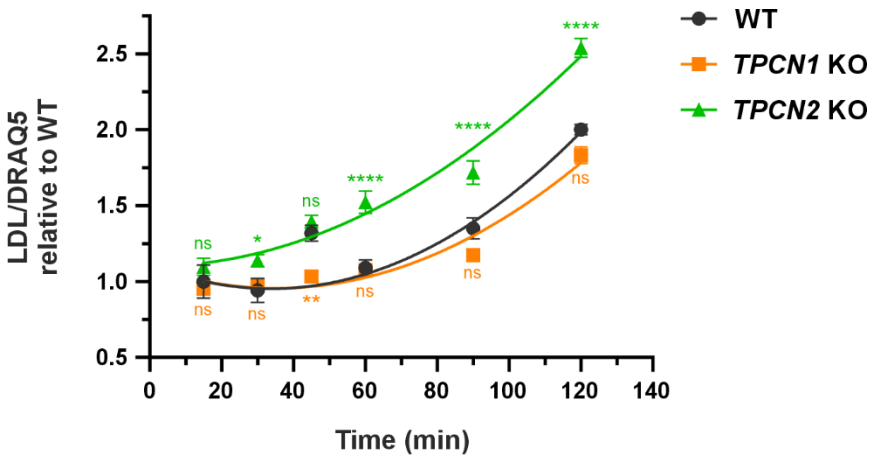

Figure 5.4: LDLR trafficking in TPC-deficient HeLa cells. Time course of LDL internalisation and trafficking in wildtype (WT), *TPCN1,* and *TPCN2* knockout (KO) HeLa cells, n = 9-12 wells. LDL fluorescence normalised to cell number (DRAQ5) and the data fitted using a non-linear regression model. Data are presented as the mean ± SEM, and probability determined using a two-way ANOVA (**** $P < 0.0001$, ** $P < 0.01$, * $P < 0.05$, ns = no significance vs WT).

5.5 Cellular pinocytosis

As an alternative endocytic mechanism to receptor-mediated endocytosis, the potential involvement of TPC1 in cellular pinocytosis was investigated in TPC1-deficient HeLa cells. Known as ‘cell drinking’, pinocytosis represents a critical form of receptor-independent endocytosis, where fluid, nutrients, and extracellular material are internalised through folding and invagination of the cell membrane (213). Whilst smaller extracellular material and nutrients are continuously internalised by micropinocytosis, actin-driven membrane protrusions extend to engulf larger particles and volumes of fluid during the process known as macropinocytosis (349). The ultimate fate of internalised material is typically digestion in lysosomal organelles; however, a significant portion of internalised

fluid and vesicular membranes are recycled back to the cell surface, to egress fluid and maintain the plasma membrane surface area (350,351).

To investigate the constitutive process of pinocytosis, HeLa wildtype, *TPCN1*, and *TPCN2* knockout cells were incubated with fluorescently-conjugated dextran for different incubation periods. A smaller 10 kDa dextran was chosen to specifically monitor receptor-independent fluid-phase micropinocytosis, since dextran size influences the mechanism of endocytosis; larger size dextrans, such as 70 kDa, are internalised through macropinocytosis (352). As shown in Figure 5.5, the kinetics and the rate of dextran internalisation and trafficking was similar between wildtype and TPC2-deficient cells, with no significant differences detected between these groups at any incubation periods. In contrast, deletion of TPC1 significantly enhanced the efficiency of dextran trafficking, resulting in increased intracellular dextran fluorescence across all incubation periods relative to wildtype cells (Figure 5.5). Specifically, the rate of dextran internalisation between 5 and 10 minute incubation periods was significantly greater in TPC1-deficient cells compared to both wildtype and TPC2-deficient cells.

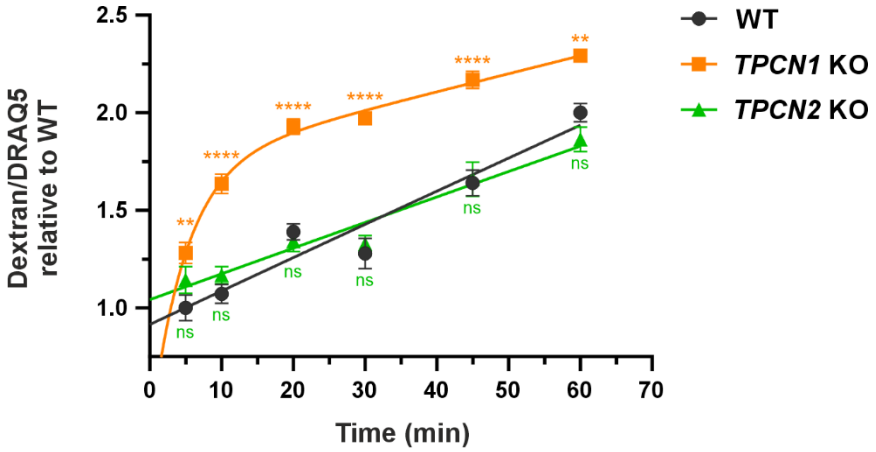

Figure 5.5: Dextran pinocytosis in TPC-deficient HeLa cells. Time course of dextran (10 kDa) internalisation and trafficking in wildtype (WT), *TPCN1,* and *TPCN2* knockout (KO) HeLa cells, n = 9-12 wells. Dextran fluorescence normalised to cell number (DRAQ5) and the data fitted using a non-linear regression model. Data are presented as the mean ± SEM, and probability determined using a two-way ANOVA (**** $P < 0.0001$, ** $P < 0.01$, ns = no significance vs WT).

5.5.1 The cation circuitry of TPC1-dependent pinocytosis

To investigate the underlying cause of increased dextran pinocytosis in the absence of TPC1, the TPC1 signalling pathways were examined. In order to pinpoint whether TPC1-mediated Na^+, or Ca^{2+} fluxes stabilise normal dextran pinocytosis, wildtype TPC1 and the previously verified Na^+-deficient channel mutant TPC1-mut3 ($TPC1^{A280S/V646M/N647G}$) (Chapter 4) were reconstituted in *TPCN1* knockout HeLa cells. Re-expression of wildtype TPC1 restored the pinocytic defect in TPC1-deficient cells, reducing the number of dextran-positive vesicles in line to levels in wildtype cells (Figure 5.6A). Additional analysis showed that alongside an increase in the number of dextran-positive vesicles, the fluorescence intensity of these vesicles was also increased by approximately 10% in TPC1-deficient cells (Figure 5.6B), indicating that dextran was accumulating within intracellular vesicles. Similar to TPC1 re-expression restoring the number of dextran vesicles in *TPCN1* knockout cells, it likewise reduced the fluorescence intensity of these

vesicles back to wildtype values. In regard to TPC1-mut3, overexpression of the Na^+-deficient mutant channel did not rescue the pinocytosis change in *TPCN1* knockout cells. This finding is consistent with the Na^+ modality of TPC1 being required for efficient pinocytic dextran internalisation.

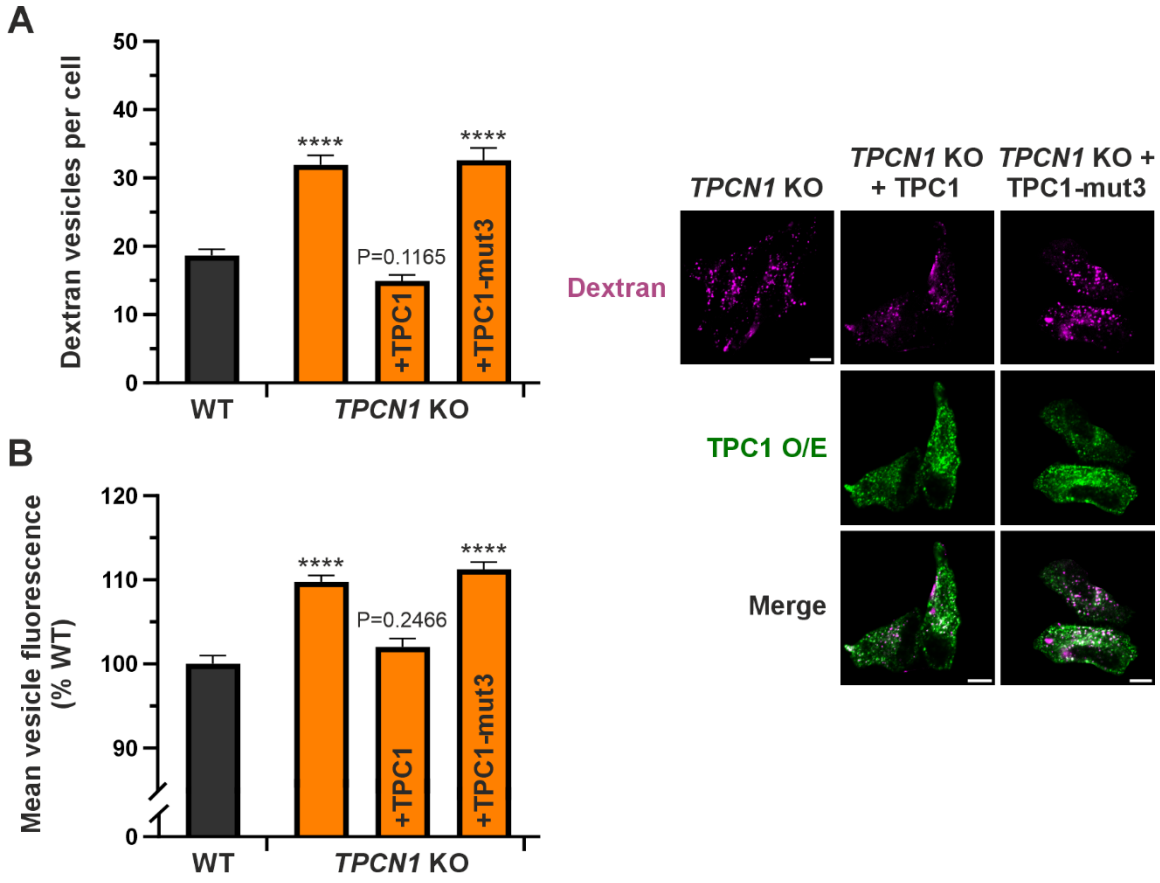

Figure 5.6: Accumulation of dextran in TPC1-deficient cells. Expression of wildtype (WT) TPC1, but not the Na^+-deficient Ca^{2+}-permeable TPC1-mut3 ($TPC1^{A280S/V646M/N647G}$) tagged with mStayGold, restores dextran pinocytosis (30 minute incubation) in *TPCN1* knockout (KO) HeLa cells relative to WT cells. Pinocytosis analysed in respect to the **(A)** number (n = 51-75 cells) and **(B)** fluorescence intensity (n = 759-1556 vesicles) of dextran-positive vesicles. Representative single-cell images, scale bars = 10 µm. Data are presented as the mean ± SEM, and probability determined using a one-way ANOVA (**** $P < 0.0001$ vs WT).

Whilst the above findings show that the pinocytic defect in *TPCN1* knockout cells is TPC1-dependent, they tentatively suggest that TPC1-mediated Na^+ fluxes stabilise pinocytosis. To exclude the involvement of localised Ca^{2+} signals in dextran pinocytosis,

intracellular local and global Ca^{2+} domains were chelated using the same methodology that was used to investigate the requirement of global and local intracellular Ca^{2+} domains during TfR trafficking. It was hypothesised that if TPC1-mediated Na^{+} rather than Ca^{2+} fluxes modulate pinocytosis, then the chelation of localised intracellular Ca^{2+} would not impair pinocytosis. Intracellular local and global Ca^{2+} domains were chelated by the cell-permeant ester (-AM) variants of BAPTA and EGTA respectively. As shown in Figure 5.7, dextran internalisation and trafficking was unaffected by intracellular Ca^{2+} chelation. Although a miniscule increase in dextran fluorescence was observed in cells pre-incubated with the low affinity BAPTA variant TF-BAPTA, this likely represents off-target effects, since BAPTA did not significantly affect dextran pinocytosis. This suggests that intracellular Ca^{2+} signalling is not critical for dextran uptake and that TPC1 likely regulates pinocytosis through a Ca^{2+}-independent mechanism.

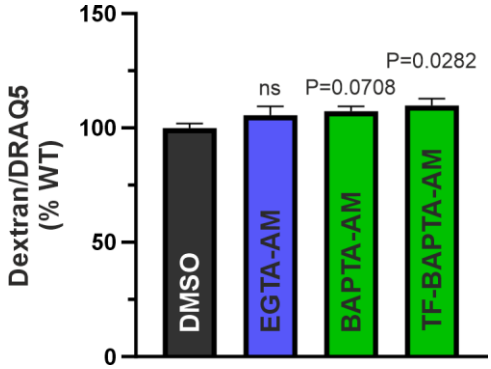

Figure 5.7: Pinocytosis is unaffected by intracellular Ca^{2+} chelation. HeLa dextran uptake and trafficking (30 minute incubation) is unaffected by local Ca^{2+} chelation (BAPTA-AM or TF-BAPTA-AM, 25 µM), or global Ca^{2+} chelation (EGTA-AM, 100 µM), *n* = 18-20 wells. Dextran fluorescence normalised to cell number (DRAQ5). Data are presented as the mean ± SEM, and probability determined using a one-way ANOVA (ns = not significant vs DMSO).

5.6 NAADP regulation of TPC1

5.6.1 Deletion of NAADP-binding proteins

Although the transferrin cycle, LDL pathway, and pinocytosis are constitutive cellular process that require TPCs for efficient trafficking, it remains unclear how TPC cation fluxes are initiated and regulated. The most characterised endogenous activator of TPCs is NAADP, which binds to and gates TPCs via the intermediate accessory proteins Lsm12 and JPT2 (90,91). It was therefore hypothesised that if NAADP-induced TPC1 signalling is required for any of the above endo-lysosomal trafficking pathways, deletion of either NAADP-binding protein would result in the same trafficking defect that was observed in *TPCN1* knockout HeLa cells. To test this hypothesis, CRISPR/Cas9-edited *LSM12* and *JPT2* HAP1 knockout cells were utilised. To verify the deletion of either Lsm12, or JPT2, cell lysates were prepared by Dr Lianne Davis and blotted against both proteins. As shown in Figure 5.8, bands representing Lsm12 (~22 kDa) and JPT2 (~20 kDa) were identified in wildtype and the opposing accessory protein knockout lysates. In contrast, no bands were observed for Lsm12 or JPT2 in their respective knockout cell lysates, confirming that Lsm12 and JPT2 was deleted from these cell lines.

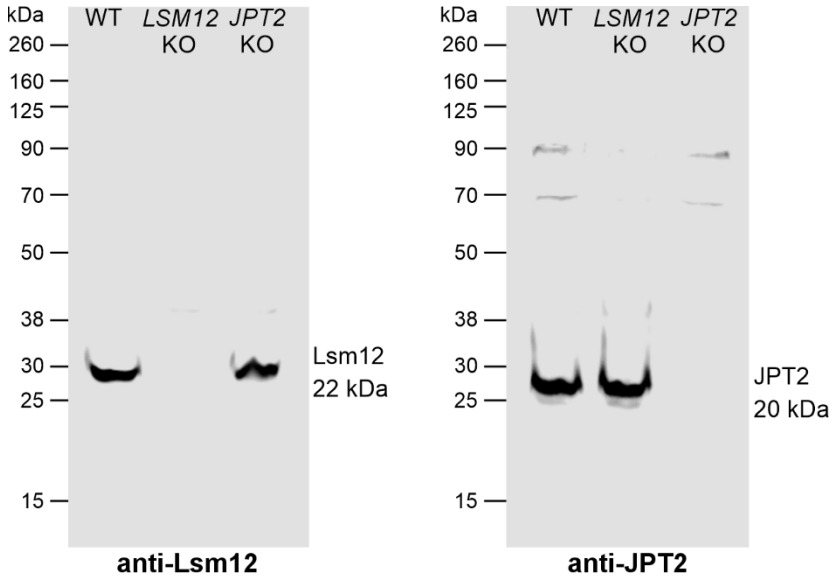

Figure 5.8: Confirmation of *LSM12* and *JPT2* knockout in HAP1 cells. Western blot image of HAP1 wildtype (WT), *LSM12* and *JPT2* knockout (KO) whole-cell protein lysates. Blots were labelled using an anti-Lsm12 and anti-JPT2 antibody and detected using a secondary antibody labelled with a fluorescent near-infrared dye. Experiment performed by Dr Lianne Davis.

In order to evaluate if NAADP modulates TPC1 during the internalisation and trafficking of transferrin, LDL, or dextran, the trafficking of each ligand was monitored in wildtype, Lsm12-, and JPT2-deficient HAP1 cells. In relation to TfR trafficking, the effect of Lsm12 or JPT2 deletion was enigmatic. In JPT2-deficient cells, transferrin uptake and trafficking was suppressed, with this impairment more pronounced after prolonged transferrin incubation times of 20 and 30 minutes (Figure 5.9). In contrast, Lsm12 deletion increased transferrin uptake relative to wildtype cells across the majority of time intervals, returning to wildtype levels after 30 minutes. Detailed analysis indicated that it was only the amount of transferrin internalised which was increased in *LSM12* knockout cells. As the regression gradient was identical between Lsm12-deficient and wildtype cells, this suggests that these cells exhibit the same rate of TfR trafficking.

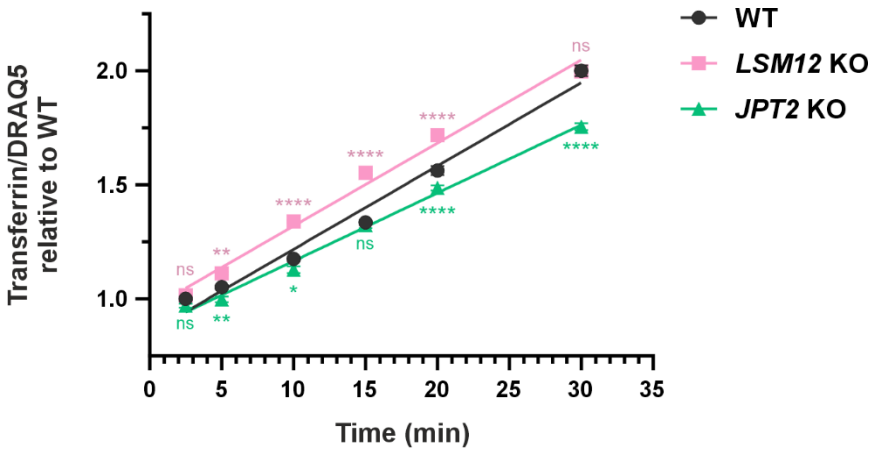

Figure 5.9: TfR trafficking in NAADP-binding protein deficient HAP1 cells. Time course of transferrin internalisation and trafficking in wildtype (WT), *LSM12,* and *JPT2* knockout (KO) HAP1 cells, n = 11-18 wells. Transferrin fluorescence normalised to cell number (DRAQ5) and the data fitted using a linear regression model. Data are presented as the mean ± SEM, and probability determined using a two-way ANOVA (**** $P < 0.0001$, ** $P < 0.01$, * $P < 0.05$, ns = no significance vs WT).

Although the data in Figure 5.4 suggests that TPC1 does not regulate LDLR trafficking, it was still considered appropriate to evaluate the involvement of NAADP within the LDL cycle, given TPC2s clear regulatory role. The fitted regression line indicated that deletion of Lsm12 reduced LDL internalisation and trafficking relative to wildtype HAP1 cells; however, when analysed at single time points, this impairment was only significant at an incubation time of 90 minutes. In contrast, LDL trafficking was significantly altered across several time points in JPT2-deficient cells. At these incubation periods (30, 45, 60, and 120 minutes), LDL trafficking was increased relative to wildtype and *LSM12* knockout cells (Figure 5.10). As the deletion of only one NAADP-binding protein impaired LDL trafficking, future experiments are required to determine if this impairment was a direct consequence of the abolishment of NAADP-induced TPC2 activation.

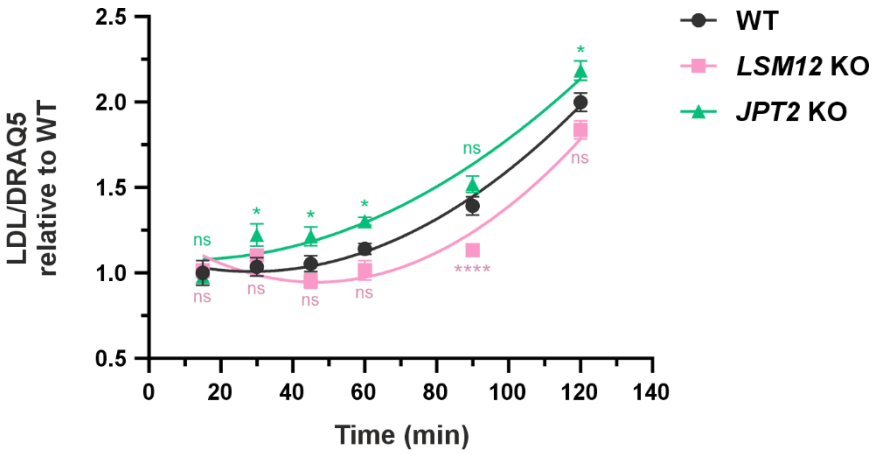

Figure 5.10: LDLR trafficking in NAADP-binding protein deficient cells. Time course of LDL internalisation and trafficking in wildtype (WT), *LSM12,* and *JPT2* knockout (KO) HAP1 cells, n = 9-12 wells. LDL fluorescence normalised to cell number (DRAQ5) and the data fitted using a non-linear regression model. Data are presented as the mean ± SEM, and probability determined using a two-way ANOVA (**** $P < 0.0001$, * $P < 0.05$, ns = no significance vs WT).

Finally, the involvement of NAADP for dextran pinocytosis was investigated using NAADP-binding protein deficient HAP1 cells. Whilst dextran trafficking was unaltered in *JPT2* knockout cells, deletion of Lsm12 drastically enhanced the internalisation and trafficking of dextran by almost 4-fold relative to wildtype cells (Figure 5.11). This increase in dextran pinocytosis mirrored that observed in *TPCN1* knockout HeLa cells (Figure 5.5), tentatively suggesting that Lsm12 *may* facilitate NAADP-mediated TPC1 activation.

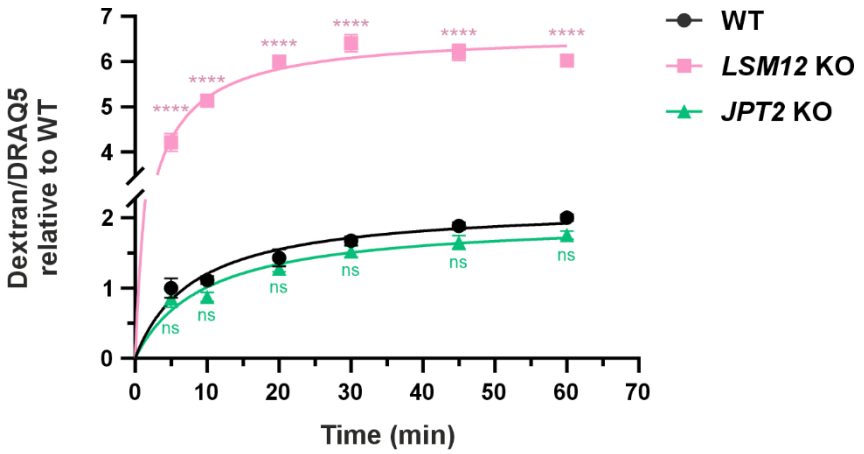

Figure 5.11: Dextran pinocytosis in NAADP-binding protein deficient cells. Time course of dextran internalisation and trafficking in wildtype (WT), *LSM12,* and *JPT2* knockout (KO) HAP1 cells, n = 9-12 wells. Dextran fluorescence normalised to cell number (DRAQ5) and the data fitted using a non-linear regression model. Data are presented as the mean ± SEM, and probability determined using a two-way ANOVA (**** $P < 0.0001$, ns = no significance vs WT).

5.6.2 Inhibition of NAADP-induced TPC activation

As a secondary approach to investigate the NAADP regulation of TPC1 in the context of cell-membrane protein trafficking, cells were pre-incubated with the TPC/NAADP antagonist Ned-19. In parallel to Ned-19, the TPC-dependent inhibitor tetrandrine was used as an alternate method of pharmacologically inhibiting TPC1 activity. As shown in Figure 5.12, dextran trafficking was unaffected by Ned-19 at inhibitor concentrations of 10 µM and 100 µM. In contrast, tetrandrine significantly increased dextran trafficking by approximately 19% relative to DMSO-treated control cells. This pinocytic defect aligned with the increased intracellular accumulation of dextran observed in TPC1-deficient HeLa cells (Figure 5.5). As tetrandrine increased pinocytosis, this suggests that the absence of a Ned-19 effect was likely due to the drugs mechanism of NAADP antagonism.

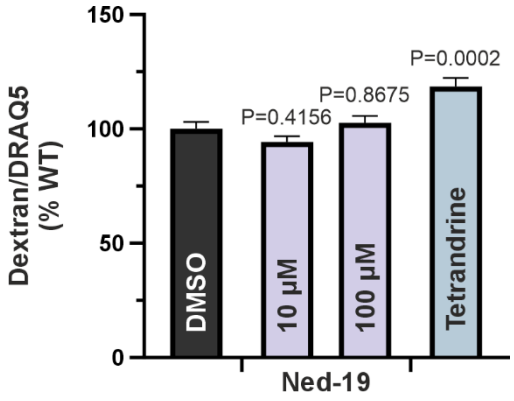

Figure 5.12: Dextran pinocytosis is unaffected by Ned-19. HeLa dextran pinocytosis (30 minute incubation) is unaffected by Ned-19 (10 or 100 µM) but not tetrandrine (10 µM) TPC inhibition, n = 19-20 wells. Dextran fluorescence normalised to cell number (DRAQ5). Data are presented as the mean ± SEM, and probability determined using a one-way ANOVA.

5.7 Phosphoinositide regulation of TPC1

5.7.1 Phosphoinositide synthesis

As the experimental findings from *LSM12* and *JPT2* knockout HAP1 cells and Ned-19 antagonism were inconclusive, the importance of phosphoinositides for TPC1-dependent cell-membrane protein trafficking was investigated. Phosphoinositides, particularly $PI(3,5)P_2$ and PI(3)P, are recognised to regulate both endosomal membrane trafficking (200,240,241) and TPC1 channel activity (106,108,122,138,156). Given this intriguing convergence, it was hypothesised that specific phosphoinositide lipids might mediate cell-membrane protein trafficking.

To evaluate whether the presence of phosphoinositides influence TfR trafficking, the endo-lysosomal phosphoinositides $PI(3,5)P_2$ and PI(3)P were depleted through pharmacological inhibition of their respective catalytic enzymes PIKfyve or PI3K (Figure 5.13A) (236,238). Multiple PI3K inhibitors (wortmannin and VPS34-IN1) and PIKfyve inhibitors (vacuolin-1, YM201636 and apilimod) were pre-incubated in HeLa cells, to validate that any

observation was specifically attributable to enzyme and phosphoinositide synthesis inhibition. Depletion of intracellular PI(3)P or PI(3,5)P_2 was indirectly confirmed through the observation of endosomal vesicle swelling, a consequence of PIKfyve/PI3K inhibition caused by impaired membrane fusion/fission (236,241,353). As shown in Figure 5.13B and Figure 5.13C respectively, HeLa wildtype transferrin trafficking was reduced across all PI3K or PIKfyve inhibitor treatment conditions relative to DMSO-treated cells. To strengthen the idea that inhibition by these agents was through a TPC1-dependent pathway, the same treatments were performed in TPC1-deficient cells. Although a small reduction in transferrin internalisation and trafficking was observed in TPC1-deficient HeLa cells following PI3K and PIKfyve inhibition (~17% and ~15% decrease respectively), the magnitude of this decrease was modest compared with the effect in wildtype-treated cells (~25% and ~30% decrease respectively). The data are therefore consistent with the effect of these inhibitors being mediated partly via a TPC1-dependent pathway, and that phosphoinositide levels impact TPC1 activity. Taken together, these findings suggest a crucial role for phosphoinositides in TfR-mediated iron trafficking.

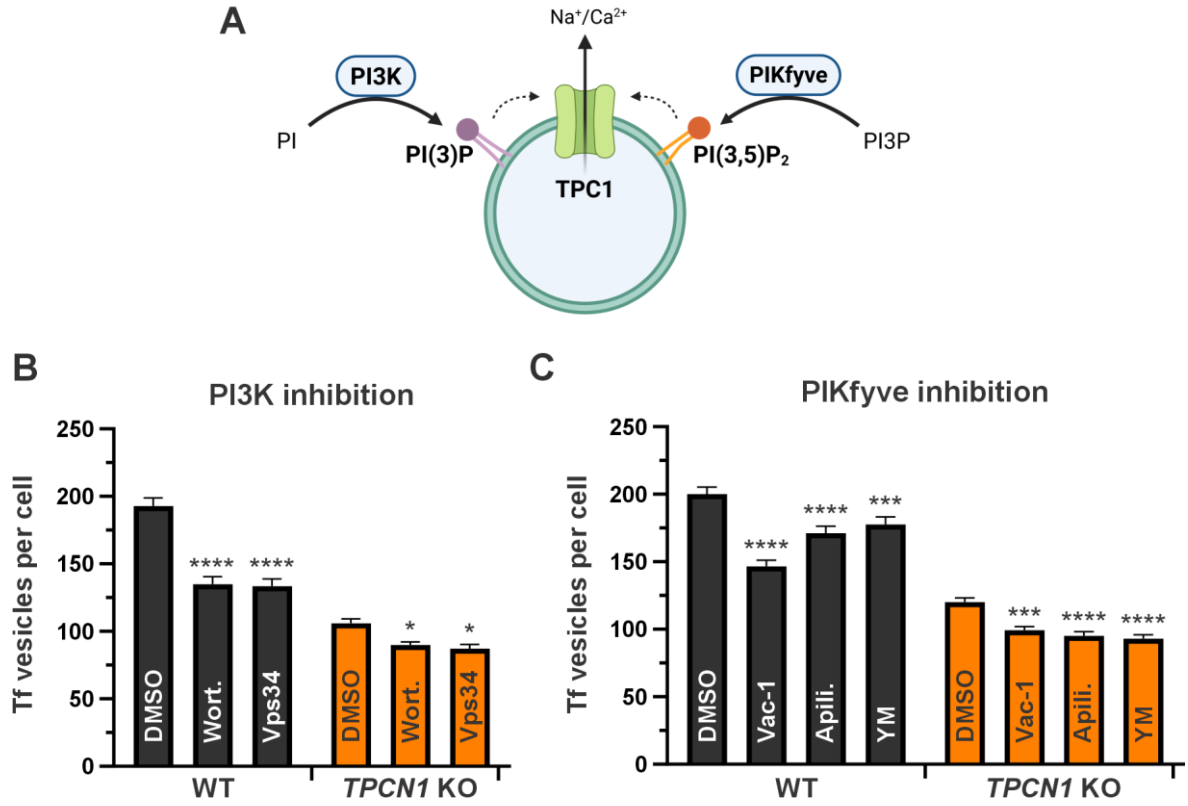

Figure 5.13: Phosphoinositides are required for TfR trafficking. (A) Cartoon of the synthesis pathways of the putative TPC1 activators, PI(3)P and PI(3,5)P_2, by their respective catalytic enzymes PI3K or PIKfyve. Inhibition of the enzymes **(B)** PI3K (1 µM Vps34-IN1, 0.5 µM Wortmannin; n = 60-73 cells) or **(C)** PIKfyve (2 µM Vacuolin-A1, 1 µM Apilimod, 0.5 µM YM201636; n = 70-105 cells), reduce transferrin trafficking. Data are presented as the mean ± SEM, and probability determined using a one-way ANOVA (**** $P < 0.0001$, *** $P < 0.001$, * $P < 0.05$ vs DMSO).

5.7.2 Validation and overexpression of lipid-insensitive mutant

In light of the above findings that phosphoinositides mediate TfR trafficking, it was investigated whether phospholipids regulate TPC1 channel activity during TfR trafficking. To test this, a genetic approach was taken to prevent phosphoinositide-induced activation of TPC1. Previous research by She *et al*. identified key *Mm*TPC1 residues that are essential for TPC1 PI(3,5)P_2 binding and activation, in particular, the IS6 residue Lys331 (106). As the IS6 amino acid sequence is near-identical between human and mouse TPC1

(Figure 1.3), it was hypothesised that mutation of the analogous lipid-binding lysine residue in human TPC1 to alanine (K330A) would also abolish $PI(3,5)P_2$-induced activation. First, the compartmental targeting of the $TPC1^{K330A}$ channel mutant was assessed to ensure correct endosomal localisation. Colocalisation was determined in an identical manner to what is detailed in section 4.7.1 for the Na^+-deficient mutant channel TPC1-mut3 – using markers of early and recycling endosomes and the ER. As expected, $TPC1^{K330A}$ colocalised with wildtype TPC1, as well as Rab5- and Rab11-positive early and recycling endosomes (Figure 5.14).

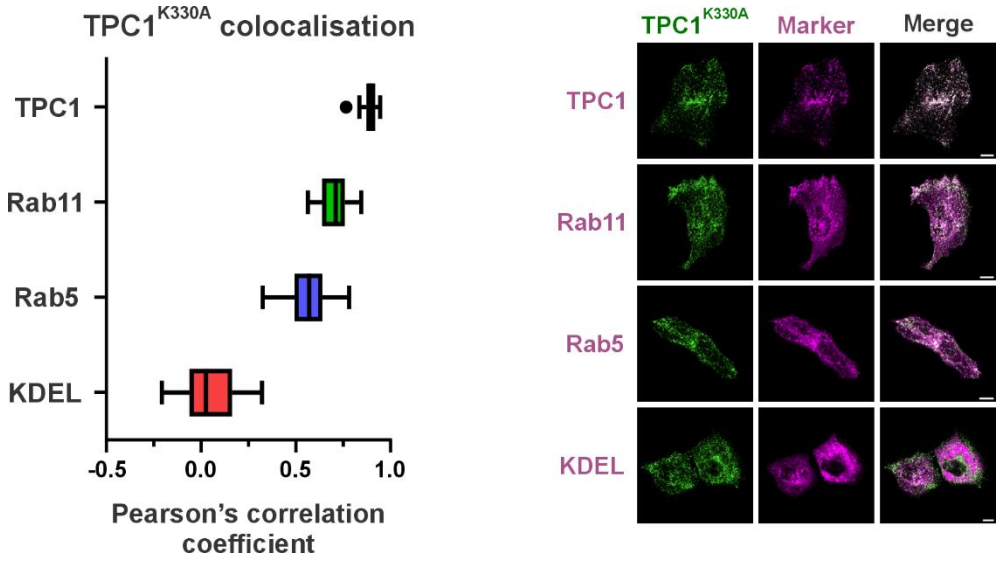

Figure 5.14: $TPC1^{K330A}$ colocalisation. Colocalisation of $TPC1^{K330A}$ tagged with mNeonGreen (in green), in respect to wildtype TPC1, recycling endosome marker Rab11, early endosome marker Rab5, all tagged with mScarlet-I (in magenta), and the fluorescent protein mCherry targeted to the ER lumen by the C-terminus ER retention amino sequence KDEL (in magenta). Colocalisation determined via Pearson's correlation coefficient, n = 28-35 cells. Representative images of each condition, scale bars = 10 µm.

Although *Mm*$TPC1^{K331A}$ does not elicit channel current in response to $PI(3,5)P_2$ (106), abolishment of $PI(3,5)P_2$ activation for the analogous human mutation *Hs*$TPC1^{K330A}$ has not been validated. To directly demonstrate that *Hs*$TPC1^{K330A}$ was insensitive to $PI(3,5)P_2$

activation, whole-endosomal patch-clamp experiments were conducted to record and measure PI(3,5)P_2-induced current amplitudes of isolated wildtype- and *Hs*TPC1^{K330A}-positive endosomes. The following electrophysiology experiments were collaboratively performed by Alice Lin, of Prof. Cheng-Chang Chen's laboratory in Taiwan, and I. As shown in Figure 5.15, mutation of Lys330 to Ala rendered TPC1^{K330A} almost completely insensitive to lipid activation. Specifically, TPC1^{K330A} elicited a significant ~13-fold reduction in PI(3,5)P_2-induced current amplitudes compared to wildtype TPC1, as determined from the respective channel I-V plots (Figure 5.15). These findings support the hypothesis that phosphoinositide activation is abolished by the TPC1^{K330A} mutant.

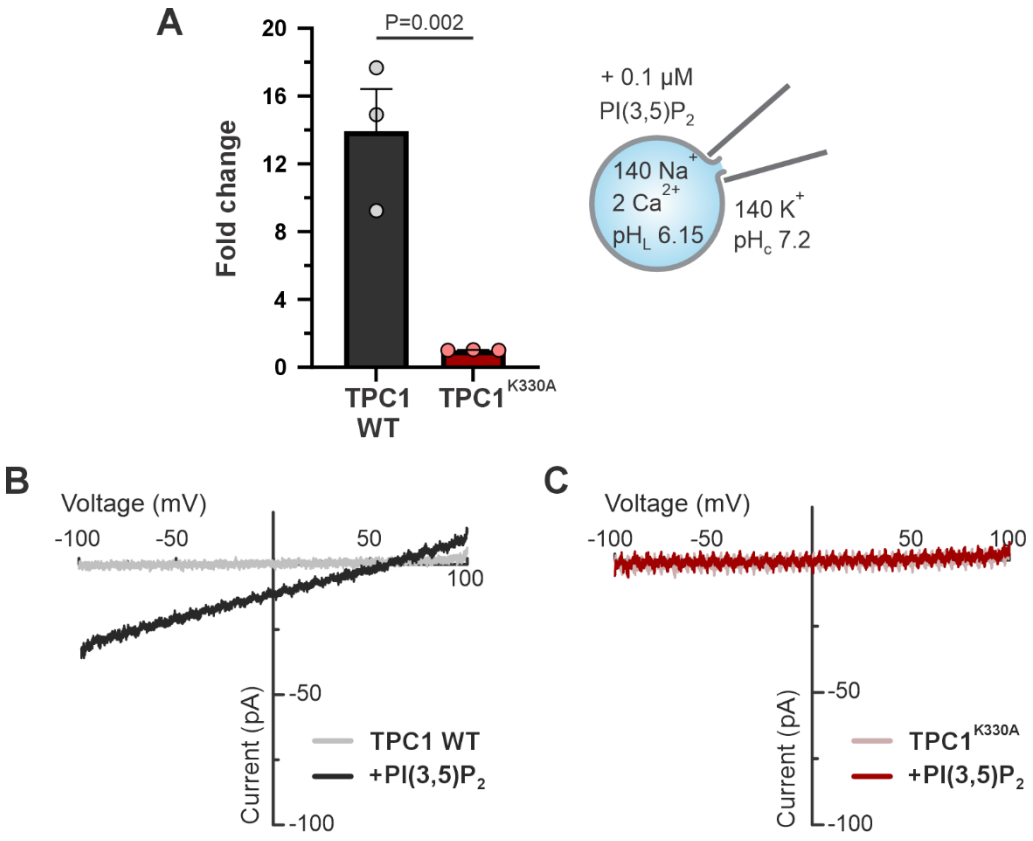

Figure 5.15: TPC1^{K330A} PI(3,5)P$_2$-insensitivity. PI(3,5)P$_2$ activation is abolished in the TPC1^{K330A} channel mutant. **(A)** Fold activation calculated as current amplitude after 0.1 µM PI(3,5)P$_2$ application normalised to basal current (n = 3 recordings). The schematic depicts endosomal patch-clamp recording conditions, with the luminal solution containing 140 mM Na^+ and 2 mM Ca^{2+} (pH 6.15), and cytoplasmic solution containing 140 mM K^+ (pH 7.2). Representative I-V relationships of **(B)** wildtype (WT) TPC1 and **(C)** TPC1^{K330A} mNeonGreen-tagged channels before and after bath application of 0.1 µM PI(3,5)P$_2$, showing robust activation in WT but no activation in the TPC1^{K330A} mutant. Data are presented as the mean ± SEM, and probability determined by a two-tailed t-test.

To evaluate whether direct phosphoinositide activation of TPC1 is required for efficient TfR internalisation and trafficking, the PI(3,5)P$_2$ phospholipid-binding mutant TPC1^{K330A} was transiently expressed alongside wildtype TPC1 in *TPCN1* knockout HeLa cells. In terms of supporting TfR trafficking, whilst the wildtype TPC1 channel fully restored transferrin trafficking in *TPCN1* knockout cells, expression of the mutant channel TPC1^{K330A} did not rescue TfR trafficking in knockout cells (Figure 5.16).

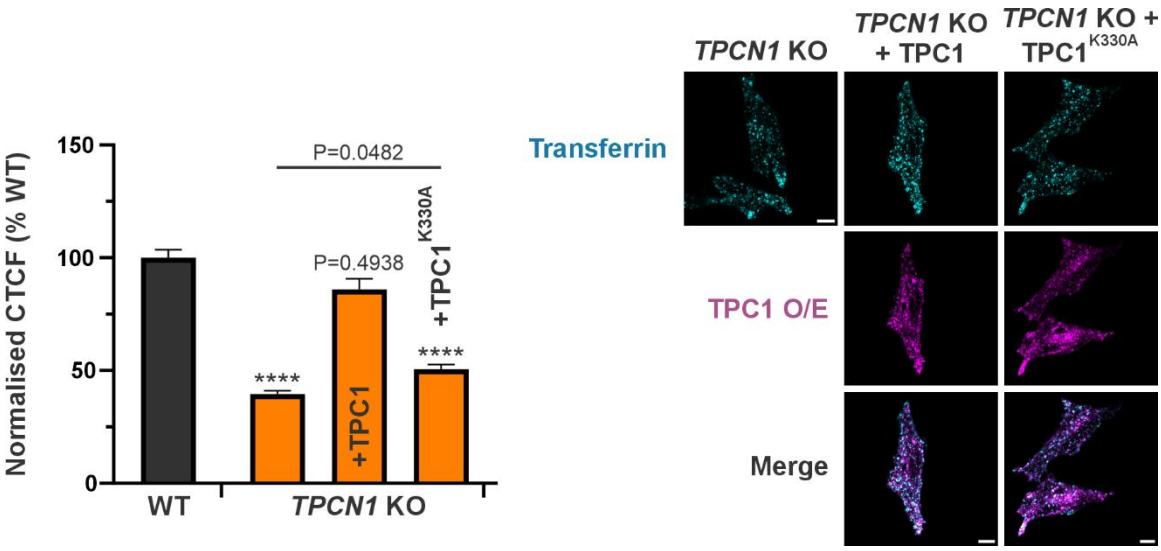

Figure 5.16: PI(3,5)P_2 regulates TPC1-dependent TfR trafficking. Expression of the validated PI(3,5)P_2-binding mutant TPC1^{K330A}-mScarlet-I fails to fully restore transferrin trafficking in *TPCN1* knockout (KO) HeLa cells relative to wildtype (WT) TPC1 re-expression, n = 42-69 cells. Representative single-cell images, scale bars = 10 µm. Data are presented as the mean ± SEM, and probability determined using a one-way ANOVA (**** $P < 0.0001$ vs WT).

Since the data from HAP1 cells and Ned-19 inhibition was ambiguous, it was investigated whether PI(3,5)P_2-evoked TPC1 cation release could be equally important for pinocytosis. To address this possibility, dextran uptake was quantified in *TPCN1* knockout HeLa cells overexpressing TPC1^{K330A} by analysing the number and fluorescence intensity of dextran-positive vesicles. As anticipated, in the absence of TPC1, dextran uptake was increased by approximately 72% (Figure 5.17A). Unlike wildtype TPC1 which completely restored the trafficking defect in TPC1-null cells, the number of dextran-positive vesicles was unaltered in TPC1-deficient cells overexpressing TPC1^{K330A}. In contrast, the fluorescence intensity of dextran-positive vesicles was only modestly restored relative to wildtype fluorescence values (Figure 5.17B), suggesting that PI(3,5)P_2 gating of TPC1 is critical for pinocytosis. Together, these findings establish TPC1^{K330A} as a PI(3,5)P_2-insensitive channel and identify TPC1 as an important target of phosphoinositides for driving TfR trafficking and pinocytosis.

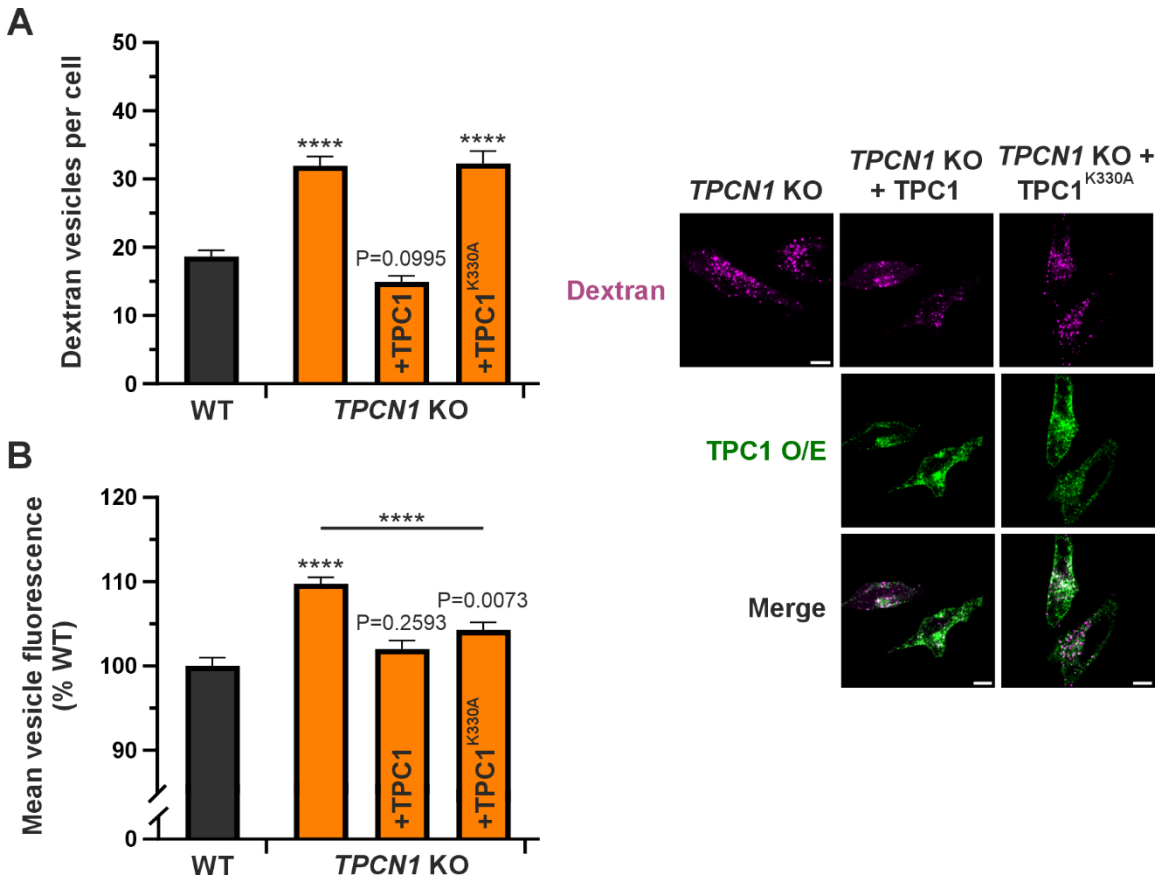

Figure 5.17: PI(3,5)P_2 regulates TPC1-dependent dextran pinocytosis. Expression of the PI(3,5)P_2-binding mutant TPC1^{K330A}-mStayGold fails to fully restore dextran pinocytosis in *TPCN1* knockout (KO) HeLa cells relative to wildtype (WT) TPC1 re-expression. Pinocytosis analysed in respect to the **(A)** number (n = 51-75 cells) and **(B)** fluorescence intensity (n = 759-1556 vesicles) of dextran-positive vesicles. Representative single-cell images, scale bars = 10 µm. Data are presented as the mean ± SEM, and probability determined using a one-way ANOVA (**** $P < 0.0001$).

5.8 Discussion

The aim of this chapter was to determine the specificity of TPC1 in various endo-lysosomal trafficking pathways, in addition to addressing which endogenous messenger(s) regulates TPC1 during these processes. Various molecular tools and techniques, some of which were established in previous chapters, were used to explore the wider role of TPC1 within cell membrane- and protein-trafficking.

5.8.1 TPC1 tissue specificity

Many cellular processes are ubiquitous across multiple cell lines and tissues. In particular, fundamental processes such as vesicular transport and homeostasis are crucial for maintaining a stable intracellular environment. As previously mentioned, the transferrin cycle represents the universal cellular mechanism for iron uptake and homeostasis. Despite all cells expressing and transporting the TfR, certain tissues and cell lines demonstrate enhanced regulation of transferrin internalisation, transport, and recycling. Within this chapter, transferrin/iron trafficking was additionally explored within MEFs (Figure 5.3) and RAW264.7 macrophages (Figure 5.2), two systems physiologically implicated in iron metabolism. In addition to acting as fundamental immune cells, macrophages phagocytose and degrade damaged erythrocytes, the product of which is haem-derived iron. This iron is recycled back to the cell surface and released into the circulation to be internalised by other cells via transferrin-mediated uptake (246). In contrast, fibroblasts are important for regulating iron in connective tissues and the consequent prevention of fibrosis, as well as wound healing and coordinating tissue inflammatory responses (354). Macrophages and fibroblasts therefore represent appropriate cellular models to investigate transferrin and iron transport within, as these cells exhibit enhanced rates of iron absorption and recycling.

Through comparison of the transferrin uptake and trafficking kinetics between wildtype and TPC1- or TPC2-deficient HeLa, RAW264.7, and MEF cells, conclusions were drawn surrounding the selective role of TPC1 within iron homeostasis. All three cell lines exhibited a reduction in TfR internalisation and trafficking following the deletion of TPC1; however, the trafficking defect in TPC1-deficient RAW264.7 cells was modest (~13-20%; Figure 5.2) compared to *Tpcn1*$^{-/-}$ MEF cells (~45%; Figure 5.3). A notable finding was that within *Tpcn1/2*$^{-/-}$ MEF cells, TfR trafficking was further reduced almost to the extent that it

was completely inhibited (Figure 5.3). This finding suggests that TPC1 and TPC2 function in parallel to regulate the transferrin cycle, similar to EGFR trafficking and NAADP-evoked Ca^{2+} signalling in MEF cells, where the loss of both TPC isoforms produces an exacerbated impairment (87,186). This contrasts with the circuitry of phagocytosis, where TPC1 and TPC2 appear to act in series, as deletion of both isoforms has no greater effect on FcR-dependent Ca^{2+} signals or bead uptake (81).

Despite both TPC isoforms regulating the transferrin cycle, TPC2 was unable to restore the transferrin trafficking defect in TPC1-deficient HeLa cells (Figure 3.5). Although TPC2 deletion did reduce TfR trafficking in all the examined cell lines, the magnitude of this impairment was less pronounced than in the absence of TPC1. The reasons why TPC1 is required more than TPC2, are only partially understood. This thesis indicates that the localisation of TPC1 to TfR-positive organelles provides a local source of endosomal Ca^{2+} to drive TfR trafficking. Lysosomal Ca^{2+} appears to drive endo-lysosomal trafficking in a similar way, with lysosomal TPC2-mediated Ca^{2+} signals regulating the transport and trafficking of the EGFR and pathogens towards the lysosome (169,185,269). If the transferrin trafficking defect observed in TPC2-null cells is associated with impaired lysosomal Ca^{2+} efflux, the spatial segregation between lysosomal Ca^{2+} signals and endosomal Ca^{2+} signals could explain the reduced trafficking disruption compared to TPC1 deletion. Nevertheless, the findings presented throughout this thesis suggest that the specific expression and endosomal compartmentalisation of TPC1 is a significant contributing factor.

Combined, the findings from these three cell lines strongly suggest that TPC1 represents a universal conserved mechanism for cellular TfR trafficking and iron regulation. In the context of disease therapeutics, the similar phenotype across TPC1-silenced models shows

that this was not a tissue-specific phenomenon. This could provide efficacious advantages when targeting TPC1 for the treatment of iron-overload disorders, such as hereditary hemochromatosis (355). A limitation of these conclusions is that there is insufficient evidence to say with certainty that TPC1-mediated Ca^{2+} fluxes drive transferrin and iron trafficking across all the investigated tissue types, since the TPC1 ion modality was not evaluated in macrophage and fibroblast cells. Experiments detailing the involvement of TPC1-mediated Ca^{2+} fluxes will first need to be confirmed in multiple tissues before the mechanisms behind TPC1 can be generalised and targeted clinically.

An unexpected observation was the slight increase in TfR trafficking in TPC-deficient macrophages following prolonged transferrin incubation (Figure 5.2). Although this occurrence could be attributed to TPC-deficient cells compensating for the initial reduction in TfR internalisation, this is unlikely, as the same phenotype was not observed in TPC-deficient HeLa or MEF cells (Figure 5.1 and Figure 5.3 respectively). An alternative explanation is that at these later incubation periods, some of the internalised transferrin is recycled back to the cell surface for subsequent transferrin cycles. In relation to other cell types, macrophages exhibit enhanced recycling of endocytosed material, including iron from degraded erythrocytes (246). It is therefore plausible that increased quantities of TfR remained intracellularly within the recycling endosomes of TPC-deficient macrophage cells due to dysfunction of the fast iron recycling kinetics in the absence of TPC1. This hypothesis is strengthened by the findings from HeLa cell recycling experiments, where deletion of TPC1 slowed the recycling of the transferrin-TfR complex back to the cell surface (Figure 3.4B).

5.8.2 TPC1 regulation of endo-lysosomal pathways

It is known that numerous endo-lysosomal trafficking pathways use the same endocytic processes and machinery to facilitate the transport of extracellular cargo. In particular, the transferrin and LDL cycles are both examples of receptor-mediated endocytosis, sharing the same principle of endosomal pH-driven ligand dissociation, as well as similar receptor recycling pathways (210,220). Although TPC2 has already been associated with LDL cholesterol degradation (185), the role of TPC1 in this process is ambiguous. This gap in the literature presented the opportunity to investigate whether near-identical endocytic processes such as receptor-mediated endocytosis are TPC1-dependent.

Astonishingly, deletion of TPC1 in HeLa cells had no effect on the rate or kinetics of LDL internalisation and trafficking relative to wildtype cells (Figure 5.4). In contrast, TPC2-deficient cells exhibited a striking increase in LDL uptake. This finding was consistent with previous studies which have shown that TPC2-deficient mice exhibit phenotypes associated with increased LDL uptake, including increased cholesterol metabolism, fatty liver disease, and obesity (185,356). More importantly, these findings suggest that the role of TPC1 within cell-membrane protein trafficking is beyond a generic requirement. Instead, there is preference for the particular endo-lysosomal pathway TPC1 regulates. This specificity exists between analogous trafficking pathways that share similar endocytic and recycling machinery, such as clathrin recruitment proteins and Rab-GTPases (210,220).

The specific role of TPC isoforms in cellular function is also evident in neurodegenerative disorders. For example, LRRK2^{G2019S}-associated TPC2-dependent lysosomal defects disrupt Ca^{2+} signalling and endo-lysosomal trafficking, resulting in Parkinson's-like symptoms such as impaired vision and movement (255,256). In comparison, TPC1 Ca^{2+}

channel activity does not contribute towards these phenotypes, supporting the conclusions from this chapter that TPC isoforms differentially regulate endo-lysosomal pathways depending on the localised signal required. A logical rationalisation for specific isoform regulation is to ensure the precise decoding of localised ion signals by pathway-specific protein machinery. In macrophages, lysosomal Ca^{2+} signals are segregated between channels on the same vesicle, with TPC2- and TRPML1-mediated Ca^{2+} release regulating dynamin and synaptotagmin-7 activity respectively, thereby affecting the internalisation of different size particles (81,184).

With respect to the kinetics of cell-membrane protein trafficking in wildtype HeLa cells, there were striking differences between the pathway kinetics of each ligand. Despite both representing receptor-mediated endocytic pathways, the fastest membrane trafficking pathway was the transferrin cycle, whilst the slowest was the LDL cycle. These observations are consistent with the reported kinetics of TfR and LDLR trafficking (357); however, exactly why the kinetics of parallel receptor-mediated pathways diverge is unclear. One suggestion is that cell surface TfR levels are increased by approximately 10-fold relative to cell surface LDLR levels (357). This is particularly evident in HeLa cells (358), in which the slower kinetics of LDLR trafficking in this chapter were observed (Figure 5.4). Additionally, the distinct fate of transferrin versus LDL could account for varying trafficking kinetics. Whilst transferrin remains bound to the TfR for rapid recycling, LDL must first dissociate from the LDLR for lysosomal degradation (208,348). Although both the TfR and LDLR are recycled back to the cell surface for subsequent cycles, the recycling of the LDLR is more stringently regulated through its interaction with proprotein convertase subtilisin/kexin-9. This proteinase prevents the pH-induced conformational change of the LDLR necessary for ligand release and receptor recycling (359), resulting in its lysosomal degradation. This protein interaction further sorts the

LDLR for either recycling back to the plasma membrane, or for lysosomal degradation alongside LDL, which further slows trafficking. In contrast, >99% of the apo-transferrin-TfR complex is rapidly recycled back to the cell surface from early endosomes (220).

Despite involved in various endo-lysosomal pathways, the data presented in this chapter suggests that there is specificity in how TPC1 regulates different endo-lysosomal pathways. Whilst TPC1-mediated Ca^{2+} fluxes drive TfR trafficking, TPC1-mediated Na^{+} fluxes are required to stabilise pinocytosis. This was concluded from the opposing trafficking defects in *TPCN1* knockout HeLa cells, where a decrease in TfR trafficking (Figure 5.1), but increase in pinocytosis (Figure 5.6), was observed. These differences could be attributed to the contrasting mechanisms of receptor-mediated endocytosis and pinocytosis, the latter not requiring the formation of a clathrin coat and instead dependent on membrane tension and folding (213). TPC1 deficiency also enhances histamine-induced Ca^{2+} release and the onset of anaphylaxis in mast cells (360), demonstrating that TPC1-mediated ion release selectively regulates cellular processes through the maintenance of endosomal homeostasis.

A recent study has shown that in TRPML1-deficient fibroblast cells, the uptake and trafficking of both transferrin and dextran were unaltered (361). This supports the conclusions portrayed in this chapter, that endo-lysosomal channels exhibit a preference for the precise membrane trafficking pathways which they regulate. Despite TRPML1 and TPC2 residing on acidic lysosomal organelles (80,196), the evidence in this chapter suggests that TPC2 expression is required (to an extent) for transferrin trafficking. This conflicting finding can be explained by the extreme compartmentalisation and segregation of TRPML1- and TPC2-mediated Ca^{2+} signals on the same lysosomal organelle, which have been shown to drive different phagocytic processes (81,184). Unlike TfR trafficking,

dextran uptake and trafficking was increased in TPC1-deficient cells, but unaltered in TPC2-deficient cells (Figure 5.5). Since both global and local intracellular Ca^{2+} domains were nonessential for pinocytosis (Figure 5.7), the TPC1-dependent mechanism regulating pinocytosis is likely different to that of the transferrin cycle, which could explain why TPC1, but not TPC2 cellular expression is required. Although intracellular Ca^{2+} may not be important for micropinocytosis, several studies have shown that extracellular Ca^{2+} is a critical regulator of pinocytosis in *Amoeba proteus* (362,363). Extracellular Ca^{2+} facilitates pinocytosis by concentrating on negatively-charged surface sites at the plasma membrane, which promotes membrane remodelling for the formation of intracellular vesicles (363).

In addition to opposing trafficking kinetics, the findings in Figure 5.6 suggest that the Na^+ modality of TPC1 stabilises dextran pinocytosis. This is a striking contrast to the regulation of iron-bound transferrin trafficking, which was shown in Chapter 4 to require TPC1-mediated Ca^{2+}, but not Na^+ fluxes. Exactly how these TPC1-mediated Na^+ fluxes support pinocytosis will form the basis for future experiments. The current working hypothesis is that in resting cells, TPC1 regulates endosomal membrane potential, osmolarity and membrane tension, through Na^+ efflux (341,353). In the absence of TPC1, the endosomal Na^+ balance is disrupted, resulting in the retention of Na^+ and fluid which leads to endosomal swelling and increased membrane tension (353). The increased tension and rigidity of the endosomal membrane impairs membrane fission, subsequently affecting dextran trafficking and recycling, resulting in the intracellular accumulation of dextran in TPC1-deficient cells (Figure 5.6A). This hypothesis is supported by the findings in Figure 5.6B, which shows that it was not just the number of dextran-positive vesicles which were increased in TPC1-deficient cells but also the amount of dextran within each vesicle. Interestingly, macropinocytosis is also upregulated in Ras-mutant cancer cells, to provide tumour cells with the necessary nutrients for growth and survival (364,365). Given the

clear role of TPC1 in micropinocytosis, it would be beneficial to assess if this regulation also affects macropinocytosis, as this could implicate TPC1 as a therapeutic target for treating drug-resistant macropinocytic tumour cells. Mechanistic details aside, these diverse trafficking defects suggest that TPC1 specifically regulates cell membrane trafficking through distinct ion modalities, thereby addressing the first aim of this chapter.

5.8.3 Phosphoinositide regulation of TPC1

Phosphoinositides are well characterised regarding their regulation of membrane trafficking pathways. The development of pharmacological compounds such as vacuolin-1, YM201636, and VPS34-IN1, has advanced research in vesicular trafficking by enabling researchers to pinpoint the regulatory mechanisms behind cell-membrane protein trafficking. Whilst the aforementioned compounds are inhibitors of either PI3K or PIKfyve, they also exert potent off-site actions on numerous proteins. In particular, wortmannin is a notoriously promiscuous non-specific compound, strongly inhibiting regulatory kinases involved in cellular process such as mitosis (Polo-like kinase 1) (366) and muscle contraction (myosin light chain kinase) (367). The off-site effects elicited by PI3K and PIKfyve inhibitors were exemplified in respect to TfR internalisation and trafficking in TPC1-deficient cells, where trafficking was impaired to a greater extent than in DMSO-treated knockout cells (Figure 5.13B and C). Upon initial comparison, this suggests that these compounds inhibit transferrin trafficking independently of TPC1. However, closer analysis revealed that the effects of PI3K or PIKfyve inhibition were reduced ≤50% in TPC1-deficient cells relative to wildtype cells, indicating that these inhibitors partly exert their action via a TPC1-dependent pathway.

Wortmannin and VPS34-IN1 have previously been shown to reduce transferrin uptake and recycling respectively (236,368), exerting their effect through the regulation of cell surface TfRs or inhibiting endosomal fusion and maturation. Unlike the majority of experiments presented throughout this thesis, the effect of lipid kinase inhibition on TfR trafficking was analysed relative to the number of transferrin vesicles per cell (Figure 5.13). This was a deliberate consideration since these very inhibitors are recognised to cause endo-lysosomal swelling due to the inhibition of membrane fusion/fission (236,272,353,369). Therefore, the enlargement of endo-lysosomal vesicles could increase the size of transferrin-positive vesicles, subsequently increasing total-cell transferrin fluorescence. This means that any reduction in TfR internalisation and trafficking attributed to the inhibition of PI3K or PIKfyve could be obscured. This same logic was also applied when analysing the effect of endo-lysosomal luminal Ca^{2+} chelation on TfR trafficking (Figure 4.8B), since endo-lysosomal swelling and storage disorders have similarly been observed following luminal Ca^{2+} chelation (37,81).

The molecular tools available to investigate phosphoinositide-regulated TPC1 signalling pathways in cellular processes are limited. Therefore, to directly assess the requirement of $PI(3,5)P_2$-induced activation of TPC1 in TfR trafficking, a new $PI(3,5)P_2$-insensitive *Hs*TPC1 channel mutant (K330A) was generated and characterised by electrophysiology. Similar to its *Mm*TPC1 equivalent (K331A), the analogous channel mutant *Hs*TPC1^{K330A} did not demonstrate any channel activity in response to $PI(3,5)P_2$ (Figure 5.15). Although Lys330 appears vital for TPC1 $PI(3,5)P_2$ binding and the subsequent conformational change of IS6 which enables channel opening (106), as with any channel mutation, indirect secondary functional effects are often present. A recent comprehensive study by Saito *et al*. revealed that the mutation of several TPC2 channel residues originally detailed as essential for $PI(3,5)P_2$-induced activation, including Lys204, Lys207, and Ser322 (108), were

likewise required for NAADP stimulation (143). Of particular relevance to this discussion is the Ser322 residue of TPC2. Sequence alignment of *Hs*TPC2 shows that Ser322 represents the IS6 residue equivalent of Lys330 and Lys331 in *Hs*TPC1 and *Mm*TPC1 respectively (Figure 1.3). Therefore, it is reasonable to speculate that the *Hs*TPC1^{K330A} channel mutant characterised in Figure 5.15 may exhibit insensitivity to both PI(3,5)P_2 and NAADP, which would complicate interpretation. Future experiments are required to definitely determine whether this mutation also impairs NAADP-induced activation via the accessory proteins Lsm12 and JPT2.

Details aside, the findings presented in this chapter largely point to TPC1 as a target of phosphoinositides in cell membrane trafficking. This was specifically demonstrated by the inability of the validated TPC1 lipid-insensitive channel mutant TPC1^{K330A} to completely restore the TfR (Figure 5.16) and dextran trafficking (Figure 5.17) defect in TPC1-deficient cells. Previously, it was believed that TPCs were simply activated by phosphoinositides due to the endogenous presence of compartmental-specific phospholipids on endo-lysosomal membranes. However, emerging research has discovered that phosphoinositide gating of TPCs is crucial for Na^+-dependent processes, including the regulation of endo-lysosomal membrane tension, potential, and osmolarity (122,341). This is expected, since Na^+ represents the prominent permeant cation following TPC1 (Figure 4.17) or TPC2 phosphoinositide activation (107,138,141,149). Given that TPC1-mediated Na^+ fluxes were not required for efficient TfR trafficking (Figure 4.20), the data presented in Figure 5.16 provides indirect evidence that phosphoinositide-induced TPC1-mediated Ca^{2+} fluxes are essential for efficient TfR trafficking. Unlike TPC2, TPC1 is also gated by the endosomal-specific phospholipid PI(3)P (156,235). Although depletion of intracellular PI(3)P impaired transferrin uptake and trafficking (Figure 5.13B), its direct requirement for TPC1 activation was not shown, since the TPC1^{K330A} channel mutant was only assessed in

relation to $PI(3,5)P_2$-induced activation. In the future, it would be useful to evaluate if TPC1 exhibits phospholipid specificity for either PI(3)P or $PI(3,5)P_2$ during membrane protein trafficking, in addition to if PI(3)P alters the $P_{Na/Ca}$ relative to $PI(3,5)P_2$.

5.8.4 Role of NAADP in trafficking events

The discovery of the NAADP-binding proteins Lsm12 (90) and JPT2 (91) led to the development of new strategies for investigating the NAADP-TPC signalling axis, specifically through the genetic ablation of these accessory proteins. Using this methodology, previous studies have demonstrated that deletion of NAADP-binding proteins impairs the trafficking of viral particles through the endo-lysosomal system (92,269). It is unclear from the *LSM12* and *JPT2* knockout experiments performed in this chapter whether NAADP is implicated in TfR and LDL trafficking and pinocytosis. This conclusion was based on the findings that only the deletion of a single NAADP-binding protein impaired receptor trafficking and that significant effects were not sustained across the entire time course (Figure 5.9, Figure 5.10, and Figure 5.11). It has previously been shown that the single knockout or knockdown of either *LSM12* or *JPT2* eliminates NAADP-evoked Ca^{2+} release and impairs viral particle trafficking in HAP1 cells (90–92). Despite the availability of the remaining converse singular binding protein, this suggests that co-expression of both Lsm12 and JPT2 is essential for maintaining NAADP-dependent Ca^{2+} signals and trafficking events. Based on this premise, if NAADP was essential for regulating TfR, LDLR, or dextran trafficking, it would be anticipated that the deletion of either binding protein would impair these trafficking pathways. However, as trafficking was only impaired following the deletion of a single accessory protein, this suggests that the observed defect could be associated with impaired local Ca^{2+} signalling mediated by different NAADP-binding proteins, or off-site non-TPC specific effects.

Furthermore, as the effect of TPC deletion on TfR trafficking, LDLR trafficking, and micropinocytosis was not assessed in HAP1 cells, it cannot be definitively concluded whether, or to what extent, TPCs regulate these processes in HAP1 cells.

A striking finding was the substantial increase in dextran pinocytosis in *LSM12* knockout HAP1 cells relative to wildtype cells (Figure 5.11), a finding that mirrored the kinetics and increased trafficking observed in TPC1-deficient HeLa cells (Figure 5.5). In comparison, dextran trafficking was unaltered in *JPT2* knockout HAP1 cells, a somewhat unexpected result, considering that JPT2 has been shown to preferentially bind to TPC1 over TPC2 (91,92). Although JPT2 exhibits a preference for TPC1 binding, both Lsm12 and JPT2 converge to activate TPC1 (92). It has recently been suggested that Lsm12 might act as a potential negative regulator of $PI(3,5)P_2$-dependent TPC activation, by reducing the sensitivity of TPCs to $PI(3,5)P_2$ in the presence of Lsm12 – an inhibition which is relieved following NAADP binding to Lsm12 (370). Given the importance of $PI(3,5)P_2$-mediated TPC1 activation for pinocytosis (Figure 5.17), one explanation for the findings in Figure 5.11 is that Lsm12 regulates $PI(3,5)P_2$-dependent endosomal Na^+ homeostasis via TPC1. In this model, TPC1 and Lsm12 deletion disrupt dextran pinocytosis through two distinct mechanisms that converge on the imbalance of endosomal Na^+ homeostasis. While the loss of TPC1-mediated Na^+ flux in TPC1-deficient cells increases luminal Na^+ retention, Lsm12 deletion uncouples $PI(3,5)P_2$-dependent TPC1 gating, leading to abnormal persistent endosomal Na^+ efflux. In both cases, controlled endosomal TPC1-mediated Na^+ flux is lost, disrupting the maintenance of the endosomal luminal and peri-endosomal Na^+ environment which is required for endo-lysosomal maturation and cargo sorting. As a result, dextran does not progress through the endo-lysosome system and instead accumulates in vesicles, resulting in an increase in dextran vesicle number and fluorescence intensity (Figure 5.6). In line with this hypothesis, an increase and decrease in

endosomal luminal Na^+ concentration would be expected in TPC1- and Lsm12-deficient cells respectively, as a direct consequence of endosomal Na^+ homeostasis dysregulation.

One of the most popular methodologies used to investigate NAADP-induced TPC activation is to inhibit NAADP binding using the antagonist Ned-19 (166). Numerous studies have successfully used Ned-19 to demonstrate that endo-lysosomal pathways are dependent upon NAADP-mediated Ca^{2+} signalling (81,87,169,302,371). However, in relation to the endocytic pathways investigated within this thesis, Ned-19 did not impair TfR trafficking (Figure 3.6) or pinocytosis (Figure 5.12) to any degree. Even at high concentrations (100 μM), no effect was observed, suggesting that the inefficacious effect represents the mechanistic action of Ned-19. It is important to consider if Ned-19 is capable of inhibiting $PI(3,5)P_2$-induced TPC1 activation, especially as $PI(3,5)P_2$ channel gating appears critical for TfR and dextran trafficking (Figure 5.16 and Figure 5.17). Channel recordings of TPC1 reconstituted in lipid bilayers suggest that TPC1 may not share the same biphasic properties as does TPC2, as shown by TPC1 exhibiting insensitivity to NAADP desensitisation (1 mM) and low concentrations of Ned-19 (1 μM) (141). These findings contrast with results from cellular experiments, which indicate that Ned-19 does inhibit TPC1-dependent NAADP Ca^{2+} signalling (193,360). Despite these conflicting findings, evidence supporting Ned-19-induced inhibition of $PI(3,5)P_2$-mediated TPC1 channel activity remains limited. To date, only two supplementary experiments have demonstrated that $PI(3,5)P_2$-induced TPC2 currents were modestly suppressed by high concentrations of Ned-19 (138,169). Although Ned-19 has been shown to directly bind to *At*TPC1 (105), the residues which Ned-19 interacts with on *At*TPC1 are not the equivalent conserved residues on *Mm*TPC1 that $PI(3,5)P_2$ interacts with to induce channel activation (106). It is therefore inappropriate to conclude that NAADP does not regulate TPC1 in the context of TfR trafficking and pinocytosis solely based on the Ned-19 data, as the

inhibitory mechanism of Ned-19 in regard to phosphoinositide TPC1 activation is poorly understood.

Although Ned-19 was ineffective in HeLa cells, a trafficking defect was observed after pharmacologically inhibiting TPCs with tetrandrine (Figure 3.6 and Figure 5.12). The direction of this defect mirrored that observed in *TPCN1* knockout HeLa cells (Figure 5.1 and Figure 5.5), suggesting that the mechanism of tetrandrine was likely attributed to inhibition of TPCs. These results are somewhat conflicting, since both Ned-19 and tetrandrine are suggested to inhibit NAADP-dependent Ca^{2+} release, albeit tetrandrine indirectly through LIMP-2 inhibition and NAADP desensitisation (178). Despite Ned-19 having been reported to reverse high cytosolic labile Fe^{2+} levels in cells overexpressing TPCs (302), Ned-19 did not elicit any detectable effects in iron-bound transferrin trafficking in HeLa cells (Figure 3.6), similar to that observed for MERS-CoV endo-lysosomal trafficking (269). These differences highlight a potential divergence in the underlying mechanisms regulating cellular iron homeostasis. Whilst phosphoinositides appear crucial for the trafficking and recycling of the transferrin-TfR complex (Figure 5.13 and Figure 5.16), NAADP may contribute more extensively to a transferrin-independent regulation of cytosolic labile Fe^{2+} levels, such as through ferritinophagy, which was demonstrated in Figure 3.15B as TPC1-dependent.

Based on the above discussion, a naïve conclusion would be that NAADP is not required for TfR trafficking and pinocytosis. An additional possibility is that cell membrane trafficking is regulated by both phosphoinositide and NAADP second messenger signalling molecules. Whilst microinjection of NAADP has clearly been shown to elicit TPC1-mediated Ca^{2+} release (85,92,123,291), electrophysiological evidence of NAADP-evoked TPC activation on native endo-lysosomal membranes is lacking, possibly due to the loss of

NAADP-binding proteins during endo-lysosome isolation. Emerging research has shown that in the presence of both NAADP and $PI(3,5)P_2$ mimetics, TPC2-A1-N and TPC2-A1-P respectively, synergistic activation of TPC2 occurs (83,143,150), increasing Ca^{2+} release and channel activity to increase lysosomal Ca^{2+} signalling. It remains to be seen if this also transpires for TPC1, since the methodologies and molecular compounds available for evoking NAADP- or $PI(3,5)P_2$-induced TPC1-mediated Ca^{2+} release are either technically challenging, or limited.

5.9 Conclusions

In conclusion, the work presented in this chapter reveals that TPC1 selectively regulates cell-membrane protein trafficking. Through the evaluation of three distinct endo-lysosomal pathways, this chapter shows that TPC1 is not just a general mediator of endo-lysosomal trafficking, but rather precisely coordinates specific membrane trafficking through distinct gating and signalling mechanisms. This chapter also endeavoured to provide an insight into the gating mechanisms of TPC1 in the context of cell-membrane protein trafficking. The findings here reveal that phosphoinositide-induced TPC1-mediated Ca^{2+} fluxes are required for TfR trafficking, but not pinocytosis, instead requiring endosomal TPC1-dependent Na^+ efflux to sustain dextran trafficking. This chapter provides an overview of the specificity of TPC isoforms and their upstream regulation within cell membrane trafficking. As the contribution of NAADP within cell membrane trafficking was not transparent, the possibility that the collective synergy of both phosphoinositides and NAADP is required, remains to be determined.

Chapter 6 – Conclusions and outlook

This thesis has addressed fundamental questions surrounding the lesser known TPC isoform TPC1 in the context of cell-membrane protein trafficking, including why multiple TPC isoforms exist, and how the cation fluxes of TPC1 differentially mediate cellular processes. The aims of this thesis were (1) to understand how TPC1 regulates cell membrane trafficking, (2) to evaluate how the different cation modalities of TPC1 contribute to this regulation, (3) to assess the preferential requirement of TPC1 within various trafficking pathways, and finally, (4) to postulate how TPC1 activation is gated during cell membrane trafficking. These aims have been addressed throughout the thesis by assessing the receptor-mediated endocytosis of the transferrin-TfR complex, using this pathway as the main trafficking model. Specifically, TPC1-null cells have been used to evaluate the importance of TPC1 within several endo-lysosomal trafficking pathways. Additionally, genetic mutation of TPC1 channel properties and Ca^{2+} buffering techniques have assisted in formulating the molecular circuitry of TPC1 activation and the cation fluxes that govern these trafficking processes. Overall, the work from this thesis shows that TPC1 selectively mediates specific cell-membrane protein trafficking pathways through distinct signalling pathways, likely gated by the phosphoinositide $PI(3,5)P_2$.

6.1 Cell-membrane protein trafficking and disease

The findings from this thesis have established a new role for TPC1 within the transferrin cycle and cellular iron homeostasis. I have shown that TPC1-mediated Ca^{2+} nanodomains regulate the endosomal trafficking and recycling of the transferrin-TfR complex (Chapter

4), as well as the cell surface levels of the TfR (Chapter 3). In the absence of TPC1, cell surface levels of the TfR are decreased, as shown by cell-surface immunofluorescence and biotin labelling (Chapter 3), and this consequently reduces the amount of exogenous transferrin which can be internalised across various cell types (Chapter 5). I have also determined how this iron trafficking defect translates to a disease phenotype in cells and mice. Reduced iron-bound transferrin uptake in cells reduces the intracellular iron available for haem synthesis, resulting in a disease-like anaemic iron-deficiency phenotype in mice (Chapter 3). In an attempt to restore intracellular iron levels, ferritin is degraded within lysosomes during the process of ferritinophagy (Chapter 3). Figure 6.1 illustrates the TPC1-dependent mechanism regulating transferrin trafficking and iron homeostasis discovered in this thesis.

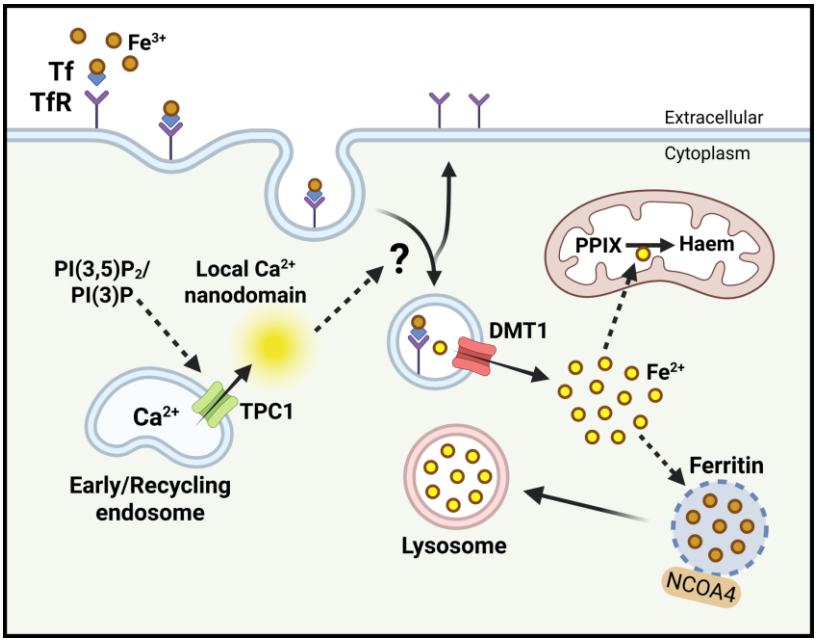

Figure 6.1: Regulatory mechanism of TPC1 within iron homeostasis. Schematic of the hypothesised role of TPC1 in transferrin/TfR trafficking and iron homeostasis. Endosomal phosphoinositide-induced TPC1-mediated Ca^{2+} nanodomains are required for TfR uptake and recycling. TPC1 dysfunction disrupts iron-bound transferrin internalisation, reducing the cytosolic labile Fe^{2+} pool and consequently, the availability of Fe^{2+} for haem synthesis. In response to reduced cytosolic Fe^{2+}, NCOA4 binds to ferritin, tagging ferritin for lysosomal degradation and Fe^{3+} reduction in an attempt to restore cellular Fe^{2+} homeostatic balance.

As a result of the work characterising TPC1 within the transferrin cycle, there is now potential for the therapeutic targeting of TPC1 in the treatment of iron-related disorders. Specifically, individuals suffering from iron-overload disorders, such as haemochromatosis (355), could benefit from the inhibition of TPC1-evoked Ca^{2+} release, thereby complementing existing iron chelation therapies by reducing the rate of transferrin-mediated iron uptake and storage in cells. Inhibiting transferrin/iron uptake via TPC1 could also be beneficial for targeting cancer cells, which require iron to sustain rapid DNA replication and proliferation (283,284). Inhibition of the Fe^{2+}-selective channel TRPML1 has already been shown to eliminate breast cancer cells by increasing lysosomal Fe^{2+} accumulation and triggering ferroptosis (372). Since TPC1 deletion similarly increases lysosomal Fe^{2+} accumulation (Chapter 3), and TPC inhibition has already been shown to suppress tumour growth (160,262,263), inducing ferroptosis through TPC inhibition could represent a potential alternative therapy for treating cancers. However, owing to the diverse role of TPCs in cellular processes, long-term TPC1 inhibition could have adverse effects, including weight gain (356), social behavioural disorders (257), and impaired immune responses (81,360).

In addition to the transport of the transferrin-TfR complex, this thesis has also focused on other membrane trafficking processes including LDLR trafficking and pinocytosis. Although these processes utilise near-identical intracellular trafficking pathways, there are key differences between the uptake mechanism and the fate of the internalised molecule. Whilst TfR and LDLR internalisation represent clathrin-dependent receptor-mediated processes (208,250), the type of pinocytosis investigated in this thesis, fluid-phase micropinocytosis, is clathrin- and receptor-independent, predominantly utilising the CLIC/GEEC endocytic pathway (213). These contrasting endocytic mechanisms could account for the differences in TPC1-dependent ion signalling observed with TfR

trafficking and pinocytosis, whereby receptor stimulation is coupled to intracellular Ca^{2+} signalling to regulate Ca^{2+}-dependent transport machinery (discussed more in subsequent sections).

In view of the findings in this thesis, a potential receptor-mediated cell-membrane protein trafficking pathway regulated by TPC1, is the regulation of glucose transporter protein translocation by the insulin receptor in adipocytes and skeletal muscle cells. This is a trafficking process with tentative links to NAADP-mediated Ca^{2+} signalling and TPC1 regulation, which requires further research to confirm (373–375). Additionally, the analogous process of vasopressin receptor-regulated aquaporin protein translocation in kidney collecting ducts represents a strong candidate for TPC1 involvement, particularly given the high expression of TPC1 in kidney tissues (86,116).

6.2 TPC1 signalling pathways

6.2.1 Endosomal Ca^{2+} fluxes

A common theme presented throughout this thesis is that endo-lysosomes represent a distinct intracellular source of Ca^{2+}. This is one of the few studies which have successfully measured and quantified endosomal luminal [Ca^{2+}] (Chapter 4). Having established endosomes as Ca^{2+}-storing organelles, the necessity for local endosomal TPC1-mediated Ca^{2+} nanodomains in cell-membrane protein trafficking was demonstrated by chelating endosomal luminal Ca^{2+} and buffering peri-endosomal Ca^{2+} (Chapter 4). It is hypothesised that endosomal-derived TPC1-mediated Ca^{2+} efflux drives TfR trafficking by regulating the activity of Ca^{2+}-dependent fusion and trafficking proteins (see section 6.4). Although most of the focus of this thesis has been on TPC1, this thesis also suggests that Ca^{2+} signals from endosomal channels, such as TPC1 and TRPML2, are segregated from one another.

This segregation is similar to how TPC2- and TRPML1-dependent Ca^{2+} signals are differentially decoded on lysosomes (81,184), thereby enabling endosomal channels to recruit specialised Ca^{2+}-binding proteins, such as calbindin and calcineurin, to drive different cellular physiologies.

Alongside establishing endosomes as a Ca^{2+}-regulated organelle, this thesis has shown that endosomal Ca^{2+} signalling can be segregated from global ER-dependent Ca^{2+} signals. Given their size and low luminal [Ca^{2+}], it might be expected that ER-amplification of endosomal Ca^{2+} signals would be required to convert small Ca^{2+} signals into large global transients (83,191,192). Remarkably, the findings from this thesis show that endosomal Ca^{2+} fluxes can drive completely different cellular processes compared to ER global Ca^{2+}. Whilst this is true for transferrin trafficking, others have observed that TPC-ER crosstalk via CICR occurs for complex processes such as phagophore formation during autophagy (190,192). Whether endosomal Ca^{2+} signalling operates independently, or in combination with ER-evoked Ca^{2+} signals likely depends upon the requirement for a localised or global source of Ca^{2+}. Cellular processes which have previously been shown to require localised Ca^{2+} signals mediated by TPC1, such as viral and bacterial toxin trafficking (116,117,169), are therefore likely to be exclusively dependent on Ca^{2+} release originating from endosomal, rather than ER Ca^{2+} stores. For physiological processes where local Ca^{2+} release from either TPC isoform is important, it would be interesting to know the relative contribution of endosomal Ca^{2+} and lysosomal Ca^{2+} signals for these processes, by monitoring TPC1- and TPC2-mediated Ca^{2+} signals using GECIs. This would assist in understanding how Ca^{2+} signals are compartmentalised between organelles and how channel-specific Ca^{2+} signals are decoded.

6.2.2 Endosomal Na^+ fluxes

A significant contribution this thesis has made to the TPC1 field is the generation of two new *Hs*TPC1 channel mutants, namely TPC1-mut3 ($TPC1^{A280S/V646M/N647G}$; Chapter 4) and the PI(3,5)P_2-insensitive channel $TPC1^{K330A}$ (Chapter 5). These channel mutants behave in a similar way to their *Hs*TPC2 (107) and *Mm*TPC1 (106) equivalents, suggesting that both the selectivity filter and the PI(3,5)P_2 binding site are conserved across mammalian TPC isoforms. With these new channel mutants it is now possible to examine which cellular processes require either Na^+ or Ca^{2+} fluxes as well as the gating mechanism responsible for these fluxes, by overexpressing these channels in mammalian TPC1-deficient cells. In the case of TPC1-mut3, the criticality of Ca^{2+} and Na^+ fluxes was demonstrated for TfR trafficking (Chapter 4) and pinocytosis (Chapter 5) respectively. It is believed that these tools will benefit not just researchers interested in how the TPC1 ion modalities regulate cell-membrane protein trafficking, but studies asking why TPC1 maintains multiple ion modalities to drive different signalling pathways and cellular processes.

It was not just the Ca^{2+} modality of TPC1 which was evaluated in this thesis. In Chapter 4 the relative permeability of TPC1 was assessed in relation to Na^+ and Ca^{2+} ions. Despite showing that TPC1 is a Na^+-selective channel when activated by PI(3,5)P_2, residual currents were still detected in the absence of Na^+ conductance, indicating that TPC1 is also permeable to other cations such as Ca^{2+}. These two ionic fluxes drive either electrical (Na^+) or biochemical (Ca^{2+}) signalling pathways. Exactly how these two ion fluxes differentially mediate membrane trafficking is not yet clear, since both cations pass through TPC1 when activated by PI(3,5)P_2.

As the techniques and tools for measuring intracellular [Na^+], such as small molecule-based and genetically encodable Na^+ indicators (376), are limited, the circuitry of TPC1-

dependent Na^+ fluxes within pinocytosis (Chapter 5) was not explored. It is unlikely that TPC1 stabilises pinocytosis through TPC1-dependent changes in endosomal pH, since TPC1 expression does not affect the resting luminal pH of early endosomes (Chapter 4) or other endo-lysosomal compartments (116,137). One explanation is that TPC1 stabilises pinocytosis by regulating the ionic and osmotic composition of the endosomal lumen through phosphoinositide-evoked Na^+ release. In this context, TPC1 Na^+ efflux supports the extrusion of water from endosomes, in turn, lowering membrane tension by reducing the hydrostatic pressure within the endosomal lumen, which is essential for vesicle fission and trafficking (353). A similar precedent is required for phagosome fission and tubulation. Here, TPC-mediated Na^+ fluxes assist in maintaining the Na^+ gradient between the endo-lysosomal lumen and cytosol, which is critical for regulating endomembrane tension during phagosome membrane deformation (341). Alternatively, TPC1-mediated ion release may indirectly modulate putative endo-lysosomal membrane transporters, such as NHE3/5/6, which transports Na^+ into the endosomal lumen (324), thereby influencing endosomal membrane potential and osmolarity.

In addition to driving osmotic changes, TPC1-mediated Na^+ efflux also acts as a counter-ion to reduce the lumen-positive charge in early endosomes, contributing to the regulation of the endosomal membrane potential (approximately +153 mV, lumen relative to cytosol) (225). It is important to consider how the electrical potential across endosomal membranes may influence cell membrane trafficking, especially as TPC1-mediated Na^+ fluxes appear to stabilise micropinocytosis (Chapter 5). TPC1 dysfunction will increase the lumen-positive membrane potential, as Na^+/Ca^{2+} counter fluxes are disrupted. Changes in membrane voltage will affect the surface charge of endosomes and potentially, the electrostatic interactions between negatively-charged endosomal phosphoinositides and lipid-binding proteins (377). This could affect the recruitment of proteins such as EEA1,

which rely on electrostatic interactions for the tethering and fusion of Rab5-positive early endosomal membranes (378). As TPC1 is voltage-sensitive (106), TPC1 functions as a negative-feedback regulator of membrane potential, whereby increased lumen-positive voltage reduces the open probability of TPC1 for cation efflux (122). The voltage-sensitivity of TPC1 likely represents a conserved evolutionary feature, as TPC2 is voltage-independent (108). Whether the loss of TPC1 voltage-sensitivity contributes to the pinocytic defect observed in TPC1-deficent cells is unclear; expression of the voltage-insensitive channel mutant *Hs*TPC1^{R539I} (122) would provide functional clues if the VSD2 of TPC1 is required.

6.2.3 Endosomal pH

Finally the importance of endosomal pH regulation by TPC1 was investigated. The work presented in Chapter 4 precisely quantified the absolute pH of early endosomes in the presence and absence of TPC1. Despite being a pH-sensitive channel (122), these findings demonstrate that the resting luminal pH of early endosomes is not influenced by TPC1. Although TPC1 and TPC2 appear to not influence endo-lysosomal pH (116,185), other H^+ permeant channels such as TRPML1 have been shown to regulate lysosomal pH (203,379). Dysregulation of endo-lysosomal pH results in the luminal accumulation of ions, lipids and substances, inevitably leading to endo-lysosomal storage disorders such as MLIV and Niemann–Pick disease type C1 (37,203). Despite TPC1 being reported as a H^+-selective channel (141), TPC1 deletion did not alter early endosomal pH (Chapter 4). This suggests that TPC1 may not be coupled to V-ATPase function and that other pH-sensitive endosomal channels such as TRPML2, might represent the more prominent counter-ion pathway for endosomal pH regulation (196).

6.3 Regulation of TPC1 cation release

The most important finding from this study was that $PI(3,5)P_2$-induced TPC1-mediated Ca^{2+} signals are essential for regulating cell-membrane trafficking pathways. This is the first time that $PI(3,5)P_2$-evoked Ca^{2+} signals have been associated with TPC1 for a physiological process. Cell surface phospholipids such as $PI(4,5)P_2$ are well-established in regulating plasma membrane VGCCs for intracellular Ca^{2+} signalling (234); however, there is limited evidence of phosphoinositides regulating TPC Ca^{2+}-dependent processes. Although TPC2-A1-P/$PI(3,5)P_2$-evoked TPC2 Ca^{2+} release supports the Ca^{2+}-dependent fusion process of lysosomal exocytosis (149), these findings are ambiguous, as the NAADP mimetic TPC2-A1-N did not affect exocytosis (149). Nevertheless, there is strong evidence that phosphoinositides can drive Ca^{2+}-dependent cellular processes via endo-lysosomal channel modulation. In particular, TRPML1 $PI(3,5)P_2$-mediated Ca^{2+} signalling influences endo-lysosomal trafficking through the activation of calmodulin and the regulation of membrane fusion and fission proteins (200,380). Similarly, $PI(3,5)P_2$ and PI(3)P mediate TRPML2 and TRPML3 Ca^{2+} channel activity respectively. These localised Ca^{2+} signals regulate key membrane fusion proteins involved in mediating endo-lysosomal vesicle motility and autophagy (198,381). The finding that phosphoinositides also modulate TPC1 Ca^{2+} signals for endo-lysosomal trafficking paves the way for a relatively unexplored avenue in endo-lysosomal Ca^{2+} signalling.

A major misconception within the literature is that the plastic ion-permeability of TPCs renders the channel selective to either Ca^{2+} or Na^{+} ions when activated by NAADP or $PI(3,5)P_2$ respectively. Whilst it is reasonable to say that the relative permeability of TPC2 is dependent upon the activating ligand, it is inaccurate to exclusively associate NAADP with Ca^{2+} release, and $PI(3,5)P_2$ with Na^{+} release. Indeed, TPC2 still exhibits substantial

Ca^{2+} signals in response to the $PI(3,5)P_2$ mimetic compound TPC2-A1-P (143,149,150). Within Chapter 4, the $P_{Na/Ca}$ of TPC1 was shown to be more Na^+-selective in response to $PI(3,5)P_2$ activation. It is currently unknown if TPC1 also exhibits biased agonism, as only a modest change in the $P_{Na/Ca}$ has been detected in response to NAADP (141). Measuring NAADP-evoked Ca^{2+} currents on isolated endosomes is technically challenging, since NAADP responses are notoriously fragile and seldom preserved, meaning they cannot be reliably reconstituted. Whilst measuring NAADP-evoked Ca^{2+} responses *in situ* would be an alternative approach, the instability and availability of membrane-permeant compounds (NAADP-AM and MASTER-NAADP (161,162)) have precluded these experiments within this thesis. The future development of stable TPC1 NAADP (and $PI(3,5)P_2$) mimetics will hopefully enable robust current and Ca^{2+} measurements in response to NAADP, to elucidate if TPC1 is similarly promiscuous.

Despite a poor selection of molecular tools available to investigate the contribution of NAADP in the context of cell-membrane protein trafficking, efforts were made to determine the role of NAADP and $PI(3,5)P_2$ on TPC1 gating. Whilst the role of NAADP in cell membrane trafficking was ambiguous, a clear involvement for $PI(3,5)P_2$ and PI(3)P was established (Chapter 5). Two possible explanations exist for how $PI(3)P/PI(3,5)P_2$ are recruited for membrane trafficking pathways. The first is that the resting levels of phosphoinositides might provide sufficient constitutive Ca^{2+} efflux for membrane trafficking. Alternatively, cell surface receptors such as the TfR could evoke endosomal Ca^{2+} signals through synthesis of new phosphoinositides.

A receptor-stimulated increase in phospholipids, particularly PIP_2, has been reported in numerous cell types, including platelets (thrombin receptor) (382), macrophages (FcR) (383), and neuronal (NMDA receptor) cells (384). In these cells, cell surface receptor

stimulation couples to kinase activation, resulting in phosphorylation of PI(4)P and the rapid synthesis of PIP_2 at the plasma membrane, which is required for membrane rearrangement and receptor uptake. Similar to how stimulation of the aforementioned receptors activate lipid kinases, the binding of transferrin to the TfR activates Src-tyrosine kinases and PI3Ks. Although the specific transferrin-induced TfR structural changes that activate kinases are unknown, Src-tyrosine kinases have been shown to phosphorylate endocytic machinery necessary for TfR internalisation (385), whilst PI3Ks coordinate the synthesis of PI(3)P for TfR trafficking (386,387). Considering the importance of phosphoinositide TPC1 regulation for transferrin trafficking (Chapter 5), the coupling of TfR stimulation and PI3K/PIKfyve-dependent phosphoinositide synthesis may provide one mechanism by which transferrin-induced phosphoinositide-evoked TPC1 Ca^{2+} signals (Chapter 4) are stringently regulated.

Few groups have provided a detailed analysis of the levels of phosphoinositides or NAADP in TPC-dependent processes. Therefore, it would be interesting to know the exact levels and cellular distribution of PI(3)P/$PI(3,5)P_2$ (or NAADP) during cell-membrane protein trafficking. Whilst radioactive measurement of these molecules is not permitted in the Galione laboratory, the emergence of new phosphoinositide biosensors might assist in visualising phospholipid dynamics. These biosensors rely on lipid-binding protein motifs, such as FYVE and 2xPX, to detect cellular levels of PI(3)P and $PI(3,5)P_2$ respectively, with high affinity and selectivity (235,241). If the interaction of the TfR and transferrin *does* act as a stimuli that couples to PI(3)P/$PI(3,5)P_2$ synthesis, an increased accumulation and brightness of fluorescently-tagged FYVE and 2xPX proteins would be anticipated on early and recycling endosomes, in order to evoke TPC1-mediated Ca^{2+} release.

6.4 Downstream TPC1 cation decoding

An exciting and somewhat unexplored avenue within this thesis is how localised TPC1-mediated Ca^{2+} release couples to downstream decoding proteins to regulate membrane trafficking. Several groups have performed TPC interactome studies which have identified TPC1-protein interactions within cells, some of which are Ca^{2+}-dependent proteins crucial for mediating endocytic uptake and membrane fusion/fission within endo-lysosomal trafficking pathways. Examples of interaction proteins include vesicle trafficking and SNARE complexes such as syntaxins-7, -8, -12, and -16 (175,187), which facilitate membrane docking and the fusion of vesicle lipid bilayers (388). Whilst the above syntaxins mediate bacterial toxin (117) and cell-membrane channel transport (389,390), syntaxins 7 and 16 do not appear to regulate TfR trafficking and recycling (391,392), which is instead regulated by Rab-GTPases. Rab fusion proteins, including Rab5, 7, and 11, have been identified in TPC interactome screens (175,187), with Rab7 implicated in TPC2-depedent trafficking pathways (175,176). Given that the endosomal Rab5 physically interacts with TPC1 (176) and that Rab5 expression stringently regulates endo-lysosomal TfR trafficking (393,394), Rab5 may enhance $PI(3,5)P_2$-induced TPC1 activation and Ca^{2+} release to drive TfR trafficking, similar to Rab7 and TPC2 in the context of melanoma progression (176). Alternatively, TPC1-mediated Ca^{2+} release may couple to Rab5/11 modulation to increase membrane fusion and endosomal trafficking and recycling.

In the context of phagocytosis, TPC1-mediated Ca^{2+} release appears to stimulate the fission protein dynamin to a greater extent than TPC2-mediated Ca^{2+} release (81). Endocytosis and recycling of the transferrin-TfR complex is also dynamin-dependent; Upon GTP hydrolysis, the structural helices of dynamin constrict, facilitating the fission of invaginated cell-surface TfR clathrin-coated pits and recycling endosomes as they return to

the plasma membrane (395,396). A pilot experiment ($N = 2$) performed with the dynamin inhibitors Dynasore and Dyngo-4a (397) supports the premise that the transferrin cycle is dynamin-dependent in HeLa cells, since these inhibitors ablated the transferrin cycle in wildtype cells. If TPC1-mediated Ca^{2+} release regulates dynamin, stimulating dynamin activity independently of Ca^{2+} using a selective activator (398), or expression of a constitutively active dephosphorylated form of dynamin (S764A) (399), should restore the TfR uptake and trafficking defect in *TPCN1* knockout cells. In view of this, TPC1-mediated Ca^{2+} signals may control dynamin activity across multiple clathrin- and receptor-mediated endocytic pathways, such as phagocytic, transferrin, LDL, and EGF uptake, which are triggered by interactions between cell surface receptors and interacting ligands.

6.5 Final conclusions

In summary, the results in this thesis have identified a role for TPC1 within a new homeostatic cell-membrane trafficking pathway, the transferrin cycle, which TPC1 regulates to ensure cellular iron balance. Using this pathway, this thesis has shown that endosomes exist as phosphoinositide-regulated Ca^{2+}-containing organelles, that generate their own localised Ca^{2+} nanodomains to support cell membrane trafficking. These endosomal signalling pathways are distinct from global ER-mediated Ca^{2+} signals and segregated from other endo-lysosomal channels, a trait likely used to ensure the recruitment of specialised endocytic machinery. This thesis also shows that the Ca^{2+} modality of TPC1 is more than just an evolutionary trait, and that TPC isoforms differentially mediate distinct endo-lysosomal trafficking pathways through selective Ca^{2+} and Na^{+} channel fluxes. Overall, this thesis highlights the importance of TPCs within cellular physiology, by expanding our current knowledge of how TPC1 specifically regulates cell membrane- and protein-trafficking.

Appendix A – Supplementary Figures

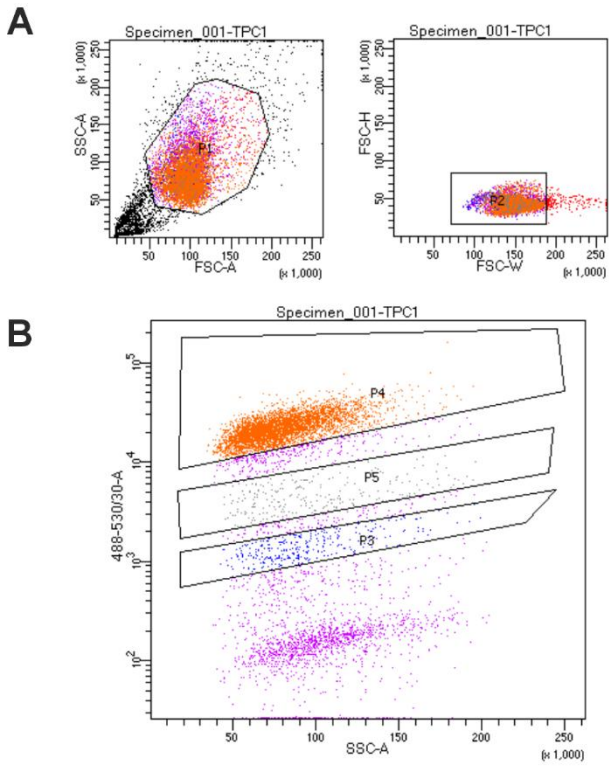

Figure A.1: Cell sorting parameters. (A) Single HeLa cells overexpressing *Hs*TPC1-mNeonGreen-ERES were gated according to size. **(B)** Single cells were sorted by protein expression, based on the relative fluorescence of mNeonGreen. Low, moderate, and high TPC1 expression is represented by P3, P5, and P4 gates respectively.

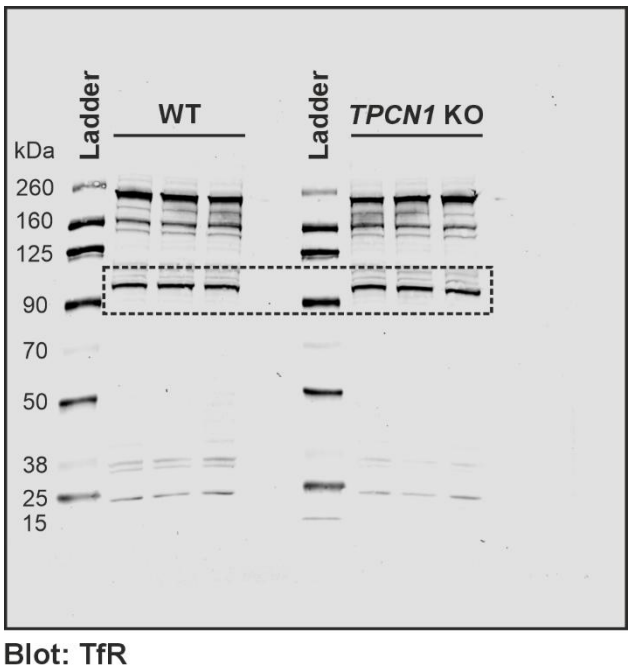

Figure A.2: TfR expression in whole-cell HeLa lysates. Representative Western blot image of endogenous TfR protein in wildtype (WT) and *TPCN1* knockout (KO) HeLa whole-cell lysates, in triplicate (cropped where indicated by dotted box in Figure 3.7).

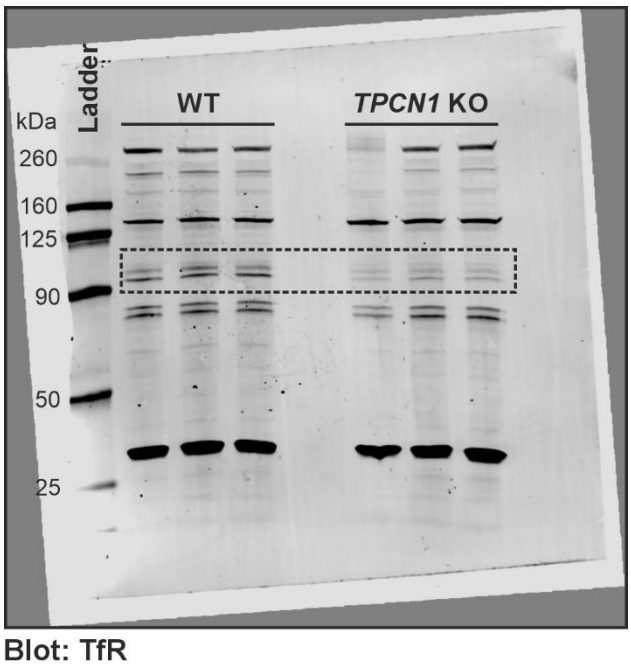

Figure A.3: Cell surface biotinylated TfR protein levels. Representative Western blot image of biotinylated cell surface TfR protein in wildtype (WT) and *TPCN1* knockout (KO) HeLa biotin-isolated protein fractions, in triplicate (cropped where indicated by dotted box in Figure 3.9).

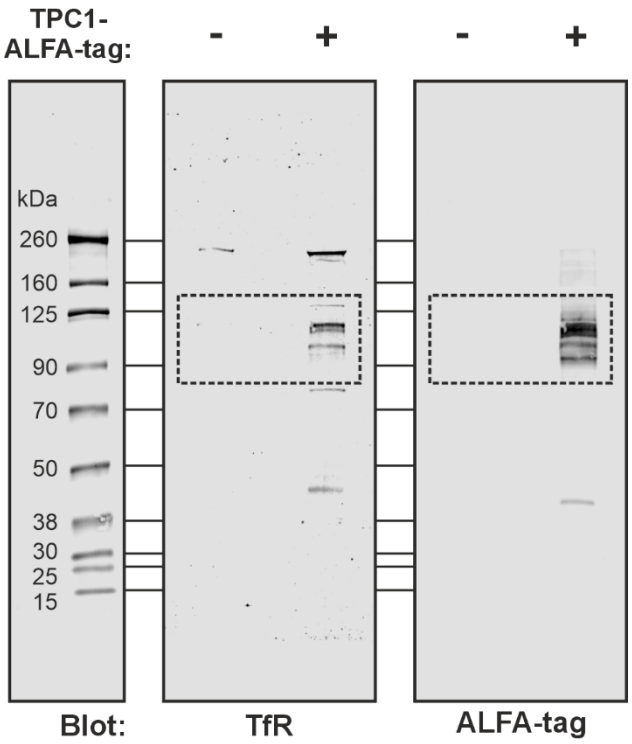

Figure A.4: TPC1 forms a complex with the TfR. Western blot image of a representative co-immunoprecipitation reaction of the TfR and TPC1 fused to an ALFA-tag epitope (cropped where indicated by dotted box in Figure 3.10). Blots were co-labelled with anti-ALFA-tag and anti-TfR antibodies and detected using secondary antibodies labelled with spectrally distinct NIR fluorescent dyes (results shown as separate channel images for clarity).

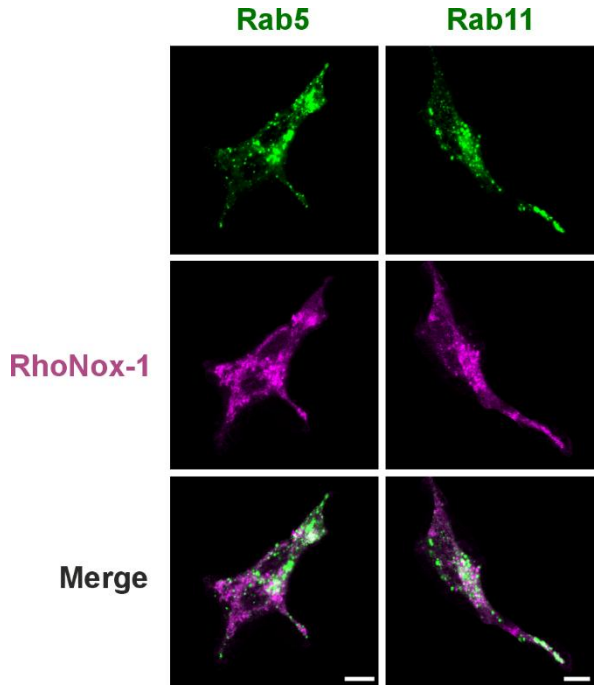

Figure A.5: RhoNox-1 endosomal distribution. Single-cell images of cytosolic labile Fe^{2+} staining using RhoNox-1 show no overlap with Rab5-positive early endosomes, or Rab11-positive recycling endosomes, scale bars = 10 μm.

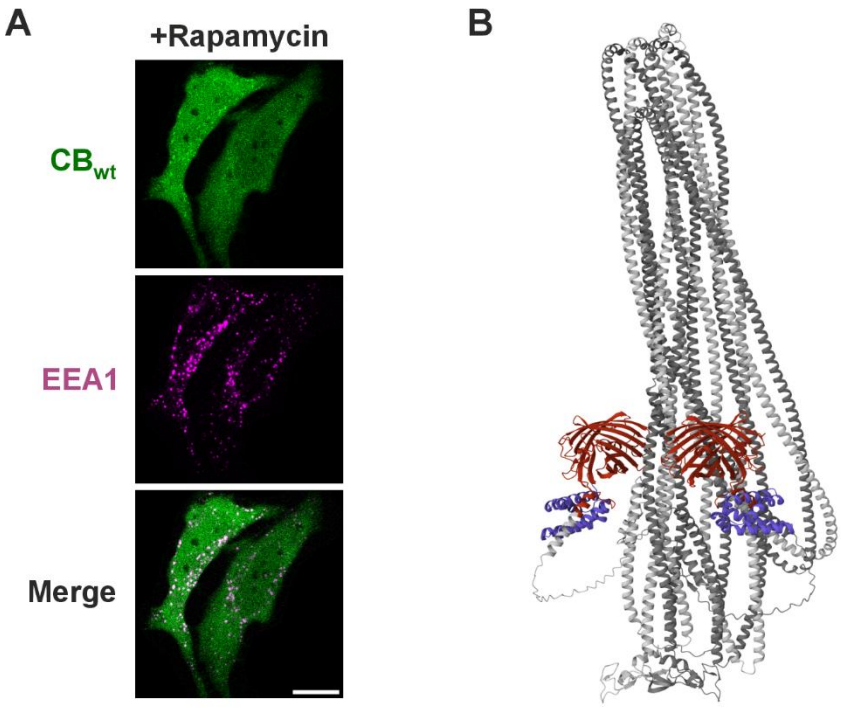

Figure A.6: Unsuccessful EEA1-targetted calbindin translocation. (A) Single-cell images of unsuccessful rapamycin-induced (1 µM) calbindin-2 (CB_{wt}) translocation to EEA1-positive early endosomes, scale bar = 20 µm. **(B)** AlfaFold-predicted 3D structure of the FRB*-mScarlet-I-EEA1 protein complex (293). The two homologous domains of EEA1 are coloured in grey, the mScarlet-I fluorescent proteins are coloured in red, and the FRB* proteins are coloured in blue.

Appendix B – Supplementary Tables

Table A.1: Endo-lysosomal patch pipette pulling program

Cycle	Heat	Pull	Velocity	Time
1	Predetermined by ramp protocol	Blank	30	150
2	"	"	25	150
3	"	"	25	150
4	"	"	25	150
5	"	"	25	150
6	"	"	16	150

Note. Table adapted from Chen *et al.* (136).

Table A.2: PCR thermocycling conditions

Step	Temperature	Time
Initial denaturation	98°C	30 seconds
Cycles x30	98°C *50 - 72°C 72°C	10 seconds 30 seconds 30 seconds/kb
Final extension	72°C	2 minutes
Hold	8°C	Infinite

Note. *, primer binding temperature determined using the NEB T_m calculator (https://tmcalculator.neb.com/#!/main). 35 cycles performed for site-directed mutagenesis.

References

1. Zhou Y, Xue S, J Yang J. Calciomics: integrative studies of Ca^{2+}-binding proteins and their interactomes in biological systems. *Metallomics*. 2013 Jan;5(1):29–42. doi: 10.1039/c2mt20009k

2. Ringer S. A further contribution regarding the influence of the different constituents of the blood on the contraction of the heart. *J Physiol*. 1883 Jan;4(1):29–42. doi: 10.1113/jphysiol.1883.sp000120

3. Clapham DE. Calcium signaling. *Cell*. 2007 Dec;131(6):1047–58. doi: 10.1016/j.cell.2007.11.028

4. Bagur R, Hajnóczky G. Intracellular Ca^{2+} sensing: role in calcium homeostasis and signaling. *Mol cell*. 2017 Jun;66(6):780. doi: 10.1016/j.molcel.2017.05.028

5. Berridge MJ, Bootman MD, Roderick HL. Calcium signalling: dynamics, homeostasis and remodelling. *Nat Rev Mol Cell Biol*. 2003 Jul;4(7):517–29. doi: 10.1038/nrm1155

6. Ghibelli L, Cerella C, Diederich M. The dual role of calcium as messenger and stressor in cell damage, death, and survival. *Int J Cell Biol*. 2010 Mar;2010(1):1–14. doi: 10.1155/2010/546163

7. Carafoli E. Calcium - a universal carrier of biological signals. *FEBS J*. 2005 Feb;272(5):1073–89. doi: 10.1111/j.1742-4658.2005.04546.x

8. Brini M, Carafoli E. Calcium pumps in health and disease. *Physiol Rev*. 2009 Oct;89(4):1341–78. doi: 10.1152/physrev.00032.2008

9. DeSantiago J, Batlle D, Khilnani M, Dedhia S, Kulczyk J, Duque R, et al. Ca^{2+}/H^{+} exchange via the plasma membrane Ca^{2+} ATPase in skeletal muscle. *Front Biosci*. 2007 May;12(7):4641–60. doi: 10.2741/2414

10. Brini M, Carafoli E. The plasma membrane Ca^{2+} ATPase and the plasma membrane sodium calcium exchanger cooperate in the regulation of cell calcium. *Cold Spring Harb Perspect Biol*. 2011 Feb;18(4):a004168. doi: 10.1101/cshperspect.a004168

11. Catterall WA. Voltage-gated calcium channels. *Cold Spring Harb Perspect Biol*. 2011 Aug;3(8):a003947. doi: 10.1101/cshperspect.a003947

12. Kopecky BJ, Liang R, Bao J. T-type calcium channel blockers as neuroprotective agents. *Pflugers Archiv*. 2014 Feb;466(4):757–65. doi: 10.1007/s00424-014-1454-x

13. Ritter JM, Flower RJ, Henderson G, Loke YK, MacEwan D, Rang HP. *Rang & Dale's pharmacology*. 9th ed. Edinburgh: Elsevier; 2018.

14. Berridge MJ. Smooth muscle cell calcium activation mechanisms. *J Physiol*. 2008 Nov;586(21):5047–61. doi: 10.1113/jphysiol.2008.160440

15. Parekh AB, Putney JW. Store-operated calcium channels. *Physiol Rev*. 2005 Apr;85(2):757–810. doi: 10.1152/physrev.00057.2003

16. Parekh AB, Penner R. Store depletion and calcium influx. *Physiol Rev*. 1997 Oct;77(4):901–30. doi: 10.1152/physrev.1997.77.4.901

17. Lewis RS. The molecular choreography of a store-operated calcium channel. *Nature*. 2007 Mar;446(1):284–7. doi: 10.1038/nature05637

18. Lemmon MA, Schlessinger J. Cell signaling by receptor tyrosine kinases. *Cell*. 2010 Jun;141(7):1117–34. doi: 10.1016/j.cell.2010.06.011

19. Streb H, Irvinet RF, Berridge MJ, Schulz I. Release of Ca^{2+} from a nonmitochondrial intracellular store in pancreatic acinar cells by inositol-1,4,5-trisphosphate. *Nature*. 1983 Nov;306(1):67–9. doi: 10.1038/306067a0

20. Berridge MJ. The inositol trisphosphate/calcium signaling pathway in health and disease. *Physiol Rev*. 2016 Oct;96(4):1261–96. doi: 10.1152/physrev.00006.2016

21. Taylor CW, Richardson A. Structure and function of inositol trisphosphate receptors. *Pharmacol Ther*. 1991;51(1):97–137. doi: 10.1016/0163-7258(91)90043-l

22. Pinton P, Pozzan T, Rizzuto R. The Golgi apparatus is an inositol 1,4,5-trisphosphate-sensitive Ca^{2+} store, with functional properties distinct from those of the endoplasmic reticulum. *EMBO J*. 1998 Sep;17(18):5298–308. doi: 10.1093/emboj/17.18.5298

23. Malviya AN. The nuclear inositol 1,4,5-trisphosphate and inositol 1,3,4,5-tetrakisphosphate receptors. *Cell Calcium*. 1994 Jul;16(1):301–13. doi: 10.1016/0143-4160(94)90094-9

24. Cheung Lee H. Mechanisms of calcium signaling by cyclic ADP-ribose and NAADP. *Physiol Rev*. 1997 Oct;77(4):1133–64. doi: 10.1152/physrev.1997.77.4.1133

25. Meissner G. Ryanodine receptor/Ca^{2+} release channels and their regulation by endogenous effectors. *Annu Rev Physiol*. 1994 Mar;56(1):485–508. doi: 10.1146/annurev.ph.56.030194.002413

26. Noguchi N, Takasawa S, Nata K, Tohgo A, Kato I, Ikehata F, et al. Cyclic ADP-ribose binds to FK506-binding protein 12.6 to release Ca^{2+} from islet microsomes. *J Biol Chem*. 1997 Feb;272(6):3133–6. doi: 10.1074/jbc.272.6.3133

27. Verkhratsky A. Physiology and pathophysiology of the calcium store in the endoplasmic reticulum of neurons. *Physiol Rev*. 2005 Jan;85(1):201–79. doi: 10.1152/physrev.00004.2004

28. Lytton J, Westlins M, Burkll SE, Shulln GE, Maclennanll DH. Functional comparisons between isoforms of the sarcoplasmic or endoplasmic reticulum family of calcium pumps. *J Biol Chem*. 1992 Jul;267(20):14483–9. doi: 10.1016/s0021-9258(19)49738-x

29. Xu Z, Zhang D, He X, Huang Y, Shao H. Transport of calcium ions into mitochondria. *Curr Genomics*. 2016 Apr;17(3):215–9. doi: 10.2174/1389202917666160202215748

30. Duchen MR. Mitochondria and calcium: from cell signalling to cell death. *J Physiol*. 2000 Nov;529(1):57. doi: 10.1111/j.1469-7793.2000.00057.x

31. Vandecaetsbeek I, Vangheluwe P, Raeymaekers L, Wuytack F, Vanoevelen J. The Ca^{2+} pumps of the endoplasmic reticulum and Golgi apparatus. *Cold Spring Harb Perspect Biol*. 2011 May;3(5):a004184. doi: 10.1101/cshperspect.a004184

32. Dode L, Andersen JP, Raeymaekers L, Missiaen L, Vilsen B, Wuytack F. Functional comparison between secretory pathway Ca^{2+}/Mn^{2+}-ATPase (SPCA) 1 and sarcoplasmic reticulum Ca^{2+}-ATPase (SERCA) 1 isoforms by steady-state and transient kinetic analyses. *J Biol Chem*. 2005 Nov;280(47):39124–34. doi: 10.1074/jbc.m506181200

33. Morgan AJ. Ca^{2+} dialogue between acidic vesicles and ER. *Biochem Soc Trans*. 2016 Apr;44(2):546–53. doi: 10.1042/bst20150290

34. Narayanaswamy N, Chakraborty K, Saminathan A, Zeichner E, Leung KH, Devany J, et al. A pH-correctable, DNA-based fluorescent reporter for organellar calcium. *Nat Methods*. 2018 Dec;16(1):95–102. doi: 10.1038/s41592-018-0232-7

35. Morgan AJ, Platt FM, Lloyd-Evans E, Galione A. Molecular mechanisms of endolysosomal Ca^{2+} signalling in health and disease. *Biochem J*. 2011 Nov;439(3):349–78. doi: 10.1042/bj20110949

36. Sherwood MW, Prior IA, Voronina SG, Barrow SL, Woodsmith JD, Gerasimenko OV, et al. Activation of trypsinogen in large endocytic vacuoles of pancreatic acinar cells. *Proc Natl Acad Sci USA*. 2007 Mar;104(13):5674–9. doi: 10.1073/pnas.0700951104

37. Lloyd-Evans E, Morgan AJ, He X, Smith DA, Elliot-Smith E, Sillence DJ, et al. Niemann-Pick disease type C1 is a sphingosine storage disease that causes deregulation of lysosomal calcium. *Nat Med*. 2008 Nov;14(11):1247–55. doi: 10.1038/nm.1876

38. Scott CC, Wasnik V, Nunes-Hasler P, Demaurex N, Kruse K, Gruenberg J. Calcium storage in multivesicular endo-lysosome. *Phys Biol*. 2023 Oct;20(6):066004. doi: 10.1088/1478-3975/acfe6a

39. Ezaki J, Himeno M, Kato K. Purification and characterization of (Ca^{2+}-Mg^{2+})-ATPase in rat liver lysosomal membranes. *Biochem J*. 1992 Nov;112(1):33–9. doi: 10.1042/bj2070225

40. Gonçalves PP, Meireles SM, Neves P, Vale MGP. Distinction between Ca^{2+} pump and Ca^{2+}/H^{+} antiport activities in synaptic vesicles of sheep brain cortex. *Neurochem Int*. 2000 Oct;37(4):387–96. doi: 10.1016/s0197-0186(00)00009-7

41. Fernández-Suárez ME, Bush R, Brenton JW, Pereira G, Grant-Peters M, Reynolds R, et al. Alternate splicing directs PMCA2 to lysosomes and is linked to neurodegeneration. *bioRxiv* [Preprint]. 2025 Oct. doi: 10.1101/2025.10.01.679724

42. Melchionda M, Pittman JK, Mayor R, Patel S. Ca^{2+}/H^{+} exchange by acidic organelles regulates cell migration *in vivo*. *J Cell Biol*. 2016 Mar;212(7):803. doi: 10.1083/jcb.201510019

43. Hirschi KD, Zhen RG, Cunningham KW, Rea PA, Fink GR. CAX1, an H^{+}/Ca^{2+} antiporter from *Arabidopsis*. *Proc Natl Acad Sci USA*. 1996 Aug;93(16):8782–6. doi: 10.1073/pnas.93.16.8782

44. Churchill GC, Okada Y, Thomas JM, Genazzani AA, Patel S, Galione A. NAADP mobilizes Ca^{2+} from reserve granules, lysosome-related organelles, in sea urchin eggs. *Cell*. 2002 Nov;111(5):703–8. doi: 10.1016/s0092-8674(02)01082-6

45. Hu YB, Dammer EB, Ren RJ, Wang G. The endosomal-lysosomal system: from acidification and cargo sorting to neurodegeneration. *Trans Neurodegener*. 2015 Sep;4(1):1–10. doi: 10.1186/s40035-015-0041-1

46. Zajac M, Mukherjee S, Anees P, Oettinger D, Henn K, Srikumar J, et al. A mechanism of lysosomal calcium entry. *Sci Adv*. 2024 Feb;10(7):eadk2317. doi: 10.1126/sciadv.adk2317

47. Chen R, Liu B, Jaślan D, Kucej L, Kudrina V, Warnke B, et al. Lysosomal TMEM165 controls cellular ion homeostasis and survival by mediating lysosomal Ca^{2+} import and H^{+} efflux. *Nat Commun*. 2025 Jun;16(1):5209. doi: 10.1038/s41467-025-60349-5

48. Wang W, Zhang X, Gao Q, Lawas M, Yu L, Cheng X, et al. A voltage-dependent K^{+} channel in the lysosome is required for refilling lysosomal Ca^{2+} stores. *J Cell Biol*. 2017 Jun;216(6):1715–30. doi: 10.1083/jcb.201612123

49. Yamasaki M, Thomas JM, Churchill GC, Garnham C, Lewis AM, Cancela JM, et al. Role of NAADP and cADPR in the induction and maintenance of agonist-evoked Ca^{2+} spiking in mouse pancreatic acinar cells. *Curr Biol*. 2005 May;15(9):874–8. doi: 10.1016/j.cub.2005.04.033

50. Aarhus R, Graeff RM, Dickey DM, Walseth TF, Hon CL. ADP-ribosyl cyclase and CD38 catalyze the synthesis of a calcium-mobilizing metabolite from $NADP^{+}$. *J Biol Chem*. 1995 Dec;270(51):30327–33. doi: 10.1074/jbc.270.51.30327

51. Fang C, Li T, Li Y, Xu GJ, Deng QW, Chen YJ, et al. CD38 produces nicotinic acid adenosine dinucleotide phosphate in the lysosome. *J Biol Chem*. 2018 May;293(21):8151–60. doi: 10.1074/jbc.ra118.002113

52. Lin WK, Bolton EL, Cortopassi WA, Wang Y, O'Brien F, Maciejewska M, et al. Synthesis of the Ca^{2+}-mobilizing messengers NAADP and cADPR by intracellular CD38 enzyme in the mouse heart: role in β-adrenoceptor signaling. *J Biol Chem*. 2017 Aug;292(32):13243–57. doi: 10.1074/jbc.m117.789347

53. Zhao ZY, Xie XJ, Li WH, Liu J, Chen Z, Zhang B, et al. A cell-permeant mimetic of NMN activates SARM1 to produce cyclic ADP-ribose and induce non-apoptotic cell death. *iScience*. 2019 May;15(1):452–66. doi: 10.1016/j.isci.2019.05.001

54. Angeletti C, Amici A, Gilley J, Loreto A, Trapanotto AG, Antoniou C, et al. SARM1 is a multi-functional NAD(P)ase with prominent base exchange activity, all regulated by multiple physiologically relevant NAD metabolites. *iScience*. 2022 Jan;25(2):103812. doi: 10.1016/j.isci.2022.103812

55. Gu F, Krüger A, Roggenkamp HG, Alpers R, Lodygin D, Jaquet V, et al. Dual NADPH oxidases DUOX1 and DUOX2 synthesize NAADP and are necessary for Ca^{2+} signaling during T cell activation. *Sci Signal*. 2021 Nov;14(709):eabe3800. doi: 10.1126/scisignal.abe3800

56. Winterberg KJ, Schwentner V, Gu F, Möckl F, Li G, Bauche A, et al. Multiple signaling events are required for NAADP synthesis by DUOX2 and formation of Ca^{2+} microdomains to initiate T cell activation. *Sci Signal*. 2026 Jan;19(920):eadp4326. doi: 10.1126/scisignal.adp4326

57. Graeff R, Liu Q, Kriksunov IA, Hao Q, Lee HC. Acidic residues at the active sites of CD38 and ADP-ribosyl cyclase determine nicotinic acid adenine dinucleotide phosphate (NAADP) synthesis and hydrolysis activities. *J Biol Chem*. 2006 Sep;281(39):28951–7. doi: 10.1074/jbc.m604370200

58. Schmid F, Fliegert R, Westphal T, Bauche A, Guse AH. Nicotinic acid adenine dinucleotide phosphate (NAADP) degradation by alkaline phosphatase. *J Biol Chem*. 2012 Sep;287(39):32525–34. doi: 10.1074/jbc.m112.362715

59. Lee HC, Aarhus R. A derivative of NADP mobilizes calcium stores insensitive to inositol trisphosphate and cyclic ADP-ribose. *J Biol Chem*. 1995 Feb;270(5):2152–7. doi: 10.1074/jbc.270.5.2152

60. Genazzani AA, Galione A. Nicotinic acid-adenine dinucleotide phosphate mobilizes Ca^{2+} from a thapsigargin-insensitive pool. *Biochem J*. 1996 May;315(3):721–5. doi: 10.1042/bj3150721

61. Lee HC, Aarhus R. Functional visualization of the separate but interacting calcium stores sensitive to NAADP and cyclic ADP-ribose. *J Cell Sci*. 2000 Dec;113(24):4413–20. doi: 10.1242/jcs.113.24.4413

62. Berg TO, Stromhaug PE, Lovdal T, Seglen PO, Berg T. Use of glycyl-L-phenylalanine 2-naphthylamide, a lysosome-disrupting cathepsin C substrate, to distinguish between lysosomes and prelysosomal endocytic vacuoles. *Biochem J*. 1994 May;300(1):229–36. doi: 10.1042/bj3000229

63. Atakpa P, van Marrewijk LM, Apta-Smith M, Chakraborty S, Taylor CW. GPN does not release lysosomal Ca^{2+} but evokes Ca^{2+} release from the ER by increasing the cytosolic pH independently of cathepsin C. *J Cell Sci*. 2019 Feb;132(3):jcs223883. doi: 10.1242/jcs.223883

64. Yuan Y, Kilpatrick BS, Gerndt S, Bracher F, Grimm C, Schapira AH, et al. The lysosomotrope GPN mobilises Ca^{2+} from acidic organelles. *J Cell Sci*. 2021 Mar;134(6):jcs256578. doi: 10.1242/jcs.256578

65. Morgan AJ, Yuan Y, Patel S, Galione A. Does lysosomal rupture evoke Ca^{2+} release? a question of pores and stores. *Cell Calcium*. 2020 Mar;86(1):102139. doi: 10.1016/j.ceca.2019.102139

66. Cancela JM, Charpentier G, Petersen OH. Co-ordination of Ca^{2+} signalling in mammalian cells by the new Ca^{2+}-releasing messenger NAADP. *Pflugers Archiv*. 2003 Jun;446(3):322–7. doi: 10.1007/s00424-003-1035-x

67. Cancela JM, Churchill GC, Galione A. Coordination of agonist-induced Ca^{2+}-signalling patterns by NAADP in pancreatic acinar cells. *Nature*. 1999 Mar;398(6722):74–6. doi: 10.1038/18032

68. Aley PK, Mikolajczyk AM, Munz B, Churchill GC, Galione A, Berger F. Nicotinic acid adenine dinucleotide phosphate regulates skeletal muscle differentiation via action at two-pore channels. *Proc Natl Acad Sci USA*. 2010 Nov;107(46):19927–32. doi: 10.1073/pnas.1007381107

69. Kinnear NP, Boittin FX, Thomas JM, Galione A, Evans AM. Lysosome-sarcoplasmic reticulum junctions: a trigger zone for calcium signaling by nicotinic acid adenine dinucleotide phosphate and endothelin-1. *J Biol Chem*. 2004 Dec;279(52):54319–26. doi: 10.1074/jbc.m406132200

70. Aley PK, Noh HJ, Gao X, Tica AA, Brailoiu E, Churchill GC. A functional role for nicotinic acid adenine dinucleotide phosphate in oxytocin-mediated contraction of uterine smooth muscle from rat. *J Pharmacol Exp Ther*. 2010 Jun;333(3):726–35. doi: 10.1124/jpet.110.165837

71. Aarhus R, Dickey DM, Graeff RM, Gee KR, Walseth TF, Lee HC. Activation and inactivation of Ca^{2+} release by NAADP. *J Biol Chem*. 1996 Apr;271(15):8513–6. doi: 10.1074/jbc.271.15.8513

72. Genazzani AA, Empson RM, Galione A. Unique inactivation properties of NAADP-sensitive Ca^{2+} release. *J Biol Chem*. 1996 May;271(20):11599–602. doi: 10.1074/jbc.271.20.11599

73. Churchill GC, Galione A. Prolonged inactivation of nicotinic acid adenine dinucleotide phosphate-induced Ca^{2+} release mediates a spatiotemporal Ca^{2+} memory. *J Biol Chem*. 2001 Apr;276(14):11223–5. doi: 10.1074/jbc.m009335200

74. Berg I, Potter BVL, Mayr GW, Guse AH. Nicotinic acid adenine dinucleotide phosphate ($NAADP^+$) is an essential regulator of T-lymphocyte Ca^{2+}-signaling. *J Cell Biol*. 2000 Aug;150(3):581–8. doi: 10.1083/jcb.150.3.581

75. Davis LC, Morgan AJ, Chen JL, Snead CM, Bloor-Young D, Shenderov E, et al. NAADP activates two-pore channels on T cell cytolytic granules to stimulate exocytosis and killing. *Curr Biol*. 2012 Dec;22(24):2331–7. doi: 10.1016/j.cub.2012.10.035

76. Rosen D, Lewis AM, Mizote A, Thomas JM, Aley PK, Vasudevan SR, et al. Analogues of the nicotinic acid adenine dinucleotide phosphate (NAADP) antagonist Ned-19 indicate two binding sites on the NAADP receptor. *J Biol Chem*. 2009 Dec;284(50):34930–4. doi: 10.1074/jbc.m109.016519

77. Yamaguchi S, Jha A, Li Q, Soyombo AA, Dickinson GD, Churamani D, et al. Transient receptor potential mucolipin 1 (TRPML1) and two-pore channels are functionally independent organellar ion channels. *J Biol Chem*. 2011 Jul;286(26):22934–42. doi: 10.1074/jbc.m110.210930

78. Zhang F, Zhang G, Zhang AY, Koeberl MJ, Wallander E, Li PL. Production of NAADP and its role in Ca^{2+} mobilization associated with lysosomes in coronary arterial myocytes. *Am J Physiol Heart Circ Physiol*. 2006 Jul;291(1):274–82. doi: 10.1152/ajpheart.01064.2005

79. Steen M, Kirchberger T, Guse AH. NAADP mobilizes calcium from the endoplasmic reticular Ca^{2+} store in T-lymphocytes. *J Biol Chem*. 2007 Jun;282(26):18864–71. doi: 10.1074/jbc.m610925200

80. Calcraft PJ, Ruas M, Pan Z, Cheng X, Arredouani A, Hao X, et al. NAADP mobilizes calcium from acidic organelles through two-pore channels. *Nature*. 2009 Apr;459(7246):596–600. doi: 10.1038/nature08030

81. Davis LC, Morgan AJ, Galione A. NAADP-regulated two-pore channels drive phagocytosis through endo-lysosomal Ca^{2+} nanodomains, calcineurin and dynamin. *EMBO J*. 2020 Jul;39(14):e104058. doi: 10.15252/embj.2019104058

82. Brailoiu GC, Gurzu B, Gao X, Parkesh R, Aley PK, Trifa DI, et al. Acidic NAADP-sensitive calcium stores in the endothelium. *J Biol Chem*. 2010 Nov;285(48):37133–7. doi: 10.1074/jbc.c110.169763

83. Yuan Y, Arige V, Saito R, Mu Q, Brailoiu GC, Pereira GJS, et al. Two-pore channel-2 and inositol trisphosphate receptors coordinate Ca^{2+} signals between lysosomes and the endoplasmic reticulum. *Cell Rep*. 2024 Jan;43(1):113628. doi: 10.1016/j.celrep.2023.113628

84. Peiter E, Maathuis FJM, Mills LN, Knight H, Pelloux J, Hetherington AM, et al. The vacuolar Ca^{2+}-activated channel TPC1 regulates germination and stomatal movement. *Nature*. 2005 Mar;434(7031):404-8. doi: 10.1038/nature03381

85. Brailoiu E, Churamani D, Cai X, Schrlau MG, Brailoiu GC, Gao X, et al. Essential requirement for two-pore channel 1 in NAADP-mediated calcium signaling. *J Cell Biol*. 2009 Jul;186(2):201–9. doi: 10.1083/jcb.200904073

86. Zong X, Schieder M, Cuny H, Fenske S, Gruner C, Rötzer K, et al. The two-pore channel TPCN2 mediates NAADP-dependent Ca^{2+}-release from lysosomal stores. *Pflugers Arch*. 2009 Sep;458(5):891–9. doi: 10.1007/s00424-009-0690-y

87. Ruas M, Davis LC, Chen CC, Morgan AJ, Chuang KT, Walseth TF, et al. Expression of Ca^{2+}-permeable two-pore channels rescues NAADP signalling in TPC-deficient cells. *EMBO J*. 2015 Jul;34(13):1743–58. doi: 10.15252/embj.201490009

88. Lin-Moshier Y, Walseth TF, Churamani D, Davidson SM, Slama JT, Hooper R, et al. Photoaffinity labeling of nicotinic acid adenine dinucleotide phosphate (NAADP) targets in mammalian cells. *J Biol Chem*. 2012 Jan;287(4):2296–307. doi: 10.1074/jbc.m111.305813

89. Wilusz CJ, Wilusz J. Lsm proteins and Hfq. *RNA Biol*. 2013 Apr;10(4):592–601. doi: 10.4161/rna.23695

90. Zhang J, Guan X, Shah K, Yan J. Lsm12 is an NAADP receptor and a two-pore channel regulatory protein required for calcium mobilization from acidic organelles. *Nat Commun*. 2021 Aug;12(1):4739. doi: 10.1038/s41467-021-24735-z

91. Gunaratne GS, Brailoiu E, He S, Unterwald EM, Patel S, Slama JT, et al. Essential requirement for JPT2 in NAADP-evoked Ca^{2+} signaling. *Sci Signal*. 2021 Mar;14(675): eabd5605. doi: 10.1126/scisignal.abd5605

92. Gunaratne GS, Brailoiu E, Kumar S, Yuan Y, Slama JT, Walseth TF, et al. Convergent activation of two-pore channels mediated by the NAADP-binding proteins JPT2 and LSM12. *Sci Signal*. 2023 Aug;16(799):eadg0485. doi: 10.1126/scisignal.adg0485

93. Kumar S, Gunaratne GS, Cornish J, Silvey KM, Mu Q, Guan Z, et al. Liquid liquid phase separation of the intrinsically disordered protein JPT2 compartmentalizes components of NAADP-evoked Ca^{2+} signaling. *bioRxiv* [Preprint]. 2026 Jan. doi: 10.64898/2026.01.10.698830

94. Roggenkamp HG, Khansahib I, Hernandez C. LC, Zhang Y, Lodygin D, Krüger A, et al. HN1L/JPT2: a signaling protein that connects NAADP generation to Ca^{2+} microdomain formation. *Sci Signal*. 2021 Mar;14(675):eabd5647. doi: 10.1126/scisignal.abd5647

95. Chen X, Song QL, Ji R, Wang JY, Cao ML, Guo DY, et al. JPT2 affects trophoblast functions and macrophage polarization and metabolism, and acts as a potential therapeutic target for recurrent spontaneous abortion. *Adv Sci (Weinh)*. 2024 Feb;11(16):e2306359. doi: 10.1002/advs.202306359

96. Ishibashi K, Suzuki M, Imai M. Molecular cloning of a novel form (two-repeat) protein related to voltage-gated sodium and calcium channels. *Biochem Biophys Res Commun*. 2000 Apr;270(2):370–6. doi: 10.1006/bbrc.2000.2435

97. Yu FH, Catterall WA. The VGL-chanome: a protein superfamily specialized for electrical signaling and ionic homeostasis. *Sci STKE*. 2004 Oct;2004(253):re15. doi: 10.1126/stke.2532004re15

98. Furuichi T, Cunningham KW, Muto S. A putative two pore channel AtTPC1 mediates Ca^{2+} flux in *Arabidopsis* leaf cells. *Plant Cell Physiol*. 2001 Sep;42(9):900–5. doi: 10.1093/pcp/pce145

99. Kurusu T, Yagala T, Miyao A, Hirochika H, Kuchitsu K. Identification of a putative voltage-gated Ca^{2+} channel as a key regulator of elicitor-induced hypersensitive cell death and mitogen-activated protein kinase activation in rice. *Plant J*. 2005 Jun;42(6):798–809. doi: 10.1111/j.1365-313x.2005.02415.x

100. Sahin AT, Zachariae U. *In silico* characterization of the gating and selectivity mechanism of the human TPC2 cation channel. *J Gen Physiol*. 2025 Feb 21;157(3):e202313506. doi: 10.1085/jgp.202313506

101. Rahman T, Cai X, Brailoiu GC, Abood ME, Brailoiu E, Patel S. Two-pore channels provide insight into the evolution of voltage-gated Ca^{2+} and Na^{+} channels. *Sci Signal*. 2014 Nov;7(352):ra109. doi: 10.1126/scisignal.2005450

102. Churamani D, Hooper R, Brailoiu E, Patel S. Domain assembly of NAADP-gated two-pore channels. *Biochem J*. 2012 Jan;441(1):317–23. doi: 10.1042/bj20111617

103. Rietdorf K, Funnell TM, Ruas M, Heinemann J, Parrington J, Galione A. Two-pore channels form homo- and heterodimers. *J Biol Chem*. 2011 Oct;286(43):37058–62. doi: 10.1074/jbc.C111.289835

104. Guo J, Zeng W, Chen Q, Lee C, Chen L, Yang Y, et al. Structure of the voltage-gated two-pore channel TPC1 from *Arabidopsis thaliana. Nature*. 2016 Mar;531(7593):196-201. doi: 10.1038/nature16446

105. Kintzer AF, Stroud RM. Structure, inhibition and regulation of two-pore channel TPC1 from *Arabidopsis thaliana*. *Nature*. 2016 Mar;531(7593):258-62. doi: 10.1038/nature17194

106. She J, Guo J, Chen Q, Zeng W, Jiang Y, Bai XC. Structural insights into the voltage and phospholipid activation of mammalian TPC1 channel. *Nature*. 2018 Apr;556(7699):130–4. doi: 10.1038/nature26139

107. Guo J, Zeng W, Jiang Y. Tuning the ion selectivity of two-pore channels. *Proc Natl Acad Sci USA*. 2017 Jan;114(5):1009–14. doi: 10.1073/pnas.1616191114

108. She J, Zeng W, Guo J, Chen Q, Bai X chen, Jiang Y. Structural mechanisms of phospholipid activation of the human TPC2 channel. *eLife*. 2019 Mar;8(1):e45222. doi: 10.7554/elife.45222

109. Schulze C, Sticht H, Meyerhoff P, Dietrich P. Differential contribution of EF-hands to the Ca^{2+}-dependent activation in the plant two-pore channel TPC1. *Plant J*. 2011 Nov;68(3):424–32. doi: 10.1111/j.1365-313x.2011.04697.x

110. Churamani D, Hooper R, Rahman T, Brailoiu E, Patel S. The N-terminal region of two-pore channel 1 regulates trafficking and activation by NAADP. *Biochem J*. 2013 Jun;453(1):147–51. doi: 10.1042/bj20130474

111. Brailoiu E, Rahman T, Churamani D, Prole DL, Brailoiu GC, Hooper R, et al. An NAADP-gated two-pore channel targeted to the plasma membrane uncouples triggering from amplifying Ca^{2+} signals. *J Biol Chem*. 2010 Dec;285(49):38511–6. doi: 10.1074/jbc.m110.162073

112. Larisch N, Kirsch SA, Schambony A, Studtrucker T, Böckmann RA, Dietrich P. The function of the two-pore channel TPC1 depends on dimerization of its carboxy-terminal helix. *Cell Mol Life Sci*. 2016 Jul;73(1):2565–81. doi: 10.1007/s00018-016-2131-3

113. Hedrich R, Mueller TD, Becker D, Marten I. Structure and function of TPC1 vacuole SV channel gains shape. *Mol Plant*. 2018 Jun;11(6):764–75. doi: 10.1016/j.molp.2018.03.017

114. Hon Cheung Lee, Aarhus R. A derivative of NADP mobilizes calcium stores insensitive to inositol trisphosphate and cyclic ADP-ribose. *J Biol Chem*. 1995 Feb;270(5):2152–7. doi: 10.1074/jbc.270.5.2152

115. Rice KL, Chan CM, Kelu JJ, Miller AL, Webb SE. A role for two-pore channel type 2 (TPC2)-mediated regulation of membrane contact sites during zebrafish notochord biogenesis? *Contact*. 2023 Nov;6(1):1–17. doi: 10.1177/25152564231211409

116. Ruas M, Chuang KT, Davis LC, Al-Douri A, Tynan PW, Tunn R, et al. TPC1 has two variant isoforms, and their removal has different effects on endo-lysosomal functions compared to loss of TPC2. *Mol Cell Biol*. 2014 Nov;34(21):3981–92. doi: 10.1128/mcb.00113-14

117. Castonguay J, Orth JHC, Müller T, Sleman F, Grimm C, Wahl-Schott C, et al. The two-pore channel TPC1 is required for efficient protein processing through early and recycling endosomes. *Sci Rep*. 2017 Aug;7(1):10038. doi: 10.1038/s41598-017-10607-4

118. Morgan AJ, Martucci LL, Davis LC, Galione A. Two-pore channels: going with the flows. *Biochem Soc Trans*. 2022 Aug;50(4):1143–55. doi: 10.1042/bst20220229

119. Larisch N, Schulze C, Galione A, Dietrich P. An N-terminal dileucine motif directs two-pore channels to the tonoplast of plant cells. *Traffic*. 2012 Jul;13(7):1012–22. doi: 10.1111/j.1600-0854.2012.01366.x

120. Bonifacino JS, Traub LM. Signals for sorting of transmembrane proteins to endosomes and lysosomes. *Annu Rev Biochem*. 2003 Mar;72(1):395–447. doi: 10.1146/annurev.biochem.72.121801.161800

121. Catterall WA, Wisedchaisri G, Zheng N. The chemical basis for electrical signaling. *Nat Chem Biol*. 2017 Apr;13(5):455–63. doi: 10.1038/nchembio.2353

122. Cang C, Bekele B, Ren D. The voltage-gated sodium channel TPC1 confers endolysosomal excitability. *Nat Chem Biol*. 2014 Apr;10(6):463–9. doi: 10.1038/nchembio.1522

123. Patel S, Churamani D, Brailoiu E. NAADP-evoked Ca^{2+} signals through two-pore channel-1 require arginine residues in the first S4-S5 linker. *Cell Calcium*. 2017 Dec;68(1):1–4. doi: 10.1016/j.ceca.2017.09.003

124. Gouet P, Courcelle E, Stuart DI, Métoz F. ESPript: analysis of multiple sequence alignments in PostScript. *Bioinformatics*. 1999 Apr;15(4):305–8. doi: 10.1093/bioinformatics/15.4.305

125. Hedrich R, Flügge UI, Fernandez JM. Patch-clamp studies of ion transport in isolated plant vacuoles. *FEBS Letters*. 1986 Aug;204(2):228–32. doi: 10.1016/0014-5793(86)80817-1

126. Hedrich R, Neher E. Cytoplasmic calcium regulates voltage-dependent ion channels in plant vacuoles. *Nature*. 1987 Oct;329(6142):833–6. doi: 10.1038/329833a0

127. Allen GJ, Sanders D. Control of ionic currents in guard cell vacuoles by cytosolic and luminal calcium. *Plant J*. 1996 Dec;10(6):1055–69. doi: 10.1046/j.1365-313x.1996.10061055.x

128. Schulz-Lessdorf B, Hedrich R. Protons and calcium modulate SV-type channels in the vacuolar-lysosomal compartment - channel interaction with calmodulin inhibitors. *Planta*. 1995 Nov;197(4):655–71. doi: 10.1007/bf00191574

129. Amodeo G, Escobar A, Zeiger E. *A* cationic channel in the guard cell tonoplast of *Allium cepa*. *Plant Physiol*. 1994 Jul;105(3):999–1006. doi: 10.1104/pp.105.3.999

130. Pottosin II, Tikhonova LI, Hedrich R, Schönknecht G. Slowly activating vacuolar channels can not mediate Ca^{2+}-induced Ca^{2+} release. *Plant J*. 1997 Dec;12(6):1387–98. doi: 10.1046/j.1365-313x.1997.12061387.x

131. Ranf S, Wünnenberg P, Lee J, Becker D, Dunkel M, Hedrich R, et al. Loss of the vacuolar cation channel, *At*TPC1, does not impair Ca^{2+} signals induced by abiotic and biotic stresses. *Plant J*. 2007 Oct;53(2):287–99. doi: 10.1111/j.1365-313x.2007.03342.x

132. Beyhl D, Hörtensteiner S, Martinoia E, Farmer EE, Fromm J, Marten I, et al. The *fou2* mutation in the major vacuolar cation channel TPC1 confers tolerance to inhibitory luminal calcium. *Plant J*. 2009 May;58(5):715–23. doi: 10.1111/j.1365-313X.2009.03820.x

133. Schönknecht G. Calcium signals from the vacuole. *Plants*. 2013 Oct;2(4):589–614. doi: 10.3390/plants2040589

134. Walker DJ, Leigh RA, Miller AJ. Potassium homeostasis in vacuolate plant cells. *Proc Natl Acad Sci USA*. 1996 Sep;93(19):10510–4. doi: 10.1073/pnas.93.19.10510

135. Ward J, Schroeder J. Calcium-activated K^+ channels and calcium-induced calcium release by slow vacuolar ion channels in guard cell vacuoles implicated in the control of stomatal closure. *Plant cell*. 1994 May;6(5):669–83. doi: 10.1105/tpc.6.5.669

136. Chen CC, Cang C, Fenske S, Butz E, Chao YK, Biel M, et al. Patch-clamp technique to characterize ion channels in enlarged individual endolysosomes. *Nat Protoc*. 2017 Jul;12(8):1639–58. doi: 10.1038/nprot.2017.036

137. Cang C, Zhou Y, Navarro B, Seo YJ, Aranda K, Shi L, et al. mTor regulates lysosomal ATP-sensitive two-pore Na^+ channel to adapt to metabolic state. *Cell*. 2013 Feb;152(4):778–90. doi: 10.1016/j.cell.2013.01.023

138. Wang X, Zhang X, Dong XP, Samie M, Li X, Cheng X, et al. TPC proteins are phosphoinositide-activated sodium-selective ion channels in endosomes and lysosomes. *Cell*. 2012 Oct;151(2):372–83. doi: 10.1016/j.cell.2012.08.036

139. Lagostena L, Festa M, Pusch M, Carpaneto A. The human two-pore channel 1 is modulated by cytosolic and luminal calcium. *Sci Rep*. 2017 Mar;7(1):43900. doi: 10.1038/srep43900

140. Rybalchenko V, Ahuja M, Coblentz J, Churamani D, Patel S, Kiselyov K, et al. Membrane potential regulates nicotinic acid adenine dinucleotide phosphate (NAADP) dependence of the pH- and Ca^{2+}-sensitive organellar two-pore channel TPC1. *J Biol Chem*. 2012 Jun 8;287(24):20407–16. doi: 10.1074/jbc.m112.359612

141. Pitt SJ, Lam AKM, Rietdorf K, Galione A, Sitsapesan R. Reconstituted human TPC1 is a proton-permeable ion channel and is activated by NAADP or Ca^{2+}. *Sci Signal*. 2014 May;7(326):ra46. doi: 10.1126/scisignal.2004854

142. Jha A, Ahuja M, Patel S, Brailoiu E, Muallem S. Convergent regulation of the lysosomal two-pore channel-2 by Mg^{2+}, NAADP, $PI(3,5)P_2$ and multiple protein kinases. *EMBO J*. 2014 Mar;33(5):501–11. doi: 10.1002/embj.201387035

143. Saito R, Mu Q, Yuan Y, Rubio-Alarcón M, Eznarriaga M, Zhao P, et al. Convergent activation of Ca^{2+} permeability in two-pore channel 2 through distinct molecular routes. *Sci Signal*. 2023 Aug;16(799):eadg0661. doi: 10.1126/scisignal.adg0661

144. Zaki AM, Çınaroğlu SS, Rahman T, Patel S, Biggin PC. Plasticity of the selectivity filter is essential for permeation in lysosomal TPC2 channels. *Proc Natl Acad Sci USA*. 2024 Aug;121(32):e2320153121. doi: 10.1073/pnas.2320153121

145. Şahin AT, Zachariae U. *In silico* characterization of the gating and selectivity mechanism of the human TPC2 cation channel. *J Gen Physiol*. 2025 Feb;157(3):e202313506. doi: 10.1085/jgp.202313506

146. Pitt SJ, Funnell TM, Sitsapesan M, Venturi E, Rietdorf K, Ruas M, et al. TPC2 is a novel NAADP-sensitive Ca^{2+} release channel, operating as a dual sensor of luminal pH and Ca^{2+}. *J Biol Chem*. 2010 Nov;285(45):35039–46. doi: 10.1074/jbc.m110.156927

147. Schieder M, Rötzer K, Brüggemann A, Biel M, Wahl-Schott CA. Characterization of two-pore channel 2 (TPCN2)-mediated Ca^{2+} currents in isolated lysosomes. *J Biol Chem*. 2010 Jul;285(28):21219–22. doi: 10.1074/jbc.c110.143123

148. Chappe YL, Pierredon S, Joushomme A, Molle P, Garenne A, Canovi A, et al. Genetically-encoded BRET probes shed light on ligand bias–induced variable ion selectivity in TRPV1 and P2X5/7. *Proc Natl Acad Sci USA*. 2022 Nov;119(46):e2205207119. doi: 10.1073/pnas.2205207119

149. Gerndt S, Chen CC, Chao YK, Yuan Y, Burgstaller S, Rosato AS, et al. Agonist-mediated switching of ion selectivity in TPC2 differentially promotes lysosomal function. *eLife*. 2020 Mar;9(1):e54712. doi: 10.7554/elife.54712

150. Yuan Y, Jaślan D, Rahman T, Bolsover SR, Arige V, Wagner LE, et al. Segregated cation flux by TPC2 biases Ca^{2+} signaling through lysosomes. *Nat Commun*. 2022 Aug;13(1): 4481. doi: 10.1038/s41467-022-31959-0

151. Brailoiu E, Hooper R, Cai X, Brailoiu GC, Keebler MV, Dun NJ, et al. An ancestral deuterostome family of two-pore channels mediates nicotinic acid adenine dinucleotide phosphate-dependent calcium release from acidic organelles. *J Biol Chem*. 2010 Jan;285(5):2897–901. doi: 10.1074/jbc.c109.081943

152. Cai X, Patel S. Degeneration of an intracellular ion channel in the primate lineage by relaxation of selective constraints. *Mol Biol Evol*. 2010 Oct;27(10):2352–9. doi: 10.1093/molbev/msq122

153. Cang C, Aranda K, Ren D. A non-inactivating high-voltage-activated two-pore Na^+ channel that supports ultra-long action potentials and membrane bistability. *Nat Commun*. 2014 Sep;5(1):5015. doi: 10.1038/ncomms6015

154. Ruas M, Rietdorf K, Arredouani A, Davis LC, Lloyd-Evans E, Koegel H, et al. Purified TPC isoforms form NAADP receptors with distinct roles for Ca^{2+} signaling and endolysosomal trafficking. *Curr Biol*. 2010 Apr;20(8):703–9. doi: 10.1016/j.cub.2010.02.049

155. Dickinson MS, Myasnikov A, Eriksen J, Poweleit N, Stroud RM. Resting state structure of the hyperdepolarization activated two-pore channel 3. *Proc Natl Acad Sci USA*. 2020 Jan;117(4):1988–93. doi: 10.1073/pnas.1915144117

156. Feng X, Xiong J, Cai W, Tian JB, Zhu MX. The three two-pore channel subtypes from rabbit exhibit distinct sensitivity to phosphoinositides, voltage, and extracytosolic pH. *Cells*. 2022 Jun;11(13):2006. doi: 10.3390/cells11132006

157. Shimomura T, Kubo Y. Phosphoinositides modulate the voltage dependence of two-pore channel 3. *J Gen Physiol*. 2019 Jun;151(8):986–1006. doi: 10.1085/jgp.201812285

158. Zhang X, Chen W, Li P, Calvo R, Southall N, Hu X, et al. Agonist-specific voltage-dependent gating of lysosomal two-pore Na^+ channels. *eLife*. 2019 Dec;8(1):e51423. doi: 10.7554/eLife.51423

159. Genazzani AA, Mezna M, Dickey DM, Michelangeli F, Walseth TF, Galione A. Pharmacological properties of the Ca^{2+}-release mechanism sensitive to NAADP in the sea urchin egg. *Br J Pharmacol*. 1997 Aug;121(7):1489–95. doi: 10.1038/sj.bjp.0701295

160. Netcharoensirisuk P, Abrahamian C, Tang R, Chen CC, Rosato AS, Beyers W, et al. Flavonoids increase melanin production and reduce proliferation, migration and invasion of melanoma cells by blocking endolysosomal/melanosomal TPC2. *Sci Rep*. 2021 Apr;11(1):8515. doi: 10.1038/s41598-021-88196-6

161. Krukenberg S, Möckl F, Weiß M, Dekiert P, Hofmann M, Gerlach F, et al. MASTER-NAADP: a membrane permeable precursor of the Ca^{2+} mobilizing second messenger NAADP. *Nat Commun*. 2024 Sep;15(1):8008. doi: 10.1038/s41467-024-52024-y

162. Parkesh R, Lewis AM, Aley PK, Arredouani A, Rossi S, Tavares R, et al. Cell-permeant NAADP: a novel chemical tool enabling the study of Ca^{2+} signalling in intact cells. *Cell Calcium*. 2008 Jun;43(6):531–8. doi: 10.1016/j.ceca.2007.08.006

163. Pafumi I, Festa M, Papacci F, Lagostena L, Giunta C, Gutla V, et al. Naringenin impairs two-pore channel 2 activity and inhibits VEGF-induced angiogenesis. *Sci Rep*. 2017 Jul;7(1):5121. doi: 10.1038/s41598-017-04974-1

164. Ogunbayo OA, Duan J, Xiong J, Wang Q, Feng X, Ma J, et al. mTORC1 controls lysosomal Ca^{2+} release through the two-pore channel TPC2. *Sci Signal*. 2018 Apr;11(525):eaao5775. doi: 10.1126/scisignal.aao5775

165. Davidson SM, Foote K, Kunuthur S, Gosain R, Tan N, Tyser R, et al. Inhibition of NAADP signalling on reperfusion protects the heart by preventing lethal calcium oscillations via two-pore channel 1 and opening of the mitochondrial permeability transition pore. *Cardiovasc Res*. 2015 Dec;108(3):357–66. doi: 10.1093/cvr/cvv226

166. Naylor E, Arredouani A, Vasudevan SR, Lewis AM, Parkesh R, Mizote A, et al. Identification of a chemical probe for NAADP by virtual screening. *Nat Chem Biol*. 2009 Apr;5(4):220–6. doi: 10.1038/nchembio.150

167. Müller M, Gerndt S, Chao YK, Zisis T, Nguyen ONP, Gerwien A, et al. Gene editing and synthetically accessible inhibitors reveal role for TPC2 in HCC cell proliferation and tumor growth. *Cell Chem Biol*. 2021 Aug;28(8):1119–31. doi: 10.1016/j.chembiol.2021.01.023

168. Höglinger D, Haberkant P, Aguilera-Romero A, Riezman H, Porter FD, Platt FM, et al. Intracellular sphingosine releases calcium from lysosomes. *eLife*. 2015 Nov;4(1):e10616. doi: 10.7554/elife.10616

169. Sakurai Y, Kolokoltsov AA, Chen CC, Tidwell MW, Bauta WE, Klugbauer N, et al. Two pore channels control Ebola virus host cell entry and are drug targets for disease treatment. *Science*. 2015 Feb;347(6225):995–8. doi: 10.1126/science.1258758

170. Du C, Guan X, Yan J. Two-pore channel blockade by phosphoinositide kinase inhibitors YM201636 and PI-103 determined by a histidine residue near pore-entrance. *Commun Biol*. 2022 Jul;5(1):738. doi: 10.1038/s42003-022-03701-5

171. Galione A, Davis LC, Martucci LL, Morgan AJ. NAADP-mediated Ca^{2+} signalling. In: Wahl-Schott C, Biel M, editors. *Endolysosomal voltage-gated cation channels*. Handbook of Experimental Pharmacology. Cham: Springer; 2023. p. 3–34. doi: 10.1007/164_2022_607

172. Galione A, Chuang KT, Funnell TM, Davis LC, Morgan AJ, Ruas M, et al. Synthesis of NAADP-AM as a membrane-permeant NAADP analog. *Cold Spring Harb Protoc*. 2014 Oct;2014(10):pdb.prot076927. doi: 10.1101/pdb.prot076927

173. Posor Y, Eichhorn-Grünig M, Haucke V. Phosphoinositides in endocytosis. *Biochim Biophys Acta*. 2015 Jun;1851(6):794–804. doi: 10.1016/j.bbalip.2014.09.014

174. Mallmann RT, Mantuano MCG, Polomski K, Knerr J, Klugbauer N. Small molecule agonist TPC2-A1-N increases intracellular Ca^{2+} independent of two-pore channels. *J Biol Chem*. 2025 Aug;301(9):110576. doi: 10.1016/j.jbc.2025.110576

175. Lin-Moshier Y, Keebler MV, Hooper R, Boulware MJ, Liu X, Churamani D, et al. The two-pore channel (TPC) interactome unmasks isoform-specific roles for TPCs in endolysosomal morphology and cell pigmentation. *Proc Natl Acad Sci USA*. 2014 Sep;111(36):13087–92. doi: 10.1073/pnas.1407004111

176. Abrahamian C, Tang R, Deutsch R, Ouologuem L, Weiden EM, Kudrina V, et al. Rab7a is an enhancer of TPC2 activity regulating melanoma progression through modulation of the GSK3β/β-Catenin/MITF-axis. *Nat Commun*. 2024 Nov;15(1):10008. doi: 10.1038/s41467-024-54324-9

177. Abrahamian C, Ouologuem L, Tang R, Fröhlich T, Bartel K, Grimm C. TPC2: from blond hair to melanoma? *Cancers*. 2024 Dec;16(23):4065. doi: 10.3390/cancers16234065

178. Chan WC, Zhao Q, Wong KH, Tang HH, Mok DKW, Pardeshi L, et al. Tetrandrine regulates NAADP-mediated calcium signaling through a LIMP-2-dependent and sphingosine-mediated mechanism. *Nat Commun*. 2025 Jul;16(1):6308. doi: 10.1038/s41467-025-61565-9

179. Chi G, Jaślan D, Kudrina V, Böck J, Li H, Pike ACW, et al. Structural basis for inhibition of the lysosomal two-pore channel TPC2 by a small molecule antagonist. *Structure*. 2024 May;32(8):1137–49. doi: 10.1016/j.str.2024.05.005

180. Clementi N, Scagnolari C, D'Amore A, Palombi F, Criscuolo E, Frasca F, et al. Naringenin is a powerful inhibitor of SARS-CoV-2 infection *in vitro*. *Pharmacol Res*. 2021 Jan;163(1):105255. doi: 10.1016/j.phrs.2020.105255

181. Gayle S, Landrette S, Beeharry N, Conrad C, Hernandez M, Beckett P, et al. Identification of apilimod as a first-in-class PIKfyve kinase inhibitor for treatment of B-cell non-Hodgkin lymphoma. *Blood*. 2017 Mar;129(13):1768–78. doi: 10.1182/blood-2016-09-736892

182. Jefferies HBJ, Cooke FT, Jat P, Boucheron C, Koizumi T, Hayakawa M, et al. A selective PIKfyve inhibitor blocks PtdIns(3,5)P_2 production and disrupts endomembrane transport and retroviral budding. *EMBO Rep*. 2008 Feb;9(2):164–70. doi: 10.1038/sj.embor.7401155

183. Cerny J, Feng Y, Yu A, Miyake K, Borgonovo B, Klumperman J, et al. The small chemical vacuolin-1 inhibits Ca^{2+}-dependent lysosomal exocytosis but not cell resealing. *EMBO Rep*. 2004 Sep;5(9):883–8. doi: 10.1038/sj.embor.7400243

184. Davis LC, Morgan AJ, Galione A. Optical profiling of autonomous Ca^{2+} nanodomains generated by lysosomal TPC2 and TRPML1. *Cell Calcium*. 2023 Dec;116(1):102801. doi: 10.1016/j.ceca.2023.102801

185. Grimm C, Holdt LM, Chen CC, Hassan S, Müller C, Jörs S, et al. High susceptibility to fatty liver disease in two-pore channel 2-deficient mice. *Nat Commun*. 2014 Aug;5(1):4699. doi: 10.1038/ncomms5699

186. Müller T, Grossmann S, Mallmann RT, Rommel C, Hein L, Klugbauer N. Two-pore channels affect EGF receptor signaling by receptor trafficking and expression. *iScience*. 2021 Feb;24(2):102099. doi: 10.1016/j.isci.2021.102099

187. Krogsaeter EK, Biel M, Wahl-Schott C, Grimm C. The protein interaction networks of mucolipins and two-pore channels. *Biochim Biophys Acta Mol Cell Res*. 2018 Nov; 1866(7):1111–23. doi: 10.1016/j.bbamcr.2018.10.020

188. Faris P, Casali C, Negri S, Iengo L, Biggiogera M, Maione AS, et al. Nicotinic acid adenine dinucleotide phosphate induces intracellular Ca^{2+} signalling and stimulates proliferation in human cardiac mesenchymal stromal cells. *Front Cell Dev Biol*. 2022 Mar;10(1):874043. doi: 10.3389/fcell.2022.874043

189. Pereira GJS, Antonioli M, Hirata H, Ureshino RP, Nascimento AR, Bincoletto C, et al. Glutamate induces autophagy via the two-pore channels in neural cells. *Oncotarget*. 2016 Dec;8(8):12730–40. doi: 10.18632/oncotarget.14404

190. Eden ER. The formation and function of ER-endosome membrane contact sites. *Biochim Biophys Acta Mol Cell Biol Lipid*. 2016 Aug;1861(8):874–9. doi: 10.1016/j.bbalip.2016.01.020

191. Zhu MY, Guo YJ, Zhu YQ, Wang HZ, Wang HD, Chen HY, et al. Activation of lysosomal retrograde transport triggers TPC1-IP_3R1 Ca^{2+} crosstalk at lysosome-ER MCSs leading to lethal depleting of ER calcium. *Adv Sci (Weinh)*. 2025 Jul;12(39):e15313. doi: 10.1002/advs.202415313

192. Graça JD, Thiola C, Rouabah M, Guerrera IC, Khallouki NE, Romao M, et al. ER-endosome contacts generate a local environment promoting phagophore formation. *Cell Rep*. 2025 Jul;44(7):115993. doi: 10.1016/j.celrep.2025.115993

193. Kilpatrick BS, Eden ER, Hockey LN, Yates E, Futter CE, Patel S. An endosomal NAADP-sensitive two-pore Ca^{2+} channel regulates ER-endosome membrane contact sites to control growth factor signaling. *Cell Rep*. 2017 Feb;18(7):1636–45. doi: 10.1016/j.celrep.2017.01.052

194. Garrity AG, Wang W, Collier CM, Levey SA, Gao Q, Xu H. The endoplasmic reticulum, not the pH gradient, drives calcium refilling of lysosomes. *eLife*. 2016 May;5(1):e15887. doi: 10.7554/elife.15887

195. López-Sanjurjo CI, Tovey SC, Prole DL, Taylor CW. Lysosomes shape Ins(1,4,5)P_3-evoked Ca^{2+} signals by selectively sequestering Ca^{2+} released from the endoplasmic reticulum. *J Cell Sci*. 2013 Jan;126(1):289–300. doi: 10.1242/jcs.116103

196. Dong XP, Cheng X, Mills E, Delling M, Wang F, Kurz T, et al. The type IV mucolipidosis-associated protein TRPML1 is an endo-lysosomal iron release channel. *Nature*. 2008 Oct;455(7215):992–6. doi: 10.1038/nature07311

197. Plesch E, Chen CC, Butz E, Scotto Rosato A, Krogsaeter EK, Yinan H, et al. Selective agonist of TRPML2 reveals direct role in chemokine release from innate immune cells. *eLife*. 2018 Nov;7(1):e39720. doi: 10.7554/elife.39720

198. Gu ZQ, Wang HT, Li Y, Krogsaeter E, Lin AC, Lin J, et al. TRPML2 channel modulation by PI(3,5)P_2 and small-molecule agonists controls endosomal vesicle dynamics. *Biomed Pharmacother*. 2025 Aug;189(1):118350. doi: 10.1016/j.biopha.2025.118350

199. Venkatachalam K, Hofmann T, Montell C. Lysosomal localization of TRPML3 depends on TRPML2 and the mucolipidosis-associated protein TRPML1. *J Biol Chem*. 2006 Jun;281(25):17517–27. doi: 10.1074/jbc.M600807200

200. Dong XP, Shen D, Wang X, Dawson T, Li X, Zhang Q, et al. PI(3,5)P_2 controls membrane traffic by direct activation of mucolipin Ca^{2+} release channels in the endolysosome. *Nat Commun*. 2010 Jul;1(4):38. doi: 10.1038/ncomms1037.

201. Clement D, Szabo EK, Krokeide SZ, Wiiger MT, Vincenti M, Palacios D, et al. The lysosomal calcium channel TRPML1 maintains mitochondrial fitness in NK cells through interorganelle cross-talk. *J Immunol*. 2023 Nov;211(9):1348–58. doi: 10.4049/jimmunol.2300406

202. Cuajungco MP, Basilio LC, Silva J, Hart T, Tringali J, Chen CC, et al. Cellular zinc levels are modulated by Trpml1-Tmem163 interaction. *Traffic*. 2014 Nov;15(11):1247–65. doi: 10.1111/tra.12205

203. Raychowdhury MK, González-Perrett S, Montalbetti N, Timpanaro GA, Chasan B, Goldmann WH, et al. Molecular pathophysiology of mucolipidosis type IV: pH dysregulation of the mucolipin-1 cation channel. *Hum Mol Genet*. 2004 Mar;13(6):617–27. doi: 10.1093/hmg/ddh067

204. Novick P, Zerial M. The diversity of Rab proteins in vesicle transport. *Curr Opin Cell Biol*. 1997 Aug;9(4):496–504. doi: 10.1016/s0955-0674(97)80025-7

205. Pfeffer SR. Rab GTPase regulation of membrane identity. *Curr Opin Cell Biol*. 2013 Aug;25(4):414–9. doi: 10.1016/j.ceb.2013.04.002

206. Schwartz AL. Receptor cell biology: receptor-mediated endocytosis. *Pediatr Res*. 1995 Dec;38(6):835–43. doi: 10.1203/00006450-199512000-00003

207. Laporte SA, Oakley RH, Zhang J, Holt JA, Ferguson SSG, Caron MG, et al. The β2-adrenergic receptor/βarrestin complex recruits the clathrin adaptor AP-2 during endocytosis. *Proc Natl Acad Sci USA*. 1999 Mar;96(7):3712–7. doi: 10.1073/pnas.96.7.3712

208. Brown MS, Goldstein JL. A receptor-mediated pathway for cholesterol homeostasis. *Science*. 1986 Apr;232(4746):34–47. doi: 10.1126/science.3513311

209. Chao YK, Chang SY, Grimm C. Endo-lysosomal cation channels and infectious diseases. *Rev Physiol Biochem Pharmacol*. 2020 Aug;185(1):259–76. doi: 10.1007/112_2020_31

210. Kaksonen M, Roux A. Mechanisms of clathrin-mediated endocytosis. *Nat Rev Mol Cell Biol*. 2018 Feb;19(5):313–26. doi: 10.1038/nrm.2017.132

211. Gao H, Shi W, Freund LB. Mechanics of receptor-mediated endocytosis. *Proc Natl Acad Sci USA*. 2005 Jul;102(27):9469–74. doi: 10.1073/pnas.0503879102

212. Ferguson SM, De Camilli P. Dynamin, a membrane-remodelling GTPase. *Nat Rev Mol Cell Biol*. 2012 Jan;13(2):75–88. doi: 10.1038/nrm3266

213. Mayor S, Parton RG, Donaldson JG. Clathrin-independent pathways of endocytosis. *Cold Spring Harb Perspect Biol*. 2014 Jun;6(6):a016758. doi: 10.1101/cshperspect.a016758

214. Flannagan RS, Jaumouillé V, Grinstein S. The cell biology of phagocytosis. *Annu Rev Pathol: Mechanisms of Disease*. 2012 Feb;7(7):61–98. doi: 10.1146/annurev-pathol-011811-132445

215. Damke H, Baba T, van der Bliek AM, Schmid SL. Clathrin-independent pinocytosis is induced in cells overexpressing a temperature-sensitive mutant of dynamin. *J Cell Biol*. 1995 Oct;131(1):69–80. doi: 10.1083/jcb.131.1.69

216. Kiss AL, Botos E. Endocytosis via caveolae: alternative pathway with distinct cellular compartments to avoid lysosomal degradation? *J Cell Mol Med*. 2009 Jul;13(7):1228–37. doi: 10.1111/j.1582-4934.2009.00754.x

217. Botos E, Turi Á, Müllner N, Kovalszky I, Tátrai P, Kiss AL. Regulatory role of kinases and phosphatases on the internalisation of caveolae in HepG2 cells. *Micron*. 2007 Apr;38(3):313–20. doi: 10.1016/j.micron.2006.03.012

218. Chadda R, Howes MT, Plowman SJ, Hancock JF, Parton RG, Mayor S. Cholesterol-sensitive Cdc42 activation regulates actin polymerization for endocytosis via the GEEC pathway. *Traffic*. 2007 Jun;8(6):702–17. doi: 10.1111/j.1600-0854.2007.00565.x

219. Cullen PJ, Steinberg F. To degrade or not to degrade: mechanisms and significance of endocytic recycling. *Nat Rev Mol Cell Biol*. 2018 Sep;19(11):679–96. doi: 10.1038/s41580-018-0053-7

220. Maxfield FR, McGraw TE. Endocytic recycling. *Nat Rev Mol Cell Biol*. 2004 Feb;5(2):121–32. doi: 10.1038/nrm1315

221. Grant BD, Donaldson JG. Pathways and mechanisms of endocytic recycling. *Nat Rev Mol Cell Biol*. 2009 Sep;10(9):597–608. doi: 10.1038/nrm2755

222. Smith SM, Renden R, von Gersdorff H. Synaptic vesicle endocytosis: fast and slow modes of membrane retrieval. *Trends Neurosci*. 2008 Nov;31(11):559–68. doi: 10.1016/j.tins.2008.08.005

223. Freeman SA, Grinstein S, Orlowski J. Determinants, maintenance and function of organellar pH. *Physiol Rev*. 2022 Jan;103(1):515–606. doi: 10.1152/physrev.00009.2022

224. Lafourcade C, Sobo K, Kieffer-Jaquinod S, Garin J, van der Goot FG. Regulation of the V-ATPase along the endocytic pathway occurs through reversible subunit association and membrane localization. *PLoS One*. 2008 Jul;3(7):e2758. doi: 10.1371/journal.pone.0002758

225. Saminathan A, Devany J, Veetil AT, Suresh B, Pillai KS, Schwake M, et al. A DNA-based voltmeter for organelles. *Nat Nanotechnol*. 2021 Jan;16(1):96–103. doi: 10.1038/s41565-020-00784-1

226. Koivusalo M, Steinberg BE, Mason D, Grinstein S. *In situ* measurement of the electrical potential across the lysosomal membrane using FRET. *Traffic*. 2011 Aug;12(8):972–82. doi: 10.1111/j.1600-0854.2011.01215.x

227. Leray X, Hilton JK, Nwangwu K, Becerril A, Mikusevic V, Fitzgerald G, et al. Tonic inhibition of the chloride/proton antiporter ClC-7 by $PI(3,5)P_2$ is crucial for lysosomal pH maintenance. *eLife*. 2022 Jun;11(1):e74136. doi: 10.7554/elife.74136

228. Wu JZ, Zeziulia M, Kwon W, Jentsch TJ, Grinstein S, Freeman SA. ClC-7 drives intraphagosomal chloride accumulation to support hydrolase activity and phagosome resolution. *J Cell Biol*. 2023 Apr;222(6):e202208155. doi: 10.1083/jcb.202208155

229. Maeda K, Kato Y, Sugiyama Y. pH-dependent receptor/ligand dissociation as a determining factor for intracellular sorting of ligands for epidermal growth factor receptors in rat hepatocytes. *J Control Release*. 2002 Jul;82(1):71–82. doi: 10.1016/s0168-3659(02)00126-8

230. Dautry-Varsat A, Ciechanover A, Lodish HF. pH and the recycling of transferrin during receptor-mediated endocytosis. *Proc Natl Acad Sci USA*. 1983 Apr;80(8):2258–62. doi: 10.1073/pnas.80.8.2258

231. Yadati T, Houben T, Bitorina A, Shiri-Sverdlov R. The ins and outs of cathepsins: physiological function and role in disease management. *Cells*. 2020 Jul;9(7):1679. doi: 10.3390/cells9071679

232. Galaris D, Barbouti A, Pantopoulos K. Iron homeostasis and oxidative stress: an intimate relationship. *Biochim Biophys Acta Mol Cell Res*. 2019 Dec;1866(12):118535. doi: 10.1016/j.bbamcr.2019.118535

233. Chen Y, Xie B, Hu Y, Sun J, Xu J, Shen Y, et al. Transient receptor potential mucolipin 1 circumvents oxidative stress in primary human melanocytes. *Skin Res Technol*. 2024 Jun;30(1):e13772. doi: 10.1111/srt.13772

234. Dickson EJ, Hille B. Understanding phosphoinositides: rare, dynamic, and essential membrane phospholipids. *Biochem J*. 2019 Jan;476(1):1–23. doi: 10.1042/bcj20180022

235. Gillooly DJ, Morrow IC, Lindsay M, Gould R, Bryant NJ, Gaullier JM, et al. Localization of phosphatidylinositol 3-phosphate in yeast and mammalian cells. *EMBO J*. 2000 Sep;19(17):4577–88. doi: 10.1093/emboj/19.17.4577

236. Marcelić M, Mahmutefendić LH, Jurak BA, Blagojević ZG, Lučin P. Early endosomal Vps34-derived phosphatidylinositol-3-phosphate is indispensable for the biogenesis of the endosomal recycling compartment. *Cells*. 2022 Mar;11(6):962. doi: 10.3390/cells11060962

237. Jean S, Kiger AA. Classes of phosphoinositide 3-kinases at a glance. *J Cell Sci*. 2014 Mar;127(5):923–8. doi: 10.1242/jcs.093773

238. Shisheva A. PIKfyve: partners, significance, debates and paradoxes. *Cell Biol Int*. 2008 Jun;32(6):591–604. doi: 10.1016/j.cellbi.2008.01.006

239. Yoshida S, Hoppe AD, Araki N, Swanson JA. Sequential signaling in plasma-membrane domains during macropinosome formation in macrophages. *J Cell Sci*. 2009 Sep;122(18):3250–61. doi: 10.1242/jcs.053207

240. Orr A, Wickner W. PI3P regulates multiple stages of membrane fusion. *Mol Biol Cell*. 2023 Mar;34(3):1–9. doi: 10.1091/mbc.e22-10-0486

241. Vines JH, Maib H, Buckley CM, Gueho A, Zhu Z, Soldati T, et al. A PI(3,5)P_2 reporter reveals PIKfyve activity and dynamics on macropinosomes and phagosomes. *J Cell Biol*. 2023 Jun;222(9):e202209077. doi: 10.1083/jcb.202209077

242. Rizzollo F, More S, Vangheluwe P, Agostinis P. The lysosome as a master regulator of iron metabolism. *Trends Biochem Sci*. 2021 Dec;46(12):960–75. doi: 10.1016/j.tibs.2021.07.003

243. Li J, Feng Y, Li Y, He P, Zhou Q, Tian Y, et al. Ferritinophagy: a novel insight into the double-edged sword in ferritinophagy–ferroptosis axis and human diseases. *Cell Prolif*. 2024 Feb;57(7):e13621. doi: 10.1111/cpr.13621

244. Ajioka RS, Phillips JD, Kushner JP. Biosynthesis of heme in mammals. *Biochim Biophys Acta Mol Cell Res*. 2006 Jul;1763(7):723–36. doi: 10.1016/j.bbamcr.2006.05.005

245. Gryzik M, Asperti M, Denardo A, Arosio P, Poli M. NCOA4-mediated ferritinophagy promotes ferroptosis induced by erastin, but not by RSL3 in HeLa cells. *Biochim Biophys Acta Mol Cell Res*. 2021 Feb;1868(2):118913. doi: 10.1016/j.bbamcr.2020.118913

246. Gkouvatsos K, Papanikolaou G, Pantopoulos K. Regulation of iron transport and the role of transferrin. *Biochim Biophys Acta Gene Subj*. 2012 Mar;1820(3):188–202. doi: 10.1016/j.bbagen.2011.10.013

247. Aisen P, Leibman A, Zweier J. Stoichiometric and site characteristics of the binding of iron to human transferrin. *J Biol Chem*. 1978 Mar;253(6):1930–7. doi: 10.1016/s0021-9258(19)62337-9

248. Kawabata H, Yang R, Hirama T, Vuong PT, Kawano S, Gombart AF, et al. Molecular cloning of transferrin receptor 2: a new member of the transferrin receptor-like family. *J Biol Chem*. 1999 Jul;274(30):20826–32. doi: 10.1074/jbc.274.30.20826

249. West AP, Bennett MJ, Sellers VM, Andrews NC, Enns CA, Bjorkman PJ. Comparison of the interactions of transferrin receptor and transferrin receptor 2 with transferrin and the hereditary hemochromatosis protein HFE. *J Biol Chem*. 2000 Dec;275(49):38135–8. doi: 10.1074/jbc.C000664200

250. Bleil JD, Bretscher MS. Transferrin receptor and its recycling in HeLa cells. *EMBO J*. 1982 Jan;3(1):351–5. doi: 10.1002/j.1460-2075.1982.tb01173.x

251. Breuer W, Hershko C, Cabantchik ZI. The importance of non-transferrin bound iron in disorders of iron metabolism. *Transfus Sci*. 2000 Dec;23(3):185–92. doi: 10.1016/s0955-3886(00)00087-4

252. Tong BCK, Wu AJ, Huang AS, Dong R, Malampati S, Iyaswamy A, et al. Lysosomal *TPCN* (two pore segment channel) inhibition ameliorates beta-amyloid pathology and mitigates memory impairment in Alzheimer disease. *Autophagy*. 2021 Jul;18(3):624–42. doi: 10.1080/15548627.2021.1945220

253. Tong BCK, Huang AS, Wu AJ, Iyaswamy A, Ho OKY, Kong AHY, et al. Tetrandrine ameliorates cognitive deficits and mitigates tau aggregation in cell and animal models of tauopathies. *J Biomed Sci*. 2022 Oct;29(85):85. doi: 10.1186/s12929-022-00871-6

254. Kilpatrick BS, Magalhaes J, Beavan MS, McNeill A, Gegg ME, Cleeter MWJ, et al. Endoplasmic reticulum and lysosomal Ca^{2+} stores are remodelled in GBA1-linked Parkinson disease patient fibroblasts. *Cell Calcium*. 2016 Jan;59(1):12–20. doi: 10.1016/j.ceca.2015.11.002

255. Hockey LN, Kilpatrick BS, Eden ER, Lin-Moshier Y, Brailoiu GC, Brailoiu E, et al. Dysregulation of lysosomal morphology by pathogenic LRRK2 is corrected by TPC2 inhibition. *J Cell Sci*. 2015 Jan;128(2):232–8. doi: 10.1242/jcs.164152

256. Gregori M, Pereira GJS, Allen R, West N, Chau KY, Cai X, et al. Lysosomal TPC2 channels disrupt Ca^{2+} entry and dopaminergic function in models of LRRK2-Parkinson's disease. *J Cell Biol*. 2025 Apr;224(6):e202412055. doi: 10.1083/jcb.202412055

257. Martucci LL, Launay JM, Kawakami N, Sicard C, Desvignes N, Dakouane-Giudicelli M, et al. Endolysosomal TPCs regulate social behaviour by controlling oxytocin secretion. *Proc Natl Acad Sci USA*. 2023 Feb;120(7):e2213682120. doi: 10.1073/pnas.2213682120

258. Sulem P, Gudbjartsson DF, Stacey SN, Helgason A, Rafnar T, Jakobsdottir M, et al. Two newly identified genetic determinants of pigmentation in Europeans. *Nat Genet*. 2008 Jul;40(7):835–7. doi: 10.1038/ng.160

259. Wang Q, Wang Z, Wang Y, Qi Z, Bai D, Wang C, et al. A gain-of-function TPC2 variant R210C increases affinity to $PI(3,5)P_2$ and causes lysosome acidification and hypopigmentation. *Nat Commun*. 2023 Dec;14(1):226. doi: 10.1038/S41467-023-35786-9

260. Chao YK, Schludi V, Chen CC, Butz E, Nguyen ONP, Müller M, et al. TPC2 polymorphisms associated with a hair pigmentation phenotype in humans result in gain of channel function by independent mechanisms. *Proc Natl Acad Sci USA*. 2017 Oct;114(41):8595–602. doi: 10.1073/pnas.1705739114

261. Barbonari S, D'Amore A, Hanbashi AA, Palombi F, Riccioli A, Parrington J, et al. Endolysosomal two-pore channel 2 plays opposing roles in primary and metastatic malignant melanoma cells. *Cell Biol Int*. 2024 Apr;48(4):521–40. doi: 10.1002/cbin.12129

262. Jin X, Hanbashi AA, Kamli F, Pan X, Goding CR, Parrington J. TPC1 regulates melanoma tumourigenesis via mTORC1 and TFEB. *Heliyon*. 2024 Nov;10(21):e39752. doi: 10.1016/j.heliyon.2024.e39752

263. Nguyen ONP, Grimm C, Schneider LS, Chao YK, Atzberger C, Bartel K, et al. Two-pore channel function is crucial for the migration of invasive cancer cells. *Cancer Res*. 2017 Mar;77(6):1427–38. doi: 10.1158/0008-5472.can-16-0852

264. Hanbashi A, Alotaibi M, Sobeai HMA, Binobaid L, Alhazzani K, Jin X, et al. Loss of two-pore channel 2 function in melanoma-derived tumours reduces tumour growth *in vivo* but greatly increases tumour-related toxicity in the organism. *Cancer Cell Int*. 2023 Dec;23(1):325. doi: 10.1186/s12935-023-03148-6

265. Sun W, Yue J. TPC2 mediates autophagy progression and extracellular vesicle secretion in cancer cells. *Exp Cell Res*. 2018 Sep;370(2):478–89. doi: 10.1016/j.yexcr.2018.07.013

266. Li S, Song Y, Quach C, Guo H, Jang GB, Maazi H, et al. Transcriptional regulation of autophagy-lysosomal function in BRAF-driven melanoma progression and chemoresistance. *Nat Commun*. 2019 Apr;10(1):1693. doi: 10.1038/s41467-019-09634-8

267. Karamooz E, Kim SJ, Peterson JC, Tammen AE, Soma S, Soll ACR, et al. Two-pore channels in MR1-dependent presentation of *Mycobacterium tuberculosis* infection. *PLoS Pathog*. 2025 Aug;21(8):e1013342. doi: 10.1371/journal.ppat.1013342

268. Xiao JH. Characterisation and application of an ebola virus glycoprotein pseudotyped influenza virus (E-S-Flu) [PhD thesis]. Oxford: University of Oxford; 2019.

269. Gunaratne GS, Yang Y, Li F, Walseth TF, Marchant JS. NAADP-dependent Ca^{2+} signaling regulates Middle East respiratory syndrome-coronavirus pseudovirus translocation through the endolysosomal system. *Cell Calcium*. 2018 Nov;75(1):30–41. doi: 10.1016/j.ceca.2018.08.003

270. Ou X, Liu Y, Lei X, Li P, Mi D, Ren L, et al. Characterization of spike glycoprotein of SARS-CoV-2 on virus entry and its immune cross-reactivity with SARS-CoV. *Nat Commun*. 2020 Mar;11(1):1620. doi: 10.1038/s41467-020-15562-9

271. Wang HT, Chen CC. Patch-clamp techniques for single endolysosomal vesicle analysis. *J Vis Exp*. 2025 Apr;4(218):e67519. doi: 10.3791/67519

272. Lu Y, Dong S, Hao B, Li C, Zhu K, Guo W, et al. Vacuolin-1 potently and reversibly inhibits autophagosome-lysosome fusion by activating RAB5A. *Autophagy*. 2014 Oct;10(11):1895–905. doi: 10.4161/auto.32200

273. Chen CC, Grimm C, Wahl-Schott C, Biel M. Endolysosomal patch clamping: approaches to measure vesicular ion channel activities. In: Gasnier B, Zhu MX, editors. *Ion and molecule transport in lysosomes*. Boca Raton. CRC Press:2020. p. 45-67. doi: 10.1201/b22460

274. Grynkiewicz G, Poenie M, Tsien RY. A new generation of Ca^{2+} indicators with greatly improved fluorescence properties. *J Biol Chem*. 1985 Mar;260(6):3440–50. doi: 10.1016/s0021-9258(19)83641-4

275. Götzke H, Kilisch M, Martínez-Carranza M, Sograte-Idrissi S, Rajavel A, Schlichthaerle T, et al. The ALFA-tag is a highly versatile tool for nanobody-based bioscience applications. *Nat Commun*. 2019 Sep;10(1):4403. doi: 10.1038/s41467-019-12301-7

276. Otsu N. A threshold selection method from gray-level histograms. *IEEE Trans Syst Man Cybern*. 1979 Jan;9(1):62–6. doi: 10.1109/tsmc.1979.4310076

277. Hirayama T, Okuda K, Nagasawa H. A highly selective turn-on fluorescent probe for iron(II) to visualize labile iron in living cells. *Chem Sci*. 2013 Feb;4(3):1250–6. doi: 10.1039/c2sc21649c

278. Hopp MT, Schmalohr BF, Kühl T, Detzel MS, Wißbrock A, Imhof D. Heme determination and quantification methods and their suitability for practical applications and everyday use. *Anal Chem*. 2020 Jul;92(14):9429–40. doi: 10.1021/acs.analchem.0c00415

279. Li J, Shang Z, Chen JH, Gu W, Yao L, Yang X, et al. Engineering of NEMO as calcium indicators with large dynamics and high sensitivity. *Nat Methods*. 2023 Jun;20(6):918–24. doi: 10.1038/s41592-023-01852-9

280. Ceresa BP, Peterson JL. Cell and molecular biology of epidermal growth factor receptor. *Int Rev Cell Mol Biol*. 2014;313(1):145–78. doi: 10.1016/b978-0-12-800177-6.00005-0

281. Mayle KM, Le AM, Kamei DT. The intracellular trafficking pathway of transferrin. *Biochim Biophys Acta*. 2012 Mar;1820(3):264–81. doi: 10.1016/j.bbagen.2011.09.009

282. Burton WJ, Lin A, Morgan AJ, Davis LC, Chen CC, Galione A. Endosomal TPC1–mediated Ca^{2+} nanodomains regulate transferrin receptor trafficking and iron homeostasis. *Proc Natl Acad Sci USA*. 2026 Jul;123(29):e2530835123. doi: 10.1073/pnas.2530835123

283. Shen Y, Li X, Dong D, Zhang B, Xue Y, Shang P. Transferrin receptor 1 in cancer: a new sight for cancer therapy. *Am J Cancer Res*. 2018 Jun;8(6):916–31.

284. Torti SV, Torti FM. Iron and cancer: more ore to be mined. *Nat Rev Cancer*. 2013 May;13(5):342–55. doi: 10.1038/nrc3495

285. Ward JH, Kushner JP, Kaplan J. Regulation of HeLa cell transferrin receptors. *J Biol Chem*. 1982 Sep;257(17):10317–23. doi: 10.1016/s0021-9258(18)34022-5

286. Lamb JE, Ray F, Ward JH, Kushner JP, Kaplan J. Internalization and subcellular localization of transferrin and transferrin receptors in HeLa cells. *J Biol Chem*. 1983 Jul;258(14):8751–8. doi: 10.1016/s0021-9258(18)32120-3

287. Chakraborty A, Dissanayake R, Wall KA. Nicotinic acid adenine dinucleotide phosphate (NAADP)-mediated calcium signaling is active in memory $CD4^+$ T cells. *Molecules*. 2024 Jan;29(4):907. doi: 10.3390/molecules29040907

288. Omary MB, Trowbridge IS. Biosynthesis of the human transferrin receptor in cultured cells. *J Biol Chem*. 1981 Dec;256(24):12888–92. doi: 10.1016/s0021-9258(18)42979-1

289. Shih YJ, Baynes RD, Hudson BG, Flowers CH, Skikne BS, Cook JD. Serum transferrin receptor is a truncated form of tissue receptor. *J Biol Chem*. 1990 Nov;265(31):19077–81. doi: 10.1016/s0021-9258(17)30627-0

290. Fuchs H, Lücken U, Tauber R, Engel A, Geßner R. Structural model of phospholipid-reconstituted human transferrin receptor derived by electron microscopy. *Structure*. 1998 Oct;6(10):1235–43. doi: 10.1016/s0969-2126(98)00124-5

291. Hooper R, Churamani D, Brailoiu E, Taylor CW, Patel S. Membrane topology of NAADP-sensitive two-pore channels and their regulation by N-linked glycosylation. *J Biol Chem*. 2011 Mar;286(11):9141–9. doi: 10.1074/jbc.m110.189985

292. Hunt RC, Riegler R, Davis AA. Changes in glycosylation alter the affinity of the human transferrin receptor for its ligand. *J Biol Chem*. 1989 Jun;264(16):9643–8. doi: 10.1016/s0021-9258(18)60579-4

293. Jumper J, Evans R, Pritzel A, Green T, Figurnov M, Ronneberger O, et al. Highly accurate protein structure prediction with AlphaFold. *Nature*. 2021 Aug;596(7873):583–9. doi: 10.1038/s41586-021-03819-2

294. Freeland-Graves JH, Sanjeevi N, Lee JJ. Global perspectives on trace element requirements. *J Trace Elem Med Biol.* 2015 Jul;31(1):135–41. doi: 10.1016/j.jtemb.2014.04.006

295. Hirayama T. Development of chemical tools for imaging of Fe(II) ions in living cells: a review. *Acta Histochem Cytochem*. 2018 Oct;51(5):137–43. doi: 10.1267/ahc.18015

296. Wang J, Wu N, Peng M, Oyang L, Jiang X, Peng Q, et al. Ferritinophagy: research advance and clinical significance in cancers. *Cell Death Discov*. 2023 Dec;9(1):463. doi: 10.1038/s41420-023-01753-y

297. Zhu Q, Zhai J, Chen Z, Guo Z, Wang N, Zhang C, et al. Ferritinophagy: molecular mechanisms and role in disease. *Pathol Res Pract*. 2024 Oct;262(1):155553. doi: 10.1016/j.prp.2024.155553

298. Massey AC. Microcytic anemia: differential diagnosis and management of iron deficiency anemia. *Med Clin North Am*. 1992 May;76(3):549–66. doi: 10.1016/s0025-7125(16)30339-x

299. Groza T, Gomez FL, Mashhadi HH, Muñoz-Fuentes V, Gunes O, Wilson R, et al. The International Mouse Phenotyping Consortium: comprehensive knockout phenotyping underpinning the study of human disease. *Nucleic Acids Res*. 2023 Jan;51(1):1038–45. doi: 10.1093/nar/gkac972

300. Trufanov SK, Rybakova EYu, Avdonin PP, Tsitrina AA, Zharkikh IL, Goncharov NV, et al. The role of two-pore channels in norepinephrine-induced $[Ca^{2+}]_i$ rise in rat aortic smooth muscle cells and aorta contraction. *Cells*. 2019 Sep;8(10):1144. doi: 10.3390/cells8101144

301. Sperandio LP, Lins IVF, Erustes AG, Leão AHFF, Antunes F, Morais IBM, et al. Blocking autophagy by the two-pore channels antagonist tetrandrine improves Sorafenib-induced death of hepatocellular carcinoma cells. *Toxicol In Vitro*. 2023 Aug;90(1):105603. doi: 10.1016/j.tiv.2023.105603

302. Fernández B, Fdez E, Gómez-Suaga P, Gil F, Molina-Villalba I, Ferrer I, et al. Iron overload causes endolysosomal deficits modulated by NAADP-regulated 2-pore channels and RAB7A. *Autophagy*. 2016 Sep;12(9):1487–506. doi: 10.1080/15548627.2016.1190072

303. Qian Z, Zhang X, Huang J, Hou Y, Hu C, Cao Y, et al. Glucose deprivation-restoration induces labile iron overload and ferroptosis in renal tubules through V-ATPase-mTOR axis-mediated ferritinophagy and iron release by TPC2. *Free Radic Biol Med*. 2025 May;236(1):204–19. doi: 10.1016/j.freeradbiomed.2025.05.390

304. Ahmed S, Javvaji N, Hammond KL, Casin KM, Elrod JW, Holloway PM, et al. Activation of TPC2 amplifies lysosome-mitochondria calcium transfer to regulate energetic stress responses. *bioRxiv* [Preprint]. 2026 Mar. doi: 10.64898/2026.03.03.709381

305. Favia A, Desideri M, Gambara G, D'Alessio A, Ruas M, Esposito B, et al. VEGF-induced neoangiogenesis is mediated by NAADP and two-pore channel-2–dependent Ca^{2+} signaling. *Proc Natl Acad Sci USA*. 2014 Nov;111(44):4706–15. doi: 10.1073/pnas.1406029111

306. Arredouani A, Ruas M, Collins SC, Parkesh R, Clough F, Pillinger T, et al. Nicotinic acid adenine dinucleotide phosphate (NAADP) and endolysosomal two-pore channels modulate membrane excitability and stimulus-secretion coupling in mouse pancreatic β cells. *J Biol Chem*. 2015 Aug;290(35):21376–92. doi: 10.1074/jbc.m115.671248

307. Capel RA, Bolton EL, Lin WK, Aston D, Wang Y, Liu W, et al. Two-pore channels (TPC2s) and nicotinic acid adenine dinucleotide phosphate (NAADP) at lysosomal-sarcoplasmic reticular junctions contribute to acute and chronic β-adrenoceptor signaling in the heart. *J Biol Chem*. 2015 Dec;290(50):30087–98. doi: 10.1074/jbc.m115.684076

308. Ruas M, Galione A, Parrington J. Two-pore channels: lessons from mutant mouse models. *Messenger*. 2015 Jun;4(1):4–22. doi: 10.1166/msr.2015.1041

309. Halcrow PW, Kumar N, Afghah Z, Fischer JP, Khan N, Chen X, et al. Heterogeneity of ferrous iron-containing endolysosomes and effects of endolysosome iron on endolysosome numbers, sizes, and localization patterns. *J Neurochem*. 2022 Apr;161(1):69–83. doi: 10.1111/jnc.15583

310. Knight DE. Calcium-dependent transferrin receptor recycling in bovine chromaffin cells. *Traffic*. 2002 Apr;3(4):298–307. doi: 10.1034/j.1600-0854.2002.030407.x

311. Sainte-Marie J, Lafont V, Pécheur EI, Favero J, Philippot JR, Bienvenüe A. Transferrin receptor functions as a signal-transduction molecule for its own recycling via increases in the internal Ca^{2+} concentration. *Eur J Biochem*. 1997 Dec;250(3):689–97. doi: 10.1111/j.1432-1033.1997.00689.x

312. Sabbir MG. Loss of Ca^{2+}/calmodulin dependent protein kinase kinase 2 leads to aberrant transferrin phosphorylation and trafficking: a potential biomarker for Alzheimer's disease. *Front Mol Biosci*. 2018 Nov;5(99):1–28. doi: 10.3389/fmolb.2018.00099

313. Sabbir MG. CAMKK2-CAMK4 signaling regulates transferrin trafficking, turnover, and iron homeostasis. *Cell Commun Signal*. 2020 May;18(80):80. doi: 10.1186/s12964-020-00575-0

314. Naraghi M, Neher E. Linearized buffered Ca^{2+} diffusion in microdomains and its implications for calculation of $[Ca^{2+}]$ at the mouth of a calcium channel. *J Neurosci*. 1997 Sep;17(18):6961–73. doi: 10.1523/jneurosci.17-18-06961.1997

315. Brini M. Effects of PMCA and SERCA pump overexpression on the kinetics of cell Ca^{2+} signalling. *EMBO J*. 2000 Sep;19(18):4926–35. doi: 10.1093/emboj/19.18.4926

316. Morgan AJ, Jacob R. Ionomycin enhances Ca^{2+} influx by stimulating store-regulated cation entry and not by a direct action at the plasma membrane. *Biochem J*. 1994 Jun;300(3):665–72. doi: 10.1042/bj3000665

317. Christensen KA, Myers JT, Swanson JA. pH-dependent regulation of lysosomal calcium in macrophages. *J Cell Sci*. 2002 Feb;115(3):599–607. doi: 10.1242/jcs.115.3.599

318. Fedele AO, Proud CG. Chloroquine and bafilomycin-A mimic lysosomal storage disorders and impair mTORC1 signalling. *Biosci Rep*. 2020 Apr;40(4):BSR20200905. doi: 10.1042/bsr20200905

319. Lewit-Bentley A, Réty S. EF-hand calcium-binding proteins. *Curr Opin Struct Biol*. 2000 Dec;10(6):637–43. doi: 10.1016/s0959-440x(00)00142-1

320. Gerasimenko JV, Tepikin AV, Petersen OH, Gerasimenko OV. Calcium uptake via endocytosis with rapid release from acidifying endosomes. *Curr Biol*. 1998 Dec;8(24):1335–8. doi: 10.1016/S0960-9822(07)00565-9

321. Sneyers F, Speelman-Rooms F, Verhelst SHL, Bootman MD, Bultynck G. Cellular effects of BAPTA: are they only about Ca^{2+} chelation? *Biochim Biophys Acta Mol Cell Res*. 2024 Feb;1871(2):119589. doi: 10.1016/j.bbamcr.2023.119589

322. Kreitzer AC, Gee KR, Archer EA, Regehr WG. Monitoring presynaptic calcium dynamics in projection fibers by *in vivo* loading of a novel calcium indicator. *Neuron*. 2000 Jul;27(1):25–32. doi: 10.1016/s0896-6273(00)00006-4

323. Albrecht T, Zhao Y, Nguyen TH, Campbell RE, Johnson JD. Fluorescent biosensors illuminate calcium levels within defined beta-cell endosome subpopulations. *Cell Calcium*. 2015 Apr;57(4):263–74. doi: 10.1016/j.ceca.2015.01.008

324. Orlowski J, Grinstein S. Na^+/H^+ exchangers of mammalian cells. *J Biol Chem*. 1997 Sep;272(36):22373–6. doi: 10.1074/jbc.272.36.22373

325. Schwarz EC, Kummerow C, Wenning AS, Wagner K, Sappok A, Waggershauser K, et al. Calcium dependence of T cell proliferation following focal stimulation. *Eur J Immunol*. 2007 Oct;37(10):2723–33. doi: 10.1002/eji.200737039

326. Vaarmann A, Gandhi S, Abramov AY. Dopamine induces Ca^{2+} signaling in astrocytes through reactive oxygen species generated by monoamine oxidase. *J Biol Chem*. 2010 Aug;285(32):25018–23. doi: 10.1074/jbc.m110.111450

327. Johnson LS, Dunn KW, Pytowski B, McGraw TE. Endosome acidification and receptor trafficking: bafilomycin A1 slows receptor externalization by a mechanism involving the receptor's internalization motif. *Mol Biol Cell*. 1993 Oct;4(12):1251–66. doi: 10.1091/mbc.4.12.1251

328. Presley JF, Mayor S, McGraw TE, Dunn KW, Maxfield FR. Bafilomycin A1 treatment retards transferrin receptor recycling more than bulk membrane recycling. *J Biol Chem*. 1997 May;272(21):13929–36. doi: 10.1074/jbc.272.21.13929

329. Kilpatrick BS, Eden ER, Schapira AH, Futter CE, Patel S. Direct mobilisation of lysosomal Ca^{2+} triggers complex Ca^{2+} signals. *J Cell Sci*. 2013 Jan;126(1):60–6. doi: 10.1242/jcs.118836

330. Gerasimenko JV, Charlesworth RM, Sherwood MW, Ferdek PE, Mikoshiba K, Parrington J, et al. Both RyRs and TPCs are required for NAADP-induced intracellular Ca^{2+} release. *Cell Calcium*. 2015 Sep;58(3):237–45. doi: 10.1016/j.ceca.2015.05.005

331. Adler EM, Augustine GJ, Duffy SN, Charlton MP. Alien intracellular calcium chelators attenuate neurotransmitter release at the squid giant synapse. *J Neurosci*. 1991 Jun;11(6):1496–507. doi: 10.1523/jneurosci.11-06-01496.1991

332. Schneggenburger R, Neher E. Presynaptic calcium and control of vesicle fusion. *Curr Opin Neurobio*l. 2005 Jun;15(3):266–74. doi: 10.1016/j.conb.2005.05.006

333. Deisseroth K, Heist EK, Tsien RW. Translocation of calmodulin to the nucleus supports CREB phosphorylation in hippocampal neurons. *Nature*. 1998 Mar;392(6672):198–202. doi: 10.1038/32448

334. Wheeler DG, Barrett CF, Groth RD, Safa P, Tsien RW. CaMKII locally encodes L-type channel activity to signal to nuclear CREB in excitation–transcription coupling. *J Cell Biol*. 2008 Dec;183(5):849–63. doi: 10.1083/jcb.200805048

335. Tucker WC, Chapman ER. Role of synaptotagmin in Ca^{2+}-triggered exocytosis. *Biochem J*. 2002 Aug;366(1):1–13. doi: 10.1042/bj20020776

336. Morgan EH. Calcium chelators induce association with the detergent-insoluble cytoskeleton and functional inactivation of the transferrin receptor in reticulocytes. *Biochim Biophys Acta Biomembranes*. 1989 May;981(1):121–9. doi: 10.1016/0005-2736(89)90089-8

337. Rudenko G, Henry L, Henderson K, Ichtchenko K, Brown MS, Goldstein JL, et al. Structure of the LDL receptor extracellular domain at endosomal pH. *Science*. 2002 Dec;298(5602):2353–8. doi: 10.1126/science.1078124

338. French AR, Tadaki DK, Niyogi SK, Lauffenburger DA. Intracellular trafficking of epidermal growth factor family ligands is directly influenced by the pH sensitivity of the receptor/ligand interaction. *J Biol Chem*. 1995 Mar;270(9):4334–40. doi: 10.1074/jbc.270.9.4334

339. Lin PH, Duann P, Komazaki S, Park KH, Li H, Sun M, et al. Lysosomal two-pore channel subtype 2 (TPC2) regulates skeletal muscle autophagic signaling. *J Biol Chem*. 2015 Feb;290(6):3377–89. doi: 10.1074/jbc.m114.608471

340. Coffey EE, Beckel JM, Laties AM, Mitchell CH. Lysosomal alkalization and dysfunction in human fibroblasts with the Alzheimer's disease-linked presenilin 1 A246E mutation can be reversed with cAMP. *Neuroscience*. 2014 Mar;263(1):111–24. doi: 10.1016/j.neuroscience.2014.01.001

341. Chadwick SR, Barreda D, Wu JZ, Ye G, Yusuf B, Ren D, et al. Two-pore channels regulate endomembrane tension to enable remodeling and resolution of phagolysosomes. *Proc Natl Acad Sci USA*. 2024 Feb;121(8):e2309465121. doi: 10.1073/pnas.2309465121

342. Campbell DL, Giles WR, Hume JR, Noble D, Shibata EF. Reversal potential of the calcium current in bull-frog atrial myocytes. *J Physiol*. 1988 Sep;403(1):267–86. doi: 10.1113/jphysiol.1988.sp017249

343. Lee KS, Tsein RW. Reversal of current through calcium channels in dialysed single heart cells. *Nature*. 1982 Jun;297(5866):498–501. doi: 10.1038/297498a0

344. Sainte-Marie J, Vidal M, Bette-Bobillo P, Philippot JR, Bienvenüe A. The influence of transferin binding to L2C guinea pig leukemic lymphocytes on the endocytosis cycle kinetics of its receptor. *Eur J Biochem*. 1991 Oct;201(1):295–302. doi: 10.1111/j.1432-1033.1991.tb16287.x

345. Gironès N, Davis RJ. Comparison of the kinetics of cycling of the transferrin receptor in the presence or absence of bound diferric transferrin. *Biochem J*. 1989 Nov;264(1):35–46. doi: 10.1042/bj2640035

346. Zhao Y, Qin G, Fan W, Zhang Y, Peng H. TF and TFRC regulate ferroptosis in swine testicular cells through the JNK signaling pathway. *Int J Biol Macromol*. 2025 May;307(4):142369. doi: 10.1016/j.ijbiomac.2025.142369

347. Lei R, Zhang K, Liu K, Shao X, Ding Z, Wang F, et al. Transferrin receptor facilitates TGF-β and BMP signaling activation to control craniofacial morphogenesis. *Cell Death Dis*. 2016 Jun;7(6):e2282. doi: 10.1038/cddis.2016.170

348. Wijers M, Kuivenhoven JA, van de Sluis B. The life cycle of the low-density lipoprotein receptor: insights from cellular and *in-vivo* studies. *Curr Opin Lipidol*. 2015 Apr;26(2):82. doi: 10.1097/mol.0000000000000157

349. Salloum G, Bresnick AR, Backer JM. Macropinocytosis: mechanisms and regulation. *Biochem J*. 2023 Mar;480(5):335–62. doi: 10.1042/bcj20210584

350. Besterman JM, Airhart JA, Woodworth RC, Low RB. Exocytosis of pinocytosed fluid in cultured cells: kinetic evidence for rapid turnover and compartmentation. *J Cell Biol*. 1981 Feb;91(3):716–27. doi: 10.1083/jcb.91.3.716

351. Steinman RM, Brodie SE, Cohn ZA. Membrane flow during pinocytosis. a stereologic analysis. *J Cell Biol*. 1976 Mar;68(3):665–87. doi: 10.1083/jcb.68.3.665

352. Li L, Wan T, Wan M, Liu B, Cheng R, Zhang R. The effect of the size of fluorescent dextran on its endocytic pathway. *Cell Biol Int*. 2015 May;39(5):531–9. doi: 10.1002/cbin.10424

353. Freeman SA, Uderhardt S, Saric A, Collins RF, Buckley CM, Mylvaganam S, et al. Lipid-gated monovalent ion fluxes regulate endocytic traffic and support immune surveillance. *Science*. 2020 Jan;367(6475):301–5. doi: 10.1126/science.aaw9544

354. Maus M, López-Polo V, Mateo L, Lafarga M, Aguilera M, De Lama E, et al. Iron accumulation drives fibrosis, senescence and the senescence-associated secretory phenotype. *Nat Metab*. 2023 Dec;5(12):2111–30. doi: 10.1038/s42255-023-00928-2

355. Chen J, Enns CA. Hereditary hemochromatosis and transferrin receptor 2. *Biochim Biophys Acta*. 2011 Aug;1820(3):256. doi: 10.1016/j.bbagen.2011.07.015

356. Lear PV, González-Touceda D, Porteiro Couto B, Viaño P, Guymer V, Remzova E, et al. Absence of intracellular ion channels TPC1 and TPC2 leads to mature-onset obesity in male mice, due to impaired lipid availability for thermogenesis in brown adipose tissue. *Endocrinology*. 2015 Mar;156(3):975–86. doi: 10.1210/en.2014-1766

357. Vidal M, Sainte-Marie J, Philippot J r., Bienvenue A. Comparison of the internalization efficiency of LDL and transferrin receptors on L2C guinea pig lymphocytes. *FEBS Lett*. 1986 Feb;196(2):242–6. doi: 10.1016/0014-5793(86)80255-1

358. Scotti E, Calamai M, Goulbourne CN, Zhang L, Hong C, Lin RR, et al. IDOL stimulates clathrin-independent endocytosis and multivesicular body-mediated lysosomal degradation of the low-density lipoprotein receptor. *Mol Cell Biol*. 2013 Apr;33(8):1503–14. doi: 10.1128/mcb.01716-12

359. Guan Y, Liu X, Yang Z, Zhu X, Liu M, Du M, et al. PCSK9 promotes LDLR degradation by preventing SNX17-mediated LDLR recycling. *Circulation*. 2025 May;151(21):1512–26. doi: 10.1161/circulationaha.124.072336

360. Arlt E, Fraticelli M, Tsvilovskyy V, Nadolni W, Breit A, O'Neill TJ, et al. TPC1 deficiency or blockade augments systemic anaphylaxis and mast cell activity. *Proc Natl Acad Sci USA*. 2020 Jul;117(30):18068–78. doi: 10.1073/pnas.1920122117

361. Weiden EM, Serianz Z, Klingl Y, Jörs S, Jaślan D, Keller M, et al. TRPML1 suppresses pulmonary fibrosis by limiting collagen and elastin deposition. *EMBO J*. 2026 Feb;45(7):2182–209. doi: 10.1038/s44318-026-00712-4

362. Prusch RD, Hannafin JA. Sucrose uptake by pinocytosis in *Amoeba proteus* and the influence of external calcium. *J Gen Physiol*. 1979 Oct;74(4):523–35. doi: 10.1085/jgp.74.4.523

363. Prusch RD. Calcium and initial surface binding phase of pinocytosis in *Amoeba proteus*. *Am J Physiol*. 1986 Aug;251(2):153–8. doi: 10.1152/ajpcell.1986.251.2.c153

364. Commisso C, Davidson SM, Soydaner-Azeloglu RG, Parker SJ, Kamphorst JJ, Hackett S, et al. Macropinocytosis of protein is an amino acid supply route in Ras-transformed cells. *Nature*. 2013 May;497(7451):633–7. doi: 10.1038/nature12138

365. Kim SM, Nguyen TT, Ravi A, Kubiniok P, Finicle BT, Jayashankar V, et al. PTEN deficiency and AMPK activation promote nutrient scavenging and anabolism in prostate cancer cells. *Cancer Discov*. 2018 Jul;8(7):866–83. doi: 10.1158/2159-8290.cd-17-1215

366. Liu Y, Shreder KR, Gai W, Corral S, Ferris DK, Rosenblum JS. Wortmannin, a widely used phosphoinositide 3-kinase inhibitor, also potently inhibits mammalian polo-like kinase. *Chem Biol*. 2005 Jan;12(1):99–107. doi: 10.1016/j.chembiol.2004.11.009

367. Nakanishi S, Kakita S, Takahashi I, Kawahara K, Tsukuda E, Sano T, et al. Wortmannin, a microbial product inhibitor of myosin light chain kinase. *J Biol Chem*. 1992 Feb;267(4):2157–63. doi: 10.1016/s0021-9258(18)45857-7

368. Spiro DJ, Boll W, Kirchhausen T, Wessling-Resnick M. Wortmannin alters the transferrin receptor endocytic pathway *in vivo* and *in vitro*. *Mol Biol Cell*. 1996 Mar;7(3):355–67. doi: 10.1091/mbc.7.3.355

369. Ikonomov OC, Sbrissa D, Shisheva A. YM201636, an inhibitor of retroviral budding and PIKfyve-catalyzed PtdIns(3,5)P_2 synthesis, halts glucose entry by insulin in adipocytes. *Biochem Biophy Res Commun*. 2009 May;382(3):566–70. doi: 10.1016/j.bbrc.2009.03.063

370. Guan X, Du C, Shah KR, Yan J. NAADP elicits two-pore channel currents by lifting Lsm12-mediated inhibition of PI(3,5)P_2 activation. *bioRxiv* [Preprint]. 2026 Apr 23. doi: 10.64898/2026.04.13.718294

371. Thakur A, Saran S. Elucidating the impact of trans-ned-19 on two-Pore channel 2 mutants of *Dictyostelium*: changes in intracellular calcium levels and subsequent effect on autophagic flux. *Exp Cell Res*. 2026 Jan;454(2):114829. doi: 10.1016/j.yexcr.2025.114829

372. Fan C, Wu H, Du X, Li C, Zeng W, Qu L, et al. Inhibition of lysosomal TRPML1 channel eliminates breast cancer stem cells by triggering ferroptosis. *Cell Death Discov*. 2024 May;10(1):256. doi: 10.1038/s41420-024-02026-y

373. García-Rúa V, Feijóo-Bandín S, García-Vence M, Aragón-Herrera A, Bravo SB, Rodríguez-Penas D, et al. Metabolic alterations derived from absence of two-pore channel 1 at cardiac level. *J Biosci*. 2016 Dec;41(4):643–58. doi: 10.1007/s12038-016-9647-4

374. Song EK, Lee YR, Kim YR, Yeom JH, Yoo CH, Kim HK, et al. NAADP mediates insulin-stimulated glucose uptake and insulin sensitization by PPARγ in adipocytes. *Cell Rep*. 2012 Dec;2(6):1607–19. doi: 10.1016/j.celrep.2012.10.018

375. Park DR, Park KH, Kim BJ, Yoon CS, Kim UH. Exercise ameliorates insulin resistance via Ca^{2+} signals distinct from those of insulin for GLUT4 translocation in skeletal muscles. *Diabetes*. 2015 Apr;64(4):1224–34. doi: 10.2337/db14-0939

376. Wu SY, Shen Y, Shkolnikov I, Campbell RE. Fluorescent indicators for biological imaging of monatomic ions. *Front Cell Dev Biol*. 2022 Apr;10(1):885440. doi: 10.3389/fcell.2022.885440/full

377. Mulgrew-Nesbitt A, Diraviyam K, Wang J, Singh S, Murray P, Li Z, et al. The role of electrostatics in protein–membrane interactions. *Biochim Biophys Acta Mol Cell Biol L*. 2006 Aug;1761(8):812–26. doi: 10.1016/j.bbalip.2006.07.002

378. Dumas JJ, Merithew E, Sudharshan E, Rajamani D, Hayes S, Lawe D, et al. Multivalent endosome targeting by homodimeric EEA1. *Mol Cell*. 2001 Nov;8(5):947–58. doi: 10.1016/s1097-2765(01)00385-9

379. Soyombo AA, Tjon-Kon-Sang S, Rbaibi Y, Bashllari E, Bisceglia J, Muallem S, et al. TRP-ML1 regulates lysosomal pH and acidic lysosomal lipid hydrolytic activity. *J Biol Chem*. 2006 Mar;281(11):7294–301. doi: 10.1074/jbc.m508211200

380. Cao Q, Yang Y, Zhong XZ, Dong XP. The lysosomal Ca^{2+} release channel TRPML1 regulates lysosome size by activating calmodulin. *J Biol Chem*. 2017 May;292(20):8424–35. doi: 10.1074/jbc.m116.772160

381. Kim SW, Kim MK, Hong S, Choi A, Choi JH, Muallem S, et al. The intracellular Ca^{2+} channel TRPML3 is a PI3P effector that regulates autophagosome biogenesis. *Proc Natl Acad Sci USA*. 2022 Oct;119(43):e2200085119. doi: 10.1073/pnas.2200085119

382. Nolan RD, Lapetina EG. Thrombin stimulates the production of a novel polyphosphoinositide in human platelets. *J Biol Chem*. 1990 Feb;265(5):2441–5. doi: 10.1016/s0021-9258(19)39818-7

383. Botelho RJ, Teruel M, Dierckman R, Anderson R, Wells A, York JD, et al. Localized biphasic changes in phosphatidylinositol-4,5-bisphosphate at sites of phagocytosis. *J Cell Biol*. 2000 Dec;151(7):1353–68. doi: 10.1083/jcb.151.7.1353

384. Micheva KD, Holz RW, Smith SJ. Regulation of presynaptic phosphatidylinositol 4,5-biphosphate by neuronal activity. *J Cell Biol*. 2001 Jul;154(2):355–68. doi: 10.1083/jcb.200102098

385. Cao H, Chen J, Krueger EW, McNiven MA. Src-mediated phosphorylation of dynamin and cortactin regulates the “constitutive” endocytosis of transferrin. *Mol Cell Biol*. 2010 Feb;30(3):781–92. doi: 10.1128/mcb.00330-09

386. Yang Y, Ning Y, Chen Y, Tian T, Gao X, Kong Y, et al. Transferrin receptor promotes endometrial cancer proliferation by activating the iron-dependent PI3K/AKT/mTOR signaling pathway. *Cancer Sci*. 2025 Mar;116(5):1352–65. doi: 10.1111/cas.70015

387. Puri C, Park SJ, Wrobel L, Rubinsztein DC. Transferrin receptor controls both autophagosome formation and closure via phosphatidylinositol 3-phosphate synthesis. *Dev Cell*. 2025 Oct;60(20):2715–29. doi: 10.1016/j.devcel.2025.05.016

388. Teng FYH, Wang Y, Tang BL. The syntaxins. *Genome Biol*. 2001 Oct;2(11):30121–7. doi: 10.1186/gb-2001-2-11-reviews3012

389. Bilan F, Thoreau V, Nacfer M, Dérand R, Norez C, Cantereau A, et al. Syntaxin 8 impairs trafficking of cystic fibrosis transmembrane conductance regulator (CFTR) and inhibits its channel activity. *J Cell Sci*. 2004 Apr;117(10):1923–35. doi: 10.1242/jcs.01070

390. Proctor KM, Miller SCM, Bryant NJ, Gould GW. Syntaxin 16 controls the intracellular sequestration of GLUT4 in 3T3-L1 adipocytes. *Biochem Biophys Res Commun*. 2006 Aug;347(2):433–8. doi: 10.1016/j.bbrc.2006.06.135

391. Prekeris R, Yang B, Oorschot V, Klumperman J, Scheller RH, Bonifacino J. Differential roles of syntaxin 7 and syntaxin 8 in endosomal trafficking. *Mol Biol Cell*. 1999 Nov;10(11):3891–908. doi: 10.1091/mbc.10.11.3891

392. Amessou M, Fradagrada A, Falguières T, Lord JM, Smith DC, Roberts LM, et al. Syntaxin 16 and syntaxin 5 are required for efficient retrograde transport of several exogenous and endogenous cargo proteins. *J Cell Sci*. 2007 Apr;120(8):1457–68. doi: 10.1242/jcs.03436

393. Bucci C, Parton RG, Mather IH, Stunnenberg H, Simons K, Hoflack B, et al. The small GTPase rab5 functions as a regulatory factor in the early endocytic pathway. *Cell*. 1992 Sep;70(5):715–28. doi: 10.1016/0092-8674(92)90306-w

394. Stenmark H, Parton RG, Steele-Mortimer O, Lütcke A, Gruenberg J, Zerial M. Inhibition of rab5 GTPase activity stimulates membrane fusion in endocytosis. *EMBO J*. 1994 Mar;13(6):1287–96. doi: 10.1002/j.1460-2075.1994.tb06381.x

395. Kirchhausen T, Macia E, Pelish HE. Use of dynasore, the small molecule inhibitor of dynamin, in the regulation of endocytosis. *Methods Enzymol*. 2008 Jan;438(1):77–93. doi: 10.1016/s0076-6879(07)38006-3

396. van Dam EM, Stoorvogel W. Dynamin-dependent transferrin receptor recycling by endosome-derived clathrin-coated vesicles. *Mol Biol Cell*. 2002 Jan;13(1):169–82. doi: 10.1091/mbc.01-07-0380

397. McCluskey A, Daniel JA, Hadzic G, Chau N, Clayton EL, Mariana A, et al. Building a better dynasore: the dyngo compounds potently inhibit dynamin and endocytosis. *Traffic*. 2013 Dec;14(12):1272–89. doi: 10.1111/tra.12119

398. Lees JG, Gorgani NN, Ammit AJ, McCluskey A, Robinson PJ, O'Neill GM. Role of dynamin in elongated cell migration in a 3D matrix. *Biochim Biophy Acta Mol Cell Res*. 2015 Mar;1853(3):611–8. doi: 10.1016/j.bbamcr.2014.12.008

399. Chircop M, Malladi CS, Lian AT, Page SL, Zavortink M, Gordon CP, et al. Calcineurin activity is required for the completion of cytokinesis. *Cell Mol Life Sci*. 2010 Nov;67(21):3725–37. doi: 10.1007/s00018-010-0401-z